Dissertation

submitted to the

Combined Faculties of the Natural Sciences and Mathematics

of the Ruperto-Carola-University of Heidelberg, Germany

for the degree of

Doctor of Natural Sciences

put forward by

Mgr. Jiří Daněk

born in Prostějov, Česká republika

Oral examination: May 16$^{\text{th}}$, 2018

Coulomb effects in the dipole and nondipole regimes of strong-field ionization

Referees: Honorarprof. Dr. Christoph H. Keitel

Prof. Dr. Björn Malte Schäfer

Zusammenfassung

Aufgrund der jüngsten Verbesserungen der experimentellen Genauigkeit sowie den Fortschritten bei Techniken der Laserfeldgenerierung wurden neue Phänomenen in der Starkfeld-Laserionisation beobachtet. Die Erklärung der neuen Phänomene basiert auf bisher unidentifizierten Auswirkungen des Coulombfeldes des Atomkerns auf das ionisierte Elektron und auf der Wechselwirkung zwischen dem Coulomb Feld und den *Non-Dipole*-Effekten.

Diese Doktorarbeit verfolgt zwei Ziele. Erstens entwickeln wir analytische Methoden für die genauere Beschreibung der Starkfeld-Laserionisation unter besonderer Berücksichtigung der *Non-Dipole*-Effekte. Diese Methoden basieren auf der genaueren Behandlung der Dynamik des ionisierten Elektrons im Laserfeld und Coulombfeld des Atomkerns. Zweitens verwenden wir die entwickelten analytischen Methoden zusammen mit der üblichen theoretischen Maschinerie der Starkfeld-Ionisationsphysik für die Erklärung von Ergebnissen der gegenwärtigen und weiterlaufenden Experimente, die der Wechselwirkung zwischen dem Coulombfeld und den *Non-Dipole*-Effekten in der Starkfeld-Laserionisation mit linear oder elliptisch polarisierten mittinfraroten Laserfeldern gewidmet sind. Ebenso verwenden wir unsere Methoden für die Erweiterung von Techniken der Starkfeld-Holographie auf das *Non-Dipole*-Regime. Im Rahmen des ersten Zieles erweitern wir die Coulomb-korrigierte "Starkfeld-Näherung" (Strong-field approximation), indem wir die höheren Terme in der Reihenentwicklung der Kontinuums-Wellenfunktion des Elektrons im Laser- und Coulombfeld (der sogenannten Eikonal-Volkov-Approximation) berücksichtigen. Dank der Erweiterung ermitteln wir eine nicht-adiabatische Verschiebung des Photoelektronimpulses. Des Weiteren entwickeln wir die klassische Theorie für die Beschreibung von mehrfachen Kollisionen des ionisierten Elektrons mit dem Atomkern, welche die Ursache für den sogenannten Effekt der Coulombfokussierung (Coulomb focusing) sind. Die Hauptidee ist die Beschränkung der Coulombwechselwirkung auf unterscheidbare und wohl definierte Rekollisionspunkte an der klassischen Trajektorie des Elektrons. Diese Beschränkung führt zu analytischen Einschätzungen von Impulsübertragungen an diesen Punkten und schließlich zur Einschätzung der totalen Coulombimpulsübertragung für jedes bei beliebiger Phase getunnelte Elektron. Obwohl wir das Coulombfeld wie eine Störung in der Nähe der Kollisionen behandeln, scheint es die globale Dynamik durch mehrfache Kollisionen wesentlich zu stören.

Es werden die von der klassischen Theorie abgeleiteten analytischen Formeln für die Coulombimpulsübertragung verwendet, um ein besseres Verständnis von Eigenschaften der Coulombfokussierung in verschiedenen Feldkonfigurationen zu bekommen. Konkret liefern wir die Erklärung und Skalierung der nicht intuitiven Beugung der zentralen und vertikalen Coulombfokussierungsspitze, die in gegenwärtigen Experimenten mit linear polarisiertem mittinfrarotem Laserfeld beobachtet wurde und zeigen die Abhängigkeit der Beugung von der Photoelektronenergie. Auch erklären wir die Beobachtung von einer scharfen, aus niederenergetischen Elektronen bestehenden Spitze in der experimentellen Photoelektron-Impulsverteilung im Laserfeld mit elliptischer Polarisation, und zeigen wie sie mit der von den *Non-Dipole*-Effekten verursachten Verschiebung der Photoelektron-Impulsverteilung gegen die Propagationsrichtung des Lasers zusammenhängt.

Zum Schluss bieten wir eine Interpretation der Messungen im Rahmen der Starkfeld-

Holographie im *Non-Dipole*-Regime. Wir verwenden drei unterschiedliche theoretischen Modelle für die Berechnung des Interferenzmusters: Coulomb-korrigierte "Starkfeld-Näherung", Quantum-Trajektorie Monte-Carlo-Simulation und (simple-man's) Dreischritt-modell, um die Auswirkung der *Non-Dipole*-Effekte auf die Interferenzmaxima zu be-schreiben. Wir analysieren die Signatur der Atomsorte in den Interferenzmustern der Photoelektron-Impulsverteilung und diskutieren zwei Fälle im Detail: Xenon, sowie das Sauerstoffmolekül.

Abstract

Due to recent advancements in measurement precision and in laser field generation techniques, new phenomena were observed in strong-field ionization physics. It appeared that the explanation of new phenomena were based on the previously unidentified Coulomb field effects of the atomic core on the ionized electron, and on the interrelations of the Coulomb field and nondipole effects.

The aim of this thesis is two fold. Firstly, we develop analytical methods for more accurate description of the strong-field ionization process, which is based on a more accurate treatment of the electron dynamics in the laser and Coulomb field of the atomic core, with an emphasize on nondipole effects. Secondly, we apply the developed analytical methods, along with the common theoretical machinery of strong-field physics, for explanation of the results of recent and ongoing experiments devoted to the interplay of the Coulomb and nondipole effects in strong-field ionization process in mid-infrared laser fields of linear and elliptical polarization, as well as for extension of the strong-field holography technique into the nondipole regime.

Within the first aim, we advance the quantum theory of the Coulomb-corrected strong-field approximation, calculating the high-order correction terms to the electron continuum wave function in the laser and Coulomb fields using the eikonal-Volkov approximation and describe nonadiabatic momentum shifts for photoelectrons. Further, we develop a classical theory for the description of multiple recollisions of the ionized electron with the atomic core, which is the basis for understanding of the, so-called, Coulomb focusing phenomenon. The key point is a restriction of the interaction to well specified and defined rescattering points along the electron classical trajectory, which leads to analytical estimates for the momentum transfer at these points and, subsequently, for the total momentum transfer to any electron tunneled at any arbitrary phase of the laser field. Although, the Coulomb field is treated as a perturbation near each scattering point, it appears to disturb the global dynamics significantly via multiple recollisions.

The derived analytical formulas for the Coulomb momentum transfer of the classical theory are employed to gain a deeper insight into the features of Coulomb focusing in different field configurations. In particular, we provide an explanation and scaling for the counterintuitive negative shift of the Coulomb focusing cusp in a recent experiment with a linearly polarized mid-infrared laser field, and show its dependence on the photoelectron energy. Further, we explain the appearance of the sharp ridge of low-energy electrons in the experimental photoelectron momentum distribution in an elliptically polarized laser field, and show how it is related to the shift of photoelectron momentum distribution against the laser propagation direction due to nondipole effects.

Finally, we give an interpretation of the experimental results on strong-field photoelectron holography in the nondipole regime. We employ three different theoretical techniques for calculation of interference patterns: Coulomb-corrected strong-field approximation, Quantum-Trajectory Monte Carlo simulations and Simple-man's three-step model, and provide a description of the nondipole features of the interference fringes. We analyze the signature of atomic species for the interferometric holography pattern in the photoelectron distribution, discussing the cases of a xenon atom and an O_2 molecule.

In the course of this thesis, the following articles have been published in peer-reviewed journals:

- Michael Klaiber, Jiří Daněk, Enderalp Yakaboylu, Karen Z. Hatsagortsyan, and Christoph H. Keitel
  Strong-field ionization via a high-order Coulomb-corrected strong-field approximation
  Phys. Rev. A **95**, 023403 (2017)

- Jochen Maurer, Benjamin Willenberg, Jiří Daněk, Benedikt W. Mayer, Christopher R. Phillips, Lukas Gallmann, Michael Klaiber, Karen Z. Hatsagortsyan, Christoph H. Keitel, and Ursula Keller
  Probing the ionization wave packet and recollision dynamics with an elliptically polarized strong laser field in the nondipole regime
  Phys. Rev. A **97**, 013404 (2018)

Moreover, the following articles have been submitted for publication in peer-reviewed journals:

- Jiří Daněk, Michael Klaiber, Karen Z. Hatsagortsyan, Christoph H. Keitel, Benjamin Willenberg, Jochen Maurer, Benedikt W. Mayer, Christopher Phillips, Lukas Gallmann, Ursula Keller
  Interplay between Coulomb-focusing and non-dipole effects in strong-field ionization with elliptical polarization
  submitted to J. Phys. B: Special issue celebrating 25 years of re-collision physics (2018)

- Jiří Daněk, Karen Z. Hatsagortsyan, Christoph H. Keitel
  Analytical approach to Coulomb focusing in strong field ionization
  submitted, preprint on arXiv:1707.06921v2 (2017)

In addition, the following article is in preparation:

- Jochen Maurer, Benjamin Willenberg, Jiří Daněk, Benedikt W. Mayer, Christopher R. Phillips, Lukas Gallmann, Michael Klaiber, Karen Z. Hatsagortsyan, Christoph H. Keitel, and Ursula Keller
  Photoelectron holography
  in preparation

Contents

Introduction

For the last fifty years, the dominant analytical theory used in strong-field ionization physics was the strong-field approximation (SFA) [1–3]. Although SFA in its simplest form omits the influence of the Coulomb field on the ionized wave packet, it celebrated a triumph and became the workhorse in the strong-field physics as it was successful in the explanation of many strong-field phenomena, e.g., the above-threshold ionization (ATI) [4,5] as a special case of multiphoton ionization [6], high-order harmonic generation (HHG) [7–10], and nonsequential double ionization (NSDI) [11–14].

For intuitive understanding of strong-field phenomena, the two-step model (also called the simple-man's or three-step model) [15] has been put forward. The model is based on the classical propagation of the electron in the ionizing laser field, while neglecting the Coulomb interaction, and introducing the recollision concept when the laser driven electron returns to the atomic core. Upon recollision the electron may scatter off the atomic core absorbing additional photons from the laser field (ATI), or kick out the second electron at the rescattering (NSDI), or recombine with the atom emitting the excess of energy as a high energy photon (HHG). The simple three-step model provides an excellent framework for investigation and understanding of many strong-field phenomena, because it catches the main essence of the processes - the recollisions.

The SFA in its simplest form is based on calculation of the transition amplitude between the atomic bound state and the Volkov wave function of a free electron in an external laser field [16]. Because of the neglected Coulomb potential of the atomic core, the SFA is strongly speaking suitable only for description of ionization processes of negative ions. In this respect, the approximation of the atomic potential as a short-range or a zero-range potential has been applied [17, 18]. The deficiency of SFA is that the transition amplitude is not gauge invariant and a proper choice of the gauge appears to be crucial for a good agreement with the experiments [19–23].

Although SFA describes qualitatively correct the features of strong-field phenomena, it does not provide the correct ionization rates for neutral atoms. This was well known since the seminal works of Perelomov, Popov, Terent'ev (PPT) [24–29] that the ionization rate of the atom in a strong laser field can be significantly disturbed by the Coulomb field of the atomic core and therefore by the Coulomb interaction during the ionization should not be neglected. The Coulomb-corrected rates of strong-field ionization in the quasistatic regime are given by the Ammosov-Delone-Krainov theory (ADK) [30, 31]. Nevertheless, the results of ADK are already contained in PPT theory in the limit of of zero-frequency field and both theories coincide for mid-IR wavelengths.

Recently, several extensions to the SFA incorporating the Coulomb effects on the ionizing electron were proposed: Coulomb-corrected SFA (CCSFA) [32–34] generalized also for the relativistic regime [34–36], more rigorous Analytical R-matrix theory (ARM) [37–39], or the Coulomb-corrected quantum-orbit based SFA (CQSFA) [40] including the

Coulomb interaction for the quantum-orbits [41].

In this thesis we are going to address the CCSFA more closely in Chap. 1. We will explain the basic idea behind the SFA in Sec. 1.1 and to explain the inclusion of the Coulomb potential via first-order corrections obtained from eikonal expansion of the electron wave function in the continuum Sec. 1.2. We will repeat the calculation from [34, 42] avoiding the Coulomb singularity via saddle-point approximation and show that the first-order correction leads to reproduction of the PPT tunneling rate. The contribution of this thesis to the topic of strong-field ionization physics is analysis of the higher-order correction terms in the eikonal expansion, which are neglected in the standard CCSFA. We are going to identify quasiclassical and quantum contributions in the second-order correction and discuss their influence for the nonadiabatic momentum shift [43–45] in 1D case and discuss the implications for the 3D case in the Sec. 1.3.

Nowadays, improvements in the molecular imaging and the molecular tomography techniques based on the strong-field phenomena with molecules, triggered interest for theoretical description of such processes. Molecules unlike atoms do not manifest spherical symmetry due to their complex spatial structure and their orientation with respect to the linearly polarized ionizing laser field plays role for the measured photoelectron momentum distribution (PMD) [46–49]. The main difference to the ionization of an atom is the alignment-dependent ionization rate [50, 51] arising due to the multi-core interference [52], since the tunneled electron can originate from proximity of any atomic core. This interference also plays a role for phase structure of the tunneled wave packet and can influence the structure of the PMD [49, 53] as we will discus later. The first theoretical approach to the ionization of molecules was described by extension of the ADK theory for molecules MO-ADK [54] which can explain the orientation dependent ionization rate, but does not account for the phase of the tunneled wave packet. The latter issue can be addressed with the molecular strong-field approximation (MO-SFA) [46, 55–58]. Nevertheless, the MO-SFA suffers under the same issues as the atomic SFA. Recently, a new method of partial-Fourier-transformation (MO-PFT) was proposed [59–61]. This method relies on partial transformation of the bound electron wave function, which reduces the ionization process to a 1D tunneling problem in the zero-range potential. MO-PFT was able to reproduce the ADK tunneling rates for atoms [59] and explain the alignment-dependent ionization rate for CO_2 [62].

In the Sec. 1.5, we are going to generalize the tunneling rate and phase structure of the tunneled electron packet for any arbitrary orientation of the O_2 molecule from [60]. We will analyze how both features depend on the alignment and also on the initial transversal momentum of the tunneled electron. These results will be used in the last chapter of the thesis, where we will address their influence on the measured PMD.

As we already mentioned, it has been known for a long time that the Coulomb effects influence the ionization process and have to be accounted for properly. Nevertheless, later it has been realized that the Coulomb field of the atomic core also imprints specific signatures on the momentum distribution of photoelectrons [63] during the electron's excursion in the laser field after the release (tunneling) from the bound state. The Coulomb field effect on the electron dynamics is conspicuous, first of all, near the tunnel exit [64], and further during rescatterings [65]. While the first effect exists at any polarization of the laser field, the rescattering is mostly efficient in the case of linear polarization. Al-

though even in a laser field of elliptical plarization rescattering and consequent Coulomb effects can take place [66–73].

Hard rescatterings with a small impact parameter induce well-known processes of ATI, HHG, and NSDI. In contrast to that, due to multiple forward scattering of ionized electrons by the atomic core at large impact parameters during oscillation in the laser field, the electrons with large transverse momentum at the ionization tunnel exit finally appear with low transverse momentum. Accordingly, the large initial transverse momentum space at the tunnel exit is squeezed into the asymptotic small one, i.e., the Coulomb field focuses electrons in the momentum space along the laser polarization direction which is termed as Coulomb focusing (CF) [63, 74, 75]. In early experiments the traces of CF were observed as cusps and humps in the photoelectron momentum distribution (PMD) [76–79]. Recently, due to advancements of mid-infrared laser technique [80], the interest for CF has been significantly increased with observation of rich structures in PMD near the ionization threshold in long wavelength laser fields, the, so-called, low-energy structures (LES) [81–83], very-low-energy structures [84,85], and zero-energy structures [86–91]. The origin of LES has been traced to multiple forward scattering by the Coulomb field, which induces transverse and longitudinal bunching of the electron momentum space [92–99]. LES are well resolved in mid-infrared laser fields, when the Keldysh parameter is small, the interaction is essentially in the tunneling regime, and when classical features of the three-step model [65] are evident.

The theories as CCSFA and ARM contain a quantum and nonperturbative description of the Coulomb field effects. The CCSFA approximation has been successfully applied for explanation of LES structures [94] and the more systematic ARM theory was also extended to treat recollisions in the continuum [100, 101].

It appeared that the perturbative SFA is also able to account for LES [102–107], when appropriate trajectories with soft recollisions [97] are included. However, this description is only qualitative, because for a correct quantitative description the effect of multiple recollisions should be taken into account.

In mid-infrared laser fields, the electron dynamics after tunneling is mainly classical, because the characteristic energies of the process, namely the ionization and ponderomotive potentials, greatly exceed the photon energy in this regime. Therefore the classical-trajectory Monte Carlo (CTMC) method [108–110] has been successful in explaining LES features, see e.g., [83, 93, 98, 111, 112]. Although both CCSFA and CTMC successfully predict the existence of LES, they deliver only little insight into the underlying physics as they both employ classical trajectories via numerical calculations which hide the physical picture of the transformation of the electron's initial momentum space at the tunnel exit into the asymptotic one at the detector.

CF arises due to the long range Coulomb interaction between the tunneled electron and its parent ion. This interaction is conspicuous at rescattering points when the tunneled electron revisits the atomic core during its excursion driven by the laser field. Usually the momentum transfer during high-order rescattering events is decreasing with its order. However, the decrease is not monotonous and the accurate description requires accounting also for high-order rescatterings [96, 111, 113].

Moreover, recent experiment with linearly polarized mid-infrared lasers [114] have shown that CF is significantly modified in the nondipole regime. The breakdown of

the dipole approximation was firstly observed in the case of linear polarization of the laser field [114], as a counterintuitive shift of the PMD peak opposite to the laser propagation direction which was attributed to the interaction of the tunneled electron with the Coulomb field of the parent ion. Further numerical calculations of time-dependent Schrödinger equation (TDSE) have shown that the PMD shift with respect to the dipole approximation case is not uniform but momentum dependent [115]. The same conclusion has been drawn from the classical [116], SFA [117], and CCSFA calculations [118] and corresponds to the interrelation of the CF and the magnetically induced drift as noted in [119]. However, the intuitive explanation of the nondipole features of PMD is still missing.

In course of this thesis, we will develop a classical analytical theory for the description of CF in linearly polarized laser fields with respect to the underlying momentum transfer due to the Coulomb interaction in Chap. 2. We will include nondipole effects, accounting for the laser magnetic field induced drift of the ionized electron along the laser propagation direction during the excursion in the laser field. The Coulomb field of the atomic core will be treated as a perturbation to the laser driven trajectory near the recollision point. The latter is well justified for forward-scattering of the recolliding electrons. In Sec. 2.1 we will discuss the key assumptions of our perturbative nondipole model and its applicability. Further, we are going to introduce a classification of recollision points as fast or slow with respect to the electron velocity at the recollision in Sec. 2.2. Once we will have seized the Coulomb interaction by two types of recollisions, we are going to derive analytical formulas for the Coulomb momentum transfer to the recolliding electron at these points in Sec. 2.3. The scaling of the Coulomb momentum transfer at the recollision (R-CMT) with respect to the rescattering parameters (momentum and impact parameter) as well as with respect to the laser intensity and wavelength will be also derived in the section and further analyzed for characteristic trajectories in global perturbation approach in Sec. 2.4 for dipole case. Furthermore, we will provide high-order corrections to the known formula for the initial Coulomb momentum transfer (I-CMT) which is necessary for keeping the overall precision of our model in Sec. 2.5.

Once we will have captured the Coulomb interaction through I-CMT and R-CMT, we are going to estimate the total Coulomb momentum transfer and derive the final PMD in Chap. 3 in the dipole regime. Firstly, we will discus the generalization of the recollision points for any electron trajectory and suitability of the R-CMT formulas in Sec.3.1. In Sec. 3.2, two methods will be proposed and compared: the fully perturbative and step-by-step method. While in the first method the Coulomb effect is assumed to be a perturbation with respect to the laser driven global electron trajectory, in the second method the trajectory is adjusted after each recollision. Special attention will be devoted to the contribution of high-order rescattering events, and to the derivation of the effective number of rescatterings. The two methods will be used to derive the PMD via modified CTMC simulations in Sec. 3.3 and shown to be able of reproduction of the main CF features. Further, in Sec. 3.4 we are going to propose an alternative way of PMD derivation, where we will approach the CF as transformation of the momentum phase space undisturbed by the Coulomb interaction.

Finally, we will return to the nondipole case in Chap. 4 and employ our analytical framework for investigation of the counterintuitive energy-dependent bend of the cusp

in the PMD. We will discuss the modification of rescatterings and hence of CF due to the magnetic force in Sec. 4.1. Moreover, with extending the three-step model we are going to reveal a fine interplay of the nondipole and Coulomb field effects responsible for the energy-dependent bend of the cusp. The role of the higher-order recollisions will be addressed in Sec. 4.2, where we will find a direct relationship between multiple recollisions and the fine structure of the cusp.

The breakdown of the dipole limit can be attributed to the increase of the electron pondermotive energy due to its quadratic scaling with respect to the laser wavelength. Because of this, the magnetic $\mathbf{v} \times \mathbf{B}$-term in the Lorentz force becomes significant [120,121] and the magnetic field has to be included [122–126] for longer wavelengths. Due to the scaling law, application of the mid-IR lasers increases the pondermotive energy to such an extent that, e.g., HHG of coherent soft x-rays becomes possible [127], but the nondipole effects are still small enough (in terms of the Lorentz deflection parameter [128,129]) that the recollisions are not suppressed unlike in the cases discussed in [123–126,130–133]. The Lorentz force along the propagation direction is responsible for the photon's momentum transfer to electrons observed in [134], for the momentum partition between the ion and the electron during ionization [117,135–138] and for the already mentioned modification of the Couloomb focusing (CF) [114]. The breakdown of the dipole limit manifests also in the case of elliptically polarized laser fields and similar nondipole effects on the CF as in the linear polarization case should take place. The latter holds since recollisions exist also for the elliptical polarization laser as mentioned above. CF and related caustic structures due to multiple recollisions of the electrons [96,113,139] carry important information on the rescattering dynamics [85,88,99–101,116,140,141]. Nevertheless, there were no observations of the CF caustics until recently [142], because the rescattered electrons are embedded within a large background of direct photoelectrons. The measurements presented in [142] presented first observation of CF caustics in elliptical polarization and even allowed experimental separation of the direct and rescattered electrons. Moreover, the experiment triggered our curiosity by observation of nondipole effects acting differently on direct and rescattered electrons leading to ellipticity-dependent transition of the momentum peak offset from negative to positive values with increasing ellipticity.

In the course of this thesis, we are going to address the newly observed features with our analytical framework in Chap. 5. Firstly, the extension of our perturbative model will be presented in Sec. 5.1 for dipole and nondipole case where we will expose the similarity of the drift along opposite direction to the minor axis of the polarization ellipse induced by the ellipticity and the magnetically induced drift due to the nondipole effects. In the following section 5.2, we are going to analyze the PMD in the dipole regime by CTMC simulations and reproduce the observed central cusp and reveal its inner structure. We will divide the central cusp into three parts with respect to number of recollisons experienced by the underlying trajectories and address each part with our analytical framework. The nondipole effects will be included and analyzed in Sec. 5.3, where the role of the CF and of the ellipticity for the measured transition of the peak offset will be revealed. Our understanding will be used to estimate the averaged size of CF and the width of the tunneled wave-packet from the experimental data yielding agreement with the simulations.

There are further positive aspects of the high ponderomotive energies attained by

the photoelectrons in the mid-IR laser fields except of the discussed classical behavior. Namely, the de Broglie wavelength of the tunneled electrons becomes comparable to the internuclear distances in molecules and hence increases the resolution of laser-induced electron diffraction imaging [143–145]. Furthermore, the excursion of the laser-driven electrons in the continuum is given by the amplitude of the quiver motion, which can greatly exceed the recollision impact parameter even for long wavelengths at relatively small intensities of the applied laser field, leading to the description where the recollision concept is well defined.

All three aspects are crucial for strong-field time-resolved photoelecton holography as presented in [146, 147]. The holography patterns exhibits spider-like structure with interference fringes that arise as multi-path interference of direct (i.e., "reference") and forward-scattered (i.e., "signal") electrons originating at a singular point of the tunnel exit (as we will discuss in greater detail in Chap. 6). The advantage of the holography over the diffraction imaging is that the hologram encodes both the magnitude and phase of the scattering amplitude [148] carrying the information about the parent ion and the electron dynamics with high spatial and temporal resolution (femtosecond resolution for the ion and attosecond resolution for the electron [147]). The strong-field photoelectron holography is a subcycle phenomenon and the individual features of the interferometric structure can be related to interference of electrons originating from particular parts of the laser cycle [149–152]. Interestingly, the holographic structure does not disappear when applying lasers of shorter near-infrared wavelengths [153] as long as the ponderomotive energy greatly exceeds the energy of the laser photons. Nevertheless, in such parameter region the above-threshold ionization starts to dominate over the tunnel ionization and back-scatterings becomes more favorable. The numerical analysis via TDSE indicated existence of holographic pattern created by the back-scattered electrons [47, 154, 155], which was later also found in the experiment [48]. The advantage of high-energetic back-scattered electrons is their sensitivity to the molecular target allowing investigation of ultrafast molecular dynamic with attosecond resolution [46, 156, 157]. The orientation of the molecule was shown to leave unique imprint in the spectrum of the back-scattered electrons in [46–48, 145, 158] and in the spectrum of forward-scattered electrons in [49] opening new paths in high-resolution imaging of sub-Ångström and sub-femtosecond structural dynamics in molecules. This was recently manifested by simultaneous imaging of purely electronic valence-shell dynamics via strong-field photoelectron holography and observation of electronic-rotation dynamics via laser-induced diffraction [159].

The spider-like pattern in the mid-IR holography is contributed to the interference of direct and forward-scattered electrons. The "spider legs" exhibit a nontrivial shape which can be associated with specific number of times the electron is driven past its parent ion before rescattering significantly [111].

A simple three-step model based on qualitative analysis of the holographic pattern presented in [147] neglects Coulomb potential and excludes higher-order recollisons. However, the Coulomb potential modifies the interference pattern with respect to the three-step model severely and has to be taken into account [152]. As we already discussed, the numerical CTMC simulations are able to incorporate the Coulomb interaction fully and provide an invaluable tool for investigation of CF. The CTMC simulation can be extend to account also for the interference by computation of the phase accumulated

by the electrons along the classical trajectory which we now call quantum trajectories. These trajectories are the basis of Quantum-trajectory Monte Carlo (QTMC) simulation which was developed in [160] and shown to be in good agreement with photoangular momentum distribution for ATI. Nevertheless, the QTMC should be corrected by the inclusion of the non-adiabatic effects in the case of near-IR wavelength [161]. Further improvements to the quantum trajectory yielding better correspondence to the TDSE results were presented in [162].

We should also note, that further analysis of the interferometric spider-like pattern was made via CQSFA [151, 163, 164] and resulted in good agreement with the TDSE solutions in the ATI regime.

To complete our listing, the recent progress in development of Siegert state [165] based adiabatic ionization theory [166] offers a possibility to determine the phase of scattering amplitude in the near-forward rescattering photoelectron holography and opens a new channel for extraction of structural information of ultrafast processes with highly time-resolved imaging [167]. Nevertheless, this theory can be solved only numerically and can be used only for finite-range potentials which restricts its possible implementations.

As we have seen, the topic of forward-scattering strong-field photoelectron holography is new and an unsettled branch of strong-field physics. Our contribution to the field will be presented in Chap. 6. Our main aim will be the nondipole effects and their role for the spider-like holographic structure. The nondipole effects arise inevitably in the tunneling regime with mid-infrared wavelengths and breakdown of dipole approximation is to be expected as in the classical case [114]. In Sec. 6.1, we will briefly introduce our ionization setup. In Sec. 6.2, we will derive a quantum description via perturbative SFA. We will show that the "spider legs" arise already in the second-order perturbative SFA along with the overall shift against the propagation direction of the laser field. Further, we are going to include the Coulomb interaction fully via CCSFA in Sec. 6.3 and show that the Coulomb potential of the parent ion plays an essential role for the position of the interference maxima. We will discuss the influence of the higher-order rescatterings on the number of interfering paths and hence on the holographic pattern at the end. In the following Sec. 6.4, we are going to revise the QTMC simulation. We will show that the QTMC simulation can reproduce all typical interferometric structures arising from multi-cycle ionization and also the spider-like holographic structure arising due to intracycle interference [149]. In addition, we are going to investigate the role of the target on the spider-like structure via restricted QTMC simulations (RQTMC) in Sec. 6.5. Especially, we are going to address the difference between the photoelectron holography of atoms and diatomic molecules represented by atomic xenon and molecular oxygen, respectively. Moreover, we will investigate how the polarizability of the target changes the interferometric structure via quadratic Stark shift and induced electric dipole moment for both the atom and the molecule by RQTMC. We will also address the multi-electron effects and their role on the interference in the case of xenon. As mentioned above, the molecule has an alignment-dependent tunneling rate and phase structure of the diatomic molecules as mentioned above. We will analyze this in greater detail and find a suitable orientation representing the expected holographic pattern created by an unaligned molecule in the experiment. These results will be used in QCMT simulations comparing the difference of the holographic patterns of xenon and unaligned molecular

oxygen. Finally, we are going to investigate the scaling of the characteristic features of the strong-field holography with the three-step model in the nondipole regime in Sec. 6.6. We will find that the main maximum of the interferometric spider-like structure is shifted against the laser propagation direction by the same amount as in the discussed classical case of CF and establish the connection between the classical and the quantum CF in the nondipole regime.

Chapter 1

Strong-field ionization

In this chapter, we are going to address the topic of strong-field ionization in atomic and molecular physics. First of all, we are going to introduce the famous strong-field approximation (SFA) and its Coulomb-correction version (CCSFA) in the first two sections. In order to illustrate the main ideas behind the SFA and CCSFA, we are going to repeat the calculations from [42] in the first and in the second section of this chapter, respectively. In the third section, we will analyze the role of the high-order Coulomb-correction terms and their implication for the tunneling time delay (this part will be based on [168]). Furthermore, we are going to briefly discuss various strong-field ionization theories and their advantages and drawbacks. In the last section, we will briefly discuss various analytical approaches to the strong-field ionization of diatomic molecules in the last section. We are going to put forward the Partial Fourier-transformation method for its straightforward application and generalize the results from [60] for tunnel ionization of O_2 with any arbitrary orientation of its molecular orbital.

1.1 SFA

The SFA is a quantum theory and operates with wave functions and transition amplitudes. In order to introduce the theory to the reader, let us take a small step back and start with the Schrödinger equation which fully describes the dynamics of a quantum system:

$$i\hbar\frac{\partial}{\partial t}\left|\psi(t)\right\rangle = H\left|\psi(t)\right\rangle,\tag{1.1}$$

where $\left|\psi(t)\right\rangle$ is the wave function and the H is the Hamiltonian.

The dynamics of an electron in the combined Coulomb potential $V(r)$ of a hydrogen-like atom and an external laser field $\mathbf{E}(t)$ is described by the Hamiltonian of the form

$$H = H_0 + H_{\text{int}},\tag{1.2}$$

with atomic system described by

$$H_0 \equiv \frac{\hat{\mathbf{p}}^2}{2} + V(\mathbf{r}),\tag{1.3}$$

with the momentum operator $\hat{\mathbf{p}}$ and coordinate vector $\mathbf{r}$. The interaction Hamiltonian includes only the interaction with the electric component of the laser field as

$$H_{\text{int}}(t) \equiv \mathbf{r} \cdot \mathbf{E}(t),\tag{1.4}$$

where we applied the length gauge (i.e., with the scalar potential $\phi = -\mathbf{r} \cdot \mathbf{E}(t)$). The choice of the gauge is important at this point as it not only simplifies the calculation but later also delivers good agreement with experiments [20] as the gauge invariance will be broken by further approximations.

There exist exact solutions for each of the two Hamiltonians separately. The ground state of the atomic Hamiltonian H_0 has oscillatory part due to the ionization potential I_p and the wave function solving the Schrödinger equation can be written as

$$|\phi(t)\rangle = |0\rangle \, e^{iI_p t}, \tag{1.5}$$

where $|0\rangle$ obtains the spatial component of the wave-function.

On the other hand, the free electron of the asymptotic momentum $\mathbf{p}$ in the laser field $\mathbf{E}(t)$ is governed only by the Hamiltonian H_{int} and the solution to Eq. (1.1) yields the Volkov wave-function [16]

$$\left|\psi_{\mathbf{p}}^V(t)\right\rangle = |\mathbf{p} + \mathbf{A}(t)\rangle \, e^{-i \int_{-\infty}^t \frac{[\mathbf{p}+\mathbf{A}(t)]^2}{2} \mathrm{d}t'}, \tag{1.6}$$

with the standard definition of the vector potential $\mathbf{A}(t) = -\int_{-\infty}^t \mathbf{E}(t')\mathrm{d}t'$. The Volkov solution can be expressed in the coordinate space as

$$\left\langle \mathbf{r} \middle| \psi_{\mathbf{p}}^V(t)\right\rangle = \frac{1}{(2\pi)^{3/2}} e^{iS_0^{(0)}(\mathbf{r},t)}, \tag{1.7}$$

with the classical action of an electron in a laser field in the length gauge:

$$S_0^{(0)}(\mathbf{r},t) = [\mathbf{p} + \mathbf{A}(t)] \cdot \mathbf{r} + \int_t^\infty \frac{[\mathbf{p} + \mathbf{A}(t')]^2}{2} \mathrm{d}t'. \tag{1.8}$$

The SFA is based on sewing the two solutions together yielding the matrix element for the laser-induced ionization from the ground state of the atom into the Volkov continuum state as

$$M_p = -i \int_{-\infty}^\infty \mathrm{d}t \left\langle \psi_{\mathbf{p}}^V(t) \middle| H_{\text{int}}(t) |\phi(t)\rangle. \tag{1.9}$$

The matrix element can be evaluated with Eqs. (1.5) and (1.7) as

$$M_p = -i \int_{-\infty}^\infty \mathrm{d}t \, \langle \mathbf{p} + \mathbf{A}(t)| \, H_{\text{int}}(t) \, |0\rangle \, e^{-i\tilde{S}(t)}, \tag{1.10}$$

with

$$\tilde{S}(t) \equiv \int_t^\infty \mathrm{d}t' \left\{ \frac{[\mathbf{p} + \mathbf{A}(t')]^2}{2} + \frac{\kappa^2}{2} \right\}, \tag{1.11}$$

with atomic momentum $\kappa = \sqrt{2I_p}$. When the laser frequency ω is smaller than the ground-state energy I_p and the ponderomotive potential $U_p \equiv E_0^2/4\omega^2$ (i.e., the cycle-averaged energy of a free electron in the oscillatory laser field of the amplitude E_0 [169]),

one can solve the integration over time with the saddle-point method (SPM); see, e.g., [170] yielding

$$M_p = -i \sum_s \sqrt{\frac{2\pi}{i\ddot{\tilde{S}}(t_s)}} \left\langle \mathbf{p} + \mathbf{A}(t_s) \right| H_{\text{int}}(t_s) \left| 0 \right\rangle e^{-i\tilde{S}(t_s)}, \tag{1.12}$$

where we sum over so-called saddle points of the function in the exponential defined as $\dot{\tilde{S}}(t_s) = 0$ and the dot denotes derivative with respect to time t. The transition operator can be transformed from H_{int} to $V(\mathbf{r})$ via partial integration in Eq. (1.10) as

$$M_p = -i \sum_s \sqrt{\frac{2\pi}{i\ddot{\tilde{S}}(t_s)}} \left\langle \mathbf{p} + \mathbf{A}(t_s) \right| V(\mathbf{r}) \left| 0 \right\rangle e^{-i\tilde{S}(t_s)}. \tag{1.13}$$

The differential tunneling rate can be determined via the matrix element as

$$\frac{\mathrm{d}w}{\mathrm{d}^3\mathbf{p}} = \frac{\omega}{2\pi}|M_{\mathbf{p}}|^2, \tag{1.14}$$

where we sum only over the saddle-points within one laser period in Eq. (1.13).

The SFA derives excellent results for ionization of negative ions as the potential bounding the extra electron resembles the zero-range potential, which was effectively used in the derivation of Eq. (1.10). The differential tunneling rate in the case of zero-range potential yields [171]

$$\frac{\mathrm{d}w^{(z)}}{\mathrm{d}^3\mathbf{p}} = \frac{\omega}{2\pi^2 E_0} \exp\left[-\frac{2}{3}\frac{E_0}{E_a} - \frac{\kappa}{E_0}p_\perp^2 - \frac{\kappa^3\omega^2}{3E_0^3}p_E^2 \right], \tag{1.15}$$

and leads to the total ionization rate

$$w^{(z)} = \sqrt{\frac{3}{\pi}} \frac{E_0^{3/2}}{2\kappa^{5/2}} \exp\left[-\frac{2\kappa^3}{3E_0} \right]. \tag{1.16}$$

1.2 Coulomb-corrected SFA

Nevertheless, the ionization of neutral atoms poses more challenging issue as the resulting ion exhibits long range Coulomb potential, which is felt by the electron promoted into the continuum. The SFA theory can be improved by taking into account the Coulomb field effect of the ionic core by replacing the Volkov function by the eikonal wave function instead. The Volkov function given by Eq. (1.7) and the action in Eq. (1.8) is identical to the zero-order WKB approximation of the electron wave function in the laser field. Let us note that WKB stands for the famous Wentzel-Kramers-Brillouin method as explained, e.g., in Chap. 6 of [172]. A systematic improvement of the Volkov function can be achieved by inclusion of the electron into the combined laser field $\mathbf{E}(t)$ and Coulomb potential $V^{(C)}(\mathbf{r}) = -\frac{\kappa}{|\mathbf{r}|}$ into the Schrödinger equation [168]

$$i\hbar\frac{\partial}{\partial t}\psi = -\frac{\hbar^2}{2}\Delta\psi + V^{(C)}\psi + \mathbf{r} \cdot \mathbf{E}(t)\psi, \tag{1.17}$$

which can be transformed by the ansatz of $\psi(t) = e^{iS(t)/\hbar}$ into

$$-\dot{S} = \frac{(\nabla S)^2}{2} + V^{(C)} + \mathbf{r} \cdot \mathbf{E}(t) + \frac{\hbar}{i}\frac{\Delta S}{2}. \tag{1.18}$$

By using the WKB expansion $S = S_0 + \frac{\hbar}{i}S_1 + \ldots$, we obtain the equations

$$\left(\frac{\hbar}{i}\right)^0 : \quad -\dot{S}_0 = \frac{(\nabla S_0)^2}{2} + V^{(C)} + \mathbf{r} \cdot \mathbf{E}(t), \tag{1.19}$$

with the S_0 being the classical action of an electron in the laser field and the Coulomb potential of an atomic ion. In the eikonal approximation of Eq. (1.19), the solution can be found as perturbatively taking into account the atomic potential as a perturbation and expand the action as $S_0 = S_0^{(0)} + S_0^{(1)}$. The $S_0^{(0)}$ is then again equivalent to the action of free electron in the laser field from Eq. (1.8). The novelty comes with the second term proportional to the atomic potential yielding

$$S_0^{(1)}(\mathbf{r}, t) = \int_t^\infty dt' V^{(C)}(\mathbf{r}(t')), \tag{1.20}$$

with the trajectory of the free electron in the laser field $\mathbf{r}(t') = \mathbf{r} + \int_t^{t'} dt''\mathbf{p}(t'')$ and $\mathbf{p}(t) \equiv \mathbf{p} + \mathbf{A}(t)$. The time t and the coordinate $\mathbf{r}$ can be interpreted as the time and the coordinate of the ionization, respectively. At this point one has to be careful, as the eikonal $S_0^{(1)}$ can be singular at the atomic core $\mathbf{r} \to 0$. Unfortunately, this can be avoided by saddle-point integration also over the spatial coordinate. The latter actually set the matching of the two wave solutions to the saddle point which is located sufficiently far away from the core.

Therefore, we can write the approximative wave function, so-called eikonal-Volkov wave function, in the non-relativistic regime as

$$\psi_\mathbf{p}^{(C)}(\mathbf{r}, t) = \frac{1}{(2\pi)^{3/2}} e^{iS_0^{(0)}(\mathbf{r},t) + iS_0^{(1)}(\mathbf{r},t)}. \tag{1.21}$$

This wave-function accounts for the Coulomb potential of the atomic core right after the ionization and can be included in the SFA amplitude of Eq. (1.9).

Let us note at this point that we have neglected the high-order correction terms in Eq. (1.21), which also include the perturbation atomic potential. Unfortunately, it is not mathematically feasible to compute them in general and we will have to restrict the calculation to 1D. We will address the role of the high-order correction later, but for now we will stick to the eikonal-Volkov function.

Nevertheless, further simplifications are needed in order to calculate the matrix element M_p. The problem poses the additional term $S_0^{(1)}$ in the transition amplitude and we simplify its time derivative as

$$\partial_t S_0^{(1)}(\mathbf{r}, t) \approx -V^{(C)}\left(\mathbf{r} + \int_t^\infty dt'\mathbf{p}(t')\right) \approx 0. \tag{1.22}$$

Which is a reasonable assumption because the electron at the infinite time will be far away from the ion and its potential energy will be negligible (when we do not consider any recollision). Then, the additional term $S_0^{(1)}$ leaves the saddle points unchanged and only changes the preexponential factor in Eq. (1.9) as

$$M_{\mathbf{p}}^{(C)} = -i \int\limits_{-\infty}^{+\infty} dt \, \langle \mathbf{p} + \mathbf{A}(t)| \, H_{\text{int}}(t) e^{-S_0^{(1)}(\mathbf{r},t)} \left| 0^{(C)} \right\rangle e^{-i\tilde{S}(t)} \tag{1.23}$$

where $\left| 0^{(C)} \right\rangle$ denotes the electron ground state bound in the Coulomb potential.

The last challenge that remains is the evaluation of the preexponential factor at saddle point times t_s. The term $S_0^{(1)}$ can be viewed as the sum over all potential energies that the electron possessed along its trajectory from ionization till distant future. As we do not assume that the electron will return to the atomic core, we are interested only in the short period of time after the ionization moment and once the electron recedes far enough from its parent ion, we can neglect further contributions to the term $S_0^{(1)}$. Therefore, we can expand the trajectory up to the second order around the saddle point t_s as

$$\mathbf{r}(t') = \mathbf{r} + \mathbf{p}(t' - t_s) - \frac{\mathbf{E}(t_s)}{2}(t' - t_s)^2. \tag{1.24}$$

Let us note that this approximation is well valid in the tunneling adiabatic regime of small Keldysh parameter (e.i., $\gamma = \kappa \frac{\omega}{E_0} \ll 1$). Under the assumption of adiabaticity, we can simplify the three dimensional trajectory even further to a single dimension as the electron will be accelerated by the laser against the orientation of the laser field at the ionization instance t_s given by the unit vector $-\hat{\mathbf{e}}$. For instance, for the linearly polarized laser field, the electron would be accelerated along or against the axis of polarization with respect to the orientation of the laser electric field at the ionization t_s. Therefore, we can set $\mathbf{p} = p_E \hat{\mathbf{e}}$ and $\mathbf{p}(t_s) = i\kappa \hat{\mathbf{e}}$. The standard picture for tunnel ionization [173] predicts ionization happening also around the laser polarization axis and hence we can write $\mathbf{r} = r_E \hat{\mathbf{e}}$. In this light, we can simplify the Coulomb potential term in Eq. (1.20) for our case of 1D motion as

$$\frac{1}{r(t')} = \frac{1}{|r_E + p_E(t_s)(t' - t_s) - E(t_s)(t' - t_s)^2/2|}, \tag{1.25}$$

where $E(t_s) \equiv \hat{\mathbf{e}} \cdot \mathbf{E}(t_s) = E_0 \cos \omega t_s$. The first evolution from the saddle point to the tunnel exit is parallel to the imaginary axis in the time towards the real axis, where also the trajectory becomes real. Thanks to this complex trajectory, we are not interested in the contribution of the term $S_0^{(1)}$ after the electron has reached the tunnel exit as it would contribute only with some overall phase to the matrix element $M_{\mathbf{p}}^{(C)}$. Therefore, we can restrict the integration to the interval between the ionization coordinate and the location of the tunnel exit which is reached at time t_0 given by the condition

$$\omega t_0 = -\arcsin\left(\frac{p_E \omega}{E_0}\right). \tag{1.26}$$

The integral from Eq. (1.20) can be under the upper assumptions easily evaluated and leads to

$$
\begin{aligned}
e^{-iS_0^{(1)(\mathbf{r},t)}} &= \left(\frac{1+\sqrt{1+4\lambda}}{-1+\sqrt{1+4\lambda}}\right)^{\frac{1}{\sqrt{1+4\lambda}}} \\
&\approx \frac{1}{\lambda} + \mathcal{O}(\lambda),
\end{aligned}
\tag{1.27}
$$

with the small quantity $\lambda = -\frac{\mathbf{r}\cdot\mathbf{E}(t_s)}{2\kappa^2}$, which is of the order $\sqrt{\frac{E_0}{E_a}}$. If the eikonal approximation should be valid, the correction term has to be much smaller than the unperturbed Volkov action, i.e., $S_0^{(1)} \ll \tilde{S}$. One can estimate the terms as $S_0^{(1)} \ll \tilde{S} \sim 1$ and $\tilde{S} \sim E_a/E_0$ with atomic field $E_a = \kappa^3$ (see [34]) leading to the condition

$$
\frac{E_0}{E_a} \ll 1,
\tag{1.28}
$$

which is well fulfilled in tunneling ionization regimes.

We can conclude that the Coulomb-corrected SFA ionization amplitude in the nonrelativistic regime differs by the factor

$$
Q_{nr} = -\frac{4I_p}{\mathbf{r}\cdot\mathbf{E}(t_s)},
\tag{1.29}
$$

from the standard SFA. The transition amplitude can be then easily evaluated from Eq. (1.23) as

$$
M_{\mathbf{p}}^{(C)} = 4iI_p \int_{-\infty}^{\infty} dt \left\langle \mathbf{p} + \mathbf{A}(t) \middle| 0^{(C)} \right\rangle e^{-i\tilde{S}(t)},
\tag{1.30}
$$

as the dipole term $\mathbf{r}\cdot\mathbf{E}(t_s)$ cancels with the interaction Hamiltonian at the saddle point t_s. The preexponential factor can be evaluated as

$$
\begin{aligned}
\left\langle \mathbf{p} + \mathbf{A}(t) \middle| 0^{(C)} \right\rangle &= \frac{1}{\pi} \frac{2\sqrt{2}\kappa^{5/2}}{\left\{\kappa^2 + [\mathbf{p}+\mathbf{A}(t)]^2\right\}^2} \\
&\approx -\frac{\kappa}{2} \frac{1}{\pi \mathbf{E}(t_s)^2 (t-t_s)^2},
\end{aligned}
\tag{1.31}
$$

where we kept in the last step only the leasing term in E_0/E_a. As we can see, the preexponential factor is singular at the saddle point and the Eq. (1.30) has to be calculated via the modified SPM while taking into account the pole during the integration. When we compare the present result to the case of the zero-range potential $M^{(Z)}$ from [34], we arrive at

$$
\frac{M^{(C)}}{M^{(Z)}} = \frac{2^{3/2}E_a}{|E(t_0)|}.
\tag{1.32}
$$

This correction is known from the imaginary-time method [25] but was also reproduced with the SFA techniques in [34].

In this way, we arrive from the CCSFA to the known ADK [30] (or equivalently PPT [25]) differential ionization rates including Coulomb corrections:

$$\frac{\mathrm{d}w^{(C)}}{\mathrm{d}^3\mathbf{p}} = \frac{4}{\pi^2}\frac{\omega\kappa^6}{E_0^3}\exp\left[-\frac{2}{3}\frac{E_0}{E_a} - \frac{\kappa}{E_0}p_\perp^2 - \frac{\kappa^3\omega^2}{3E_0^3}p_E^2\right], \tag{1.33}$$

and the total ionization rate

$$w^{(C)} = 4\sqrt{\frac{3}{\pi}}\frac{\kappa^{7/2}}{E_0^{1/2}}\exp\left[-\frac{2\kappa^3}{3E_0}\right]. \tag{1.34}$$

The maximum of the ionization is for the electrons ionized at the peak of the laser field and hence with $p_E = 0$. The width of the tunneled wave packet is

$$\Delta_\| = \sqrt{\frac{E_0}{E_a}}\frac{E_0}{\omega}, \tag{1.35}$$

$$\Delta_\perp = \sqrt{\frac{E_0}{E_a}}\kappa, \tag{1.36}$$

along the laser polarization axis and in the transversal direction, respectively.

1.3 The role of higher-order correction terms

In the previous section, we have seen derivation of the Coulomb-corrected strong-field theory (CCSFA) based on the replacement of the Volkov wave function for free electron in laser field by the eikonal Volkov function taking into account also the Coulomb interaction. This was done by the insertion of the Coulomb potential into the eikonal equation Eq. (1.18) and by solving this equation in a perturbative manner of the WKB approximation. Even the zero-order solution of the WKB expansion demanded further simplification and we were forced to address the Coulomb interaction term as a perturbation to the unperturbed Volkov solution while ignoring the higher-order terms [see Eq. (1.19) and discussion below]. On the one hand, we have shown that the correction term is small with respect to the Volkov classical action in the tunneling regime of Eq. (1.28), but on the other hand we did not address the importance of the higher-order terms properly. Let us note that we will follow [168] and return to this matter in this section.

For simplicity, we will restrict ourselves to one dimension along the polarization of the laser field and to atomic units through this section. Eq. (1.18) simplifies then as

$$-i\partial_t S = \frac{(\partial_x)^2}{2} - xF + \alpha\left[V(x) - i\frac{\partial_{xx}S}{2}\right], \tag{1.37}$$

with the eikonal function S from ansatz on the 1D eikonal Volkov wave function $\psi_p(x,t) = e^{iS(x,t)}/\sqrt{2\pi}$, a small artificial perturbative parameter α, Coulomb force $F \equiv -E_x(t)$ on the electron and 1D Coulomb potential of an atom with nucleas charge Z:

$$V(x) = -\frac{Z}{|x|}. \tag{1.38}$$

Let us also note that we will use half-cycle laser pulse defined via the acting force

$$F(t) = \begin{cases} E_0 \cos(\omega t) & \text{for } |\omega t| < \pi/2, \\ 0 & \text{for } |\omega t| \geq \pi/2, \end{cases} \tag{1.39}$$

where the recollisions are excluded explicitly.

As our aim is to develop higher-order CCSFA and its further extension to 3D, we will not consider the very deeply bound state of a 1D atom [174, 175], we assume the first excited state with the Rydberg-like eigenenergy, $I_p = \kappa^2/2$, and with the following wave function [176]:

$$\langle x|\phi(t)\rangle = \frac{\kappa(2\kappa x)^{Z/\kappa}}{\sqrt{2Z\Gamma\left(\frac{2Z}{\kappa}\right)}}$$

$$\equiv c_a e^{S_a(x,t)}, \tag{1.40}$$

$$S_a(x,t) = -\kappa|x| + iI_p t + \frac{Z}{\kappa}\ln(2\kappa x), \tag{1.41}$$

$$c_a = \frac{\kappa}{\sqrt{2\Gamma\left(\frac{2Z}{\kappa}\right)}}. \tag{1.42}$$

Let us also note that the ground-state wave function in a 1D soft-core potential has the same asymptotic form for $x \gg 1/\kappa$, which correspond to the region relevant for our calculations.

While minding the small artificial parameter α (corresponding to the expansion parameter $\hbar/i$ in the previous section) which we will set later to one, we can expand the action with the ansatz as

$$S = S_0 + \alpha S_1 + \alpha^2 S_2, \tag{1.43}$$

which leads after insertion into Eq. (1.37) to the zeroth-, first-, and second-order equations

$$\alpha^0: \quad -\partial_t S_0 = \frac{(\partial_x S_0)^2}{2} - xF, \tag{1.44}$$

$$\alpha^1: \quad -\partial_t S_1 = \partial_x S_0 \partial_x S_1 + V - i\frac{\partial_{xx} S_0}{2}, \tag{1.45}$$

$$\alpha^2: \quad -\partial_t S_2 = \frac{(\partial_x S_1)^2}{2} + \partial_x S_0 \partial_x S_2 - i\frac{\partial_{xx} S_1}{2}. \tag{1.46}$$

The zeroth-order equation represents free electron in electric field and was already solved in previous chapter in Eq. (1.8), which yields in 1D

$$S_0(x,t) = [p + A(t)]x + \int\limits_t^{t_f} dt' \frac{[p + A(t)]^2}{2}. \tag{1.47}$$

The first- and second-order equations can be solved with the method of characteristics

$$S_1(x,t) = \int_t^{t_f} dt' V(x(t')),$$
(1.48)

$$S_2(x,t) = \int_t^{t_f} dt' \frac{\left[\int_{t'}^{t_f} dt'' \partial_x V(x(t''))\right]^2}{2} - i \int_t^{t_f} dt' \int_{t'}^{t_f} dt'' \frac{\partial_{xx} V(x(t''))}{2},$$
(1.49)

with the electron classical trajectory $x(t') = x + \int_t^{t'} ds[p + A(s)]$, where the electron is driven solely by the vector potential $A(t) = \int_{-\infty}^t dt' F(t')$. The term S_1 is the correction due to the Coulomb interaction to the ionizing electron along the laser-driven trajectory as in the previous section. The real improvement comes with the first term of S_2 which introduces corrections to the potential Coulomb energy of the ionizing atom due to the perturbation of the trajectory by the Coulomb field. The second summand in S_2 is a quantum term in order of $\hbar^0$, whereas all the other terms are classical and of order $1/\hbar$. The quantum term is a special feature of the 1D system and does not appear in the 3D Coulomb field because $\Delta V(\mathbf{r}) = 0$ for $|\mathbf{r}| > 0$.

Now, we can insert all expressions into the Eq. (1.9) which reduces to a double integral over time and space

$$M(p) = -\frac{ic_a}{\sqrt{2\pi}} \iint dt dx \ e^{-iS^*(x,t) + \ln[xF(t)] + S_a(x,t)},$$
(1.50)

where $*$ indicates complex conjugation. The two-dimensional integration can be carried out by the method of the SPM as in the previous section. The saddle points has now two coordinates (t_s, x_s) defined via equations

$$\left.\frac{d\zeta(x,t)}{dt}\right|_{(t,x)=(t_s,x_s)} = 0,$$
(1.51)

$$\left.\frac{d\zeta(x,t)}{dx}\right|_{(t,x)=(t_s,x_s)} = 0,$$
(1.52)

with $\zeta(x,t) = -iS^*(x,t) + \ln[xF(t)] + S_a(x,t)$. The equations are not solvable in the full form, but we can make use of the expansion of $S(x,t)$ and solve the equation perturbatively. Thereby, we can expand the saddle point as

$$t_s = t_s^{(0)} + \alpha t_s^{(1)} + \alpha^2 t_s^{(2)},$$
(1.53)

$$x_s = x_s^{(0)} + \alpha x_s^{(1)} + \alpha^2 x_s^{(2)}.$$
(1.54)

In such case we obtain equations

$$\alpha^0 : \ \zeta_0(x,t) = -iS_0(x,t) + \ln[xF(t)] + S_{a,0}(x,t),$$
(1.55)

$$\alpha^1 : \ \zeta_1(x,t) = -iS_1(x,t) + S_{a,1}(x),$$
(1.56)

$$\alpha^2 : \ \zeta_2(x,t) = -iS_2^*(x,t),$$
(1.57)

(1.58)

with $S_{a,0}(x,t) = -\kappa x + iI_p t$, $S_{a,1}(x) = Z/\kappa \ln[2\kappa x]$. The zero-order saddle-point equation yields then

$$-\partial_t S_0(x,t) = -I_p + i\frac{F'(t)}{F(t)} \tag{1.59}$$

$$\partial_x S_0(x,t) = i\left(\kappa - \frac{1}{x}\right), \tag{1.60}$$

where prime denotes derivation with respect to time. These equation have to be solved numerically in order to arrive at $(t_s^{(0)}, x_s^{(0)})$, but we may estimate the zeroth-order solution for a cosine-electric field as $t_s^{(0)} \sim \arcsin[i\kappa\omega/E_0]/\omega - i/\sqrt{\kappa E_s}$ and $x_s^{(0)} \sim \sqrt{\kappa/E_s}$, which corresponds to the case of the short-range potential.

The saddle point coordinate x_s can be viewed as a point, where the two wave function are sewed together. Importantly, for any value of the Keldysh parameter γ, the saddle point is under the barrier (i.e., $x_s \ll x_e$, where x_e is the tunnel exit [168]). Moreover, the saddle point is also sufficiently far away from the atomic core, so the eikonal term $S_1(x_s, t)$ is not singular (i.e., $x_s\kappa \gg 1$ [168]). The ionization happens then under the barrier but far away from the exit, $1/\kappa \ll x_s \ll x_e$. Which is in analogy to the analytical R-matrix (ARM) theory that fulfills the same condition (we will briefly introduce ARM in Sec. 1.4).

The derivation of the high-order correction to the saddle point is straightforward but rather cumbersome. Therefore, we will just show the structure of the first-order solution of the (t_s, x_s) saddle point,

$$t_s^{(1)} = \left.\frac{-\partial_{xt}\zeta_0\partial_x\zeta_1 + \partial_t\zeta_1\partial_{xx}\zeta_0}{\partial_{xt}\zeta_0^2 - \partial_{tt}\zeta_0\partial_{xx}\zeta_0}\right|_{(x,t)=(x_s^{(0)},t_s^{(0)})}, \tag{1.61}$$

$$x_s^{(1)} = \left.\frac{\partial_{tt}\zeta_0\partial_x\zeta_1 - \partial_t\zeta_1\partial_{xt}\zeta_0}{\partial_{xt}\zeta_0^2 - \partial_{tt}\zeta_0\partial_{xx}\zeta_0}\right|_{(x,t)=(x_s^{(0)},t_s^{(0)})}. \tag{1.62}$$

The structure of the SFA amplitude is as the following up to the second-order:

$$M(p) \approx -ic_a\sqrt{\frac{2\pi}{\det\zeta}}\exp\left[\left(\zeta_0 + \alpha\zeta_1 + \alpha^2\zeta_2 \right.\right.$$
$$\left.\left. + \alpha^2\frac{\partial_{xx}\zeta_0\partial_t\zeta_1^2 - 2\partial_x\zeta_1\partial_{xt}\zeta_0\partial_t\zeta_1 + \partial_{tt}\zeta_0\partial_x\zeta_1^2}{2\left(\partial_{xt}\zeta_0^2 - \partial_{tt}\zeta_0\partial_{xx}\zeta_0\right)}\right)\right|_{(x_s^{(0)},t_s^{(0)})}\right], \tag{1.63}$$

with the Van Vleck-Pauli-Morette [177] determinant of the matrix formed by the second derivatives as

$$\det\zeta = \det\begin{pmatrix} \partial_{xx}\zeta & \partial_{xt}\zeta \\ \partial_{tx}\zeta & \partial_{tt}\zeta \end{pmatrix}. \tag{1.64}$$

The prefactor of $2\pi/\sqrt{\det\zeta}$ arises from the SPM and can be interpret intuitively as the typical size of the volume element $dxdt$.

Finally, we can determine the maximum of the photoelectron momentum diagram via the extremum condition:

$$\left.\frac{\partial w(p)}{\partial p}\right|_{p=p_m} = 0, \tag{1.65}$$

which can be once again solved perturbatively, $p_m = p_m^{(0)} + p_m^{(1)} + p_m^{(2)}$, and provides the maximum of the probability SFA amplitude

$$M(p_m) \sim \left. \frac{\exp(\zeta)}{\sqrt{\det \zeta}} \right|_{p=p_m}, \tag{1.66}$$

where we expand the function in the exponent up to the second order. Furthermore, we will discuss the results obtained by the n-th order expansion and refer to them as S_n CCSFA.

S_0 CCSFA

The inization amplitude in the zeroth-order yields

$$M(p) \sim \frac{\exp(\zeta_0)}{\sqrt{\det \zeta_0}}, \tag{1.67}$$

which corresponds to the standard SFA from Eq. (1.13) with zero-range potential with $Z \ll \kappa$. As our integration method SPM is only an approximative method, we have to check its accuracy. Therefore, we calculate analytically the S_0 CCSFA amplitude for a cosine-laser pulse and compare it to the PPT result [25]. We can estimate the saddle point for the most probable final momentum analytically, in an approximation where the higher-order terms in E_0/E_a are dropped as

$$x_s^{(0)} \approx \sqrt{\frac{\kappa}{E_s}} \tag{1.68}$$

$$t_s^{(0)} \approx \frac{\arcsin[i\gamma]}{\omega} - \frac{i}{\sqrt{\kappa E_s}}. \tag{1.69}$$

The PMD distribution for ionization from a short-range potential in the leading terms in E_0/E_a reads as

$$w(p) = \frac{\pi \kappa^2}{e E_s} \exp \left[-\frac{\kappa^3 \left(-\sqrt{\gamma^2 + 1}\gamma + 2\gamma^2 \sinh^{-1} \gamma + \sinh^{-1} \gamma \right)}{2\gamma^3 E_0} - \frac{(p - p^{(0)})^2}{\Delta^2} \right],$$

where

$$p^{(0)} = \int\limits_0^\infty \mathrm{d}t F(t) = \frac{E_0}{\omega} \tag{1.70}$$

is the most probable momentum, $E_s = E_0\sqrt{1 + \gamma^2}$, and the width of the distribution

$$\Delta = \frac{\sqrt{E_s}}{\sqrt{\kappa \left[\sqrt{1 + 1/\gamma^2} \sinh^{-1}(\gamma) - 1 \right]}}. \tag{1.71}$$

The derived amplitude differs from the PPT result for a short-range potential by a constant overall factor of $\pi/e \approx 1.16$, which we contribute to the difference between

the approximate integration over x with the SPM and the exact integration in PPT. Unfortunately, this will be also the case for the higher-order CCSFA terms. Luckily, the PSI does not change the overall scaling of the probability with respect to the laser field and atomic parameters but gives only approximated overall factor (for more details please see p. 4 in [168]).

Moreover, one could improve the saddle-point approximation in time while including the third-order term $\partial_{ttt}\zeta_0(x_s^{(0)}, t_s^{(0)})(t - t_s^{(0)})/6$ in the integration at the saddle point. Nevertheless, this term has no influence on the momentum distribution of the ionized electron and its contribution to the ionization probability is minor due to its relative smallness $\sim (E_0/E_a)/72$.

S_1 CCSFA

The Coulomb field effect on the PMD is included in the first-order correction term to the eikonal wave function. This correction yields a qualitative change to the case of the short-range potential by the correction term in the exponent

$$\frac{\exp(\zeta_0 + \zeta_1)}{\sqrt{\det \zeta_0}}. \tag{1.72}$$

Let us note that the preexponential term $\det \zeta_1$ is small in comparison to the leading term in the order of E_0/E_a and will be included in in the wave function of the next order and discussed in S_2 CCSFA. The Coulomb-correction term $\exp(\zeta_1)$ in the S_1 CCSFA has two consequences. Firstly, it changes the magnitude of the ionization probability due to the following factor

$$\left| \frac{c_a}{c_a, 0} \exp\left[\zeta_1\left(x_s^{(0)}, t_s^{(0)}\right)\right] \right|^2 \approx \frac{4^{Z/\kappa} \left(\sqrt[4]{\gamma^2 + 1}\sqrt{f}\right)^{-\frac{2Z}{\kappa}}}{\Gamma\left(\frac{2Z}{\kappa} + 1\right)}$$
$$\times \exp\left\{ \frac{4Z}{\kappa} \coth^{-1}\left[\frac{\sqrt{\gamma^2 + 1} - 1}{\gamma}\right] \right.$$
$$\left. \times \coth\left(\frac{\sinh^{-1}(\gamma)}{2} - \frac{\gamma\sqrt{f}}{2\sqrt[4]{\gamma^2 + 1}}\right)\right\}. \tag{1.73}$$

The upper expression contains higher-order E_0/E_a terms which should be neglected within the S_1 SFA. This leads to the result in leading order:

$$\left| \frac{c_a}{c_a, 0} \exp\left[\zeta_1\left(x_s^{(0)}, t_s^{(0)}\right)\right] \right|^2 = \frac{16^{Z/\kappa} \left(\frac{E_0}{\kappa^3}\right)^{-\frac{2Z}{\kappa}}}{\Gamma\left(\frac{2Z}{\kappa} + 1\right)}, \tag{1.74}$$

where $c_{a,0} = \sqrt{\kappa/2\pi}$. Let us note that the amplitude of S_0 CCSFA given by Eq. (1.70) corrected by the factor from Eq. (1.74) is the 1D equivalent to the Eq. (1.34) and also reproduces the PPT-ionization rate [27].

Secondly, ζ_1 yields a shift of the momentum distribution via the initial Coulomb momentum transfer (I-CMT) right after the electron leaves the tunnel exit (we still do not
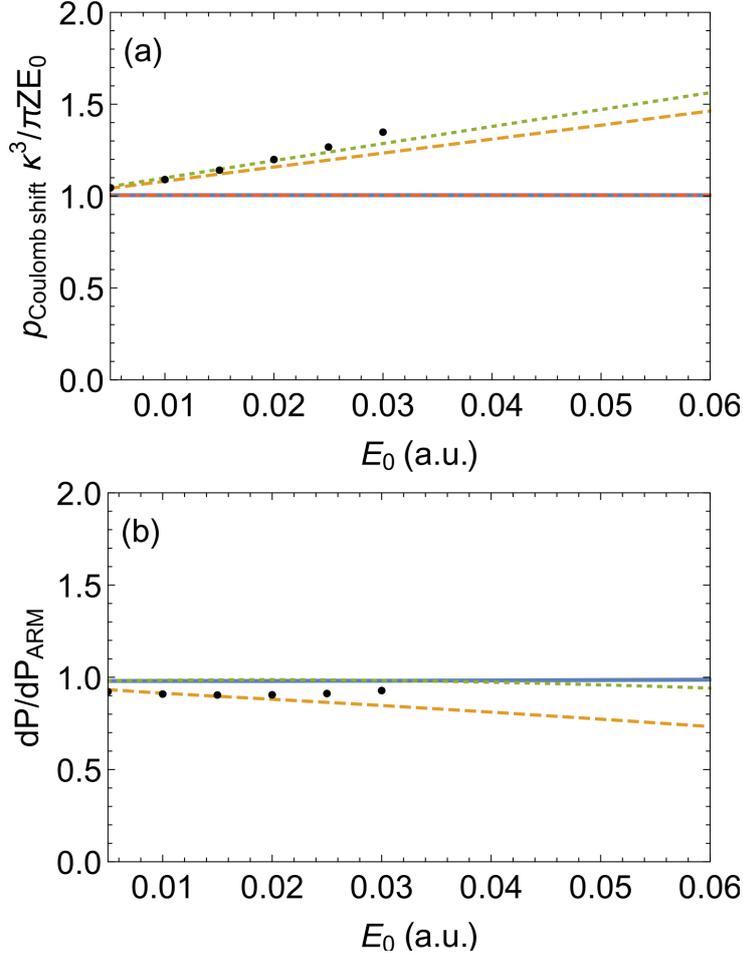
Figure 1.1: We carried out the Coulomb momentum shift vs the laser field strength E_0 in the panel (a) for the quasistatic regime of $\gamma = 0.1$ and $Z/\kappa = 1$ obtained by four methods: quasiclassical S_1 CCSFA (solid line), the quasiclassical S_2 CCSFA (dashed line), the quantum S_2 CCSFA (dotted line), and the ARM theory (dot-dashed line) which coincides exactly with the line obtained by the S_1 CCSFA. The ratio of the ionization rate at the peak of the momentum distribution to the corresponding ARM-ionization rate in the same quasistatic regime are plotted with respect to the field strengt E_0 in panel (b) for the quasiclassical S_1 (solid line), the quasiclassical S_2 CCSFA (dashed line), and the quantum S_2 CCSFA (dotted line). The dots in both panels were obtained by heuristic quasiclassical method (see [168]).

consider any recollisions). This momentum shift derived from the condition on the extremum of $M(p)$ stated in Eq. (1.65) with S_1 CCSFA is shown in Fig. 1.1. Moreover, we can also give the analytical estimation on the momentum shift via $\partial_x \zeta_1$ consisting of two terms: $\Delta p_C^{(1)}$ arising during the motion in the half-cycle of the laser pulse from Eq. (1.39) and $\Delta p_C^{(2)}$ arising during the motion of the electron in the field-free time region after the
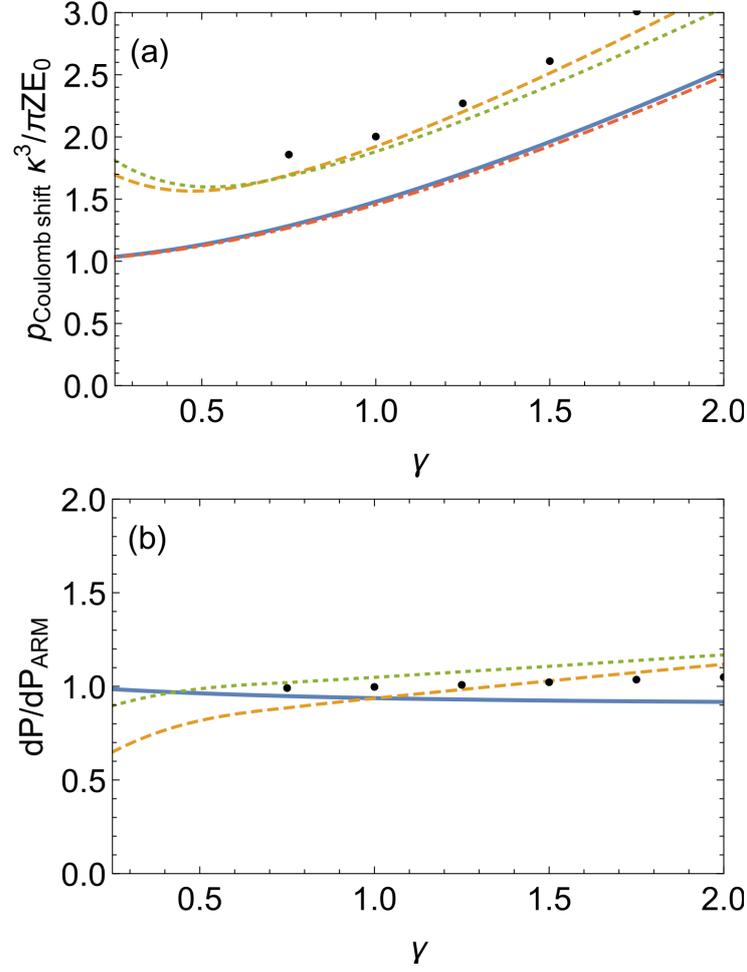
Figure 1.2: This figure is analogous to Fig. 1.1 except that we carried out the dependency of the Coulomb momentum shift [in panel (a)] and of the ratio of the ionization with respect to the ARM-ionization yield [in panel (b)] on the Keldysh parameter γ in the nonadiabatic regime of $\omega = 0.02$ and $Z/\kappa = 1$. The black dots display again the results of the heuristic quasiclassical method.

laser pulse,

$$
\begin{aligned}
\Delta p_C^{(1)} &= \frac{E_0 Z}{2\sqrt{1+\gamma^2}\kappa^3}\left[\pi\gamma^2 - 2(\gamma^2+1)\tan^{-1}(\gamma) + 2(\gamma^2+1)\tan^{-1}\left(\frac{\gamma-i}{\sqrt{\gamma^2+1}}\right)\right.\\
&\qquad\left. + 2(\gamma^2+1)\tan^{-1}\left(\frac{\gamma+i}{\sqrt{\gamma^2+1}}\right) + 2\gamma + \pi\right]\\
\Delta p_C^{(2)} &= \frac{E_0 Z\gamma^3}{\sqrt{1+\gamma^2}\kappa^3},
\end{aligned}
\tag{1.75}
$$

which can be simplified in the static regime (i.e., $\gamma \ll 1$) as

$$
\begin{aligned}
\Delta p_C^{(1)} &\approx \frac{\pi Z E_0}{\kappa^3}, \\
\Delta p_C^{(2)} &= 0,
\end{aligned}
\tag{1.76}
$$

and in the nonadiabatic regime (i.e., $\gamma \gg 1$) as

$$
\begin{aligned}
\Delta p_C^{(1)} &\approx \frac{\pi Z E_0}{\kappa^3}\left(\frac{\gamma}{2} + \frac{1}{4\gamma} + \frac{2}{\pi}\right), \\
\Delta p_C^{(2)} &= \frac{\gamma^2 Z E_0}{\kappa^3}.
\end{aligned}
\tag{1.77}
$$

For the latter, we can assume that the trajectory $x(t) \approx x_e + E_0 t/\omega$ can be used as the drift introduced during $t < \pi/(2\omega)$ is small in comparison to the tunnel exit x_e. We can separate the I-CMT from the further Coulomb effects when $\Delta p_C^{(2)} \ll \Delta p_C^{(1)}$ (i.e., $\gamma \lesssim 2$).

We plotted the estimated Coulomb momentum shift estimated by Eqs. (1.76) and (1.77) in Figs. 1.1(a) and 1.2(a), respectively. The Coulomb momentum shift relative to the characteristic photoelectron momentum in the laser field, E_0/ω, can be derived from the values in the Figs. 1.1(a) and 1.2(a) by multiplication by a factor of $\pi Z \omega/\kappa^3$. The Coulomb momentum shift almost exactly corresponds to the prediction by the ARM theory. Physically, we can interpret this result as a verification of the simple-man model [15], where electron appears at the tunnel exit instantaneously and propagates further classically in the continuum with Coulomb induced momentum shift

$$
\Delta p_C \approx -\int_0^\infty \mathrm{d}t \partial_x V(x(t)).
\tag{1.78}
$$

This expression gives Eqs. (1.76) and (1.77) when the trajectory $x(t)$ is used along with position of the adiabatic and nonadiabatic tunnel exit, respectively. The role of the initial Coulomb momentum transfer is larger in the nonadiabatic case, since the tunnel exit is located closer to the atom than in the adiabatic case. The S_1 CCSFA is physically equivalent to the ARM theory with the only difference being how the Coulomb singularity is treated. As we will show later, the ARM theory is more rigorous as it is based on wave functions matching but also including further simplifications. Nevertheless, both the S_1 CCSFA and the ARM theory are of the same accuracy explainign the agreement in Figs. 1.1 and 1.2 (see Sec. VI in [168]).

Let us note that the S_1 CCSFA reproduces the correction factor as given in Eq. (1.32) leading to agreement with the PPT tunneling theory discussed in the previous section. On the other hand, S_1 CCSFA does not reproduce the exact tunneling rate given by the recently calculated nonadiabatic PPT theory [178]. This is due to the fact that the Coulomb potential is neglected in the continuum leading to omition of frustrated ionization [179,180] where ionized electron does not have enough kinetic energy to escape from the potential well of its parent ion. Nevertheless, we can estimate the fraction of such electrons from Eq. (1.70) and derive a correction factor $\approx \left(\frac{2\gamma}{e}\right)^{-2Z/\kappa}$ yielding agreement with the PPT theory (for more details see Sec. VII in [168]).

S_2 CCSFA

Up to now, the S_1 CCSFA was able to reproduce the results of the PPT and ARM theories avoiding necessity of wave function matching. The coincidence of the result is given by the convenient location of the saddle point which as far from the atomic core but still under the tunnel exit. In this part, we are going to address the higher-order corrections in our CCSFA approach, which will take us beyond the PPT and CCSFA theories.

As we already disscussed, S_2 CCSFA contains a quasiclassical correction term ($\sim 1/\hbar$) as well as two quantum correction terms ($\sim \hbar^0$). In the latter, also the small term from the S_1 CCSFA is included (see Eq. (1.72)). From no on, we are going to address the terms individually: the quasiclassical S_2 CCSFA will contain only the quasiclassical term and the quantum S_2 CCSFA will contain all three correction terms.

The second order corrections to the ionization amplitude are small and the change to the momentum distribution is only quantitative. The shift of the peak of PMD and the change of the probability at the peak of the momentum distribution due to the new terms are shown in Fig. 1.1 for quasistatic regime and in Fig. 1.2 for nonadiabatic regime. In both cases, the second-order correction terms do not change the ionization probability significantly, but rather increase the Coulomb momentum shift when compared to the S_1 CCSFA results.

A physical interpretation can be found for every single term. The second order term in quasiclassical S_2 CCSFA decrease the ionization probability and increase the momentum shift, which both can be contributed to the effective decrease of the potential barrier formed by the Coulomb field of the atomic core and the laser field. The position of the tunnel exit can be found from the relation

$$- I_p = -E_0 x - \frac{Z}{|x|}, \tag{1.79}$$

which one can solve exactly in x. The expansion of this solution in E_0/E_a gives

$$x_e \approx \frac{I_p}{E_0} \left(1 - \frac{4ZE_0}{\kappa E_a} \right). \tag{1.80}$$

Whereas the S_1 CCSFA contains only the simple-man exit $x_e \approx I_p/E_0$, the S_2 CCSFA incorporates also the higher-expansion term of the order E_0/E_a while effectively increasing the Coulomb interaction and hence also the momentum shift via Eq. (1.78). To be more exact, the tunneling probability decreases because of the large damping from the tunneling exponent $\exp(- \int |x| \mathrm{d}x)$, where $p(x) = i\sqrt{2(I_p - xE_0 + Z/|x|)}$. The latter can be deduced from SFA directly and poses no surprise.

The decrease in the tunneling rate is mainly due to the next-to-leading order correction factor neglected in the S_1 CCSFA (the second term in the bracket):

$$\left| \frac{c_a}{c_{a,0}} \exp\left[\zeta_1 \left(x_s^{(0)}, t_s^{(0)} \right) \right] \right|^2 \approx \frac{1}{2} \left(\frac{4\kappa^3}{E_0} - 2\kappa x_s^{(0)} \right)^{\frac{2Z}{\kappa}}. \tag{1.81}$$

This formula shows how the Coulomb correction factor decreases with an increasing saddle point coordinate, which fits to the intuitive picture discussed above.

The quantum correction to S_2 increases the tunneling probability, which corresponds to an intuitive picture of barrier lowering. As a matter of fact, the quantum correction term $-i\partial_{xx}S/2 \sim -ip'(x)$ in Eq. (1.37) is equivalent to an additional term in the effective potential $V_{\text{eff}} = V - xF(t) - i\partial_{xx}S/2$ causing its decrease and hence the decrease of the tunnel exit. As we see, the quantum correction increase ionization probability and the Coulomb momentum shift in the continuum via decrease of the barrier.

**The role of Coulomb-correction terms on ionization time delay**

Let us investigate the role of the different Coulomb quantum correction terms for the ionization amplitude, i.e., the quantum term in S_2 and the correction higher-order term obtained from S_1. As we can see from Figs. 1.1(a) and 1.2(a), the quasiclassical S_2 and quantum S_2 curves are very close meaning that the quantum corrections almost compensate for each other. The quantum term in S_2 increases the momentum shift, whereas the quantum term stemming from the determinant of S_1 decreases it, giving an approximately net zero change. We further clarify the role of the quantum correction due to the determinant in Fig. 1.3. We can deduce from the figure, that the compensation is different in the quasistatic and the nonadiabatic regime. While in the first, the overall momentum shift is positive (the determinant term contribution is less important), in the latter, the net momentum corrections are negative (the determinant term contribution is more obvious).

The momentum shift can interpreted as a time delay at the detector as measured in the attoclock experiments [44] with respect to the simple-man prediction. The quantum correction term in S_2 introduces a positive time delay and the determinant term introduces a negative time delay of the same order with respect to the simple-man prediction given by the quasiclassical S_2 CCSFA. Let us also stress that the introduced time delay due to the Coulomb quantum corrections is an additional effect on top of the Wigner delay time [181] at tunneling ionization [182], which is not described by the CCSFA.

As we already mentioned, the quantum correction term of S_2 vanishes in the more realistic 3D case due to $\Delta V(\mathbf{r}) = 0$ in Eq. (1.46). Then, the overall delay time connected to the Coulomb quantum corrections will be negative in the 3D case. Moreover, one can show that for the negative delay time the time derivatives of $S(x,t)$ in the determinant are dominant and the spatial derivatives play only minor role. Therefore, we can anticipate that the negative delay time is not connected to the spatial uncertainty of the bound state but rather to the effects due to the Coulomb quantum corrections for the continuum state. Moreover, one can see from the Fiq. 1.1 that the time delay effect is most dominant in the near-threshold regime of large E_0/E_a, but insignificant in the deep-tunneling regime. This is in correspondence to the specific properties of the tunneling ionization delay time [182].

1.4 Further theories

The SFA was also applied in the nondipole regime [183] and even reformulated fully relativistically in [184, 185]. The application of the CCSFA for the nondipole regime
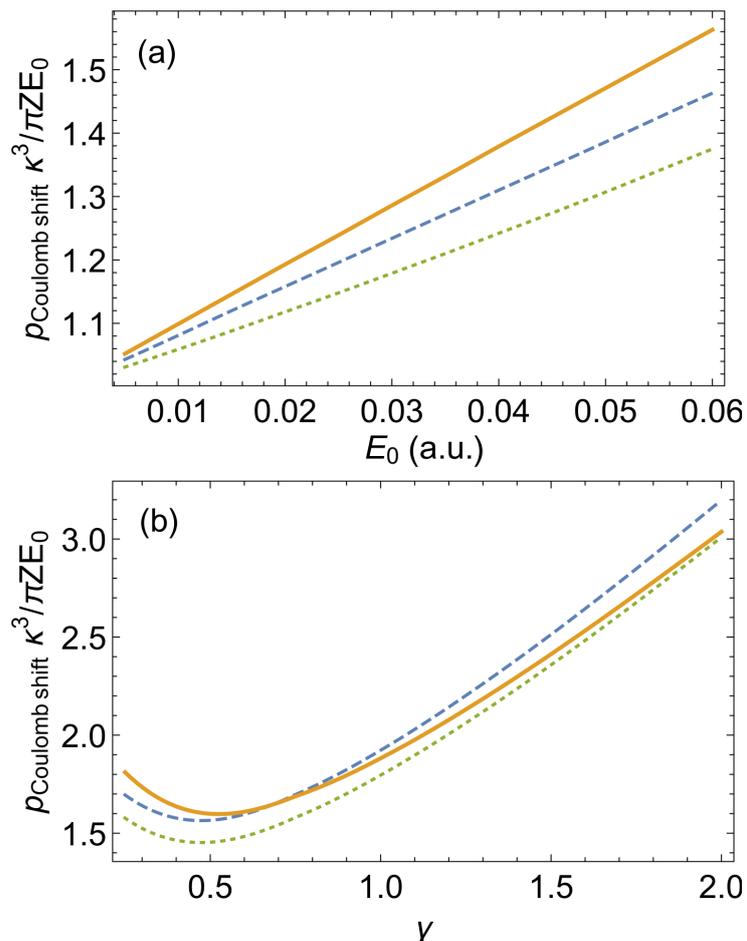
Figure 1.3: The dependency of the Coulomb momentum shift of the final momentum on the laser field strength E_0 in the quasistatic regime with $\gamma = 1$ is obtained by several methods and plotted in panel (a). In the panel (b), we plotted the dependency of the shift on the Keldysh parameter γ in the nonadiabatic regime with $\omega = 0.02$. The methods used are: classical S_2 CCSFA (dashed line), quantum S_2 CCSFA with both quantum corrections (solid line), and quantum SFA where the quantum corrections in the exponent are dropped (dotted line).

also followed in [186] along with its relativistic reformulation in [187] accounting for spin effects in the above-threshold ionization [188].

Nowadays, there exist two alternative approaches to the strong-field ionization beside the discussed CCSFA approximation. In fact, all these theories are based on the eikonal approximation and differ mainly in the treatment of the singularity introduced by the Coulomb potential in the eikonal expansion. The first theory was formulated quite recently in [189] and is based on the quantum-orbit strong-field approximation (see [40, 41]) while taking into account the Coulomb interaction in the quantum-orbits. The second theory called the analytical R-matrix theory (ARM). ARM is based on the powerful idea describing the scattering and ionization in multielectron systems embedded

into the R-matrix method: partition of the space into outer anid inner regions and was systematically developed in [37–39]. This partition allows us to address different types of underlying dynamics of two interacting systems individually. For example, the ion and the liberated electron in the case of one-electron ionization in the inner region and freed electron in the simplified description of the electron-core interaction in the outer region (e.g., neglecting electron exchange). The dynamics in the inner region could be very complex but the limited volume of the region makes its description manageable by the already developed theoretical techniques developed for bound states of multielectron systems. Another advantage of this partition is the natural division of the rescatterings into hard and soft with respect if they happen in the inner or the outer region, respectively. Moreover, the ARM preserves the gauge invariance unlike the SFA, where both wave functions are approximations and contribute to the breakdown of the invariance.

1.5 Strong-field ionization of diatomic molecules

The strong-field ionization of diatomic molecules and its understanding is the next step on our journey to investigation of more complex molecules.

Unlike the separate atoms, the diatomic molecules introduce breaking to the spherical symmetry due to the dual atomic centers. This poses new features for the strong-field ionization as dependency on the orientation of the molecule and multicenter interference. Whereas the first is well described by the Ammosov-Delone-Krainov theory for molecules (MO-ADK) [54], the latter can be addressed only by the molecular strong-field approximation (MO-SFA) [46, 55–58]. Nevertheless, MO-SFA suffers as well as the SFA form the gauge noninvariance and suffers from the absence of the Coulomb potential as discussed in the Sec. 1.2. For our later convenience, the MO-ADK would be beneficial for us as we plan to use the equivalent of the CTMC simulations for analysis of the PMD for the molecule of O_2 in the tunneling regime. Unfortunately, the lack of the multicore interference seem to play a crucial role and has to be accounted for [49, 52, 53].

Fortunately, a new method of partial-Fourier-transformation for molecules (MO-PFT) was developed recently [59–61]. This method [59] was able to reproduce the ADK tunneling rates for atoms and even to explain the alignment-dependent ionization rate of CO_2 [62]. Moreover, the MO-PFT incorporating both effects and describes also the phase structure of the tunneled wave packet at the tunnel exit, which is making this theory very convenient for our later use.

We will generalize the procedure from [60] for arbitrary orientation of the highest occupied molecular orbital (HOMO) $1\pi_g$ of the O_2 molecule consisting of two p-orbitals in anti-bonding formation as shown in Fig. 1.4. The orientation of HOMO and the interatomic distance $|\mathbf{R}|$ will be considered fixed during the strong-field ionization and the later evolution in the continuum as most of the important dynamics takes place on timescales $\sim$ 1-10 femtoseconds for mid-IR lasers, which are much smaller than the timescales associated with vibrations or rotations of molecules (i.e., 100 femtoseconds for vibrations and 100 picoseconds for rotations [190]).
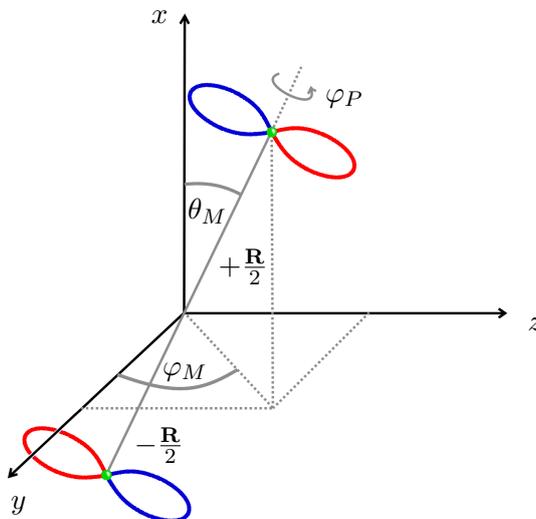
Figure 1.4: Orientation of HOMO $1\pi_g$ of the molecule O_2 with respect to the axes. The $1\pi_g$ consist of two anti-bonding p-orbitals. The position of the atoms is given by the vectors $\pm\frac{\mathbf{R}}{2}$. The alignment of HOMO is described by polar angle θ_M, azimuthal angle φ_M and angle φ_P giving the orientation of the p-orbitals with respect to the y-axis.

The PFT method can be briefly introduced via Hamiltonian in the length gauge

$$H = \frac{\hat{\mathbf{p}}^2}{2} + E_0 x, \tag{1.82}$$

where E_0 is the quasistatic field strength of the laser linearly polarized along x-axis and where we replaced the Coulomb potential by the zero-range potential.

The key to the PFT method is the mixed representation defined as

$$\Phi_{\text{atom}}(x, p_y, p_z) = \frac{1}{2\pi} \iint \mathrm{d}y \, \mathrm{d}z \, e^{-iyp_y - izp_z} \psi_{\text{atom}}(x, y, z), \tag{1.83}$$

where the wave function in the mixed representation depends on two momentum variables perpendicular to the polarization axis and one coordinate variable parallel to the polarization axis. Thanks to the mixed from, we can simplify the three-dimensional Schrödinger equation as

$$-\frac{\partial^2 \Phi_{\text{atom}}(x, p_y, p_z)}{\partial x^2} = 2\left(E' - E_0 x\right) \Phi_{\text{atom}}(x, p_y, p_z), \tag{1.84}$$

with $E' = -(I_p + p_y^2/2 + p_z^2/2)$ and ionization potential I_p. The form of the Schrödinger equation is familiar and allows us to use WKB approximation leading to the solution of the form

$$\Phi_{\text{atom}}(x, p_y, p_z) = \frac{C}{\sqrt{p_x(x)}} \, e^{iS(x, p_y, pz)}, \tag{1.85}$$

where $S(x, p_y, pz)$ is the classical action and $p_x = |\partial_x S(x, p_y, pz)|$ is the kinetic momentum along the polarization axis. The crucial step is finding such x_0 in the classically

forbidden region that $x_0 \gg 1$ and $x_0 \ll x_e$. The first ensures that we can use the asymptotic form of the field-free wave function and the latter that the the point is far away from the tunnel exit $x_e \equiv -I_p/E_0$ so the field is still small compared to the Coulomb potential. The WKB solution should match with the field-free wave-function at this point. The constant C can be determined by the matching procedure and the wave function at the tunnel exit is given as a limit $x \to x_e$ yielding

$$\Phi_{\text{atom}}(x \to x_e, p_y, p_z) = \Phi_{\text{atom}}(x_0, p_y, p_z)\sqrt{\frac{\kappa}{p_x(x)}}e^{i[S(x,p_y,p_z)-S(x_0,p_y,p_z)]} \tag{1.86}$$

where $\Phi_{\text{atom}}(x_0, p_y, p_z)$ is the field-free wave function and $\kappa = \sqrt{2I_p}$ is the momentum of the bound state.

The molecular orbital of a homonuclear diatomic molecule is given as a bonding or anti-bonding superposition of two atomic orbitals, one at each atomic center,

$$\Psi_{\text{molecule}}(\mathbf{r}) = \frac{1}{\sqrt{2 \pm 2S_{\text{OI}}}}\left[\Phi_{\text{atom}}(\mathbf{r} - \mathbf{R}/2) \pm \Phi_{\text{atom}}(\mathbf{r} + \mathbf{R}/2)\right], \tag{1.87}$$

where S_{OI} is the overlap integral and the $\mathbf{R}$ points from one atomic center to the other.

As the HOMO of the O_2 molecule is the anti-bonding configuration of two 2p-orbitals (lets say of two p_y orbitals). We can write the wave function as

$$\Psi_{O_2}(\mathbf{r}) = \frac{1}{\sqrt{2}}\sin\theta_P\, e^{-i\varphi_P}\Psi_{211}(\mathbf{r}) - \frac{1}{\sqrt{2}}\sin\theta_P\, e^{-i\varphi_P}\Psi_{21-1}(\mathbf{r}) - \cos\theta_P\Psi_{210}(\mathbf{r}), \tag{1.88}$$

which can be expressed in the mixed representation as

$$\begin{aligned}
\Psi_{O_2}(x_e, p_y, p_z) &= \frac{1}{\sqrt{2}}\sin\theta_P\, e^{-i\varphi_P}\Phi_{211}(x_e, p_y, p_z) \\
&\quad - \frac{1}{\sqrt{2}}\sin\theta_P\, e^{-i\varphi_P}\Phi_{21-1}(x_e, p_y, p_z) - \cos\theta_P\Phi_{210}(x_e, p_y, p_z).
\end{aligned}$$

We can substitute for the mixed wave functions from [60] while keeping all three orientation angles as a free parameters instead of fixing one particular angle as in the reference. The wave function at the tunnel exit then yields

$$\begin{aligned}
\Phi_{O_2}(x_e, p_{yi}, p_{zi}) &= \frac{C_{k1}}{\sqrt{\pi p_x(x_e)}}\frac{\sqrt{3}}{2}\left(\frac{2\kappa^3}{3|E(t)|}\right)^{2Z/\kappa} \\
&\quad \times \left\{\exp[-ig(p_{yi}, p_{zi})]\exp\left[\kappa\frac{R}{2}\cos\theta_M\right]\right. \\
&\quad \left. - \exp[+ig(p_{yi}, p_{zi})]\exp\left[-\kappa\frac{R}{2}\cos\theta_M\right]\right\} \\
&\quad \times \left(\sin\theta_M + i\cos\theta_M\frac{\mathbf{p}_{\perp i}\cdot\mathbf{e}_p}{\kappa}\right)\exp\left\{\left(-\frac{\kappa^3}{3|E(t)|} - \frac{\kappa\mathbf{p}_{\perp i}^2}{2|E(t)|}\right)\right\},
\end{aligned} \tag{1.89}$$

$$g(p_{yi}, p_{zi}) \equiv p_{yi}\frac{R}{2}\sin\theta_M\cos\varphi_P + p_{zi}\frac{R}{2}\sin\theta_M\sin\varphi_P. \tag{1.90}$$

With charge of the resulting ion Z, $\kappa = \sqrt{2I_p(E(t))}$, 2D-vectors: denoting orientation of the two p-orbitals $\mathbf{e}_p = (\cos\varphi_P, \sin\varphi_P)$ and the initial transversal momentum $p_{\perp i} = (p_{yi}, p_{zi})$, and distance of the atoms $R = 2.282$. The orientation of the anti-bonding orbital $1\pi_g$ is described by polar angle θ_M, azimuthal angle φ_M and orientation of the orbitals φ_P as indicated in Fig. 1.4.

The total ionization rate at instantaneous field $E(t)$ can be written as $\Gamma = \left(\frac{3E(t)}{\pi\kappa^3}\right)^{1/2} = \iint dp_{yi} dp_{zi} p_x(x_e) |\Phi_{O_2}(x_e, p_{yi}, p_{zi})|^2$ which leads to partial tunnel ionization rate

$$
\begin{aligned}
w_{O_2}(p_{yi}, p_{zi}) &\equiv \frac{\partial^2 \Gamma}{\partial p_{yi} \partial p_{zi}} \\
&= \left(\frac{3}{2\pi}\right)^{3/2} |C_{k1}|^2 \left(\frac{2\kappa^3}{|E(t)|}\right)^{\frac{2Z}{\kappa} - \frac{1}{2}} \\
&\quad \times \exp\left\{\left(-\frac{2\kappa^3}{3|E(t)|} - \frac{\kappa\left(p_{yi}^2 + p_{zi}^2\right)}{|E(t)|}\right)\right\} a^2(p_{yi}, p_{zi}),
\end{aligned}
$$

(1.91)

$$
\begin{aligned}
a^2(p_{yi}, p_{zi}) &= 4\left[\cosh^2\left(\kappa\frac{R}{2}\cos\theta_M\right) - \cos^2\left(g(p_{yi}, p_{zi})\right)\right] \\
&\quad \times \left(\sin^2\theta_M + \cos^2\theta_M \frac{(p_{yi}\cos\varphi_P + p_{zi}\sin\varphi_P)^2}{\kappa^2}\right).
\end{aligned}
$$

(1.92)

In the latter expression defines the structural factor $a^2(p_{yi}, p_{zi})$ which incorporates all the angular dependency of the tunnel ionization. Interestingly, the structural factor reproduces the structural factor from SFA [53] in the limit of $2I_p \gg p_\perp^2$.

The phase at the tunnel exit is given as $\tan[\phi_{\text{in}}(p_{yi}, p_{zi})] := \frac{\text{Im}[\Phi_{O_2}(p_{yi}, p_{zi})]}{\text{Re}[\Phi_{O_2}(p_{yi}, p_{zi})]}$ yielding

$$
\tan(\phi_{\text{in}}) = \frac{A\cos\theta_M\cos B\sinh C - \sin\theta_M\sin B\cosh C}{\sin\theta_M\cos B\sinh C - A\cos\theta_M\sin B\cosh C},
$$

(1.93)

$$
A \equiv \frac{p_{yi}\cos\varphi_P + p_{zi}\sin\varphi_P}{\kappa}
$$

(1.94)

$$
B \equiv p_{yi}\frac{R}{2}\cos\varphi_M + p_{zi}\frac{R}{2}\sin\varphi_M,
$$

(1.95)

$$
C \equiv \kappa\frac{R}{2}\cos\theta_M.
$$

(1.96)

As we can see, both tunnel ionization rate and the initial phase are strongly dependent on the orientation of the molecule θ_M, φ_M and the orbitals φ_P and depend also on the initial momenta p_{yi} and p_{zi}.
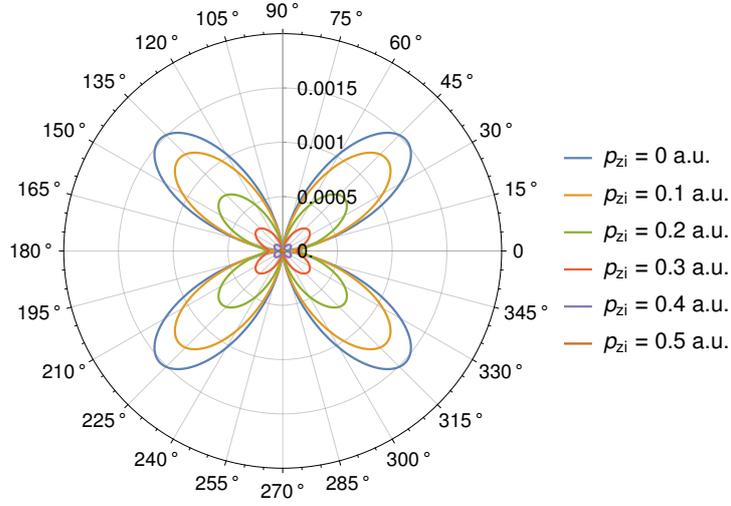
1.5.1 Ionization rates

The ionization rate depends strongly on orientation as we can see in Figs. 1.5-1.8 for various p_{zi} where we have also taken into account quadratic Stark shift (we will address

this in more detail in Sec. 6.5). Since the tunneled electron can originate from both of the atoms, interference pattern appears which manifests in the alignment dependent figures as four lobes at angles $\theta_M^{(\max)} = 42.368°$ and $137.632°$. The other two angles correspond to the obvious symmetry of the problem.

The orientation of the HOMO orbital along with the orientation of the molecule is encoded in the structural factor given in Eq. (1.92) which determines the shape of the radiation diagrams in Fig. 1.5-1.8. The investigated orientation give more or less the same radiation diagram with the most dominant angles of radiation preserved. The only difference can be found in the thickness of the lobes and whether the radiation vanishes simultaneously at the angle $0°$ and $90°$ for all values of p_{zi} as can be seen in Fig. 1.5 and 1.7 or only at the angle $90°$ but not at angle $0°$ for large values of p_{zi} as in the Fig. 1.6 or for none of those angles as can be seen on the green or red curve in Fig. 1.8. Nevertheless, the effect of the orientation of the HOMO on the radiation diagram is present mainly in the regions of suppressed radiation and, moreover, very small so we will not consider it any further.
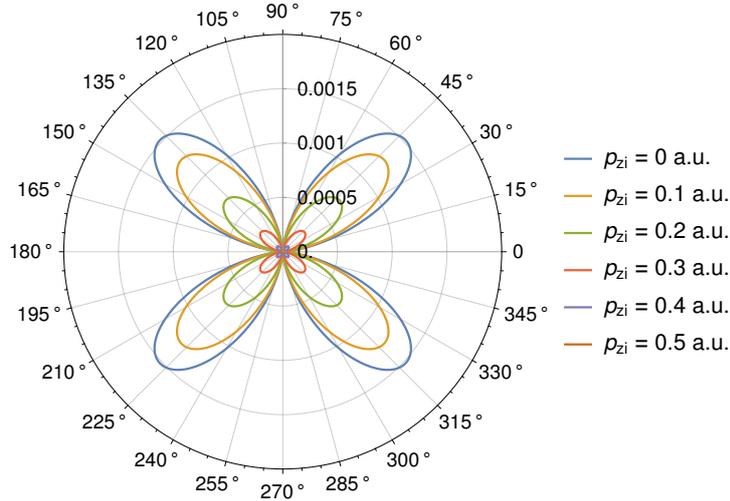
Figure 1.5: Dependence of the tunnel ionization rate $w_{MO-PFT}(0, p_{zi})$ on alignment angle θ_M for fixed angles $\varphi_M = 0$ and $\varphi_P = 0$ and several values of p_{zi}. Maximum of radiance has four lobes and their position is at $\theta_M \sim 42.368°, 137.632°, 222.368°$ and $263.632°$. The radiance vanishes for angles $\theta_M = 0°, 90°, 180°$ and $270°$ for all values of p_{zi}.

Figure 1.6: Dependence of the tunnel ionization rate $w_{MO-PFT}(0, p_{zi})$ on alignment angle θ_M for fixed angles $\varphi_M = 0$ and $\varphi_P = \pi/2$ and several values of p_{zi}. Maximum of radiance has four lobes as in the previous case in Fig. 1.5. The radiance vanishes for angles $\theta_M = 90°$ and $270°$ for all values of p_{zi}, but for large transversal momenta p_{zi} does not vanish at $\theta_M = 0°$ and $180°$.
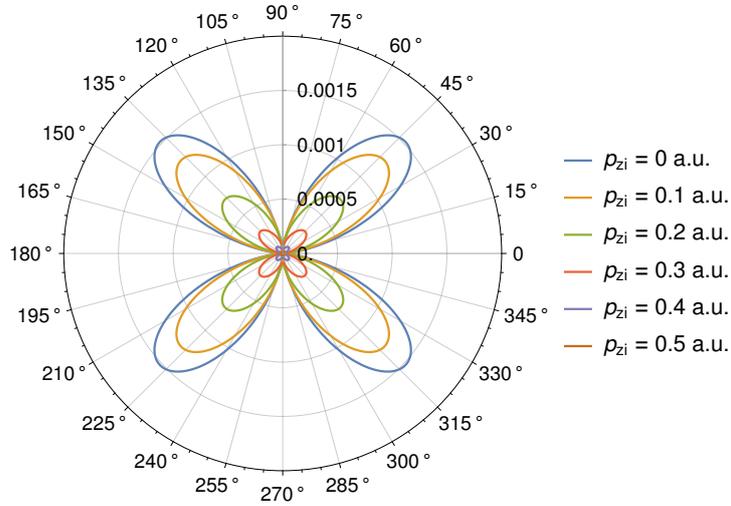
Figure 1.7: Dependence of the tunnel ionization rate $w_{MO-PFT}(0, p_{zi})$ on alignment angle θ_M for fixed angles $\varphi_M = \pi/2$ and $\varphi_P = 0$ and several values of p_{zi}. Maximum of radiance has four lobes as in the previous cases. The radiance vanishes for angles $\theta_M = 0°$ and $90°$ for all values of p_{zi}, but for large transversal momenta p_{zi} does not vanish at $\theta_M = 90°$ and $270°$ which is exactly the opposite case than in the previous figure Fig. 1.6.
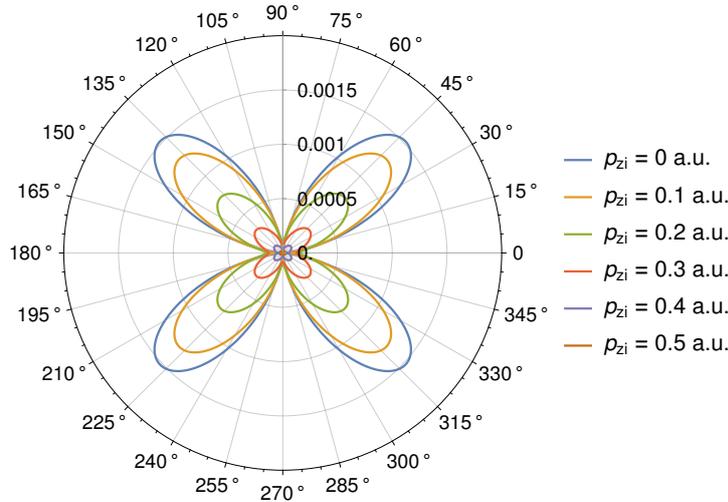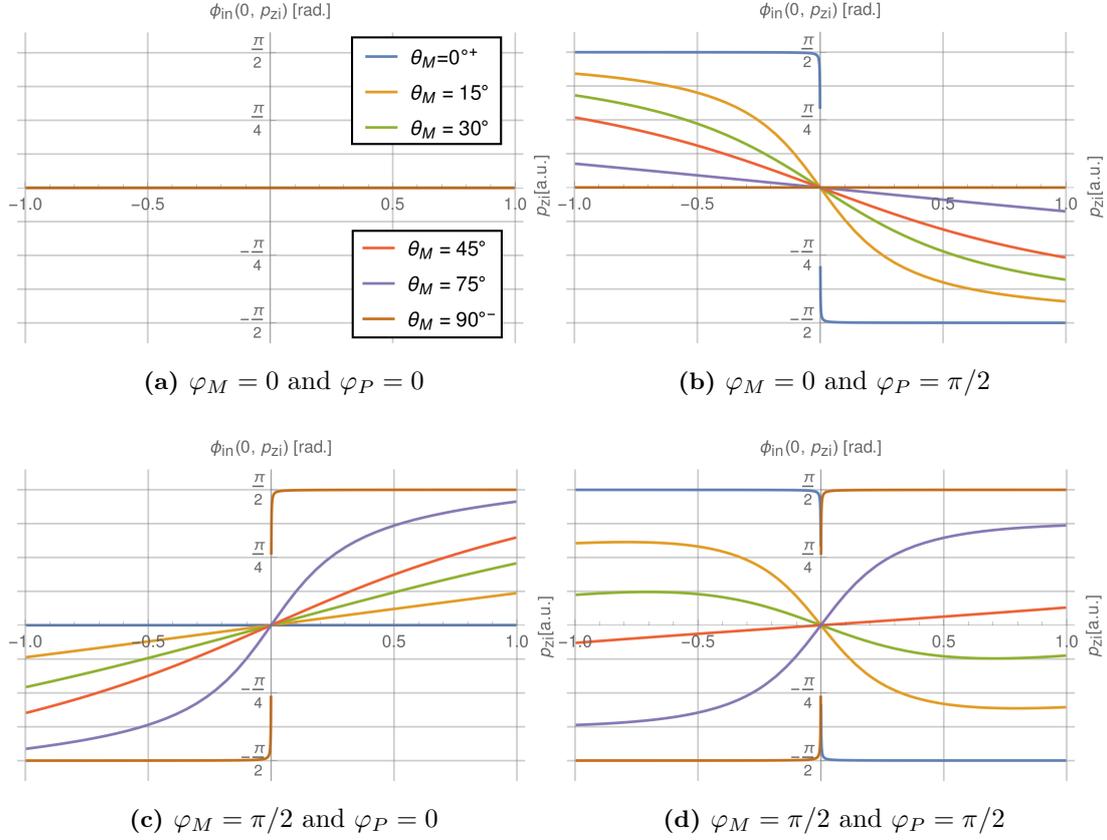
Figure 1.8: Dependence of the tunnel ionization rate $w_{MO-PFT}(0, p_{zi})$ on alignment angle θ_M for fixed angles $\varphi_M = \pi/2$ and $\varphi_P = \pi/2$ and several values of p_{zi}. Maximum of radiance has four lobes as in the previous cases. The radiance vanishes for angles $\theta_M = n\pi/2$ with integer n for small values of p_{zi}, but for large transversal momenta p_{zi} does not go completely to zero at those angles and large p_{zi} survive and dominate over small p_{zi} in the holographic structure.

1.5.2 Initial phase structure

The tunneled electron can carry some nontrivial initial phase $\Phi_{\text{in}}(p_{yi}, p_{zi})$ as given by Eq. (1.93). This is due to the fact that the origin of the tunneled electron cannot be tracked to the individual atomic orbitals but is a superposition of both of these two ionization paths. The initial phase is alignment dependent and we analyze it in the Figs. 1.9 for the various orientations of the molecule and orbitals with respect to the initial momentum p_{zi}. The initial phase strongly depends on the orientation of the molecule and has to be taken into account our further investigation of the photoelectron holography in the Chap. 6.

1.6 Summary

This chapter was concentrating on various theoretical approaches in the strong-field ionization. In the first section we introduced the basic idea behind the most used workhorse of the strong-field ionization physics: SFA and discussed its limits due to the neglecting of the Coulomb potential. In the second section, we have introduced the CCSFA which accounts for the Coulomb potential under the barrier via eikonal Volkov wave function which is found perturbatively. The CCSFA approach leads to correction factor for the tunneling rate yielding agreement with the prediction of the PPT theory. As the main contribution of this work, the role of the higher-order terms of the eikonal Volkov function and their role for the measured delay times is discussed in the third section for 1D

(a) $\varphi_M = 0$ and $\varphi_P = 0$

(b) $\varphi_M = 0$ and $\varphi_P = \pi/2$

(c) $\varphi_M = \pi/2$ and $\varphi_P = 0$

(d) $\varphi_M = \pi/2$ and $\varphi_P = \pi/2$

Figure 1.9: Dependence of the initial phase $\Phi_{in}(0, p_{zi})$ on the initial transversal momentum p_{zi} for various alignments of the molecule θ_M and for fixed φ_M and φ_P as given in sublabels. In the Fig. 1.9(a) $\Phi_{in}(0, p_{zi}) = 0$ which corresponds to the symmetry of ionization rate in Fig. 1.5. For other orientations, we can see a clear dependence of the initial phase on the alignment. The phase dependency on the momentum p_{zi} is rather moderate for the maximal ionization rates $\theta_M = 45° \approx 42.4°$, but strongly varies for special alignment of $\theta_M = n\pi/2$ and integer n which will have influence on the holographic pattern.

case and its implication for the 3D leading to negative delay times. In the fourth section, we briefly discussed the another ionization models as ARM theory or relativistic CCSFA.

In the fifth section, we have addressed the strong-field ionization of the diatomic molecule O_2 via the MO-PFT theory predicting dependency of the tunnel ionization rate on the alignment of the molecule and also a nontrivial phase structure of the tunneled wave packet in contrast to the symmetric case of single atoms. Moreover, we have generalized the known results for any arbitrary orientation of the ionized molecular orbital and we are going to apply these results later in Chap. 6 for strong-field ionization holography.

Chapter 2

Analytical model

In this chapter we are going to introduce our analytical perturbative model for treatment of the Coulomb interaction between the tunnel ionized electron and its parent ion along with the key assumption. We will follow the electron along its classical trajectories and analyze Coulomb momentum transfer (R-CMT) while restricting the interaction to specific points of rescattering on the trajectory. In this chapter we will introduce unique classes of rescattering points (RP): peak-like and plateau-like RP and estimate the R-CMT at these points. This chapter is based on the paper [191].

2.1 Introducing the model

In order to avoid complications introduced by the non-adiabatic effects during tunneling and, more importantly, during recollision, we consider such a regime of the tunneling ionization for an atom in a strong laser field where the Keldysh parameter [1] is small, i.e. , $\gamma \equiv \sqrt{I_p/2U_p} \ll 1$, with the ionization potential I_p and the ponderomotive potential $U_p = E_0^2/4\omega^2$.

For simplicity, we also assume linearly polarized laser field:

$$
\begin{aligned}
\mathbf{E}(u) &= E_0 \mathbf{e} \cos u, \\
\mathbf{B}(u) &= \mathbf{n} \times \mathbf{E}(u),
\end{aligned}
\tag{2.1}
$$

where $u = \omega(t - z/c)$ is the laser phase, $\mathbf{B}(u)$ is the laser magnetic field, E_0 and ω are the amplitude and the angular frequency of the laser field, respectively, c is the speed of light, $\mathbf{e} = (1, 0, 0)$ and $\mathbf{n} = (0, 0, 1)$ are the unit vectors along the laser polarization and propagation directions, respectively.

In our analytical model, we are going to investigate classical trajectories starting at the tunnel exit and evolving with the laser pulse. Asymptotic properties of any tunneled electron can be estimated analytically once the laser pulse has passed. The initial conditions for the classical trajectory at tunnel exit are given by the PPT theory which provides exact position of the tunnel exit and initial longitudinal momentum, but only restrictions on the ionization time t_i and initial transversal momentum $p_\perp$. The latter two parameters are therefore consider throughout this manuscript to be free parameters that determine fully the shape of the trajectory. Let us just recall that the initial transversal momentum is not represented uniformly in the final distribution, but with a

weight given in [27] as

$$w(p_\perp, t_i) \propto \exp\left(-\frac{p_\perp^2}{\Delta_\perp^2(t_i)}\right), \tag{2.2}$$

where $\Delta_\perp(t_i) = |\mathbf{E}(t_i)|^{1/2}/(2I_p)^{1/4}$.

2.1.1 Restrictions and key assumptions

In our model, we will consider the nondipole regime of interaction and will keep in the solution of the equations of motion (EOM) only leading terms with respect to $1/c$. Those terms describe the laser magnetic field induced drift of the electron in the laser propagation direction. We are not going to address the fully relativistic regime in this manuscript since we will initially assume that $v/c \ll 1$ in later introduced expansion. This is not only a pragmatic choice leading to simplification of calculations via subsequent disentanglement of EOM, but also a suitable choice for practical purposes as ongoing experiments operate in the nondipole tunneling regime delivering novel results [114, 142].

The physical condition of the applied $1/c$-expansion can be also understood as the smallness of the laser induced drift distance during the laser period $d \sim \lambda\xi^2/2$ [120] with respect to the recollision impact parameter $\rho \sim 2\pi p_\perp/\omega$: $d \ll \rho$, where $\xi = E_0/(c\omega)$ is the invariant laser field parameter, λ is the laser wavelength, $p_\perp = \sqrt{p_y^2 + p_z^2}$ is the electron transverse momentum, $p_\perp \sim 2\Delta_\perp = 2\kappa\sqrt{E_0/E_a}$, $\kappa = \sqrt{2I_p}$ is the atomic momentum, I_p is the ionization potential, and $E_a = \kappa^3$ is the atomic field. Note that the introduced small parameter $\epsilon \equiv d/\rho$, in fact, is directly related to the Lorentz deflection parameter [128, 129]:

$$\Gamma_R = \epsilon^2 = \frac{\kappa c \xi^3}{16\omega}. \tag{2.3}$$

The magnetically induced drift cannot be improvidently ignored as it changes the impact parameter of recollisions and therefore modifies CF. However, we stress that during the brief recollision time δt the effect of the magnetically induced drift is negligible, because the change of the impact parameter due to drift during the recollision time, which can be estimated as $\delta\rho \sim (\lambda\xi^2)(\omega\delta t)$, is much smaller than the impact parameter itself. In fact, we estimate the recollision time as $\delta t \sim \rho/v_\parallel$, with the electron longitudinal velocity at the recollision $v_\parallel \sim E_0/\omega$, and the ratio $\delta\rho/\rho \sim \epsilon\gamma\sqrt{E_0/E_a}$. We consider the tunneling regime when the Keldysh parameter is small $\gamma \ll 1$, and the field is too small to hinder the over-the-barrier ionization, i.e., $E_0/E_a \ll 1$. The latter means that $\delta\rho/\rho$, the change of the impact parameter due the drift during the recollision time, has an additional smallness in addition to the small parameter ϵ and, consequently, can be neglected in our discussion.

Our aim is to find an analytical expression for the CMT from the parent ion to the tunneled electron. For this purpose, we assume that the Coulomb field effect can be neglected along the most part of the trajectory, but is essential at well restricted recollision points and near the tunnel exit, where it is treated as a perturbation with respect to the laser field. The latter assumptions are valid if, firstly, the Coulomb force is small with respect

to the laser field at the recollision point and at the tunnel exit: $Z/r_r^2, Z/x_e^2 \ll E_0$, the charge of the atomic core Z, the recollision and the tunnel exit coordinates $r_r \sim \Delta_\perp/\omega$, and $x_e \sim I_p/E_0$, respectively, and secondly, if the quiver amplitude of the electron in the laser field greatly exceeds the distances of recollision and of tunnel exit $E_0/\omega^2 \gg r_r, x_e$. The first pair of these conditions reads

$$\frac{Z}{\kappa}\gamma^2 \quad \ll \quad 1, \tag{2.4}$$

$$\frac{Z}{\kappa}\frac{E_0}{E_a} \quad \ll \quad 1, \tag{2.5}$$

and the second pair gives

$$\gamma\sqrt{\frac{E_0}{E_a}} \quad \ll \quad 1, \tag{2.6}$$

$$\gamma^2 \quad \ll \quad 1. \tag{2.7}$$

Let us remark that these conditions are generally well fulfilled in the tunneling regime.

2.1.2 Expansions of equations of motions

The dynamics of the tunneled electron in the continuum is governed by Newton equations

$$\frac{d\mathbf{p}}{dt} = -\mathbf{E} - \frac{\mathbf{v}}{c} \times \mathbf{B} - \frac{Z\mathbf{r}}{r^3}, \tag{2.8}$$

where $\mathbf{v}$ is the electron velocity. The Coulomb field of the atomic core will be treated by perturbation theory during the recollision and we expand the momentum and coordinate as

$$\begin{aligned}
\mathbf{p} &= \mathbf{p}_0 + \mathbf{p}_1 + \dots, \\
\mathbf{r} &= \mathbf{r}_0 + \mathbf{r}_1 + \dots.
\end{aligned} \tag{2.9}$$

The unperturbed trajectory $\mathbf{r}_0(u)$ is determined by the laser field

$$\frac{d\mathbf{p}_0}{dt} = -\mathbf{E}\left(1 - \frac{\mathbf{n} \cdot \mathbf{v}_0}{c}\right) - \mathbf{n}\frac{\mathbf{v}_0 \cdot \mathbf{E}}{c}. \tag{2.10}$$

Momentum transfer due to the Coulomb field at the recollision is described by the trajectory in the first- and the second-order of perturbation

$$\frac{d\mathbf{p}_1}{dt} = -\frac{Z\mathbf{r}_0}{r_0^3}, \tag{2.11}$$

$$\frac{d\mathbf{p}_2}{dt} = -\frac{Zr_0^2\,\mathbf{r}_1 - 3Z\,[\mathbf{r}_0 \cdot \mathbf{r}_1]\,\mathbf{r}_0}{r_0^5}, \tag{2.12}$$

with $r_0 = |\mathbf{r}_0|$ and $\mathbf{r}_1$ being the first-order correction to the trajectory. Taking into account that $du/dt = \omega(t - v_z/c)$, and that the integral of motion in a plane laser field

$\Lambda_0 \equiv \varepsilon_0(u) - cp_{0z}(u) = \text{const}$, with the electron energy ε_0, Eq. (2.10) are integrated, providing the laser driven momentum evolution

$$
\begin{aligned}
p_{0x}(u) &= p_{xr} + [A_x(u) - A_x(u_r)], \\
p_{0y}(u) &= p_{yr}, \\
p_{0z}(u) &= p_{zr} + p_{zd}(u, u_r),
\end{aligned}
\tag{2.13}
$$

with the laser vector-potential $A_x(u) = -(E_0/\omega)\sin u$. The initial conditions are defined at the recollision point with the recollision phase u_r, and the recollision momentum $\mathbf{p}_r = (p_{xr}, p_{yr}, p_{zr})$, aiming at application of the solution near the recollision point. Here, the drift momentum induced by the laser magnetic field is

$$
p_{zd}(u, u_r) \equiv \frac{p_{xr}}{c}\left[A_x(u) - A_x(u_r)\right] + \frac{1}{2c}\left[A_x(u) - A_x(u_r)\right]^2,
\tag{2.14}
$$

where the integral of motion is approximated by $\Lambda_0 \approx c^2$, to keep the leading term in $1/c$ expansion. The unperturbed electron trajectory near the recollision point is

$$
\begin{aligned}
x_0(u) &= \frac{E_0}{\omega^2}\left[\cos u - \cos u_r + (u - u_r)\sin u_r\right] + \frac{p_{xr}}{\omega}(u - u_r) + x_r. \\
y_0(u) &= \frac{p_{yr}}{\omega}(u - u_r) + y_r, \\
z_0(u) &= \frac{p_{zr}}{\omega}(u - u_r) + z_d(u) + z_r,
\end{aligned}
\tag{2.15}
$$

with the recollision coordinate $\mathbf{r}_r = (x_r, y_r, z_r)$, and the laser magnetically induced drift coordinate

$$
z_d(u) = \int_{u_r}^{u} p_{zd}(u', u_r)\mathrm{d}u'.
\tag{2.16}
$$

Once the zero-order equations are solved, the momentum transfer due to the Coulomb field at the recollision can be derived as the first-order correction

$$
\mathbf{p}_1 = -\frac{Z}{\omega}\int_{u_r-\delta}^{u_r+\delta} \frac{\mathbf{r}_0(u')}{r_0^3(u')}\mathrm{d}u',
\tag{2.17}
$$

where $\mathbf{r}_0(u) = (x_0(u), y_0(u), z_0(u))$. The value of the parameter δ is coupled to the properties of the recollision and will be discussed in the next section.

In the discussion above, the Coulomb field effect is accounted for only near recollision points and near the tunnel exit, where it is treated as a perturbation with respect to the laser field. Still Eq. (2.17) for the Coulomb momentum transfer (CMT) includes nonperturbative Coulomb effects via dependence on the recollision parameters, i.e., the electron momentum $\mathbf{p}_r$ and coordinate $\mathbf{r}_r$ at the recollision point. In fact, the multiple recollisions preceding the currently discussed one can have significant contribution to the considered $\mathbf{p}_r$ and $\mathbf{r}_r$, although the Coulomb field is considered to be only a perturbation at every single one of them. Nevertheless, we will concentrate only on the single recollision

for now and return to the role of multiple recollisions in Chap. 3 where we address their role in the total Coulomb momentum transfer.

One may apply also a less accurate description by assuming that the Coulomb field is considered as a perturbation globally, i.e, at any moment the difference between the exact and laser driven trajectories is a perturbation. In this description the unperturbed electron trajectory is given by Eqs. (2.13)-(2.16), replacing the recollision phase u_r by the ionization phase u_i, and the recollision coordinate $\mathbf{r}_r$, and momentum $\mathbf{p}_r$ by the coordinate and momentum at the tunnel exit: $\mathbf{r}_i = (x_i, 0, 0)$, and $\mathbf{p}_i = (0, p_{yi}, p_{zi})$ leading to

$$
\begin{aligned}
p_{0x}(u) &= A_x(u) - A_x(u_i), \\
p_{0y}(u) &= p_{yi}, \\
p_{0z}(u) &= p_{zi} + p_{zd}(u, u_i),
\end{aligned}
\tag{2.18}
$$

which can be solved as

$$
\begin{aligned}
x_0(u) &= \frac{E_0}{\omega^2} \left[\cos u - \cos u_i + (u - u_i) \sin u_i \right] + x_i. \\
y_0(u) &= \frac{p_{yi}}{\omega} (u - u_i), \\
z_0(u) &= \frac{p_{zi}}{\omega} (u - u_i) + z_{di}(u),
\end{aligned}
\tag{2.19}
$$

with the tunnel exit $x_i = -I_p/E(u_i)$, and the laser magnetically induced drift coordinate

$$
z_{di}(u) = \int_{u_i}^u p_{zd}(u', u_i) \mathrm{d}u'.
\tag{2.20}
$$

Although generally we do not apply dipole approximation, we will check the accuracy of our method in Sec. 2.4 in the dipole approximation case.

2.2 Classification of recollisions

For estimation of R-CMT we first need to classify recolliding trajectories. There are two characteristic recolliding trajectories: 1) when the electron's longitudinal velocity is vanishing at the recollision point, $x_r = 0$ and $p_{xr} = 0$, and 2) when the electron has the highest velocity at the recollision point, $x_r = 0$, $|\mathbf{p}_r| \neq 0$ and $\mathbf{E}(u_r) = 0$. We will call the above-mentioned types of recollisions as a slow recollision (SR), and a fast recollision (FR), respectively. The first type of recollision corresponds to the peak of the momentum transfer in dependence on the initial ionization phase, and the second type corresponds to the plateau of the momentum transfer, as discussed in [96]. Let us remark that the SR is also known in the literature as "soft recollision" (e.g., [97]).

2.2.1 Slow recollision

In the case of the global perturbation for the Coulomb field, one uses the zero-order solutions Eqs. (2.19), and finds the recollision phases. The SR phase u_s is determined
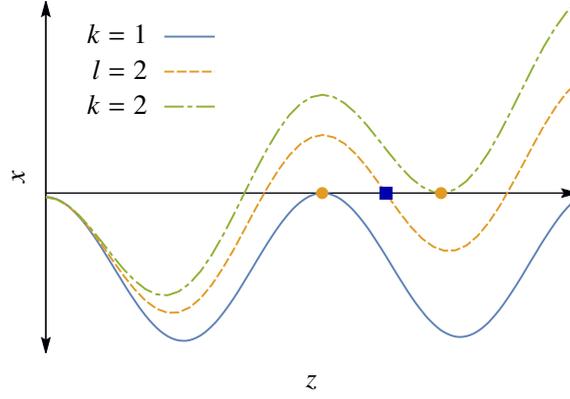
Figure 2.1: Green (dot-dashed) and blue (dashed) trajectories correspond to SR with $k = 1$ and $k = 2$ (yellow circles), respectively. Yellow trajectory corresponds to FR with $l = 2$ (blue square).

by the conditions

$$
\begin{aligned}
x_0(u_s) &= 0, \\
x_0'(u_s) &= 0, \\
x_0''(u_s) &\neq 0,
\end{aligned}
\tag{2.21}
$$

where prime denotes derivative with respect to the phase u.

The middle condition $x_0'(u) = 0$ for the kth-SR leads to

$$
u_s^{(k)} = (-1)^{k+1} u_i + \pi(k+1), \quad k \in \mathbb{N}.
\tag{2.22}
$$

Odd values of k correspond to trajectories approaching the ion from below, whereas even values to trajectories returning to the ion from above, see Fig. 2.1. The ionization phase $u_{i,s}^{(k)}$ leading to the kth-SR is derived from Eq. (2.21):

$$
\frac{E_0}{\omega^2} \sin u_i \left[\pi(k+1)\right] + x_i = 0, \quad \text{for } k \text{ odd},
\tag{2.23}
$$

$$
\frac{E_0}{\omega^2} \left\{-2\cos u_i + \left[-2u_i + \pi(k+1)\right]\sin u_i\right\} + x_i = 0, \quad \text{for } k \text{ even}.
\tag{2.24}
$$

Note that the tunnel exit $x_i(u_i)$ also depends on the ionization phase via $E(u_i)$. Taking into account that the ionization is most likely to take place near the maximum of the field $u_i \approx 0$, we expand Eqs. (2.23) and (2.24) over $u_i \ll 1$, which leads us to the solution

$$
\begin{aligned}
u_{i,s}^{(k)} &\approx \frac{\gamma^2}{2\pi(k+1)}, \quad \text{for } k \text{ odd}, \\
u_{i,s}^{(k)} &\approx \frac{4 + \gamma^2}{2\pi(k+1)}, \quad \text{for } k \text{ even},
\end{aligned}
$$

$$
\tag{2.25}
$$

where we used $x_i = -I_p/E_0$ and the definition of the Keldysh parameter γ. The γ^2 term for even values of k can be neglected with respect to the leading term in the deep tunnelling regime and hence $u_{i,s}^{(k)} \approx \frac{2}{\pi(2k-1)}$.

2.2.2 Fast recollision

FR phase u_f fulfills:

$$
\begin{aligned}
x_0(u_f) &= 0, \\
x_0'(u_f) &\neq 0, \\
x_0''(u_f) &= 0.
\end{aligned}
\tag{2.26}
$$

The phase of FR is derived from the last condition $x_0''(u_f) = 0$:

$$
u_f^{(l)} = \pi/2 + \pi l, \quad l \in \mathbb{N}
\tag{2.27}
$$

A direct substitution into the first condition of Eqs. (2.26) yields

$$
\frac{E_0}{\omega}\left[-\cos u_i + \sin u_i \left(\frac{2l+1}{2}\pi - u_i\right)\right] + x_i = 0,
\tag{2.28}
$$

which can be again solved in the approximation of small ionization phase, giving us the initial ionization phase $u_{i,f}^{(l)}$ and leading to the lth-FR

$$
u_{i,f}^{(l)} \approx \frac{2}{\pi(2l+1)}\left(1 - \frac{x_i \omega^2}{E_0}\right) \approx \frac{2+\gamma^2}{\pi(2l+1)},
\tag{2.29}
$$

We compare our estimations of the ionization phase u_i from Eqs. (2.25), (2.29) with the exact numerical solutions in Fig. 2.2. All errors are well behaved and do not exceed 5% when the γ^2 terms are taken into account. These parameters correspond to currently accessible mid-IR lasers and lead to relatively large Keldysh parameter, $\gamma \approx 0.33$, justifying the preservation of γ^2 terms in Eqs. (2.25), (2.29). With the current setup, the relative error does not exceed 6% even when the terms are omitted. Nevertheless, there is a saturation of the error with increasing k at $\approx 5\%$ for even-valued SR and with increasing l at $\approx 3\%$ for all FR. The saturated values correspond roughly to the proportionality of the leading and correction terms. Moreover, the precision for $u_{i,s}^{(k)}$ is even greater (by three orders of magnitude) for odd k which originates in the overall smallness of the ionization phase $u_{i,s}^{(k)} \to 0$ for this type of recollision. In conclusion we can say that the relative error of our estimation gets smaller as the ionization phases $u_{i,s/f}$ approach the peak of the laser field with increasing order of rescattering k or l.

2.3 Momentum transfer during recollisions

The momentum transferred to the recolliding electron by the Coulomb field of the atomic core at the kth recollision event is given by Eq. (2.17). As the main contribution to the integrals comes from the regions near the recollision points, we expand the trajectory
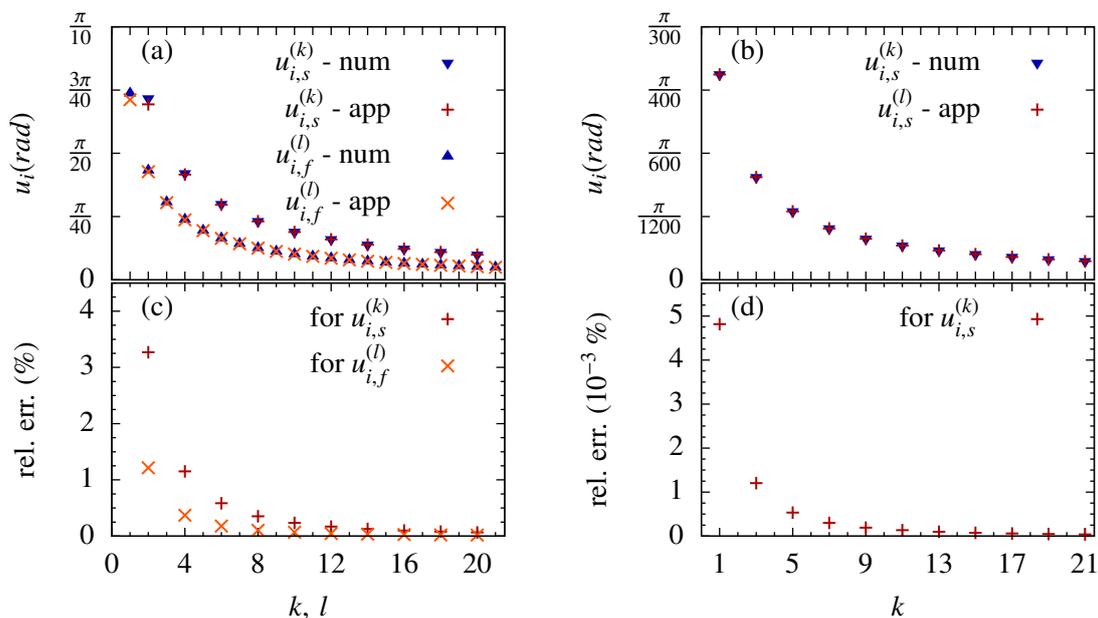
Figure 2.2: Analysis of estimated ionization phase $u_{i,s}^{(k)}$ and $u_{i,f}^{(l)}$ given by Eqs. (2.25) and (2.29), respectively. We compare the estimated values with the exact numerical results for even-valued SR and all FR in panel (a) and for odd-valued SR in panel (b). The corresponding relative errors are shown in panels (c) and (d), respectively. Parameters used for this comparison are $E_0 = 0.041$, $\omega = 0.0134$ and $I_p = 0.5$.

near the recollision phase where R-CMT takes place. The trajectory of the electron of Eq. (2.15) at the recollision point (x_r, y_r, z_r), with the recollision momentum (p_{xr}, p_{yr}, p_{zr}) can be approximated near the recollision phase u_r as an expansion in $\sigma = u - u_r$, up to the σ^2-order:

$$
\begin{aligned}
x_0(\sigma) &\approx x_r + \frac{p_{xr}}{\omega}\sigma - \frac{E(u_r)}{2\omega^2}\sigma^2 \\
y_0(\sigma) &\approx y_r + \frac{p_{yr}}{\omega}\sigma, \\
z_0(\sigma) &\approx z_r + \frac{p_{zr}}{\omega}\sigma - \frac{p_{xr}E(u_r)}{2c\omega^2}\sigma^2,
\end{aligned}
\tag{2.30}
$$

because $z_d(u_r) = 0$, and $z_d'(u_r) = p_{zd}(u_r) = 0$.

2.3.1 Slow recollisions

In the case of SR $p_{xr} = 0$, consequently, the trajectory in the leading order is

$$
x_0(\sigma) \approx x_r - \frac{E(u_r)}{2\omega^2}\sigma^2, \quad y_0(\sigma) \approx y_r, \quad z_0(u) \approx z_r.
\tag{2.31}
$$

In the latter we have neglected $p_\perp\sigma/\omega$ terms with respect to the recollision coordinate $\rho \sim p_\perp/\omega$, because the effective value of σ, derived from the condition $E_0\sigma^2/\omega^2 \sim \rho \sim p_\perp/\omega$ is

$\sigma \sim \sqrt{p_\perp \omega / E_0} \sim \sqrt{\gamma \sqrt{E_0/E_a}} \ll 1$, and the transversal motion near the recollision point can be neglected for SR. In general, the rescattering parameter x_r neither has to vanish at rescattering recollision nor has to be small. This assumption leads to generalization of the SR recollision for a larger class of recollisions with vanishing velocity. On the other hand, the extension to non-vanishing x_r requires more caution and will be discussed in further details in Chap. 3.

From Eqs. (2.17), we calculate R-CMT for SR along the the trajectory approximated by Eqs. (2.31) while extending the integration limits to infinity, i.e., $\delta \to \infty$, which leads to integrals

$$p_{1x,s} = -\frac{Z}{\omega} \int_{-\infty}^{+\infty} \frac{x_r - \frac{E(u_r)}{2\omega^2}\sigma^2}{\left[\frac{E^2(u_r)}{4\omega^4}\sigma^4 - \frac{x_r E(u_r)}{\omega^2}\sigma^2 + r_r^2\right]^{3/2}} d\sigma, \tag{2.32}$$

$$p_{1y,s} = -\frac{Z}{\omega} \int_{-\infty}^{+\infty} \frac{y_r}{\left[\frac{E^2(u_r)}{4\omega^4}\sigma^4 - \frac{x_r E(u_r)}{\omega^2}\sigma^2 + r_r^2\right]^{3/2}} d\sigma, \tag{2.33}$$

$$p_{1z,s} = -\frac{Z}{\omega} \int_{-\infty}^{+\infty} \frac{z_r}{\left[\frac{E^2(u_r)}{4\omega^4}\sigma^4 - \frac{x_r E(u_r)}{\omega^2}\sigma^2 + r_r^2\right]^{3/2}}, d\sigma. \tag{2.34}$$

with $r_r = \sqrt{x_r^2 + y_r^2 + z_r^2}$. The extension of the limits is well justified since large values of σ correspond to large deviation of the phase from the recollision point, yielding negligible contribution to the integration.

The analytical solution of the above integrals can be found for our problem in all generality. The first step is the following substitution

$$\chi \equiv \frac{|E(u_r)|}{2\omega^2 r_r}\sigma^2, \tag{2.35}$$

with corresponding differentials yielding

$$d\chi = \frac{|E(u_r)|\sigma}{\omega^2 r_r} d\sigma, \tag{2.36}$$

$$d\sigma = \sqrt{\frac{\omega^2 r_r}{2|E(u_r)|\chi}} d\chi. \tag{2.37}$$

Let us note that the substitution (2.35) is suitable since all integrated functions are even and hence we can restrict the limits of integration to 0 and $+\infty$. Further, when we replace the variable σ with χ in integrals in Eqs. (2.32)-(2.34), we obtain simplified form

of the integrals as

$$p_{1x,s} = -Z\sqrt{\frac{2}{|E(u_r)|r_r^5}} \int_0^{+\infty} \frac{x_r\chi^{-1/2} + \text{sign}\left[-E(u_r)\right]r_r\chi^{1/2}}{\left\{\chi^2 + 2x_r r_r^{-1}\,\text{sign}\left[-E(u_r)\right]\chi + 1\right\}^{3/2}}\mathrm{d}\chi, \quad (2.38)$$

$$p_{1y,s} = -Z\sqrt{\frac{2}{|E(u_r)|r_r^5}} \int_0^{+\infty} \frac{y_r\chi^{-1/2}}{\left\{\chi^2 + 2x_r r_r^{-1}\,\text{sign}\left[-E(u_r)\right]\chi + 1\right\}^{3/2}}\mathrm{d}\chi, \quad (2.39)$$

$$p_{1z,s} = -Z\sqrt{\frac{2}{|E(u_r)|r_r^5}} \int_0^{+\infty} \frac{z_r\chi^{-1/2}}{\left\{\chi^2 + 2x_r r_r^{-1}\,\text{sign}\left[-E(u_r)\right]\chi + 1\right\}^{3/2}}\mathrm{d}\chi. \quad (2.40)$$

We have brought the integrals to suitable form corresponding to the tabular integral [192]

$$\int_0^\infty \frac{x^{\mu-1}\mathrm{d}x}{(1 + 2x\cos t + x^2)^\nu} = \left(\frac{2}{|\sin t|}\right)^{\nu-1/2}\Gamma\left(\nu + \frac{1}{2}\right)$$
$$\times B(\mu, 2\nu - \mu)P_{\mu-\nu-1/2}^{1/2-\nu}(\cos t), \quad (2.41)$$

where $\Gamma(x)$ stands for the Gamma function, $B(x,y)$ for the Beta function, $P_\nu^\mu(x)$ for the Legendre function of the first kind and $-\pi < t < \pi$, $0 < \text{Re}(\mu) < \text{Re}(2\nu)$.

Once we identify $\cos t \equiv -\text{sign}\left[E(u_r)\right]\frac{x_r}{r_r}$, we can easily find the general solutions to Eqs. (2.38)-(2.40) as

$$p_{1x,s} = \frac{-\pi Z}{\sqrt{2^3|E(u_r)|(y_r^2 + z_r^2)r_r}}\left\{3\frac{x_r}{r_r}P_{-\frac{3}{2}}^{-1}\left(-\text{sign}\left[E(u_r)\right]\frac{x_r}{r_r}\right)\right.$$
$$\left. -\text{sign}\left[E(u_r)\right]\,P_{-\frac{1}{2}}^{-1}\left(-\text{sign}\left[E(u_r)\right]\frac{x_r}{r_r}\right)\right\}, \quad (2.42)$$

$$p_{1y,s} = -\frac{3\pi Z y_r}{\sqrt{2^3|E(u_r)|\left(y_r^2 + z_r^2\right)r_r^3}}\,P_{-\frac{3}{2}}^{-1}\left(-\text{sign}\left[E(u_r)\right]\frac{x_r}{r_r}\right), \quad (2.43)$$

$$p_{1z,s} = -\frac{3\pi Z z_r}{\sqrt{2^3|E(u_r)|\left(y_r^2 + z_r^2\right)r_r^3}}\,P_{-\frac{3}{2}}^{-1}\left(-\text{sign}\left[E(u_r)\right]\frac{x_r}{r_r}\right), \quad (2.44)$$

where $P_\nu^\mu(\eta)$ is the Legendre function of the first kind which emerges during the integration as shown in Eq. (2.41).

For illustration, we show the behavior of the Legendre functions in Fig 2.3. Both functions diverge for $\eta \to -1$, which is, however, out of the region of our interest since the condition $x_r \lesssim \sqrt{y_r^2 + z_r^2}$ is fulfilled at the recollision and leads to the restriction on the argument of the Legendre function $\left|\text{sign}\left[E(u_r)\right]\frac{x_r}{r_r}\right| \lesssim \frac{1}{\sqrt{2}}$. The other possible case of $x_r \gg \sqrt{y_r^2 + z_r^2}$ along with $E(u_r)x_r > 0$ does not belong to the class of soft recollisions. It corresponds to the hard recollision case with a large R-CMT which is beyond our present treatment.
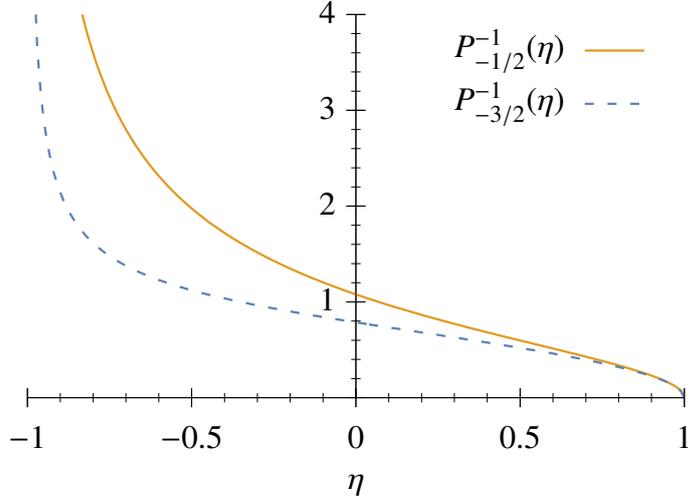
Figure 2.3: The Legendre functions within the valid range given by Eqs. (2.42)-(2.44). Distinct values are $P^{-1}_{-3/2}(0) \approx 0.787$ and $P^{-1}_{-1/2}(0) \approx 1.08$. Both functions diverge at $\eta \to -1$, which is out of the region of our interest since physically relevant cases correspond to $|\eta| < 1/\sqrt{2}$.

In the case of the commonly used SR with $x_r \to 0$, we have an approximate formula for R-CMT:

$$p_{1x,s}(u_r) \approx Z \frac{\text{sign}\,[E(u_r)]}{3\sqrt{|E(u_r)|}} \frac{2^{3/2}\mathcal{P}_1}{r_r^{3/2}}. \tag{2.45}$$

$$p_{1y,s}(u_r) \approx -Z \frac{2^{3/2}\mathcal{P}_2 y_r}{\sqrt{|E(u_r)|}r_r^{5/2}}, \tag{2.46}$$

$$p_{1z,s}(u_r) \approx -Z \frac{2^{3/2}\mathcal{P}_2 z_r}{\sqrt{|E(u_r)|}r_r^{5/2}}, \tag{2.47}$$

where $\mathcal{P}_1 = 3\pi P^{-1}_{-1/2}(0)/8 \approx 1.27$, and $\mathcal{P}_2 = 3\pi P^{-1}_{-3/2}(0)/8 \approx 0.927$ (for more details see Appendix A of [191]).

2.3.2 Fast recollisions

In the case of generalized FR we assume $x_r = 0$ and relax the condition on acceleration to $E(u_r) \approx 0$. In estimating R-CMT, the electron trajectory near the recollision point in the leading order can be then approximated by

$$\begin{aligned} x_0(\sigma) &\approx \frac{p_{xr}}{\omega}\sigma, \\ y_0(\sigma) &\approx y_r + \frac{p_{yr}}{\omega}\sigma, \\ z_0(\sigma) &\approx z_r + \frac{p_{zr}}{\omega}\sigma, \end{aligned} \tag{2.48}$$

which, when substituted into Eq. (2.17), yield

$$p_{1x,f} \quad = \quad -\omega Z \int_{\sigma_1}^{\sigma_2} \frac{p_{xr}\sigma}{\left[p_{xr}^2\sigma^2 + (p_{yr}\sigma + \omega y_r)^2 + (p_{zr}\sigma + \omega z_r)^2 \right]^{3/2}} \mathrm{d}\sigma, \qquad (2.49)$$

$$p_{1y,f} \quad = \quad -\omega Z \int_{\sigma_1}^{\sigma_2} \frac{p_{yr}\sigma + \omega y_r}{\left[p_{xr}^2\sigma^2 + (p_{yr}\sigma + \omega y_r)^2 + (p_{zr}\sigma + \omega z_r)^2 \right]^{3/2}} \mathrm{d}\sigma, \qquad (2.50)$$

$$p_{1z,f} \quad = \quad -\omega Z \int_{\sigma_1}^{\sigma_2} \frac{p_{zr}\sigma + \omega z_r}{\left[p_{xr}^2\sigma^2 + (p_{yr}\sigma + \omega y_r)^2 + (p_{zr}\sigma + \omega z_r)^2 \right]^{3/2}} \mathrm{d}\sigma, \qquad (2.51)$$

where we have replaced the lower and upper limit of integration by σ_1 and σ_2, respectively. The integrals are trivial to solve giving

$$p_{1x,f} \quad \approx \quad Z \left[\frac{p_{xr}\left[(y_r p_{yr} + z_r p_{zr})\,\sigma + \omega r_r \right]}{\left[p_{xr}^2 r_r^2 + (y_r p_{zr} - z_r p_{yr})^2 \right] \sqrt{p_{xr}^2\sigma^2 + (p_{yr}\sigma + \omega y_r)^2 + (p_{zr}\sigma + \omega z_r)^2}} \right]_{\sigma_1}^{\sigma_2} ,$$
$$(2.52)$$

$$p_{1y,f} \quad \approx \quad Z \left[\frac{-y_r p_{xr}^2\sigma - (y_r p_{zr} - z_r p_{yr})\,(\omega z_r + p_{zr}\sigma)}{\left[p_{xr}^2 r_r^2 + (y_r p_{zr} - z_r p_{yr})^2 \right] \sqrt{p_{xr}^2\sigma^2 + (p_{yr}\sigma + \omega y_r)^2 + (p_{zr}\sigma + \omega z_r)^2}} \right]_{\sigma_1}^{\sigma_2} ,$$
$$(2.53)$$

$$p_{1z,f} \quad \approx \quad Z \left[\frac{-z_r p_{xr}^2\sigma - (y_r p_{zr} - z_r p_{yr})\,(\omega y_r + p_{yr}\sigma)}{\left[p_{xr}^2 r_r^2 + (y_r p_{zr} - z_r p_{yr})^2 \right] \sqrt{p_{xr}^2\sigma^2 + (p_{yr}\sigma + \omega y_r)^2 + (p_{zr}\sigma + \omega z_r)^2}} \right]_{\sigma_1}^{\sigma_2} .$$
$$(2.54)$$

While relation $y_r p_{zr} = z_r p_{yr}$ holds due to symmetry in the dipole limit, in the nondipole case $y_r p_{zr} - z_r p_{yr} \approx y_r[p_{zd}(u_r, u_i) - \frac{1}{u_r - u_i} \int_{u_i}^{u_r} p_{zd}(u, u_i)du] \sim y_r\, c\xi^2$. The terms proportional to $(y_r p_{zr} - z_r p_{yr})^2$ in the denominators in Eqs. (2.52)-(2.54) are ξ^2 times smaller with respect to the leading term [in estimation we use $p_{xr} \sim c\xi$] and can be therefore neglected with respect to the expansion parameter ϵ of Eq. (2.3) which can be rewritten as $\epsilon \sim (\xi/\gamma)\sqrt{E_a/E_0}$. Under assumption of $p_{xr}\sigma/\omega \sim y_r \sim z_r$, one can show that the contributions of the magnetic drift terms with respect to the leading one in numerators of Eqs. (2.53) and (2.54) is smaller by factor of ξ and therefore can be neglected.

Thus, after neglecting the discussed terms, we have

$$p_{1x,f} \approx Z \left[\frac{p_{\perp r}\sigma + \omega}{p_{xr}r_r\sqrt{p_{xr}^2\sigma^2 + (p_{yr}\sigma + \omega y_r)^2 + (p_{zr}\sigma + \omega z_r)^2}} \right]_{\sigma_1}^{\sigma_2},$$

(2.55)

$$p_{1y,f} \approx Z \left[\frac{-\sigma y_r}{r_r^2\sqrt{p_{xr}^2\sigma^2 + (p_{yr}\sigma + \omega y_r)^2 + (p_{zr}\sigma + \omega z_r)^2}} \right]_{\sigma_1}^{\sigma_2},$$

(2.56)

$$p_{1z,f} \approx Z \left[\frac{-\sigma z_r}{r_r^2\sqrt{p_{xr}^2\sigma^2 + (p_{yr}\sigma + \omega y_r)^2 + (p_{zr}\sigma + \omega z_r)^2}} \right]_{\sigma_1}^{\sigma_2},$$

(2.57)

with σ_1 and σ_2 being the lower and upper limits of integration, respectively and $p_{\perp r} = \sqrt{p_{yr}^2 + p_{zr}^2}$.

In the rescattering picture, the limits σ_1 and σ_2 can be set to $\pm\infty$, yielding for FR

$$p_{1x,f} \approx \frac{2Zp_{\perp r}}{r_r p_{xr} p_r},$$

(2.58)

$$p_{1y,f} \approx -\frac{2Zy_r}{r_r^2 p_r},$$

(2.59)

$$p_{1z,f} \approx -\frac{2Zz_r}{r_r^2 p_r},$$

(2.60)

where $p_r = \sqrt{p_{xr}^2 + p_{yr}^2 + p_{zr}^2}$.

For high-order FR, the recollision picture may break down, which means that the Coulomb momentum transfer (although being rather small) is not decreasing sharply when the electron leaves the recollision point. In this case the Eqs. (2.58)-(2.60) do not provide good approximation. Our analysis shows that better approximation is achieved with $\sigma_1 = -\text{Mod}(u_r, \pi)$ and $\sigma_2 = \pi - \text{Mod}(u_r, \pi)$, which corresponds to the integration between the surrounding turning points of the trajectory. For FR (i.e., with vanishing laser field $E(u_r) \approx 0$) and beyond the recollision picture, we can set $\sigma_1 = -\sigma_2 = -\pi/2$ in Eqs. (2.55)- (2.57) yielding for FR in the leading term

$$p_{1x,fb} \approx \frac{2\pi Zp_{\perp r}}{p_{xr}r_r\sqrt{p_r^2\pi^2 + 4\omega^2 r_r^2}},$$

(2.61)

$$p_{1y,fb} \approx -\frac{2\pi Zy_r}{r_r^2\sqrt{p_r^2\pi^2 + 4\omega^2 r_r^2}},$$

(2.62)

$$p_{1z,fb} \approx -\frac{2\pi Zz_r}{r_r^2\sqrt{p_r^2\pi^2 + 4\omega^2 r_r^2}}.$$

(2.63)

Let us estimate conditions when the recollision picture is violated. This is the case once the transversal distance at FR is comparable or greater than the amplitude of the quiver motion. There is also a restriction on the longitudinal momentum p_{xr}, which

can be derived assuming Eqs. (2.46)-(2.47) and (2.59)-(2.60) to yield comparable results R-CMT. These conditions read

$$r_r \gtrsim \frac{|E(u_r)|}{\omega^2}, \tag{2.64}$$

$$p_{xr} \lesssim \sqrt{\frac{|E(u_r)|r_r}{2}}. \tag{2.65}$$

The R-CMT formulas for SR Eqs. (2.42)-(2.44)[or simplified Eqs. (2.45)-(2.47)], and for FR Eqs. (2.58)-(2.60) [or Eqs. (2.61)-(2.63) when the recollision picture fails] are expressed via parameters (coordinate and momentum) of the recollision and are valid even in the case when the global electron trajectory is significantly disturbed by the Coulomb field with respect to the laser driven one. The nondipole effects in these formulas are accounted for in the parameters z_r and p_{zr}.

2.3.3 Simple-man estimations

The leading scaling of R-CMT in Eqs. (2.45)-(2.47), (2.58)-(2.60) can be explained from the following intuitive consideration. The transverse R-CMT can be estimated as the transversal force $F_{\perp r} \sim 1/r_r^2$ acting during the recollision:

$$p_{1\perp} \sim F_{\perp r}\tau_r, \tag{2.66}$$

where τ_r is the duration of the recollision. We define half of the recollision duration as a time when the electron longitudinal distance from the core reaches the value of the recollision distance, i.e., $x(\tau_r/2) = r_r$. In the case of SR $x(t) \approx -E(u_r)t^2/2$, and

$$\tau_{r,s} \sim 2\sqrt{2r_r/|E(u_r)|}, \tag{2.67}$$

while for FR $x_F(t) \approx p_{xr}t$, and

$$\tau_{r,f} \sim 2z_r/p_{xr}. \tag{2.68}$$

Thus, from Eqs. (2.66)-(2.68), we find estimations for the transverse R-CMT,

$$p_{1\perp,s} \sim -\frac{2^{3/2}Z}{r_r^{3/2}\sqrt{|E(u_r)|}}, \tag{2.69}$$

$$p_{1\perp,f} \sim -\frac{2Z}{r_r p_{xr}}. \tag{2.70}$$

The longitudinal R-CMT at SR is easily estimated from the longitudinal force $F_{\parallel r} \sim -x_r(t)/z_r^3$ via

$$p_{1\parallel,s} \sim \int_{-\tau_{r,s}/2}^{\tau_{r,s}/2} F_{\parallel r}dt \sim -\frac{2Z}{r_r^3}\int_0^{\tau_{r,s}/2} x_s(t)dt = \frac{ZE(u_r)\tau_{r,s}^3}{2^3 3 r_r^3},$$

which yields

$$p_{1\parallel,s} \sim \frac{2^{3/2}Z}{3\sqrt{|E(u_r)|}r_r^{3/2}}. \tag{2.71}$$

For estimation of the longitudinal R-CMT at the FR one has to take into account that there is a compensation of R-CMT stemming from trajectories before and after the recollision which can be incorporated by a re-establishment of the time-dependence of $z_r(\tau) = z_r + p_{\perp r}\tau$ in $F_{\parallel r}$ and in the limit of $p_{\parallel r} \gg p_{\perp r}$:

$$p_{1\parallel,f} \sim -Z \int_0^{\tau_{r,f}/2} \left[\frac{p_{xr}\tau}{(z_r + p_{\perp r}\tau)^3} - \frac{p_{xr}\tau}{(z_r - p_{\perp r}\tau)^3} \right] d\tau \approx \frac{Zp_{xr}p_{\perp r}\tau_{r,f}^3}{2^2 z_r^4}.$$

Once substituted from Eq. (2.68), we obtain the final formula

$$p_{1\parallel,f} \sim \frac{2Zp_{\perp r}}{z_r p_{xr}^2}. \tag{2.72}$$

Thus, by the applied simple estimations the leading scaling of R-CMT from Eqs. (2.58)-(2.60) are reproduced in the limit of $p_{\perp r} \ll p_{xr}$.

2.4 Global perturbation approach for the Coulomb field

Formulas for R-CMT in Subsecs. 2.3.1 and 2.3.2 depend on the recollision parameters: momentum and coordinate. These parameters can be derived explicitly when one adopts global perturbation approach for the Coulomb field of the atomic core. In this approach the analytical description of the recolliding trajectories are provided in Sec. 2.2. We have defined two types of characteristic recolliding trajectories along with analytical description of the recolliding and ionization phase. Once inserted into the general formulas, we can investigate the direct scaling of R-CMT with respect to the laser parameters for those trajectories. For simplicity we will assume in this subsection dipole approximation and will set $p_{yi} = 0$ and $p_{zi} = p_{\perp i}$.

By employing $y_r = 0$ and $z_r = p_{\perp i}(u_r - u_i)/\omega$, the relation between the ionization and recollision phases u_r given by Eq. (2.22), and u_i by Eq. (2.25) into the Eqs. (2.45)-(2.47), we obtain for SR:

$$p_{1\parallel,s}^{(k)} = Z\frac{(-1)^{k+1}\mathcal{P}_1}{3\sqrt{E_0}} \left[\frac{2\omega}{p_{\perp i}(k+1)\pi} \right]^{3/2} \left\{ 1 + \left[1 + (-1)^k \right] \frac{7 + 2\gamma^2}{2\pi(k+1)^2} + \mathcal{O}\left(\frac{\gamma^4}{(k+1)^2} \right) \right\},$$
$$\tag{2.73}$$

$$p_{1\perp,s}^{(k)} = -Z\frac{\mathcal{P}_2}{\sqrt{E_0}} \left[\frac{2\omega}{p_{\perp i}(k+1)\pi} \right]^{3/2} \left\{ 1 + \left[1 + (-1)^k \right] \frac{7 + 2\gamma^2}{2\pi(k+1)^2} + \mathcal{O}\left(\frac{\gamma^4}{(k+1)^2} \right) \right\},$$
$$\tag{2.74}$$

where we expanded over small parameter $\frac{1}{k+1}$ in order to show the scaling dependencies in a lucid way.

At usual FR, one has $p_{xr} \gg p_{\perp r}$. The zero-order laser driven trajectory is $p_{xr} = A_x(u_r) - A_x(u_i)$. For FR using u_r from Eq. (2.27), and u_i by Eq. (2.29), in the formulas of Eqs. (2.58)-(2.60), we have

$$p_{1\parallel,f}^{(l)} \approx \frac{(-1)^{l+1}4Z\omega^3}{E_0^2\pi(2l+1)}\left\{1 - \frac{p_{\perp i}^2\omega^2}{2E_0^2} + (-1)^l\frac{4+2\gamma^2}{\pi(2l+1)} + \frac{16+14\gamma^2}{\pi^2(2l+1)^2} + \mathcal{O}\left(\frac{\gamma^4}{(2l+1)^2}\right)\right\},$$
(2.75)

$$p_{1\perp,f}^{(l)} \approx -\frac{4Z\omega^2}{E_0p_{\perp i}\pi(2l+1)}\left\{1 - \frac{p_{\perp i}^2\omega^2}{2E_0^2} + (-1)^l\frac{2+\gamma^2}{\pi(2l+1)} + \frac{8+6\gamma^2}{\pi^2(2l+1)^2} + \mathcal{O}\left(\frac{\gamma^4}{(2l+1)^2}\right)\right\},$$
(2.76)

where we employed expansion with expansion parameter $\frac{1}{2l+1}$ to manifest the roles of individual parameters.

For the FR, when the recollision picture begins to break down, we derive from Eqs. (2.61)-(2.63):

$$p_{1\parallel,fb}^{(l)} = \frac{(-1)^{l+1}4Z\omega^3}{E_0^2\pi(2l+1)\sqrt{\left[1+(-1)^{l+1}\frac{2+\gamma^2}{\pi(2l+1)}\right]^2 + \frac{p_{\perp i}^2\omega^2}{E_0^2}(2l+1)^2}}$$
$$\times\left\{1 + (-1)^l\frac{2+\gamma^2}{\pi(2l+1)} + \frac{8+6\gamma^2}{\pi^2(2l+1)^2} + \mathcal{O}\left(\frac{\gamma^4}{(2l+1)^2}\right)\right\},$$
(2.77)

$$p_{1\perp,fb}^{(l)} = -\frac{4Z\omega^2}{E_0p_{\perp i}\pi(2l+1)\sqrt{\left[1+(-1)^{l+1}\frac{2+\gamma^2}{\pi(2l+1)}\right]^2 + \frac{p_{\perp i}^2\omega^2}{E_0^2}(2l+1)^2}}$$
$$\times\left\{1 + \frac{4+2\gamma^2}{\pi^2(2l+1)^2} + \mathcal{O}\left(\frac{1}{(2l+1)^4}\right)\right\}.$$
(2.78)

The R-CMT estimations of this subsection are applicable in the case when the Coulomb field treated as a global perturbation. They provide us with the scaling of the R-CMT with respect to the laser parameters, the electron initial transverse momentum, and the order of the rescattering k or l.

Until this point, we have derived estimations for R-CMT at very specific recollision: Slow and Fast defined in the sets of Eqs. (2.21) and Eqs.(2.26), respectively, while considering the perturbation being global to the zero-order trajectory. Nevertheless, it would be appropriate to address the question of validity of the derived expressions since several approximations were made during their derivation.

The accuracy of the expressions from Eqs. (2.73), (2.74) for SF is analyzed in the left column of Fig. 2.4, where a comparisons with the exact numerical results and with the simple man formulas from Eqs. (2.69),(2.71) are given. The longitudinal and also the transverse R-CMT are described well, both with an accuracy $\lesssim 20\%$ up to the 10th recollision when R-CMT is decreased by an order of magnitude with respect to the first recollsion. From the analysis one can even deduce that the R-CMT estimation is more accurate when $\mathcal{P}_2 = 1$ in the corresponding equations.
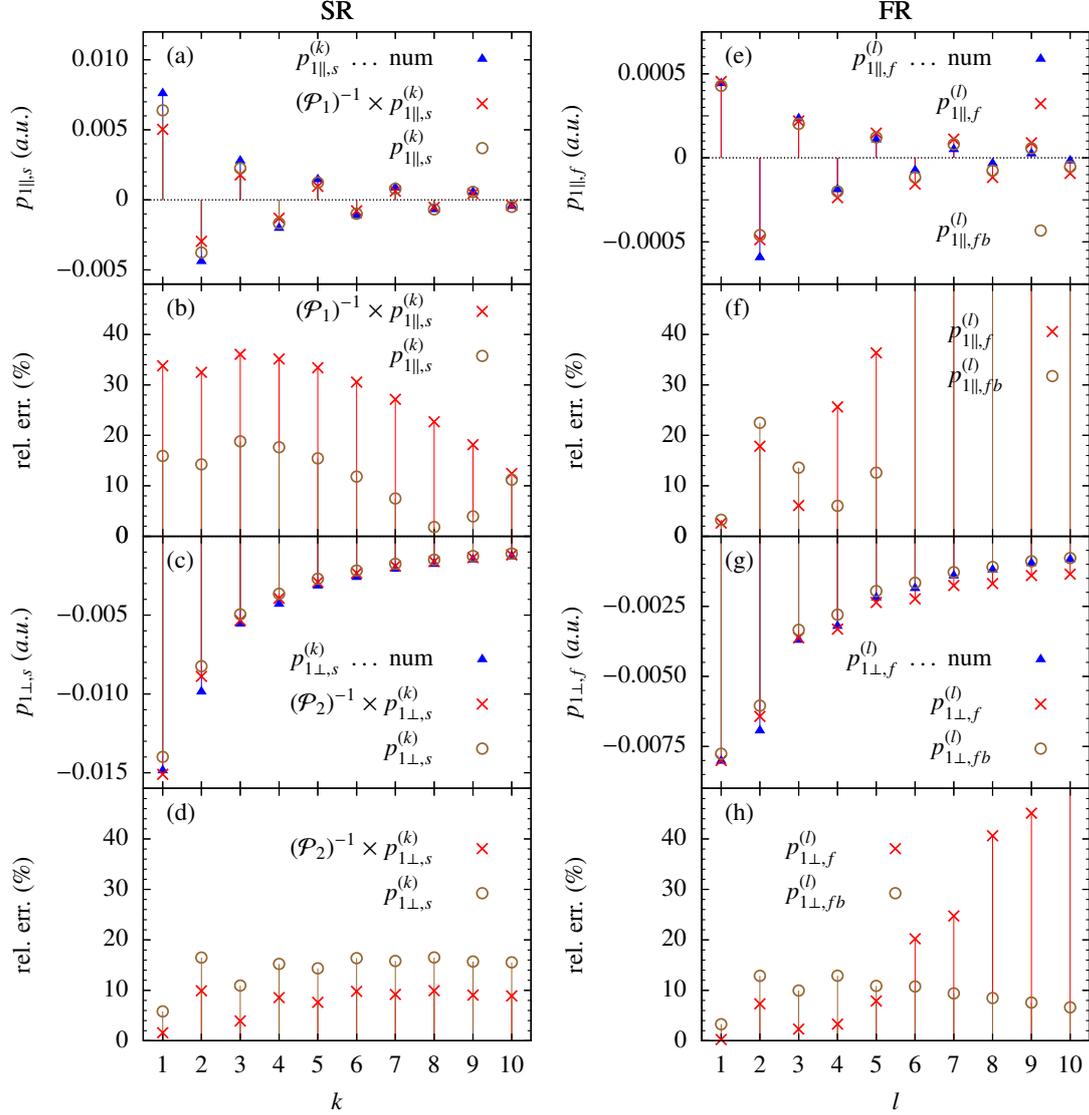
Figure 2.4: Analysis of accuracy of R-CMT estimations at the kth SR is in the in the left column: (brown circles) estimations via Eqs. (2.73), (2.74); (red crosses) simplified estimations via Eqs. (2.69), (2.71); (blue triangles) the exact numerical calculations. Analysis of accuracy of R-CMT estimations at the lth FR is in the right column: (brown circles) estimations via Eqs. (2.77), (2.78); (red crosses) estimations via (2.75), (2.76). Panels (a), (b), (e) and (f) deal with the longitudinal R-CMT; (c), (d), (g) and (h) with the transverse R-CMT. Panels (b), (d), (f) and (h) show the relative errors with respect to the numerical values. The parameters are $I_p = 0.5$ a.u., $p_{\perp i} = 0.2$ a.u. and used cosinusoidal field had $E_0 = 0.041$ a.u., $\omega = 0.0134$ a.u.

The analytical results for FR from Eqs. (2.77), (2.78) are compared with the exact numerical calculations and even with the simpler formulas from Eqs. (2.75), (2.76) in the right column of Fig. 2.4. As we can see, simple Eqs. (2.75), (2.76) are more accurate

for several first rescatterings (up to the 3th for the longitudinal and 5th for transversal) where the recollision picture holds. Meanwhile, the formulas (2.77), (2.78) provide better accuracy for high-order recollisions where the rescattering picture breaks down.

Note that the breakdown of the recollision picture can be observed also for SR. In fact, in Fig. 2.4 the accuracy of the longitudinal momentum transfer estimation starts to increase at 11th SR. However, the deviation from the exact numerical calculation is not as large as in the FR case. The reason is that the decay of the argument under the integrals in Eq. (2.17) is much weaker in the case of FR than in the case of SR, which is due to the different orders of leading terms in Eqs. (2.31) and (2.48).

At this point, it would also be appropriate to conduct a similar analysis for CMT given by Eqs. (2.42)-(2.44) for the generalized SR and by Eqs. (2.58)-(2.63) for the generalized FR. Nevertheless, we will omit such analysis here since we already have a good indications in favor of our results. The question of the overall accuracy will be addressed in a more general setup in next chapter where we will convince ourselves that the error is small and does not deviate significantly from the analyzed case in general.

The main advantage of the derived formulas in Eqs. (2.42)-(2.44) and in Eqs. (2.58)-(2.63) is their past-free nature and generalization for any relevant type of recollision. Our main goal is to use these formulas in order to estimate the total R-CMT for any arbitrary trajectory. However, before the implementation of this task, we need an estimate for I-CMT as accurate as that of R-CMT, which is carried out in the next section.

2.5 Initial Coulomb momentum transfer

For the analytical estimation of I-CMT, we have to calculate the Coulomb momentum transfer to the electron which takes place immediately after the leaving of the tunnel exit by using Eq. (2.17). The electron is at the tunnel exit x_i at ionization phase u_i with a transversal momentum $p_{\perp i}$ and is furher accelerated by the laser field $E(u_i)$ in longitudinal direction. We assume that the transversal motion is much smaller than the longitudinal one and expand the denominator of Eq. (2.17):

$$\frac{1}{[x^2(u) + y^2(u) + z^2(u)]^{3/2}} \approx \frac{1}{|x(u)|^3}\left[1 - \frac{3}{2}\frac{y^2(u) + z^2(u)}{x^2(u)}\right].$$
(2.79)

Taking into account that $y = p_{yi}\sigma/\omega$ and $z = (p_{zi} + \overline{p}_{zd})\sigma/\omega$, the second term in the bracket can be estimated as

$$\frac{y^2(u) + z^2(u)}{x^2(u)} \sim \frac{p_{\perp i}^2 \sigma^2}{\left(x_i - \frac{E_0}{2\omega^2}\sigma^2\right)^2 \omega^2} + \frac{2p_{\perp i}\overline{p}_{zd}\sigma^2}{\left(x_i - \frac{E_0}{2\omega^2}\sigma^2\right)^2 \omega^2}.$$
(2.80)

The first term in Eq. (2.80) is dominant over the second one by a factor of ϵ. The order of magnitude of the first term is $\sim E_0/E_a \ll 1$, which justifies the expansion above. We estimated the effective region of $\sigma \equiv u - u_i$ from the relation $E_0\sigma^2/\omega^2 \sim x_i$.

2.5.1 The first-order approximation

The first order approximation for I-CMT uses the unperturbed trajectory

$$
\begin{align}
x_0(\sigma) &\approx x_i - \frac{E(u_i)}{2\omega^2}\sigma^2, \tag{2.81}\\
z_0(\sigma) &\approx \frac{p_{\perp i}}{\omega}\sigma, \tag{2.82}
\end{align}
$$

with the coordinate $z_0(\sigma)$ along the initial transverse momentum with corresponding momentum corrections:

$$
\begin{align}
p_{1\parallel}(u) &= -\frac{Z}{\omega}\int_{u_i}^{u}\frac{\mathrm{sign}\,(x_0(u))}{x_0^2(u)}\mathrm{d}u, \tag{2.83}\\
p_{1\perp}(u) &= -\frac{Z}{\omega}\int_{u_i}^{u}\frac{z_0(u)}{|x_0^3(u)|}\mathrm{d}u, \tag{2.84}
\end{align}
$$

The integrals can be easily evaluated for $x_i < 0$ as

$$
\begin{align}
p_{1\parallel}(u) &= \frac{Z\sigma}{2x_i^2\omega\left[1+\sigma^2/\gamma^2(u_i)\right]} + \frac{Z\gamma(u_i)\arctan\left[\sigma/\gamma(u_i)\right]}{2x_i^2\omega}, \notag\\
p_{1\perp}(u) &= \frac{Zp_{\perp i}}{2E(u_i)x_i^2}\left\{\frac{1}{\left[1+\sigma^2/\gamma^2(u_i)\right]^2}-1\right\}, \tag{2.85}
\end{align}
$$

with $\gamma(u_i) = \sqrt{2I_p}\omega/|E(u_i)|$, which at $\sigma \to \infty$ yields I-CMT formulas as derived in [193] reading

$$
\begin{align}
p_{1\parallel,\mathrm{in}} &= \frac{Z\pi}{\sqrt{2^3|x_i|^3|E(u_i)|}} = \frac{Z\pi E(u_i)}{(2I_p)^{3/2}}, \tag{2.86}\\
p_{1\perp,\mathrm{in}} &= -\frac{Zp_{\perp}}{2x_i^2|E(u_i)|} = -\frac{2Zp_{\perp}|E(u_i)|}{(2I_p)^2}, \tag{2.87}
\end{align}
$$

2.5.2 The second-order corrections

For calculation of the second-order I-CMT we need the first-order correction to the trajectory, which is found integrating Eqs. (2.85):

$$
\begin{align}
x_1(\sigma) &= \frac{Z\sigma\gamma(u_i)}{2x_i^2\omega^2}\arctan\left(\frac{\sigma}{\gamma(u_i)}\right) \approx \frac{Z\sigma^2}{2\omega^2x_i^2}, \tag{2.88}\\
z_1(\sigma) &\approx -\frac{Zp_{\perp i}\sigma^3}{6\omega^3|x_i^3|}, \tag{2.89}
\end{align}
$$

where we keep only the leading terms in the expansion over the small σ. The correction to I-CMT is calculated using the first-order correction to the x-coordinate of the trajectory, but neglecting the correction to the z-coordinate, as it is small (determined by the small initial transverse momentum).

The second-order correction is given by the integral in Eq. (2.12) which can be written for individual components as

$$
p_{2\parallel}(u) = \frac{Z}{\omega} \int_{u_i}^{u} \frac{3x_0(u)z_0^2(u) + 4x_0^2(u)x_1(u) + 6z_0(u)x_0(u)z_1(u) - 2z_0^2(u)x_1(u)}{2|x_0(u)|^5} \mathrm{d}u,
$$
(2.90)

$$
p_{2\perp}(u) = \frac{Z}{\omega} \int_{u_i}^{u} \frac{3z_0^3(u) - 2x_0^2(u)z_1(u) + 6x_0(u)z_0(u)x_1(u) + 4z_0^2(u)z_1(u)}{2|x_0(u)|^5} \mathrm{d}u,
$$
(2.91)

where the first terms correspond to the correction due to the transversal motion from the expansion in Eq. (2.79), and the remaining terms are the proper second-order correction. The last terms in both integrals can be omitted because of their smallness. We can estimate their size with respect to the first term as

$$
\frac{x_1(u)}{x_0(u)} \approx \frac{x_1(\sigma)}{x_0(\sigma)} \approx \lim_{\sigma \to \infty} \frac{x_1(\sigma)}{x_0(\sigma)} = \frac{Z}{|E_0(u)|x_i^2} \ll 1,
$$
(2.92)

$$
\frac{z_1(u)}{z_0(u)} \approx \frac{p_{1\perp}(u)}{p_{0\perp}(u)} \approx \frac{p_{1\perp,\mathrm{in}}}{p_{\perp i}} = \frac{Z}{2|E(u_i)|x_i^2} \ll 1,
$$
(2.93)

thanks to the small expansion parameter $1/(|E(u_i)|x_i^2) \sim E_0/E_a$.

The integrals (2.90), (2.91) can be easily solved once we substitute for u from $\sigma \equiv u - u_i$, for the zero order trajectory from Eqs. (2.81), (2.82), for the first-order correction from the expanded solutions in Eqs. (2.88), (2.89) and send the upper limit of integration to infinity. By combining the first- and the second-order momentum corrections, and expanding over the small parameter $1/(|E(u_i)|x_i^2) \sim E_0/E_a$, we arrive at the following expressions for the corrected I-CMT:

$$
p_{2\parallel,\mathrm{in}} = \frac{\pi Z \operatorname{sign}(E(u_i))}{\sqrt{2^3 |E(u_i)x_i^3|}} \left[1 + \frac{4Z - 3p_{\perp i}^2 |x_i|}{8|E(u_i)|x_i^2} + \mathcal{O}\left(\frac{1}{x_i^4 E_0^2} \right) \right],
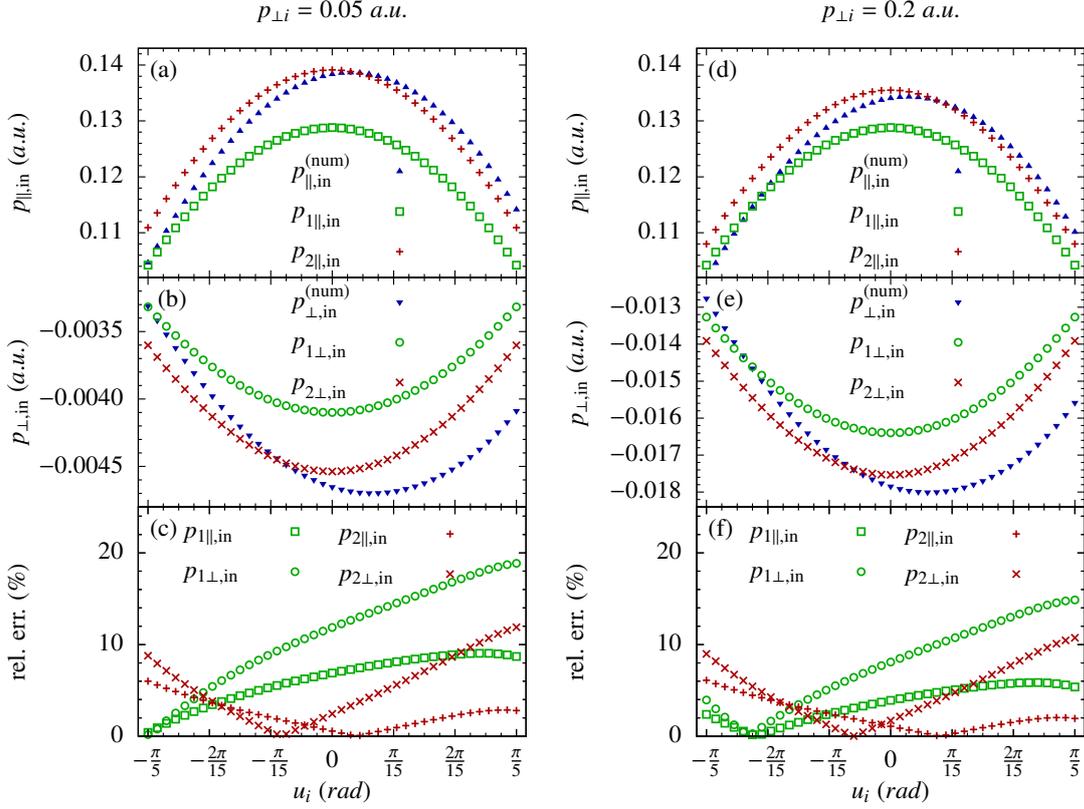$$
(2.94)

$$
p_{2\perp,\mathrm{in}} = -\frac{Zp_{\perp i}}{2|E(u_i)|x_i^2} \left[1 + \frac{4Z - 3p_{\perp i}^2 |x_i|}{6|E(u_i)|x_i^2} + \mathcal{O}\left(\frac{1}{x_i^4 E_0^2} \right) \right],
$$
(2.95)

which in the quasistatic regime with $x_i = -I_p/E(u_i)$ read:

$$
p_{2\parallel,\mathrm{in}} = \frac{Z\pi E(u_i)}{(2I_p)^{3/2}} \left[1 + \frac{2Z|E(u_i)|}{E_a\sqrt{2I_p}} - \frac{3p_{\perp i}^2}{8I_p} + \mathcal{O}\left(\frac{E_0^2}{E_a^2} \right) \right],
$$
(2.96)

$$
p_{2\perp,\mathrm{in}} = -\frac{2Zp_{\perp i}|E(u_i)|}{(2I_p)^2} \left[1 + \frac{8Z|E(u_i)|}{3E_a\sqrt{2I_p}} - \frac{p_{\perp i}^2}{2I_p} + \mathcal{O}\left(\frac{E_0^2}{E_a^2} \right) \right].
$$
(2.97)

Let us note that it is easy to identify the term $\sim Z$ in the expansions in Eqs. (2.94)-(2.97) as the second-order momentum correction and the term $\sim p_{\perp i}^2$ as the correction

Figure 2.5: Estimation of I-CMT vs ionization phase: (a), (d) transverse I-CMT; (b), (e) longitudinal I-CMT; (c), (f) relative error with respect to the exact numerical simulations, for the transverse I-CMT (red), and for the longitudinal I-CMT (blue). The initial transversal momentum $p_{\perp i} = 0.05$ was considered in the left panels whereas the initial momentum $p_{\perp i} = 0.2$ was used in the right panels. In (a), (b), (d) and (e) blue triangles correspond to numerical simulations, green squares and circles to first-order I-CMT, and red pluses and crosses to the corrected I-CMT. The remaining parameters were chosen as $E_0 = 0.041$, $\omega = 0.0134$ and $I_p = 0.5$.

in the first-order due to the transversal motion. Moreover, we can now clearly see that the neglect of the last terms in the integrals of Eqs. (2.90), (2.91) was well justified as they would contribute to the next order.

We compare our results for I-CMT with numerical calculation results in Figs. 2.5 for $p_{\perp i} = 0.05$ and $p_{\perp i} = 0.2$. As we can see the next-to-leading order corrections to I-CMT significantly decrease the error of the estimation in both cases. The corrected formulas manifest relative errors less than 5% near the peak of the laser field, where the I-CMT effect is most significant.

2.6 Summary

One of the main results of this chapter is the thorough analysis showing that the transverse R-CMT for both of the recollisions can be represented in a unified form

$$\mathbf{p}_{1\perp} \approx -Z\tau_r \frac{\mathbf{r}_r}{r_r^3}, \tag{2.98}$$

with an appropriate duration of recollision τ_r, different for SR and FR.

To summarize this chapter, we have developed an analytical model for quantitative description of CF effects in laser induced strong-field ionization. Under the assumption that the Coulomb field effect is a perturbation for the near recollision laser driven trajectory, we have derived past-free analytical formulas for the Coulomb momentum transfer at recollisions which depend on the local recollision coordinate and momentum. Moreover, for an effective treatment of Coulomb momentum transfer we classify the recollisions into two types: slow- and fast-recollisions. The obtained formulas for the momentum transfer at slow recollisions, Eqs. (2.42)-(2.44), and for fast recollisions Eqs. (2.58)-(2.60) are applied even in the case when the Coulomb field is not a perturbation to the global trajectory. In this case the recollision parameters can be derived either by the step-by-step method, or via exact numerical trajectory. The nondipole effects are shown to be negligible during the brief time of the recollision, however they are indirectly incorporated in the theory via the recollision coordinate and momentum. Within the same model we derived essential higher-order corrections to the known expressions for the initial Coulomb momentum transfer at the tunnel exit [193]. Furthermore, by applying perturbation theory for the Coulomb field globally with respect to the laser driven trajectory, the Coulomb momentum transfer has been expressed via the ionization phase and the initial transverse momentum at the tunnel exit for very special (but widely discussed in the literature) classes of recollisions while exposing scaling dependencies of the laser field parameters.

The derived analytical formulas for the Coulomb momentum transfer, employed along with numerical simulations, can help to gain insight into the detailed features of the CF effect in different laser field setups. In particular, they allow for estimation of the role of each particular rescattering event, which is usually hidden in the fully numerical CTMC simulation, but can be very helpful in developing an intuitive picture of CF. In this context, we have proven by our analytical approach (see Fig. 2.4) that assuming single rescattering may not be sufficient in order to quantitatively describe CF in mid-infrared laser fields and that the contribution of high-order rescatterings should not be neglected.

Chapter 3

Total Coulomb momentum transfer

In this section we illustrate the usefulness of our analytical approach by providing estimation of the final momenta for any arbitrary ionization phase u_i, initial transversal momentum $p_{\perp i}$. Once we master estimation on Coulomb momentum transfer for arbitrary trajectory, we derive the asymptotic photoelectron momentum diagram (PMD) via a modified Classical-trajectory Monte-Carlo simulation (CTMC). The latter will be a good check on whether the derived analytical formulas for R-CMT and I-CMT can provide physically relevant results and can help to gain greater insight into the evolution of the tunneled wave packet in the continuum. Since the evolution of the electrons is non-trivial in the combined laser and Coulomb fields, we consider two different approaches: the straightforward zero-order trajectory approach, and the more elaborate step-by-step approach. Let us note at this point, that for simplicity the dipole approximation is applied and $Z = 1$ throughout this chapter. This chapter is based on [191].

3.1 Rescattering points in the general setup

The real trajectory of a photoelectron in the continuum is in general nontrivial as the photoelectron can be driven back to the parent ion several times due to the oscillatory laser field. The closest distance at each of this returns, also called the impact parameter, can vary significantly with respect to the photoelectron's initial conditions at the tunnel exit, while yielding various R-CMT at every single return. The total CMT therefore consists not only of I-CMT but also of **multiple** R-CMT at every single recollision. Moreover, in some cases a single R-CMT can be even so large that it can no longer be considered as a perturbation to the trajectory which gets significantly distorted. When this happens, the subsequent returns can yield even larger R-CMT and hence distort the trajectory even further leading to a nontrivial form of the trajectory which strongly depends on the initial conditions of the photoelectron. We are not going to engage this problem at this point as it will be address in the next section. The aim of this section is to find the best way to break down a general photoelectron trajectory into pieces each containing only one single rescattering event, which will make it possible to estimate the total CMT measured on the detector.

In Chap. 2, we have analyzed the CMT at very specific recollison events: SR defined by Eqs. (2.21) and FR defined by Eqs. (2.26). Those recollision events are unique and may not even occur for a general trajectory as they are very sensitive to the initial conditions. Moreover, even when such recollision event appears in a some trajectory, it happen only at one recollision and not at other rescatterings in a general cosinusoidal laser field.

For this purpose, we will start with the generalized conditions on the recollisions yielding

$$
\begin{aligned}
x_0(u_s) &\neq 0, \\
x_0'(u_s) &= 0, \\
x_0''(u_s) &\neq 0,
\end{aligned}
\tag{3.1}
$$

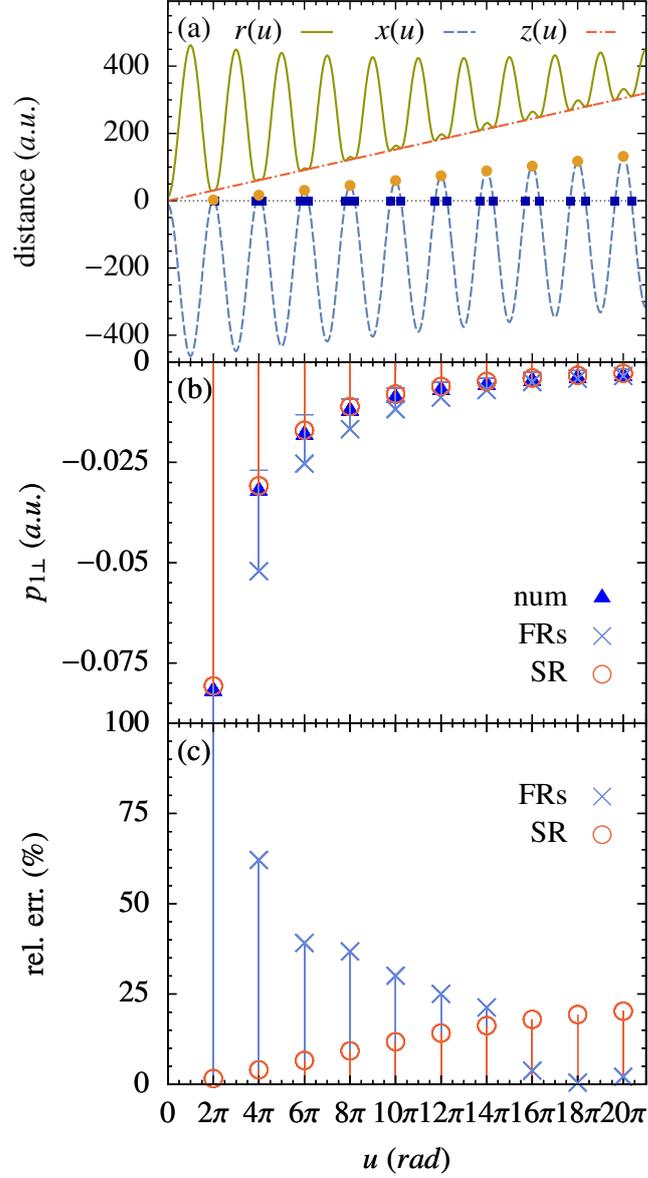for the generalized SR and

$$
\begin{aligned}
x_0(u_f) &= 0, \\
x_0'(u_f) &\neq 0, \\
x_0''(u_f) &\neq 0.
\end{aligned}
\tag{3.2}
$$

for generalized FR. Let us stress that these conditions are not new since we already used them in Sec. 2.3 in order to derive the formulas for R-CMT in the case of SR and FR.

Now, we have two candidates for a rescattering event yielding Coulomb momentum transfer. We ilustrate this situation in Fig. 3.1(a), where we plotted the zero-order positions $x(u)$, $z(u)$ from Eqs. (2.19) and the distance $r(u) \equiv \sqrt{x^2(u) + z^2(u)}$ of the tunneled electron with respect to the parent ion. For simplicity, we assume only two dimensional motion in the x-z plane, which is a reasonable simplification due to the cylindrical symmetry brought by the dipole approximation. We can use the already derived general formulas from Subsecs. 2.3.1 and 2.3.2 for estimation of the R-CMT at every single event as we did in the second panel of the figure and the relative error of the estimations is given in the last panel of the figure (see Fig. 3.1(b) and (c)). Obviously, we cannot take all three rescattering events at $u \approx 2n\pi$ for $n \in \mathbb{N}$ as this would lead to a severe overestimation of the CMT. On the other hand, the results obtained for the slow rescattering by the Eq. (2.44) seem to deliver precise estimation even for large range of $x_r > 0$, where one would expect that the separation into two FRs should deliver more precise results. The reason behind this could be tracked down to the approximations applied in the Sec. 2.3 for derivation of the used formulas.
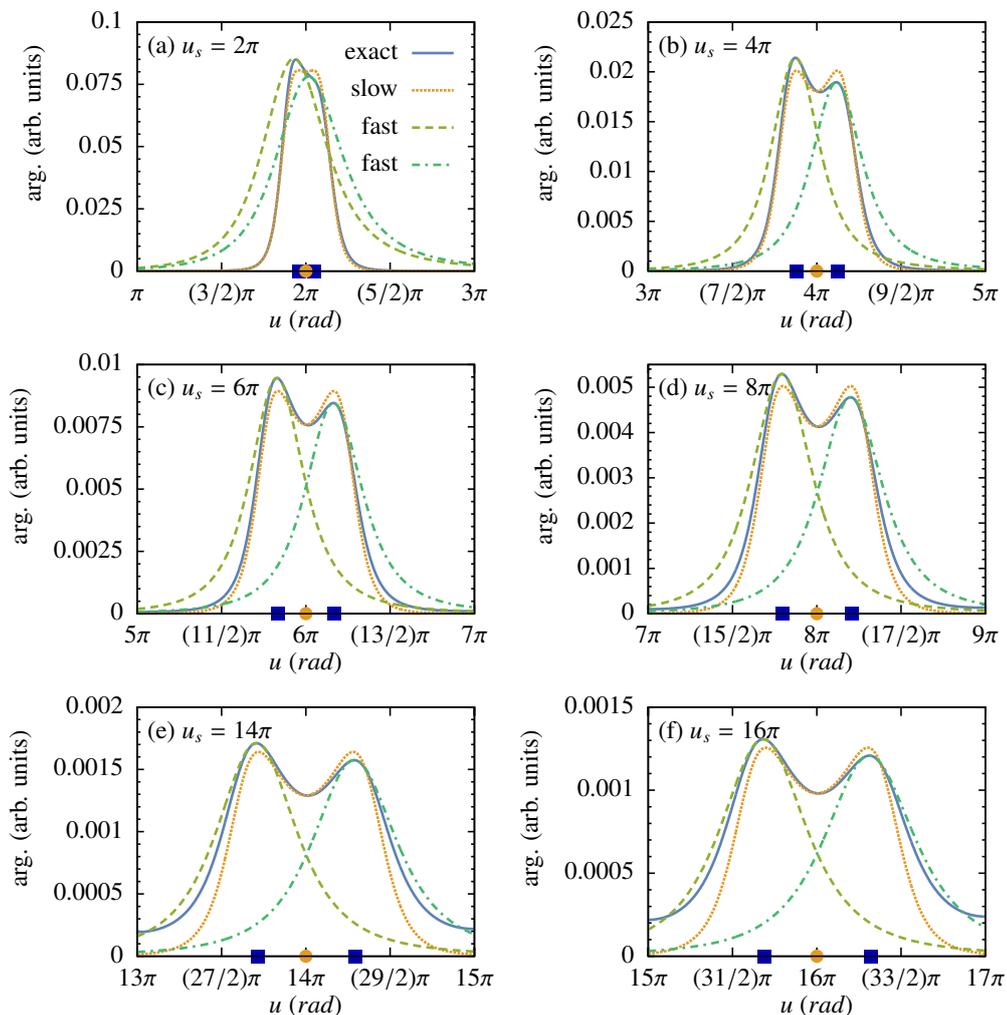
The first-order transversal momentum correction given in Eq. (2.17) poses a non-trivial problem to solve. We plotted the absolute value of the integral argument by a blue solid line in the Fig. 3.2. The approximation for SR given by Eqs. (2.31) simplifies the argument severely. We plotted the absolute value of the simplified argument from Eq. (2.34) with a yellow dotted line in the figure. Every SR is surrounded by two fast recollisions which use approximation from Eqs. (2.48). The corresponding absolute values of the arguments from Eq. (2.51) are carried out by green dashed line for the first FR and by green dash-dotted line for the second FR in the figure. In the Fig. 3.2, we also marked the rescattering phase of the SR and FRs points by yellow dots and blue squares, respectively.

The numerical estimation of R-CMT in the Fig. 3.1(b) corresponds to the area below the blue solid curve on the graphs in Fig. 3.2, the value for R-CMT at SR corresponds to the area under the yellow dotted curve, and the result of R-CMT at FRs to areas under the green dashed(-dotted) lines. The limits of the integration correspond to the closest turning points and hence to the limits of the plot's range for the numerical estimation.

Figure 3.1: The position of the tunneled electron along with all candidates for generalized SRs and FRs are plotted in panel (a). Panel (b) shows the estimated CMTs obtained for the appropriate half-cycle of the laser field: numerically (by blue triangles), from Eq. (2.44) for the SR (by red circles), and as a sum of two CMTs at the two closest FRs from the Eqs. (2.60), (2.63) while regarding the conditions in Eqs.(2.64)-(2.65) (by gray crosses and line segments separating the individual contributions). The relative errors of our estimations are carried out in the last panel (c). Used parameters were: $E_0 = 0.041$, $\omega = 0.0134$, $u_i = 0.75\,\omega$ $p_{yi} = 0$ and $p_{zi} = p_{\perp i} = 0.065$.

The limits of integration extend to $\pm\infty$ for SR and FR within rescattering picture. The rescattering picture breaks down as the argument does not vanish sufficiently fast at the

Figure 3.2: Graphical analysis of the deviation of the argument for the first-order momentum correction with respect to the approximations underlying the recollision events SR and FR. For more details see the text.

turning points, which can be seen in panels (e) and (f) in Fig. 3.1. In the latter case, the integration is applied only in the $\pi/2$ neighborhood of the fast rescattering.

In Fig. 3.1(c), we can see a discontinuous jump in the relative error for the FRs. This abrupt change is caused by the conditions given by Eqs. (2.64)-(2.65), which assure an application of the formulas for the case when the recollision picture does not hold anymore. Interestingly, the relative error before this jump approaches the relative error of the formula for SR and after the jump the precision increases significantly. We can understand such behavior when we look at the arguments in the Fig. 3.2, the yellow curve approximates the exact argument very well, although it misses the asymmetry due to the omission of the transversal motion. The largest discrepancy is found in the last two panels (e) and (f), where the approximation fails to reproduce the turning points. On

the other hand, the arguments for two FRs have the trouble that they usually account twice for the small mutual area at the center of the plots, which does not matter much when the two FRs get sufficiently spacially separated.

As we have seen, the error given by the formula for SR is bound and well behaved. Therefore, we will handle rescattering with small distance $x_r(u_{r,s})$ as a single SR before separating it into two FRs. Our analysis from Fig. 3.1 suggests that this procedure delivers good accuracy for actually quite large distances:

$$x_r(u_{r,s}) \approx \frac{1}{5} \text{ (amplitude of the quiver motion)} . \tag{3.3}$$

Otherwise, we will separate the interaction into two FRs and account for the two R-CMT separately.

Before we start applying the results of this section for a general electron trajectory, let us remark one last thing: the separation method showed here is not the best, but rather the simplest way to obtain reasonable precision for any arbitrary trajectory. For some type of recollision or special values of the laser field, the separation into two FRs can actually provide more precise results than assumption of a single SR even for $x_r(u_{r,s}) \ll \frac{1}{5}$ (amplitude of the quiver motion). Moreover, further improvement can be achieved by application of the preciser formulas from Eqs. (2.55)-(2.57) with integration limits given in the following text as $\sigma_1 = -\text{Mod}(u_r, \pi)$ and $\sigma_2 = \pi - \text{Mod}(u_r, \pi)$ evaluated individually for every FR. Nevertheless, for the sake of simplicity we will abolish any further attempts in this direction in order to keep the theory simple and accessible as our final goal is not to avoid inaccuracies but to reproduce the features of the Coulomb focusing on a large ensemble of trajectories.

3.2 Estimation of the total Coulomb momentum transfer

In the previous section, we have discussed the best ways how to apply our analytical formulas for R-CMT on an arbitrary electron trajectory. Now, we have to apply these formulas and estimate the total Coulomb momentum transfer. There are basically two straightforward schemes: zero-order and step-by-step approach. In this section we are going to introduce these schemes and discussed their difference.

3.2.1 Zero-order trajectory approach

For now, we are going to treat the Coulomb field of the atomic core as a global perturbation. Then, the zero-order trajectory describes the trajectory of the electron solely in the laser field. The total Coulomb effect mostly amounts to I-CMT and R-CMT (there is also a small asymptotic contribution after the laser pulse is switched off, which will be discussed below). For estimation of R-CMT we use the zero-order trajectory, find the rescattering points and for each rescattering event apply our R-CMT formulas derived in the previous sections. The I-CMT distorts the zero-order trajectory significantly which can have an essential impact on the rescattering points. Therefore, we include the I-CMT
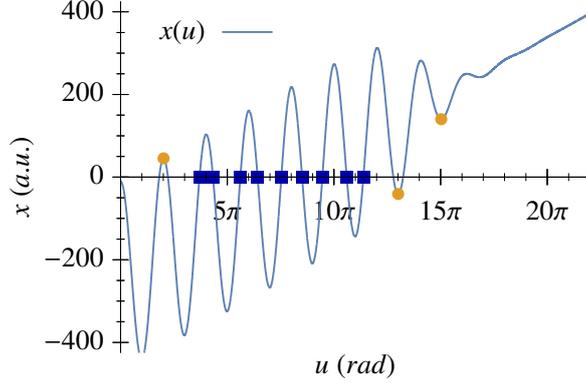
Figure 3.3: An illustrative trajectory demonstrating two different types of recollisions: SR (by orange dots) and FR (by blue squares). We keep the SR points if $|x_r| < E_0/(5\omega^2)$ for $x_r\ddot{x}_r < 0$, otherwise we find the closest FR points. We also keep those SR with $x_r\ddot{x}_r > 0$ but neglect any SR points with $\ddot{x}_r < E_0/10$.

in the zero-order trajectory via modification of the initial momentum:

$$\tilde{x}_0(u) = \frac{E_0}{\omega^2}\left[\cos u - \cos u_i + (u - u_i)\sin u_i\right] + (u - u_i)\frac{p_{2\parallel,\text{in}}}{\omega} + x_i,$$
(3.4)

$$\tilde{y}_0(u) = \frac{p_{yi} + p_{2y,\text{in}}}{\omega}(u - u_i),$$
(3.5)

$$\tilde{z}_0(u) = \frac{p_{zi} + p_{2z,\text{in}}}{\omega}(u - u_i),$$
(3.6)

with $p_{2y,\text{in}}$ and $p_{2z,\text{in}}$ being projections of the transversal I-CMT $p_{2\perp,\text{in}}\left(u_i, \sqrt{p_{yi}^2 + p_{zi}^2}\right)$ on $y-$ and $z-$direction, respectively.

The final momentum is obtained by including the contribution of all R-CMT into the momentum transfer, yielding

$$\mathbf{p}(u_i, \mathbf{p}_{\perp i}) = \mathbf{p}_0(u_i, \mathbf{p}_{\perp i}) + \mathbf{p}_{2,\text{in}}(u_i, \mathbf{p}_{\perp i}) + \sum_{j=1}^{N} \mathbf{p}_1^{(j)}(u_i, \widetilde{\mathbf{p}}_{\perp i}),$$
(3.7)

where N is the total number of effective rescatterings, $\mathbf{p}_0(u_i) = (-A(u_i), p_{yi}, p_{zi})$ the zero-order asymptotic momentum, $\mathbf{p}_{\perp i} = (0, p_{yi}, p_{zi})$ the initial transverse momentum, $\mathbf{p}_{2,\text{in}}(u_i, \mathbf{p}_{\perp i}) \equiv p_{2\parallel,\text{in}}(u_i, |\mathbf{p}_{\perp i}|)\mathbf{e} - |p_{2\perp,\text{in}}(u_i, |\mathbf{p}_{\perp i}|)|\frac{\mathbf{p}_{\perp i}}{|\mathbf{p}_{\perp i}|}$ the initial momentum correction, $\widetilde{\mathbf{p}}_{\perp i} \equiv \mathbf{p}_{\perp i} - |p_{2\perp,\text{in}}(u_i, |\mathbf{p}_{\perp i}|)|\frac{\mathbf{p}_{\perp i}}{|\mathbf{p}_{\perp i}|}$ the distorted initial transversal momentum, and $\mathbf{p}_1^{(j)}(u_i, \widetilde{\mathbf{p}}_{\perp i})$ the R-CMT at the jth recollision given by the formulas discussed in the previous sections, corresponding to the specific type of this recollision.

We treat a recollision as SR in two cases: when $\dot{x}_r = 0$ and $x_r\ddot{x}_r > 0$, as well as those when $\dot{x}_r = 0$, $x_r\ddot{x}_r < 0$ and $|x_r| < x_{\text{thresh}} = E_0/(5\omega^2)$. For the estimation of R-CMT we use Eqs. (2.42)-(2.44) in both cases. All SR with $|\ddot{x}_r| < x_{\text{thresh}} = E_0/(5\omega^2)$ are neglected
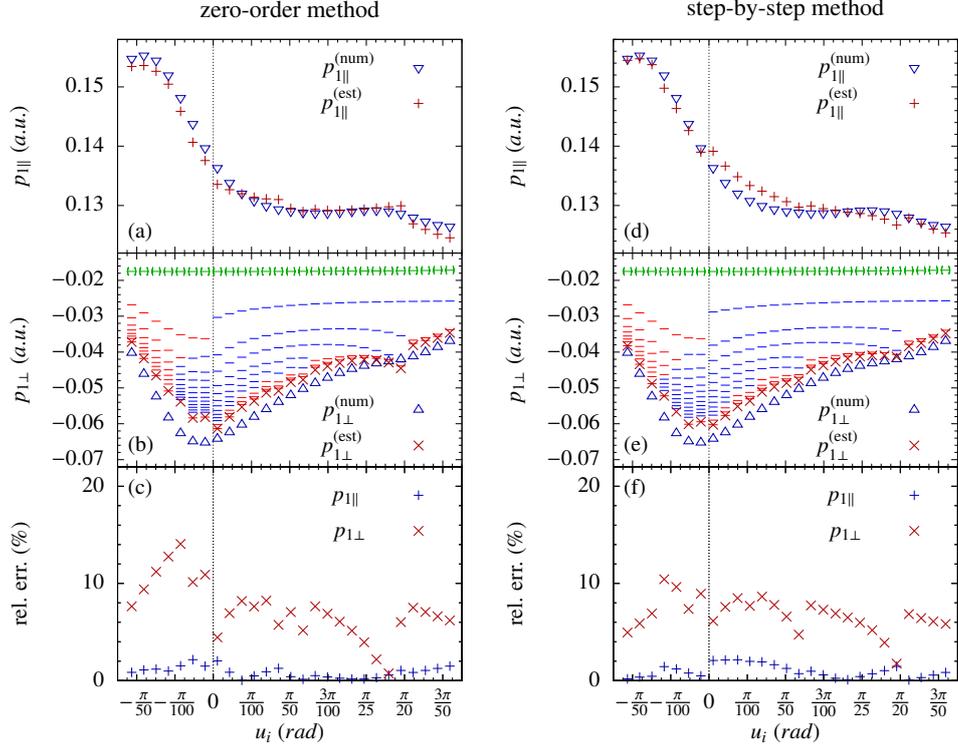
Figure 3.4: Total CMT vs. ionization phase u_i is analyzed for the zero-order method in the left column and for the step-by-step method in the right column. The longitudinal momentum transfer is shown in panels (a) and (d); the transverse momentum transfer in (b) and (e); the corresponding relative errors in panels (c) and (f). Numerical simulations are shown with triangles, the estimation (see the text) with red crosses, I-CMT with green double arrow. The contribution of each R-CMT is shown by a line segment: SR - red, FR - blue. The contributions are added to I-CMT and to the previous R-CMTs, as long as it is larger than 5% of total numerical estimate of CMT. This restriction was applied for the sake of graphical simplicity only.

because such recollisions happen at the end of the laser pulse and have negligible R-CMT, see Fig. 3.3. For some electrons this is not true, however most of them are further trapped in the Rydberg states.

Finally, we treat the remaining rescatterings as FR with Eqs. (2.58)-(2.60) or Eqs. (2.61)-(2.63), depending on the conditions given by Eqs. (2.64)-(2.65). The only exceptions are the FR closest to any SR with $x_r \ddot{x}_r < 0$ and $|x_r| < x_{thresh}$, which we neglect since the R-CMT is already taken into account via the SR (see an exemplary SR at $u_r \sim 13\pi$ replacing two closest FR in Fig. 3.3).

We compare results of our analytical estimations with numerical simulations in the left column of Fig. 3.4 (in the latter a smooth switch-off of the laser pulse is used). For $u_i > 0$, a very good agreement with the numerical simulations is achieved. The error is bound and peaks at the phases where two methods are switching, namely the single SR forks into two FRs. There is a discrepancy for $u_i < 0$, since decreasing u_i tilts the electron's

quivering trajectory down and hence the first recollision becomes slow which generally yields larger momentum transfer than FR. For some particularly small and specially negative u_i, the momentum transfer is so large that the whole zero-order trajectory is not a valid approximation anymore and our present approach fails. The accuracy issue will be discussed below in Subsec. 3.3.

3.2.2 Step-by-step approach

When the electron is ionized near the peak of the laser field, its drift velocity is small, and rescattering can happen with a small impact parameter, inducing large distortion of the laser driven trajectory. The same can happen when the electron is ionized with a small transverse momentum at other ionization phases. It is understandable that the zero-order approximation by Eqs. (3.4)-(3.6) fails in this case. However, we can improve our estimations by taking into account R-CMT at each recollision during propagation in the laser field, which will be the aim of this section. For the obvious reasons, the electron will be propagated by the laser field only step-by-step from the ionization phase u_i till the end of the laser pulse over all the rescattering events, and by correcting the electron momentum by the estimated R-CMT at every single recollision point. This approach is expected to give more precise results, with a wider range of applicability of ionization phases and initial transverse momenta. Moreover, this approach would allow us to incorporate also the, so-called, long trajectories in our model.

Although the laser driven trajectory is disturbed due to R-CMT at the recollisions, the R-CTM itself can be still calculated using perturbation theory because the latter is always applicable at least during the short time of the recollision. This allows us to use the same formulas for R-CMT as in the previous subsection. The only difference is that the zero-order trajectory is replaced by several step-by-step evolved zero-order trajectories.

The drift momentum after the nth-recollision depends on the R-CMT received at all previous recollisions and can be iteratively defined as

$$\mathbf{p}^{(n)}\left(u_i, \mathbf{p}_{\perp i}\right) = \mathbf{p}^{(n-1)}\left(u_i, \mathbf{p}_{\perp i}\right) + \mathbf{p}_1^{(n)}\left(u_i, \mathbf{p}^{(n-1)}\left(u_i, \mathbf{p}_{\perp i}\right)\right),$$

(3.8)

where we have, for simplicity, redefined the I-CMT as zero-order R-CMT: $\mathbf{p}_1^{(0)}\left(u_i, \mathbf{p}_{\perp i}\right) \equiv p_{2\parallel,\text{in}}(u_i, |\mathbf{p}_{\perp i}|)\mathbf{e} - |p_{2\perp,\text{in}}\left(u_i, |\mathbf{p}_{\perp i}|\right)| \frac{\mathbf{p}_{\perp i}}{|\mathbf{p}_{\perp i}|}$, The iteration starts at $n = -1$ with $\mathbf{p}^{(-1)}(u_i, p_{\perp i}) := -A_x(u_i)\mathbf{e} + \mathbf{p}_{\perp i}$. Let us note that $n = 0$ corresponds to the momentum after tunneling but before the first rescattering event which happens at $n = 1$. The properties of the n-th rescattering can be determined from the zero-order trajectory evolved from the $(n-1)^{\text{th}}$ event with the $\mathbf{p}^{(n-1)}(u_i, p_{\perp i})$ momentum yielding

$$x_0^{(n)}(u) = \frac{1}{\omega} \int_{u_{in}}^{u} \left(p_x^{(n)}(u_i, p_{\perp i}) + A_x(u)\right) du + x_0^{(n-1)}(u_{in}), \tag{3.9}$$

$$y_0^{(n)}(u) = p_{yi}^{(n)}(u_i, p_{\perp i}) \left(\frac{u - u_{in}}{\omega}\right) + y_0^{(n-1)}(u_{in}), \tag{3.10}$$

$$z_0^{(n)}(u) = p_{zi}^{(n)}(u_i, p_{\perp i}) \left(\frac{u - u_{in}}{\omega}\right) + z_0^{(n-1)}(u_{in}), \tag{3.11}$$
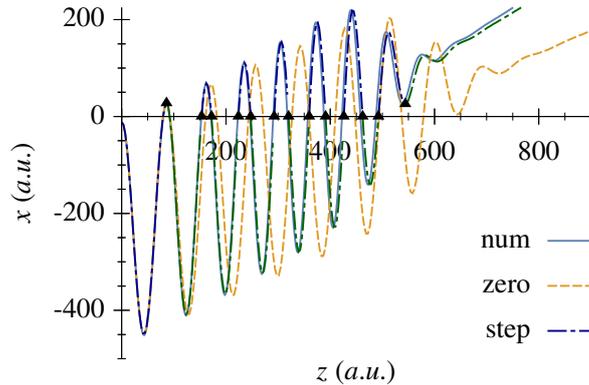
Figure 3.5: The electron trajectories in different approaches: (solid, gray) numerical solution, (dashed, orange) zero-order approach, (dot-dashed, multi-color) step-by-step approach. Rescattering points are noted by black triangles. All trajectories match well for the first half-period but start to differ after the first rescaterring event. The used parameters are $E_0 = 0.041$, $\omega = 0.0134$, $u_i = -\pi/100$ and $p_{\perp i} = 0.2$.

where we set $u_{in} = u_r$ for the n-th rescattering. The tunnel exit enters the iteration as $x_0^{(-1)} = x_i$, $y_0^{(-1)} = z_0^{(-1)} = 0$, and for $n = 0$ we have $u_{in} = u_i$.

Trajectories obtained with the step-by-step and the zero-order approaches are compared with the numerical simulation for $u_i = -\pi/100$ in Fig. 3.5. As we can see, the trajectories do not differ from each other for the first half-period which is achieved by taking the initial momentum correction into account. The difference starts to manifest during the second half-period of the laser field (i.e., after the first rescattering), however, the step-by-step zero-order trajectory approach provides a rather good approximation for the exact numerical trajectory.

We plotted the resulting CMT for various ionization phases and fixed $p_{\perp i} = 0.2$ a.u. in the right column of Fig. 3.4. The relative error does not change much for the positive phases where only few rescatterings take place. For the negative phases we can actually see an increase in the precision which is a good indication that our step-by-step approach could deliver much better results.

We underline an important message of Fig. 3.4, which has been enabled by our analytical approach. A single rescattering is not sufficient to describe the CMT. The contribution of high-order rescatterings to the total CMT is significant and should not be neglected for a good quantitative description.

Although the procedure of finding the right rescattering points seems to be straightforward, we need a quite good algorithm selecting them automatically in order to automatize the methods. The algorithms for selection of the proper rescattering point can be found in appendix C of [191].

3.2.3 Comparing the methods

Let us compare the accuracy of both methods over the whole valid parameter space. For a special class of initial conditions, the components of the final momentum can
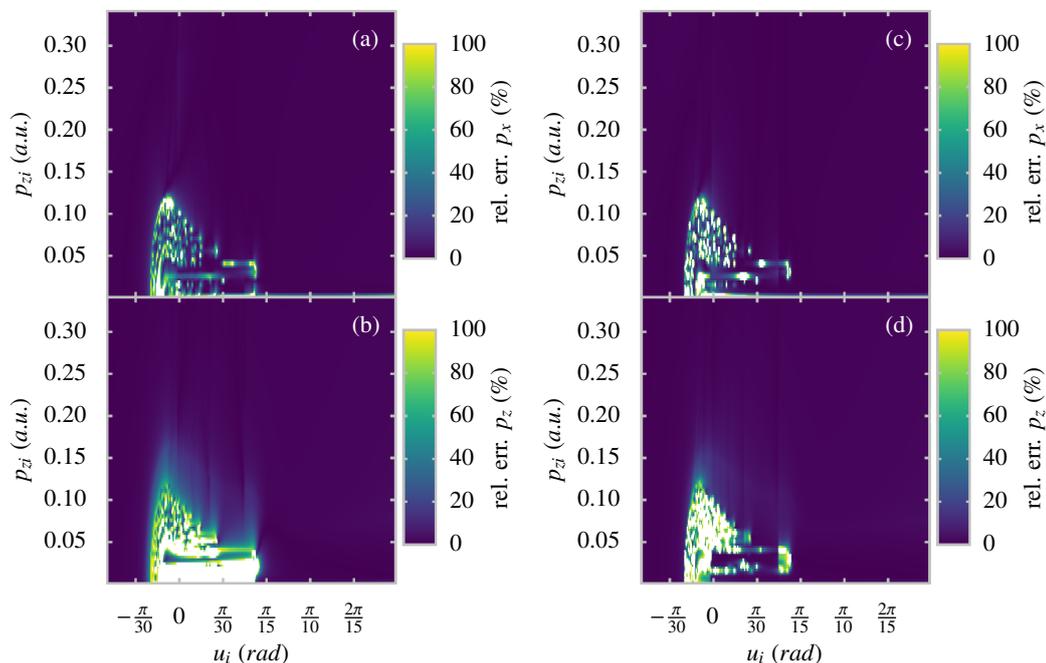
Figure 3.6: Relative error of the estimated asymptotic momentum of the photoelectron within the zero-order trajectory approach in the left column and within the step-by-step approach in the right column. The longitudinal momentum is shown in panels (a), (c) and the transverse momentum in the panels (b), (d).

be vanishing, leading to an artificial enhancement of the relative error. Therefore, we re-define the relative error as follows:

$$\delta p_{\parallel} = \left| \frac{p_{\parallel}(u_i, p_{\perp i}) - p_{\parallel}^{(\mathrm{num})}(u_i, p_{\perp i})}{\max\left[p_{\parallel}(u_i, p_{\perp i}), p_{\parallel}(u_i, p_{\perp i}) - p_{0\parallel}(u_i) \right]} \right| 100\%, \qquad (3.12)$$

$$\delta p_{\perp} = \left| \frac{p_{\perp}(u_i, p_{\perp i}) - p_{\perp}^{(\mathrm{num})}(u_i, p_{\perp i})}{\max\left[p_{\perp}(u_i, p_{\perp i}), p_{\perp}(u_i, p_{\perp i}) - p_{0\perp}(u_i) \right]} \right| 100\%, \qquad (3.13)$$

with $p_{\parallel/\perp}(u_i, p_{\perp i})$ being the proper component of the electron's final momentum given by Eq. (3.7) or by Eq. (3.8) at $n = N$ for zero-order or step-by-step method, respectively. The superscript "(num)" denotes the corresponding value obtained numerically and subscript "0" marks the value obtained from zero-order trajectory neglecting Coulomb interaction. The newly defined relative error is well behaved meaning that it is not singular for the vanishing final momentum where the momentum is replaced with the total CMT instead. We show the re-defined error for valid ranges of the ionization phase u_i, and the initial transversal momentum for our zero-order trajectory method and for the step-by-step method in the left and right column of the Fig. 3.6, respectively.

Obviously, the initial momentum $p_{\perp i}$ plays a crucial role. With decreasing $p_{\perp i}$ the first rescattering has smaller impact parameter and, therefore, induces larger CMT, which
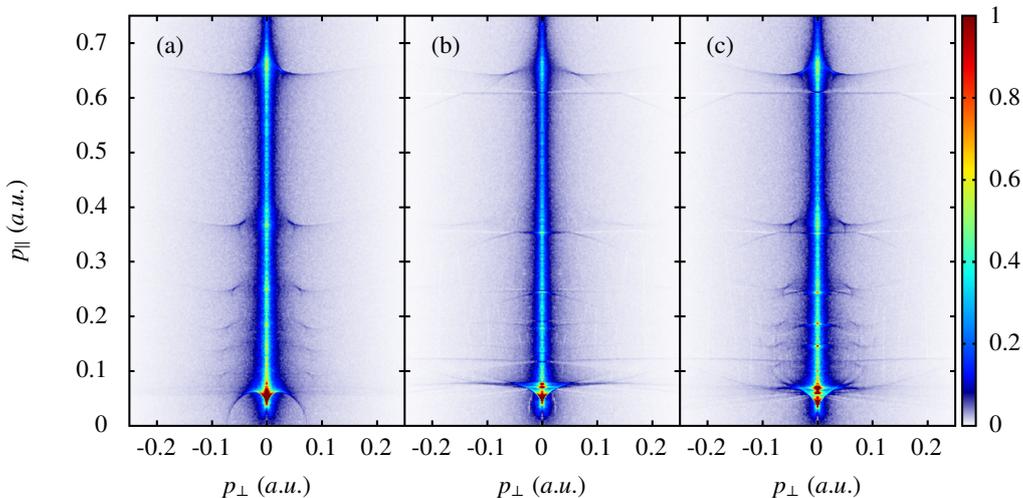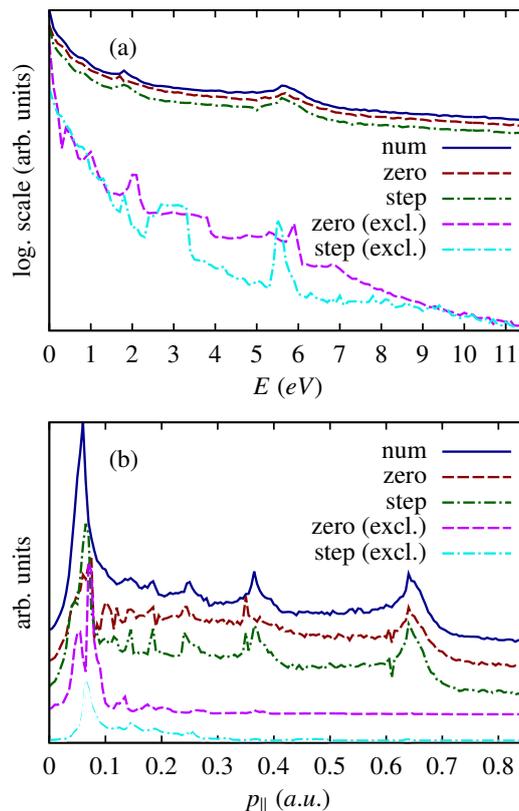
Figure 3.7: PMD: (a) numerical CTMC simulation; (b) via the zero-order trajectory method, and (c) via the step-by-step method.

will introduce discrepancy to the zero-order trajectory. Thus, our method for analytical estimation of CMT is not applicable for ionized electrons with small initial transverse momenta and at small ionization phases (i.e., near the peak of the laser field). The vertical lobes indicate the ionization phases with underlying SR. The error rises there, since the CMT at such recollision is much larger than the CMT at fast recollisions and even a small relative error has a large total contribution.

Finally, let us note that the white areas arise due to several effects: such as chaotic dynamics, hard recollisions, and the trapping of electrons in Rydberg states. Since such effects are not expected to play a significant role for Coulomb focusing, we are not concerned by the white spots at this point. The role of the errors of the present analytical approach for the description of the final PMD is going to be discussed in the next section.

3.3 Photoelectron momentum distribution

In the previous section we have seen that our analytical methods allow us to determine the photoelectron asymptotic momentum during the laser driven excursion in the continuum in the field of atomic core. However, since the accuracy is not acceptable in the whole range of the ionization phases or in the initial transverse momenta, a question arises as how accurately can be the final PMD described by our methods? In this section we compare results of fully numerical CTMC simulation of the final PMD with those of our analytical methods. In order to do this, we performed CTMC simulations in 2D due to the symmetry of the problem in the dipole approximation. Every 2D trajectory of the initial transversal momentum $p_{\perp i}$ is weighted with the PPT transverse momentum distribution $w_{\mathrm{PPT}}(p_{\perp i})$ and with an additional factor of $2\pi p_{\perp i}$. The latter accounts for the fully 3D initial phase space whose two transversal dimensions can be mapped

Figure 3.8: (a) Photoelectron energy distribution; (b) Photoelectron longitudinal momentum distribution: numerical CTMC simulation (solid, blue), via the zero-order trajectory method (dashed, red), via the step-by-step method (dash-dotted, green). We show also distributions while restricting trajectories to those with an error greater than 100% in at least one directions: via the zero-order trajectory method (dashed, magenta), via the step-by-step method (dash-dotted, cyan). The curves are shifted vertically for visibility while keeping the same shift for the same methods in individual panels.

onto a single dimension due to the symmetry via $\mathrm{d}^2 p_{\perp i} = 2\pi p_{\perp i} \mathrm{d}p_{\perp i}$. With the electron asymptotic distribution function $w_{\mathrm{sim}}(p_\parallel, p_\perp)$ provided by the 2D CTMC simulation, one restores the real final 3D PMD:

$$\frac{\mathrm{d}^3 f}{\mathrm{d}^3 p} \propto \frac{w_{\mathrm{sim}}(p_\parallel, p_\perp)}{2\pi p_\perp}, \tag{3.14}$$

where we have restored the second transversal dimension via the relation $\mathrm{d}^2 p_\perp = 2\pi p_\perp \mathrm{d}p_\perp$ for the final transversal momentum $p_\perp$.

We performed three different CTMC simulations with 10^7 trajectories to determine the PMD at the end of the laser pulse: one is fully numerical, the second uses our zero-order trajectory method, and the last uses the step-by-step method. The resulting PMDs are compared in Fig. 3.7.

As we can see, both methods reproduce the central vertical cusp as shown by the CTMC simulation. However, the width of the cusp reproduced by the step-by-step

method is more correct. On one hand, the horizontal fringes appear already by the zero-order method, which can be understood as a manifestation of the fine role of the SRs (so called, longitudinal bunching [97]). On the other hand, the step-by-step method has reconstructed even the right thickness and location of the fringes and thus concludes as a better investigative tool. Unfortunately, both simulated PMDs exhibit additional horizontal lines (e.g., at $p_x \approx 0.61$ a.u.). Such lines can be attributed to an "artificial" longitudinal bunching effect which arises when one SR is replaced by two FR yielding a slightly greater total CMT. Because of this artifact, an additional horizontal line appears underneath each SR regular fringe which demonstrates then as a twofold line in the PMDs. Luckily, the utility of the results is not jeopardized since the artificial fringe is much weaker than the real effect and can be therefore easily disclosed.

The numerical PMD possesses a half-circle fringe of radius ~ 0.08 a.u. (center at the origin) with a prominent peak structure inside. This structure is created by electrons with low transverse momenta near the peak of the laser pulse, for which the error of our analytical methods are large, see white area in Fig. 3.6. Although both analytical methods reproduce the peak, they fail to predict the correct structure of it. This is due to the fact that these electrons undergo multiple recollisions with large CMT and never really gain substantial distance from the ion during the whole laser pulse and are strongly influenced by the Coulomb field even when the pulse is long gone. For such behavior, the perturbative recollision picture does not hold and our methods fail.

Since the first observation of the LES was carried out in the photoelectron energy spectra [81], we show in Fig. 3.8 how our analytical methods reproduce the spectra and the longitudinal momentum distribution obtained by the CTMC simulations where we separated the contributions of the electrons creating the PMDs in Fig. 3.7 and of those which were not taken into account due to significant errors. As we see, the excluded contributions are negligible in the energy domain; especially, for non-vanishing energies. However, two features manifesting as sharp peaks can be found at $p_x \approx 0.65$ $a.u.$ and at $p_x \approx 0.075$ $a.u.$, which can be discerned clearly in Fig. 3.7. As we can see, already the zero-order trajectory method captures the positions of the peaks in the energy distribution quite correctly. Nevertheless, the peak at the vanishing longitudinal momentum is misplaced which is corrected by the more precise step-by-step method.

We can conclude that our analytical approach is able to predict correctly many features of PMD, in particular, width of the vertical cusp, the peaks along it, and the position of the horizontal caustic fringes due to the longitudinal bunching. Our approach fails only at very low momenta $p_x \lesssim 0.05$ a.u. While predicting the existence of the lowest momentum peak, neither of our methods provides its correct structure. The reason is that the trajectories with a large error (white areas in Figs. 3.6(a)-(d)) mostly contribute to this prominent peak at low momenta which explains the noticeable discrepancy between the numerics and our results in this region. On the bright side, the white areas contribute to the momentum peaks at larger energies only negligibly and do not threaten the utility of our approach to CF for the largest part of the PMD, see Fig. 3.8(b).
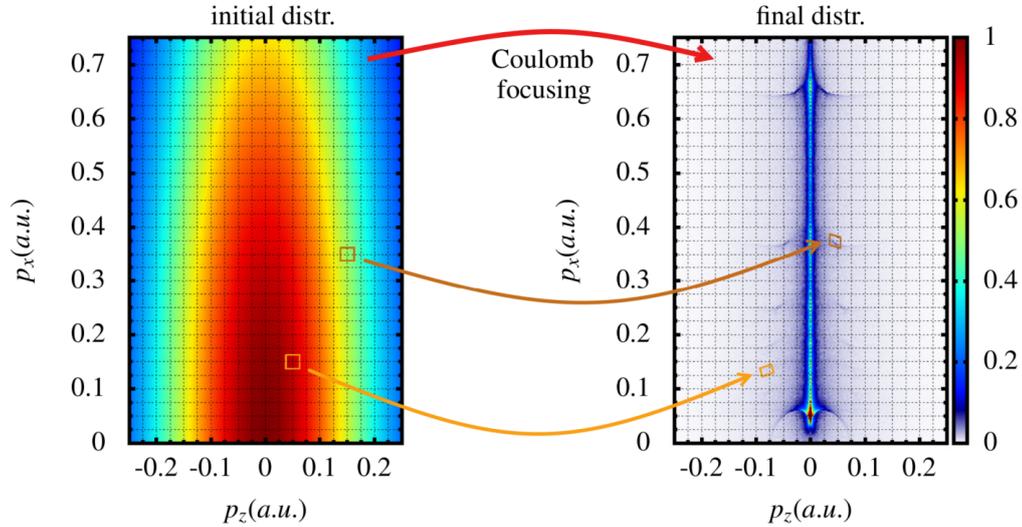
Figure 3.9: We illustrate the transformation of the initially tunneled electron distribution (on the left side) into the final distribution at the end of the laser pulse (on the right side) due to the action of Coulomb focusing (red arrow). The momentum space is divided into bins of small size with their centers located on each intersection of the grid lines as illustrate by orange squares in the left plot. In ideal case, the analytical description of Coulomb focusing predicts how the bins shift and deform due to the evolution of in the combined laser and Coulomb field, which we indicated in the right plot.

3.4 Coulomb focusing as a transformation

In the previous sections, we have calculated analytically the total momentum transfer to any tunneled electron due to multiple rescatterings during its excursion in the laser field. Moreover, we have demonstrated in the last section our ability to derive the whole asymptotic photoelectron momentum distribution analytically within the semi-classical approximation capturing all the important features of the Coulomb focusing despite all the introduced errors. Nevertheless, there are several serious drawbacks to our approach as we showed barely the feasibility of the analytical approach burden with errors to reproduce the final distribution, but we still relay on a rather extensive classical trajectory Monte-Carlo simulations with large number of trajectories. This also means that we have not really gained any deep insight into the Coulomb Focusing itself as its effect are still rather concealed by the large numbers of now analytically described trajectories.

On the other hand, we have now all the tools necessary for a complete analytical description of Coulomb focusing. Let us assume that the Coulomb interaction between the tunneled electrons driven by the external laser field and its parent ion acts like a transformation on the tunneled wave function. We illustrate this in Fig. 3.9: the initial distribution is plotted in the left plot and shows what we would measure when the Coulomb interaction is switched off directly after tunneling; the transformed distribution

at the end of the laser pulse is shown in the right plot and demonstrates the strong influence of the Coulomb focusing on the tunneled wave packet. We can significantly reduce the number of necessary trajectories when we do not sample the transformation by randomly distributed electrons as in previous section, but rather place single electrons in intersections of the grid lines and assign a small bin to them as shown demonstrated in Fig. 3.9 by two orange bins. The center of the bin will change its position focusing and its shape due to Coulomb. Whereas the first can be determined by the already derived methods, the latter has to be still addressed.

For this purpose, we will assume that the initial distribution is in the (p_x, p_z) space only. This can be done once we assume that the longitudinal momenta is connected to the ionization time t_i via the zero-order trajectory

$$
\begin{aligned}
p_x(t_i) &\equiv -A_x(t_i), & (3.15) \\
\mathrm{d}p_x &= E_x(t_i)\mathrm{d}t_i, & (3.16)
\end{aligned}
$$

leading to modification of the ADK distribution for the distribution in p_x as

$$
w_{ADK}(t_i)\mathrm{d}t_i = \frac{w_{ADK}(t_i(p_x))}{|E_x(t_i(p_x))|}\mathrm{d}p_x, \tag{3.17}
$$

where we understand $t_i(p_x)$ as the inversion of Eq. (3.15). Let us note that we also assumed that the transformation in Eq. (3.15) is an injective function, which is well fulfilled for any general sinusoidal pulse while handling its half-cycles separately as we do in our analysis. However, this may not be true for a specially tailored laser pulse and has to be accounted for. A possible bypass could provide a further division of the ionization regions in order to avoid any surjective mapping by Eq. (3.15). If fulfilled, we can distribute the electrons on the equidistant intersection of the grid lines (p_x, p_z) in Fig. 3.9 and assign them the weights from the right hand side of Eqs. (3.17) and from the standard ADK transversal distribution.

Furhter, we can define the action of the Coulomb focusing as a transformation of the unperturbed zero-order final momentum space (p_x, p_z) due to the Coulomb focusing, which is given by a function $\bar{\mathbf{p}}(p_x, p_z)$ as

$$
(p_x, p_z) \xrightarrow{\mathrm{CF}} \bar{\mathbf{p}} = \bar{\mathbf{p}}(p_x, p_z) = \bar{\mathbf{p}}(u_i, p_z). \tag{3.18}
$$

Thanks to the to the one-to-one relation between the momentum p_x and the ionization phase u_i, we can apply the results from the previous sections estimating the electron's final momentum while taking into account the total CMT; namely, the results from the zero-order and step-by-step method given in Eqs. (3.7) and (3.8), respectively.

The center of the bin is placed at some particular coordinates $\left(p_x^{(b)}, p_z^{(b)}\right)$, and it can be easily estimated how its position changes when we apply the transformation from Eq. (3.18) and one of the analytical methods and find the new coordinates $\left(\bar{p}_x^{(b)}, \bar{p}_z^{(b)}\right)$. On the other side, the bin is not a single point and we have to define its size by two small

quantities $\mathrm{d}p_x^{(b)}$ and $\mathrm{d}p_z^{(b)}$ which stretch the bin's four vertexes relatively to its center as

$$
\begin{aligned}
\mathbf{v}_1 &\equiv \left(+\mathrm{d}p_x^{(b)}, +\mathrm{d}p_z^{(b)} \right), \\
\mathbf{v}_2 &\equiv \left(-\mathrm{d}p_x^{(b)}, +\mathrm{d}p_z^{(b)} \right), \\
\mathbf{v}_3 &\equiv \left(-\mathrm{d}p_x^{(b)}, -\mathrm{d}p_z^{(b)} \right), \\
\mathbf{v}_4 &\equiv \left(+\mathrm{d}p_x^{(b)}, -\mathrm{d}p_z^{(b)} \right).
\end{aligned}
\tag{3.19}
$$

It would be unwise to sample the bin with additional points and follow the change of their position under the transformation, since we would return to the CTMC simulation described in the the previous section 3.3. Let us therefore take another approach. If the size of the bin and hence the values $\mathrm{d}p_x^{(b)}$ and $\mathrm{d}p_z^{(b)}$ is sufficiently small, we can estimate the position of vertexes of the transformed bin via the Jacobian matrix of the transformation in Eq. (3.18) yielding in our case

$$
\mathbf{J}(p_x, p_z) \equiv
\begin{pmatrix}
\frac{\partial \bar{p}_x(p_x, p_z)}{\partial p_x} & \frac{\partial \bar{p}_x(p_x, p_z)}{\partial p_z} \\
\frac{\partial \bar{p}_z(p_x, p_z)}{\partial p_x} & \frac{\partial \bar{p}_z(p_x, p_z)}{\partial p_z}
\end{pmatrix},
\tag{3.20}
$$

where the bared values denotes the components of the final vector $\bar{\mathbf{p}} = (\bar{p}_x, \bar{p}_z)$ of equivalently

$$
\mathbf{J}(u_i, p_z) =
\begin{pmatrix}
\frac{\omega}{E_x(u_i)} \frac{\partial \bar{p}_x(u_i, p_z)}{\partial u_i} & \frac{\partial \bar{p}_x(u_i, p_z)}{\partial p_z} \\
\frac{\omega}{E_x(u_i)} \frac{\partial \bar{p}_z(u_i, p_z)}{\partial u_i} & \frac{\partial \bar{p}_z(u_i, p_z)}{\partial p_z}
\end{pmatrix}
\tag{3.21}
$$

where we applied Eq. (3.16) along with $u_i \equiv \omega t_i$.

Now, when we have the bin and its vertexes defined, we can easily estimate the change of its vertexes due to the Coulomb focusing as

$$
\bar{\mathbf{v}}_i = \mathbf{J}(p_x^{(b)}, p_z^{(b)}) \cdot \mathbf{v}_i, \qquad \text{for } i = 1, 2, 3, 4.
\tag{3.22}
$$

Eventually, we have to deal with the transformed and most likely deformed bin. For simplicity, we assume that the electron density given by the ADK weights is uniformly distributed within the bin and we divide it into the grid cells accordingly to areas of their intersection with the bin. (E.g., the upper bin (by dark orange) in Fig. 3.9 has non-zero intersection with four grid cells but the lower bin (by orange) only with three cells). We repeat the whole procedure for every single bin from the initial phase space and keep adding the transformed electron densities corresponding grid cells till we reconstruct the final photoelectron distribution.

After this rather theoretical introduction, let us take a deeper look on the individual methods and see how the Jacobian matrix looks like.

3.4.1 Zero-order method

The advantage of our approach is that we successfully separated the Coulomb interaction into few rescattering points allowing an individual treatment. We can do the same for the transformation by Eq. (3.18) and also for the Jacobian matrix by Eq. (3.21) while

taking into account the definition of the method from Eq. (3.7). The Jacobian matrix yields

$$\mathbf{J}^{(N)}(u_i, p_{zi}) = \begin{pmatrix} 1 + \frac{\omega}{E_x(u_i)} \sum_{n=0}^{N} \frac{\partial p_{1x}^{(n)}(u_i, p_z)}{\partial u_i} & \sum_{n=0}^{N} \frac{\partial p_{1x}^{(n)}(u_i, p_z)}{\partial p_z} \\ \frac{\omega}{E_x(u_i)} \sum_{n=0}^{N} \frac{\partial p_{1z}^{(n)}(u_i, p_z)}{\partial u_i} & 1 + \sum_{n=0}^{N} \frac{\partial p_{1z}^{(n)}(u_i, p_z)}{\partial p_z} \end{pmatrix}, \qquad (3.23)$$

where N denotes the number of recollisions for the zero-order trajectory as given by Eqs. (3.4)-(3.6), and $p_{1x}^{(n)}$ and $p_{1z}^{(n)}$ correspond to the Coulomb momentum transfers as defined in Eq. (3.7).

3.4.2 Step-by-step method

The step-by-step approach yields difficulties because of the iterative dependency on the initial conditions in Eq. (3.8). Nevertheless, the derivation is trivial and the result can be written in a quite compact form as a product of $N + 1$ two-by-two matrices:

$$\mathbf{J}^{(N)}(p_{xi}, p_{zi}) = \prod_{n=N}^{0} \begin{pmatrix} 1 + \frac{\partial p_{1x}^{(n)}\left(p_x^{(n-1)}, p_z^{(n-1)}\right)}{\partial p_x} & \frac{\partial p_{1x}^{(n)}\left(p_x^{(n-1)}, p_z^{(n-1)}\right)}{\partial p_z} \\ \frac{\partial p_{1z}^{(n)}\left(p_x^{(n-1)}, p_z^{(n-1)}\right)}{\partial p_x} & 1 + \frac{\partial p_{1z}^{(n)}\left(p_x^{(n-1)}, p_z^{(n-1)}\right)}{\partial p_z} \end{pmatrix}. \qquad (3.24)$$

where $p_{1x}^{(n)}$ and $p_{1z}^{(n)}$ correspond to the Coulomb momentum transfers as defined in Eq. (3.8). Let us stress that the order of the matrices in the product is reversed, which is fairly easy to understand when we think of the n-th matrix as of the transformation of the phase space introduced only by the n-th recollision event and by the corresponding R-CMT only. The subsequent transformation is then given by the $(n + 1)$-th matrix placed on the left hand side of the n-th matrix in agreement with the matrix notation of transformations.

3.4.3 Comparison

As we have seen, there are ways how to construct the Jacobian matrix with both analytical methods, since we have provided differentiable formulas for $p_{1x}^{(n)}$ and $p_{1z}^{(n)}$ in the previous chapter and we can basically construct the transformation matrix for every single electron trajectory. Nevertheless, this course of action is rather tedious then complicated so we do not pursuit it any further at this moment as we expect it to be a research topic on its own.

On the other hand, it would be appropriate to demonstrate at least the feasibility of such complex task. For that purpose we resumed to our modified numerical CTMC simulation from the previous section 3.3, where we implemented the proper derivatives of the I-CMT and R-CMT and the transformation of the phase space given by the Jacobian matrices from Eq. (3.23) and (3.24) for the zero-order and step-by-step method, respectively. We have divided the initial phase into bins of size 0.00125×0.00125 and followed the procedure described above in this section. The collected electron densities are plotted in the Fig. 3.10; we show for comparison the standard numerical CTMC
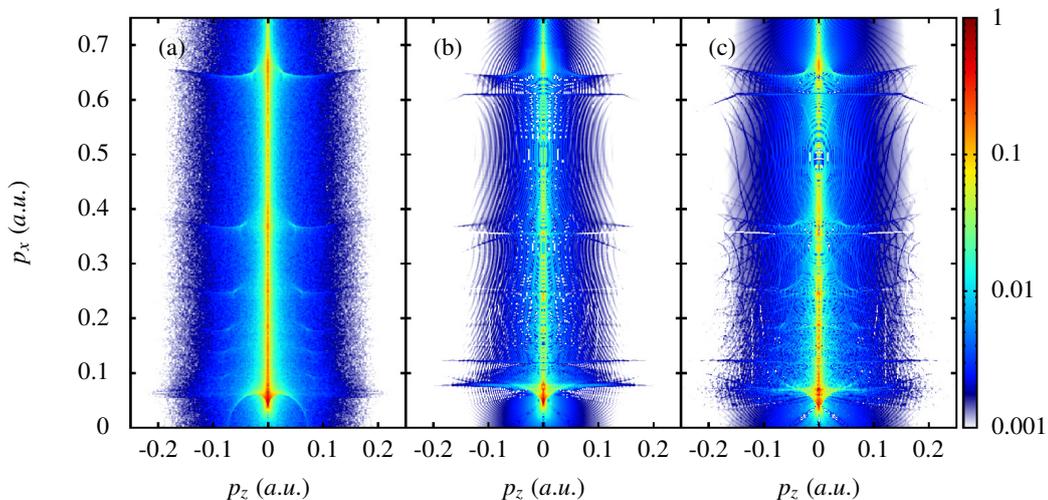
Figure 3.10: We compare our PMDs obtained by phase space transformation from Eq. (3.22) to the numerical results in (a). The zero-order trajectory method yields PMD plotted in (b) and the step-by step-method gives the PMD in (c).

simulation in the panel (a), the result of the zero-order method in the panel (b), and the result of the step-by-step method in the panel (c). As we can see, the transformation of the phase space provides very good agreement with the numerical simulation giving us hope for future applicability of the transformation for investigation of the Coulomb focusing. As expected, the step-by-step method performs slightly better, especially at the small longitudinal momenta. There are some slight drawbacks: a grading of the cusps (e.g., at $p_x \approx 0.74$ and $p_z \approx 0$ in panels (b) and (c)) or appearance of distinct vertical lines. Whereas the first could be avoided by a better coverage of the initial momentum space, the latter is the result of errors introduced by the approximation under which we have derived the analytical formulas. Nevertheless, the latter could be also diminished by a better choice of coverage (e.g., a double coverage of the initial phase space by two layers of mutually shifted bins). We plotted the projections of the energy and longitudinal momenta in the same manner as in previous section in Fig. 3.11. The energy spectra exhibit oscillations (primarily for the high energies) which can be contributed to the vertical lines in the PMD of Fig. 3.10. This we conclude from the fact that these oscillations are absent in the spectrum of the longitudinal momentum meaning that once we suppress the vertical lines (e.g., by a better coverage) the oscillations should vanish or be at least suppressed strongly. Finally, it is not a surprise that the step-by-step method provides again better results than the zero-order method.

3.4.4 Initial momentum correction and its properties

Interestingly, the forms of the Jacobi matrices in Eqs. (3.23)-(3.24) allows us to cut off the momentum transfer at any arbitrary recollision and investigate the transformation of the initial phase space taken place up to this recollision. By taking this to the extreme,
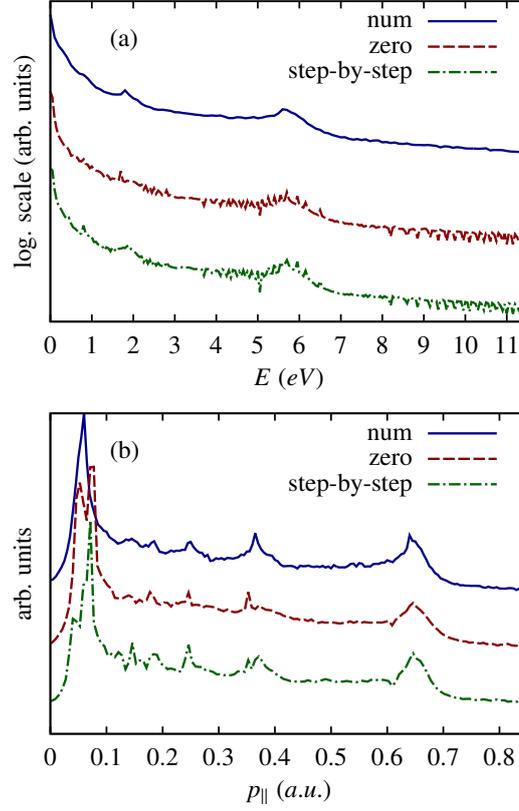
Figure 3.11: Comparison of Photoelectron energy distribution in (a); and Photoelectron longitudinal momentum distribution (b): obtained by numerical CTMC simulation (solid, blue), via transformation of the initial phase space by the zero-order trajectory method (dashed, red), via the step-by-step method (dash-dotted, green). The oscillations in the energy spectrum are caused by the error of the underlying analytical formulas and can be connected to the vertical lines in Fig. 3.10.

we can analyze the role of the I-CMT by itself as we omit all rescattering events. Not surprisingly, both methods yield the same formula:

$$\mathbf{J}^{(0)}(u_i, p_z) = \begin{pmatrix} 1 + \frac{\omega}{E_x(u_i)} \frac{\partial p_{2x,in}(u_i, p_z)}{\partial u_i} & \frac{\partial p_{2x,in}(u_i, p_z)}{\partial p_z} \\ \frac{\omega}{E_x(u_i)} \frac{\partial p_{2z,in}(u_i, p_z)}{\partial u_i} & 1 + \frac{\partial p_{2z,in}(u_i, p_z)}{\partial p_z} \end{pmatrix}. \tag{3.25}$$

Let us for simplicity use only the first-order I-CMT formulas in the form including the ionization potential I_p from Eqs. (2.86)-(2.87) leading to

$$\mathbf{J}^{(0)}(u_i, p_z) = \begin{pmatrix} 1 + \frac{Z\pi\omega}{E_a} \frac{E_x'(u_i)}{E_x(u_i)} & 0 \\ -\frac{2Z p_z}{\kappa E_a} \frac{E_x'(u_i)}{|E_x(u_i)|} & 1 - \frac{2Z|E_x(u_i)|}{\kappa E_a} \end{pmatrix}, \tag{3.26}$$

75

where the prime denoted derivative with respect to u_i. The properties of the transformation can be obtained from the determinant of the Jacobian matrix giving

$$\det \mathbf{J}^{(0)}(u_i, p_z) = 1 - \frac{2Z|E(u_i)|}{\kappa E_a} + \frac{Z\pi\omega}{E_a}\left(\frac{E_x'(u_i)}{E_x(u_i)}\right)\left(1 - \frac{2Z|E(u_i)|}{\pi\kappa E_a}\right), \qquad (3.27)$$

where the second term is always positive. The second term in the brackets can be neglected with respect to one due to the condition from Eq. (2.5) and we can write the determinant for $E_x(u_i) = E_0 \cos u_i$ as

$$\det \mathbf{J}^{(0)}(u_i, p_z) \approx 1 - \frac{2Z|E(u_i)|}{\kappa E_a}\left[1 + \frac{\sin u_i}{\cos u_i}\pi\gamma(u_i)\right], \qquad (3.28)$$

The term in the square brackets is always positive for rescattered electrons with $u_i \in [0, \pi/2)$ yielding $\det \mathbf{J}^{(0)} < 1$ and could be negative for the direct electrons with $u_i \in (-\pi/2, 0)$ meaning $\det \mathbf{J}^{(0)} > 1$. Nevertheless, the bracket is still positive for reasonable values of $\gamma < 1$ as most of the ionization happens at the peak of the laser field $u_i \sim 0$ and hence the most direct electrons will be also focused. Let us note that, although one could find such large u_i ensuring defocusing of the direct part of tunneled wave packet, the ionization phase would be quite small (i.e., $u_i \approx -\pi/4$ for the parameters $E_0 = 0.041$, $\omega = 0.0134$ and $I_p = 0.5$) leading not only to suppression of the tunneling rate but also to questioning of the validity of I-CMT in Eqs. (2.86)-(2.87) as the laser field changes rapidly at these phases (i.e., $\frac{dE(u)}{du} \propto \sin(u)$) and the approximation of the constant electric field may not be valid any more. Therefore, the Eq. (3.28) should be handled with caution for the ionization phases distant from the peaks of the laser field.

3.5 Summary

We have analyzed the accuracy of our analytical approach in the case of dipole approximation, estimating the total Coulomb momentum transfer during multiple recollisions by two different methods. Besides the simplest zero-order laser driven trajectory method, we put forward also the step-by-step method, where the electron's momentum is revised at each recollision by the Coulomb momentum transfer and the revision is also taken into account for the electron's trajectory. Both methods were used to derive the final photoelectron momentum distribution. We showed that they both satisfactory describe the asymptotic photoelectron momentum distribution in a large range of momentum space, with the step-by-step method describing more closely the fine features of Coulomb focusing. However, the accuracy of our approach fails at very low photoelectron energies, where both methods correctly predict existence of low-energy peak, but do not deliver its correct structure.

Finally, we presented an outlook for further application of our results for further investigation of Coulomb focusing: redefinition of the Coulomb focusing as a transformation of the initial, by Coulomb effects unperturbed, momentum distribution. Moreover, we have found the Jacobian matrix of this transformation and demonstrated the feasibility of this approach by modified classical trajectory Monte-Carlo simulation, and as an example we have analyzed the properties if the I-CMT within this formalism and have shown that

the electrons will be focused by the Coulomb interaction already as they departure from the parent ion.

Chapter 4

Nondipole effects in linear polarization

In this chapter, we demonstrate a practical application of the analytical formulas derived in the previous chapters as we employ them in order to gain insight into the process of Coulomb focusing in the nondipole regime. In particular, we present an explanation for the observed counterintuitive energy-dependent shift of the central vertical cusp in PMD against the propagation direction of the laser field as firstly reported in [114].

The existence of the shift is a manifestation of nondipole effects. It is contributed to the magnetic component of the Lorentz force, and is to be expected. Puzzling is rather the nature of the shift having negative sign when one would expect positive offset as the magnetic force on the tunneled electrons acts only along the propagation direction of the laser field. Additionally, extensive TDSE simulations have even shown that the shift of the cusp is not constant and the central cusp bends depending on the longitudinal momenta [115]. Let us also mention that the observation of the nondipole effects in the mid-IR regime of the relativistic parameter $\xi \equiv \frac{E_0}{c\omega} = 0.025 \ll 1$ is a praise on extremely high precision of the now-a-days spectrometers and opens new possibilities for measurement techniques.

Finally, as there are no other interactions others than the Coulomb and the magnetic forces present, this effect is a perfect candidate for the first application of our model. This chapter is based on [191].

4.1 Rescattering in the nondipole regime

Our aim is to investigate of the shift in the nondipole regime and to explain its nontrivial shape. The central cusp is shifted along the laser propagation direction by a value that varies with respect to the asymptotic longitudinal momentum. This can be seen in our CTMC simulation of PMD presented in Fig. 4.1. In the simulation, we have used the classical Newton equations from Eq. (2.8) including also the magnetic component of the Lorentz force stemming from the laser field and given in Eqs. (2.1). For practical reasons, we have used a Gaussian envelope $f(t) = \exp\left(\frac{u^2}{2(u_D)^2}\right)$ with $u_D = 3\pi$ assuring rather short pulse.

As the CTMC simulation suggests, the shift is not uniform and varies with the value of the longitudinal momenta (in agreement with [115]). The shift is positive for large longitudinal momenta, as expected, because of the positive drift momentum of the electron in the laser field along the propagation direction. Meanwhile, the shift becomes negative for small longitudinal momenta, but tends to zero at vanishing longitudinal momenta
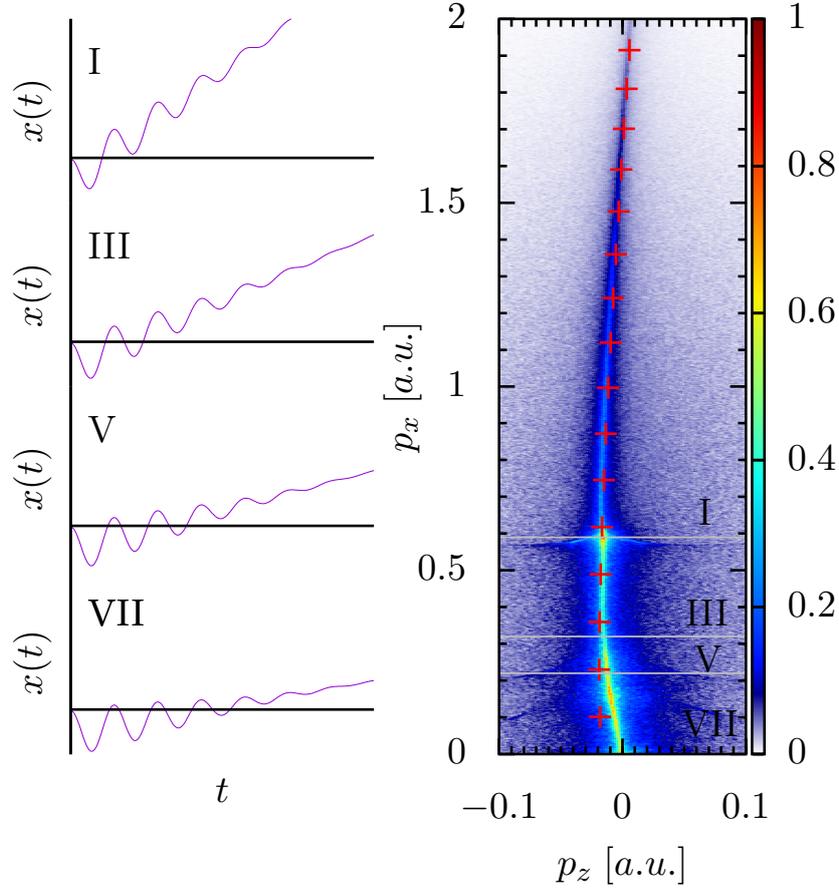
Figure 4.1: In the left panel, we present a cut with $|p_y| < 0.6$ a.u. of final PMD obtained by CTMC simulation in the nondipole regime. The central cusp is striking and manifests a clear bend towards positive p_z-momenta as long as the longitudinal momentum is $\gtrsim 1.6$, which is in agreement with expectations. On the other hand, a counterintuitive shift towards negative p_z-momenta appears at smaller longitudinal momenta, reaches its maximum along the opposite axis at $p_x \approx 0.4$, and goes towards zero at vanishing longitudinal momenta again. The horizontal gray lines correspond to trajectories with slow recollision given by the Eqs. (2.21) and hence with an even number of recollisions. The gray lines separate the spectrum into regions with odd number of recollisions as marked by the Roman numbers. The typical trajectories from each of the regions can be found in the left column of the figure. The red crosses correspond to our predictions for single recollision from Eq. (4.7) and manifest excellent agreement in the region I with the transition of the offset.

again. Such complex dependence on the longitudinal momentum (or equivalently, on the electron's energy) is intriguing and demands further investigation.

The CTMC simulation can be used for investigation of the electrons that end on the shifted cusp. We looked for electrons which end in a small bin of size $0.01 \times 0.01 \times 0.01$ whose center is placed at the cusp in the region of negative shift. Consequently, we plotted the initial momentum space in the Fig. 4.2 revealing two interesting phenomena:
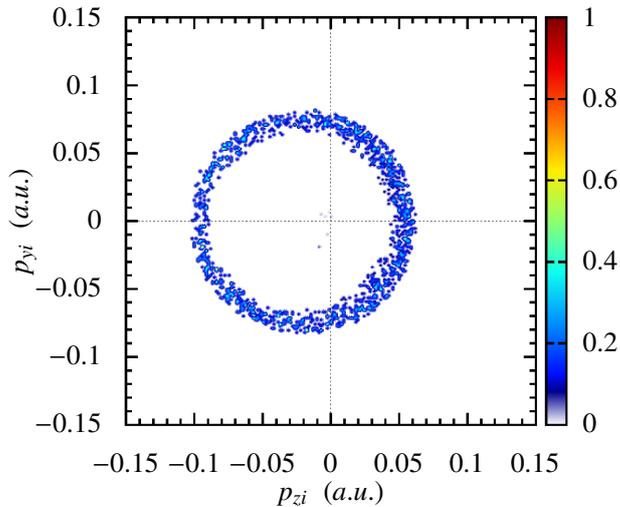
Figure 4.2: Momentum space of the initial electron distribution at the tunnel exit: the part that finally ends in the final momentum bin at $p_x = 0.588$ a.u. and $p_z = -0.0157$ a.u. The value of the longitudinal momentum corresponds to the first soft recollision. We stress that the ring is shifted to the negative p_z direction.

the electrons creating the cusp originate from a ring of radius ≈ 0.75 a.u., and the center of the ring is shifted towards negative p_{zi} momenta.

The creation of the ring can be easily understood as the Coulomb focusing pulling all the electrons placed originally at the tunnel exit with initial transversal momenta distributed over the whole (p_y, p_z)-transversal plane to a single point (or rather a bin) in the final momentum phase space. Noticeably, the circle has a rather small thickness leading to the conclusion that only distinguished electrons can be focused to the center. This along with the rotational symmetry of the ring allows us to identify the radius as the total transverse R-CMT obtained by the cusp electrons. The shift of the circle can be understood as compensation for the drift induced by the magnetic component of the laser field. Every part of the ring is shifted uniformly since all the electrons have tunneled at the same ionization phase u_i and rescattered at the same rescattering phase u_r yielding the identical drift momentum $p_{zd}(u_r, u_i)$ from Eq. (2.14). We firstly presented these results in [142].

In order to investigate the underlying physics, we employ the famous three-step model [15] separating the process into three steps: Ionization, Propagation and Rescattering. We will slightly modify the propagation to incorporate the nondipole effects. Since the cusp electrons originate on a circle, we have quite a large freedom of choice for the initial conditions. Let us pick one very special electron with $p_{yi} > 0$ and $p_{zi} = 0$ and follow its evolution as we demonstrate in Fig. 4.3. The rescattering parameter z_r will be positive due to the induced magnetic drift, which guarantees negative momentum transfer due
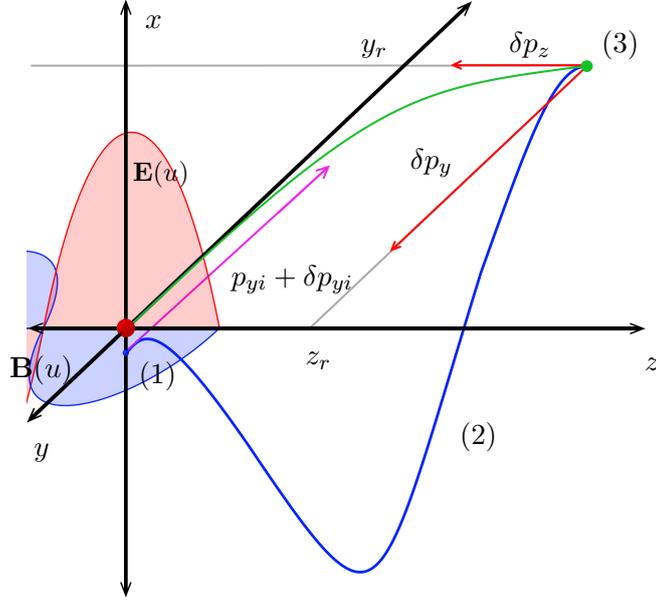
Figure 4.3: Schematic sketch of the mechanism behind the creation of the bend. The atom (red ball at the origin) is placed in the external laser field, whose electric component $\mathbf{E}(u)$ and magnetic component $\mathbf{B}(u)$ are marked as red sinusoid along the x-axis and as blue sinusoid along the y-axis, respectively. At some ionization phase, the electron appears at the tunnel exit (1) at $y_i = z_i = 0$ and with nonzero initial transversal momentum $p_{yi} + \delta p_{yi}$ only along the y-axis as marked by magenta arrow. Then, the electron propagates in the combined Coulomb and laser field as marked by the blue trajectory (2) and loses part of its initial momenta δp_{yi} due to I-CMT. Projection of the blue trajectory on the y-z plane is depicted as green curve and its bending manifests the action of the drift induced by the magnetic field leading to a nonzero rescattering parameter $z_r > 0$ at the recollision point (3). Due to the positive rescattering parameter z_r, the electron obtains a negative momentum kick at the recollision leading to the final negative momentum p_z at the detector.

to R-CMT at the recollision. Already this intuitive picture explains the origin behind the negative offset and reveals an intriguing interplay between the Coulomb focussing and magnetic drift. We have to be careful as we have only presented a rough scheme so far and we cannot be certain that the R-CMT will be sufficient to counteract the magnetic drift measured. The final momentum p_{zd} can be obtained from the zero order trajectory $p_{z0}(u \to \infty)$ from Eq. (2.18) corrected by the Coulomb momentum transfer at rescattering δp_z yielding

$$p_{zf} \equiv \frac{\mathbf{A}^2(u_i)}{2c} - \delta p_z, \tag{4.1}$$

where we substituted $\mathbf{A}(u) \to f(u)\mathbf{A}(u)$ and obtained the asymptotic drift momentum at the detector as a limit $\lim_{u \to \infty} p_{zd}(u, u_i) = \frac{f^2(u_i)\mathbf{A}^2(u_i)}{2c} \approx \frac{\mathbf{A}^2(u_i)}{2c}$ while omitting the negligible role of envelope for the central half-cycle of our pulse.

Let us also note at this point that the size of the nondipole effects matters as they could potentially drive the tunneled electron wave packet far away and no rescattering would happen in the first place. Fortunately, this situation is described with the Lorentz

deflection parameter from Eq. (2.3), which is sufficiently small for our present parameters and we do not have to worry about the tunneled wave packet missing the ion.

Let us, for the sake of clarity, neglect the envelope $f(u)$ for the following analytical derivations as its role is rather insignificant for the three central half-cycles of the laser field, which will be our main interest. The three-step-model described in Fig. 4.3 and used thorough this section can be summarize as follows:

1. **Ionization**
   Let us assume that the electron appears at the tunnel exit at ionization phase u_i with:

   $$
   \begin{aligned}
   x_i = -\frac{I_p}{E_0 \cos u_i} &< 0, \\
   y_i = z_i &= 0, \\
   p_{yi} &> 0, \\
   p_{zi} &= 0.
   \end{aligned}
   \tag{4.2}
   $$

2. **Propagation**
   Then, the electron propagates in the continuum driven only by the laser field. We assume that the electrons receives I-CMT δp_{xi} and δp_{yi} at the beginning of the propagation and we can write its position at the end of propagation t_r (or equivalently by u_r) as

   $$
   \begin{aligned}
   x_r &= \frac{E_0}{\omega^2}\left[\cos u_r - \cos u_i + (u_r - u_i)\sin u_i\right] + \delta p_{xi}(u_r - u_i) + x_i = 0, \\
   y_r &= (p_{yi} + \delta p_{yi})(t_r - t_i) > 0, \\
   z_r &= \frac{1}{2c}\int_{t_i}^{t_r} [\mathbf{A}(t) - \mathbf{A}(t_i)]^2\, dt > 0,
   \end{aligned}
   \tag{4.3}
   $$

   where the first equation uniquely defines the first rescattering point for any ionization phase u_i. The nondipole effects are included in the last equation.

3. **Rescattering**
   The electron obtains Coulomb momentum transfers at the rescattering in the transversal plane:

   $$
   \begin{aligned}
   \delta p_y &\approx -\frac{2}{|y_r p_{xr}|} < 0, \\
   \delta p_z &\approx -\frac{2z_r}{y_r^2 |p_{xr}|} < 0,
   \end{aligned}
   \tag{4.4}
   $$

   where we have taken the formulas for FR from Eqs. (2.59)-(2.60) under the assumption of $z_r \ll y_r$ and $p_{yi} \ll p_{xr}$.

Up to this point, we have described a large class of tunneled electrons with initial $p_{zi} = 0$ and have to be more specific, if we want to identify the cusp electrons. Further

restriction can be made by a simple condition assuming that the transversal momentum $p_{yi} + \delta p_{yi}$ at the recollision point cancels due to the negative R-CMT δp_y. The condition can be written as

$$\delta p_y = -(p_{yi} + \delta p_{yi}). \tag{4.5}$$

The cancelation of p_y momenta for the cusp electrons follows from the discussion of the Coulomb focusing and clearly identifies the electron with initial transverse momentum corresponding to the intersection of the circle with the positive part of the p_{yi}-axis.

At this point we can employ the formulas for I-CMT from Eq. (2.87) and derive the value of the p_{yi} from the condition on cancellation as

$$p_{yi} = \frac{\sqrt{2}}{\sqrt{|p_{xr}|(t_r - t_i)} \left[1 - \left(2x_i^2 E_0 \cos u_i\right)^{-1}\right]}. \tag{4.6}$$

Once we have found the trajectory of this one particular cusp electron, we can derive the value for the R-CMT δp_z from Eqs. (4.4) and determine the final p_{zf} momentum of this cusp electron from Eq. (4.1) as

$$p_{zf} = \frac{\mathbf{A}^2(u_i)}{2c} - \frac{1}{2c(t_r - t_i)} \int_{t_i}^{t_r} \left[\mathbf{A}(t) - \mathbf{A}(t_i)\right]^2. \tag{4.7}$$

The final formula is astonishing for two reasons. Firstly, it reveals an intriguing interplay between the magnetically induced momentum drift represented by the first positive term and the R-CMT received at the rescattering represented by the second positive term. Secondly, it is independent of the initial transversal momentum p_{yi} showing that the final momenta p_{zf} will be the same for all electrons starting on the ring of Fig. 4.2. We calculated the values of p_{zf} for several different ionization phases (and hence final longitudinal momenta) and marked the results in the right panel of Fig. 4.1 by red crosses. As we can see, the agreement with the simulation is excellent, especially in the region I, where only single rescattering happens. This is also the region where the transition from positive to negative shift happens meaning that the R-CMT exactly compensates the drift induced by the magnetic field and our formula captures this momentum well.

The discrepancy grows with the number of recollisions suggesting that we have take them into account as well. We are going to address the role of high-order recollisions in the next section.

4.2 The role of high-order rescatterings

As we have seen in the previous section, the effect of the high-order recollision cannot be omitted and is most likely the cause behind the discrepancy between our estimates from Eq. (4.7) and the simulation at intermediate and vanishing values of the longitudinal momenta presented in Fig. 4.1.

Before we generalize the derivation of the previous section to also take into account the high-order rescatterings, we point out that the overall picture of Coulomb focusing of the cusp electrons to a single point on the bend ridge also holds for multiple recollisions

(or equivalently along the whole bend cusp). In fact, the initial phase space in Fig. 4.2 corresponds to the gray line separating the regions I and III in Fig. 4.1 and hence to the class of trajectories with two rescatterings: the first being FR and the second being SR. Therefore, we can assume that the cusp electron will always originate on a circle in the initial phase momentum space. The radius of the circle or the offset of its center may vary with respect to the longitudinal momenta p_x, but the cusp electrons will always tend to originate on a circle. In case of doubts, we kindly ask the reader to wait until the next chapter, where we will present more data showing the rings in the case of linear polarization for three distinct values of the longitudinal momenta.

Thus, let us start and follow one more time the electron starting at the tunnel exit with $p_{zi} \approx 0$ and $p_{yi} \neq 0$, and ending at the cusp. According to Eq. (2.14), the final z-component of the photoelectron momentum reads:

$$p_{zf} \approx p_{1z} + \frac{A^2(u_i)}{2c} - \frac{p_{xi} A(u_i)}{c}, \tag{4.8}$$

where p_{1z} is the total R-CMT for the considered electron, which was ionized at the laser phase u_i. The laser pulse was polarized in the x-direction and propagated along the z-axis, and is polarized. While the magnetic field modifies the electron dynamics only along the z-axis in this setup, the electron dynamics in y-direction stays similar to the dipole case and we can again assume that the final y-component of the electron momentum is vanishing and rewrite the condition from Eq. (4.5) as

$$p_{yf} = p_{yi} + p_{2y,\text{in}} + p_{1y} \approx 0, \tag{4.9}$$

where p_{yi}, $p_{2y,\text{in}}$ and p_{1y} are the y-components of the electron initial momentum, of I-RMT, and of the total R-CMT, respectively. Under the assumption that the electron rescatters N times, Eq. (4.9) reads

$$p_{yi} + p_{2y,\text{in}} + \sum_{n=1}^{N} p_{1y}^{(n)} \approx 0, \tag{4.10}$$

where $p_{1y}^{(n)}$ is the R-CMT at the nth recollision. Further, we will make use of the simpleman's approach to the R-CMT (as discussed in Subsec. 2.3.3) and estimate the R-CMT as products of the acting forces during the recollisions and the durations of the recollisions τ_n:

$$p_{1y}^{(n)} \approx -Z \frac{y_n}{r_n^3} \tau_n. \tag{4.11}$$

Later we can apply the derived analytical formulas Eqs. (2.43)-(2.44), (2.56)-(2.57) and (2.62)-(2.63) to estimate the recollision duration τ_n precisely.

How the final momentum p_{1z} changes due to the Coulomb interaction can be estimated as the sum of R-CMTs reading:

$$p_{1z} = \sum_{n=1}^{N} p_{1z}^{(n)} = -Z \sum_{n=1}^{N} \frac{z_n}{r_n^3} \tau_n. \tag{4.12}$$
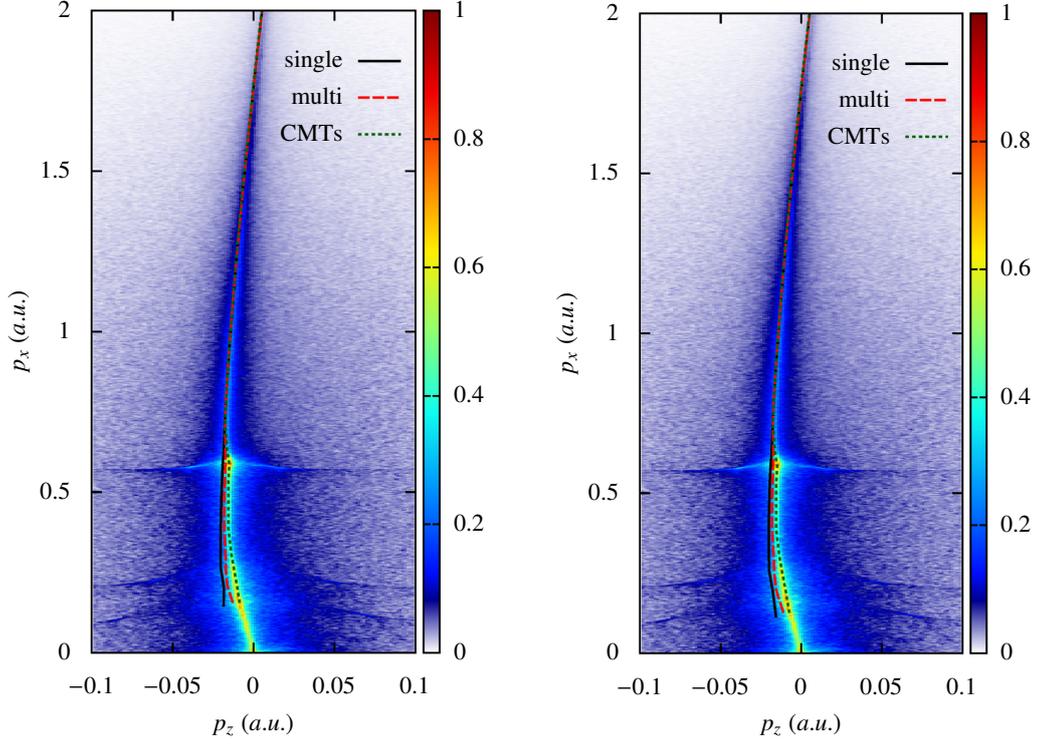
Figure 4.4: The breakdown of the dipole approximation in PMD: CTMC simulation for an atom of Hydrogen in an intense linearly polarized laser pulse with $E_0 = 0.0407$, $\omega = 0.012$ and the laser pulse duration $15.7/\omega$. The peak of the cusp was determined from the first term of Eq. (4.23), $p_{zf} = -\overline{T}_{zd}^{(1)}$ (black, solid), further via the full Eq. (4.23) (red, dashed), and finally calculated as a sum of the I-CMT and the all R-CMTs at every single recollision by the analytical formulas from Sec. 2.3 (green, dotted). In the left panel, we present the results obtained at the end of the laser pulse and, additionally, we take the Coulomb field effect after switching off the laser pulse into account in the right panel. The difference is mostly visible at small longitudinal momenta.

As the recollision time τ_n and the recollision distance r_n figure in both Eqs. (4.10) and (4.12), we may use the first to simplify the relation for p_{1z}. For the latter, we need to find the impact parameters y_n and z_n. We can determine them stepwise from one recollision to the next as

$$
\begin{aligned}
y_1 &= (p_{yi} + p_{2y,\text{in}})(t_1 - t_0), \\
y_2 &= (p_{yi} + p_{2y,\text{in}})(t_2 - t_0) - Z\frac{y_1}{r_1^3}\tau_n(t_2 - t_1), \\
&\vdots \\
y_N &= (p_{yi} + p_{2y,\text{in}})(t_N - t_0) - Z\sum_{n=1}^{N-1}\frac{y_n}{r_n^3}\tau_n(t_N - t_n),
\end{aligned}
\tag{4.13}
$$

where t_0 is the ionization time, and t_n is the recollision time of the nth for $n \geq 1$. The above relations can be inserted into Eq. (4.10) yielding

$$
\begin{aligned}
p_{yi} + p_{2y,\text{in}} &= Z \sum_{n=1}^{N} \frac{\tau_n}{r_n^3} \left(p_{yi} + p_{2y,\text{in}} \right) \left(t_n - t_0 \right) \\
&\quad - Z^2 \sum_{n=1}^{N} \frac{\tau_n}{r_n^3} \sum_{k=1}^{n-1} \frac{y_k}{r_k^3} \tau_k \left(t_n - t_k \right),
\end{aligned} \tag{4.14}
$$

where the first sum and the second iterative sum on the right-hand-side of the equation correspond to the first order corrections and to the next-order corrections to the zero-order trajectory, respectively. When neglecting higher than second-order correction terms, which are proportional to $\sim \left(\tau_n / r_n^3 \right)^2$, after a rearrangement, we obtain:

$$
Z \sum_{n=1}^{N} \frac{\tau_n}{r_n^3} \left(t_n - t_0 \right) \approx 1 + Z^2 \sum_{k<n}^{N} \frac{\tau_n \tau_k}{r_n^3 r_k^3} \left(t_n - t_k \right) \left(t_k - t_0 \right). \tag{4.15}
$$

The impact parameter z_r along the laser propagation direction depends on the magnetically induced drift momentum of the photoelectron of $p_{zi} = 0$:

$$
\begin{aligned}
z_1 &= \bar{p}_{zd}^{(1)} \left(t_1 - t_0 \right), \\
z_2 &= \bar{p}_{zd}^{(2)} \left(t_2 - t_0 \right) - Z \frac{z_1}{r_1^3} \tau_n \left(t_2 - t_1 \right), \\
&\vdots \\
z_N &= \bar{p}_{zd}^{(N)} \left(t_N - t_0 \right) - Z \sum_{n=1}^{N-1} \frac{z_n}{r_n^3} \tau_n \left(t_N - t_n \right),
\end{aligned} \tag{4.16}
$$

where we used the magnetic drift from Eq. (2.14) to define the averaged drift momentum as

$$
\bar{p}_{zd}^{(n)} \equiv \frac{1}{t_n - t_0} \int_{t_0}^{t_n} \left\{ \frac{p_{xi}}{c} \left[A_x(t) - A_x(t_0) \right] + \frac{1}{2c} \left[A_x(t) - A_x(t_0) \right]^2 \right\} \mathrm{d}t. \tag{4.17}
$$

Although the initial momentum is zero (i.e., $p_{xi} = 0$) in the tunneling regime, we embody the I-CMT of Eq. (2.94) into p_{xi} and set $p_{xi} = p_{2\parallel,\text{in}}(u_i, p_{yi})$. When we substitute Eq. (4.16) into Eq. (4.12), we obtain

$$
\begin{aligned}
p_{1z} &= -Z \sum_{n=1}^{N} \bar{p}_{zd}^{(n)} \frac{\tau_n}{r_n^3} \left(t_n - t_0 \right) \\
&\quad + Z^2 \sum_{n=1}^{N} \frac{\tau_n}{r_n^3} \sum_{k=1}^{n-1} \frac{z_k}{r_k^3} \tau_k \left(t_n - t_k \right),
\end{aligned} \tag{4.18}
$$

where the first sum corresponds again to the first-order correction for the unperturbed trajectory and the second iterative sum to the next-order corrections. When neglecting

the higher than the second-order corrections ($\sim \left(Z\tau_n/r_n^3\right)^2$) and employing the relationship of Eq. (4.15), we arrive at

$$p_{1z} \approx -\overline{p}_{zd}^{(1)} + Z \sum_{n=1}^{N} \left(\overline{p}_{zd}^{(1)} - \overline{p}_{zd}^{(n)}\right) \frac{\tau_n \left(t_n - t_0\right)}{r_n^3}.$$

(4.19)

The first term in the equation describes R-CMT at the first recollision and the sum emerges only due to multiple recollisions.

The presented cumbersome derivation becomes transparent in the case of a single recollision:

$$p_{1z} = -Z\frac{z_1}{r_1^3}\tau_1 = -\frac{z_1}{y_1}p_{1y} = -\frac{z_1}{t_1 - t_0} = -\overline{p}_{zd}^{(1)},$$

(4.20)

saying that the z-component of R-CMT is equal to the averaged drift momentum in the laser propagation direction evaluated between the ionization and recollision time.

Another intuitive perspective to Eq. (4.20) for the single recollision case arises during investigation of the nondipole cusp electron's dynamics. Let us assume that the cusp electron has an initial momentum only along the propagation direction of the laser (i.e., $\mathbf{p}_i = (0, 0, p_{iz})$), and compare it to the dipole case. The electron's dynamics can be considered similar in the nondipole and in the dipole case, when the recollision coordinates are the same $z_r = z_r^{(0)}$, where the upper index $^{(0)}$ indicates the dipole case. The impact parameter in the nondipole case is $z_r = (p_{zi} + \overline{p}_{zd})(t_1 - t_0)$ and in the dipole case simply $z_r^{(0)} = p_{zi}^{(0)}(t_1 - t_0)$. Thus, we can consider the electron's dynamics similar in both cases when $p_{zi} = p_{zi}^{(0)} - \overline{p}_{zd}$, i.e., whether the electron in the nondipole case possesses additional initial momentum opposite to the magnetically induced drift. In particular, the similar dynamics yields also the similar R-CMT: $p_{1z} \approx p_{1z}^{(0)}$. Because the cusp is located in the nondipole case at the vanishing momentum, i.e., $p_{zi}^{(0)} + p_{1z}^{(0)} \approx 0$, we derived the relation $p_{1z} = -p_{zi} - \overline{p}_{zd}$, which corresponds to Eq. (4.20) with $p_{zi} \approx 0$. The procedure connects the averaged drift momentum before the first rescattering directly to the asymptotic momentum of the cusp electrons. Now, we can derive the asymptotic momentum from Eq. (4.8) as

$$p_{zf} = p_{zi} + p_{1z} + \frac{A^2(u_i)}{2c} \approx -\overline{p}_{zd} + \frac{A^2(u_i)}{2c}.$$

(4.21)

In the last relation, we reproduced the results from Eq. (4.7) together with the intriguing interplay between the R-CMT and the magnetically induced drift leading to negative and positive shifts, respectively.

In general, we derive the asymptotic momentum from Eq. (4.19) in the case of multiple recollisions as

$$p_{zf} \approx \frac{A^2(u_i)}{2c} - \frac{p_{xi}A(u_i)}{c} - \overline{p}_{zd}^{(1)} + Z \sum_{n=1}^{N} \left(\overline{p}_{zd}^{(1)} - \overline{p}_{zd}^{(n)}\right) \frac{\tau_n \left(t_n - t_0\right)}{r_n^3},$$

(4.22)

where summation takes place over all N-recollisions. We can simplify the equation, when we combine the first three terms yielding

$$p_{zf} \approx -\overline{T}_{zd}^{(1)} + Z \sum_{n=1}^{N} \left(\overline{p}_{zd}^{(1)} - \overline{p}_{zd}^{(n)}\right) \frac{\tau_n \left(t_n - t_0\right)}{r_n^3},$$

(4.23)
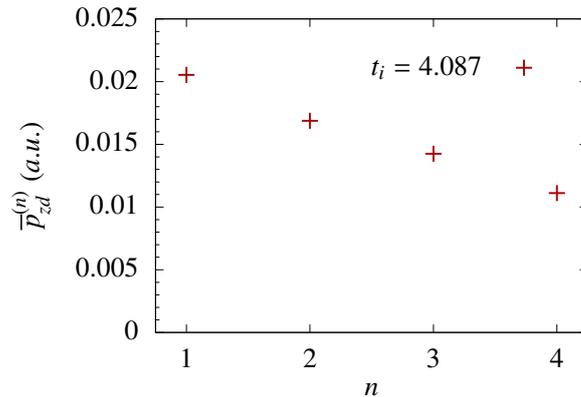
Figure 4.5: The averaged magnetically induced drift momentum $\overline{p}_{zd}^{(n)}$ obtained between the ionization time $t_i = 4.087$ a.u. and the nth rescattering time for the ionization time. The electron has final longitudinal momentum $p_x \approx 0.3$ a.u. and experiences four rescatterings.

where

$$\overline{T}_{zd}^{(1)} \equiv \frac{1}{u_1 - u_0} \int_{u_0}^{u_1} \left[\frac{p_{xf} A(u)}{c} + \frac{A^2(u)}{2c} \right] \mathrm{d}u, \tag{4.24}$$

with $u_0 = u_i$ and with the asymptotic longitudinal momentum $p_{xf} \equiv -A(u_i) + p_{xi}$. We point out the unobvious coincidence of the term $-\overline{T}_{zd}^{(1)}$ with the single rescattering of case of Eq. (4.21).

We compare our results with the CTMC simulations in Fig. 4.4. Let us note that throughout this section we have determined all rescattering parameters from the numerically found trajectories.

The main contribution to the negative shift of the cusp is given by the first term in Eq. (4.23), $-\overline{T}_{zd}^{(1)}$, which originates from the first recollision and coincides with the result of Ref. [116]. This term also captures well the peak of the cusp for large longitudinal momenta ($p_x \gtrsim 0.52$), leading only to a single recollision of the tunneled electron. However, at intermediate momenta a noticeable disagreement shows and even grows for vanishing momenta where the negative shift of the cusp decreases and tends to zero. The horizontal fringes correspond to the soft recollision condition and separate regions with respect to number of rescatterings. While crossing the horizontal line towards lower energies, the number of recollisions increases by one.

When the electron undergoes more than one rescattering, which is the case for $p_x \lesssim 0.52$ in Fig. 4.4, the nondipole dynamics cannot be considered similar to the dipole case any longer. In fact, it is not possible to adjust the single parameter (i.e., the initial transverse momentum) and ensure that all the recollision parameters of the electron's multiple revisit will correspond to the parameters in the dipole case. The influence of the multiple recollisions is described by the second term in Eq. (4.23) expressed as a sum. We carried out the averaged magnetically induced drift momentum at all four recollisions of a particular trajectory in Fig. 4.5. As we can see, the averaged drift momentum is decreasing with the order of the recollision n meaning that the elements in the sum are
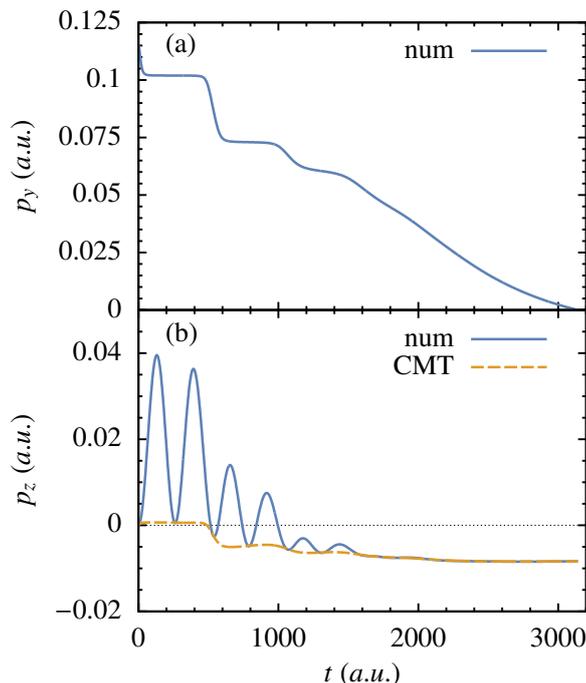
Figure 4.6: The evolution of the electron's momentum compensated by the vector-potential, i.e., $\mathbf{p}(t) + \mathbf{A}(t)$, which shows the history of the Coulomb momentum transfer. The example shows the electron originating at $t_i = -1.25$ with $p_{yi} = 0.116$ and $p_{zi} = 0$ and ending at the PMD cusp. Panel (a) shows that the p_y momentum changes significantly even at the end of the laser pulse ($t \approx 2200$). Panel (b) shows negative total Coulomb momentum transfer on the p_z momentum at the end of the laser pulse. We also isolated the contribution of the time-dependent Coulomb momentum transfer and plotted it by yellow dashed line.

positive or zero. Thus, the sum yields the decrease of the negative shift of the cusp in the intermediate and low energy part of the PMD.

Whereas the positive offset of the bend cusp at large longitudinal energies can be connected to the magnetically induced drift $p_{zd} = A^2(u_i)/2c$, the negative offset can be explained as the interplay between the Coulomb momentum transfer p_{1z} and magnetically induced drift $p_{zd}(u, u_i)$. The electron moves in the positive z-coordinate direction because of the magnetically induced drift, acquires positive impact parameter z_r and hence negative Coulomb momentum transfer against the propagation direction of the laser at the rescattering. For decreasing longitudinal momenta, the recollision phase grows, which leads to increase of the acquired impact parameter z_r and therefore of the R-CMT in the opposite direction. Thus, the bend cusp undergoes a transition from positive to negative shifts.

Such simple picture is true for relatively large longitudinal momenta leading to single recollision. Nevertheless, the simulations manifest a bend of the cusp towards the zero momentum at lower longitudinal momenta again, which we assigned to increasing number of recollisions. In the case of multiple recollisions, the averaged effective drift decreases with the recollision's order n as $\bar{p}_{zd}^{(n)} < \bar{p}_{zd}^{(1)}$, which yields a consequent decrease of the

total R-CMT in z-direction.

Another reason can be given for the PMD cusp to shift towards vanishing momentum at very low energies. Namely, the low energetic electrons are more likely to be still close to the atomic core at the end of the laser pulse. At this point and later on, the focusing properties of the Coulomb field dominate and the close electrons will be dragged towards the atomic core, which decreases their momentum even further, see an example in Fig. 4.6. Fig. 4.6(a) shows the p_y momentum changing significantly even at the tail of the laser pulse. In such situation, the recollision picture breaks down and the condition given in Eq. (4.10) cannot be applied any longer. Part (b) shows nontrivial behavior of the negative CMT on the p_z momentum at the end of the laser pulse. Our analytical perturbative framework is not suitable for description of the electron's dynamics at the end of the laser pulse as the decreasing intensity leads to breakdown of the recollision picture. Because of the recollision picture breakdown, we cannot apply our analytical model at the end of the laser pulse. At least, we can take into account the additional role of the Coulomb potential for the photoelectron's momentum when the laser pulse is gone. This we do in Fig. 4.4, where we determined the position of all the electrons from asymptotic Kepler formula. The asymptotic Kepler formula will be introduced in greater detail in Sec. 6.4 of the last chapter and for now, we just have to know only that it uses the position and the momentum of a photoelectron placed in the conservative Coulomb potential to compute the electron's asymptotic momentum at infinity (which we would measure with a detector). These parameters can be obtained from the numerical trajectories and the momenta via the Eqs. (4.21), (4.23). From the figure we can see that only the low-energetic photoelectrons near the low longitudinal momenta are appreciably effected by the Coulomb field resulting in better agreement with the simulation in this low energy region.

4.3 Summary

In this chapter, we have addressed the recently observed nondipole effect of energy-dependent bend central cusp with the famous three-step-model within our classical analytical framework derived in Chap. 2. We explained the seemingly counterintuitive transition of the bend to the negative transversal momentum p_z as the result of an interplay between the momentum drift induced by the magnetic component of the laser field and the Coulomb focusing represented by the Coulomb momentum transfer at the first recollision in Sec. 4.1 while deriving analytical expression leading to the excellent agreement with the CTMC simulation for large and intermediate values of longitudinal momenta with only one rescattering.

Further, the discrepancy for the small values of longitudinal momenta between our model and the simulation was explained as the influence of the high-order rescattering events in Sec. 4.2, where we achieved improvement of our estimations once we had taken the high-order recollisions into account.

Eventually, the discrepancy for vanishing longitudinal momentum, where the bend cusp tends towards the zero transversal momentum, was contributed to the breakdown of the recollision picture and to further non-negligible Coulomb interaction after disappearance

of the laser pulse.

Chapter 5

Nondipole effects in elliptical polarization

So far, we have analyzed the modification of the Coulomb focusing due to the nondipole effects in linearly polarized laser fields. The modifications were traced back to the drift momentum induced by the magnetic field of the laser which alters the initial conditions of the cusp electrons manifesting as the shift of the Coulomb focused rings in initial phase space as discussed in the previous chapter. This shift assures compensation for the magnetically induced drift momentum leading to the same or similar R-CMT as in the dipole case. A similar situation can be induced by the introduction of ellipticity to the ionizing laser field, where additional drift momentum arises due to the laser driven evolution also in the one, so far, symmetrical transversal direction. Therefore, we can effectively stage a situation with two perpendicular momentum drifts of the tunneled electrons in the transversal plane (with respect to the major axis of polarization) and see how they modify the Coulomb focusing.

We would like to point out at this point that the results of this chapter were obtained in an extensive and fruitful collaboration with Dr. Jochen Maurer and his student Benjamin Willenberg from the experimental group of professor Ursula Keller at the ETH Zürich leading to several publications [142, 194] on which this chapter is based.

Before we start with analytical search for trajectories of tunneled electrons in elliptical polarized laser field beyond the dipole limit in Sec. 5.1, let us show the results of the experiment that has motivated our research. In the measurements, our collaborators measured how the photoelectron momentum spectrum (PMD) of gaseous Xe changes under variation of the ellipticity of the ionizing laser pulse while keeping the overall intensity of the pulse constant. The results can be found in Fig. 5.1 (taken from [194]) for laser pulse of peak intensity $6 \cdot 10^{13}$ W/cm^2, 50 fs duration, central wave-length 3400 nm, major axis of polarization along x-axis and propagation direction along z-axis. The results manifest two prominent features: two main lobes and a thin central spot along the major axis of polarization at low ellipticities. The central cusp fades and vanishes once the two lobes get spatially separated at $\epsilon \approx 0.11 \ldots 0.15$. The structure was related to rescattered electrons (called type B electrons) and it is present along with the two lobes of direct electrons (called type A electrons). This is true also in the dipole limits as we will show in Sec. 5.2.

The nondipole effects were also observed in this experiment and measured as the peak offset of measured p_z, which was obtained from the projections of the full 3D PMDs onto single dimension, namely, the p_z axis. The case of zero ellipticity corresponds to the case of the previous chapter and the negative sign of the offset is therefore no
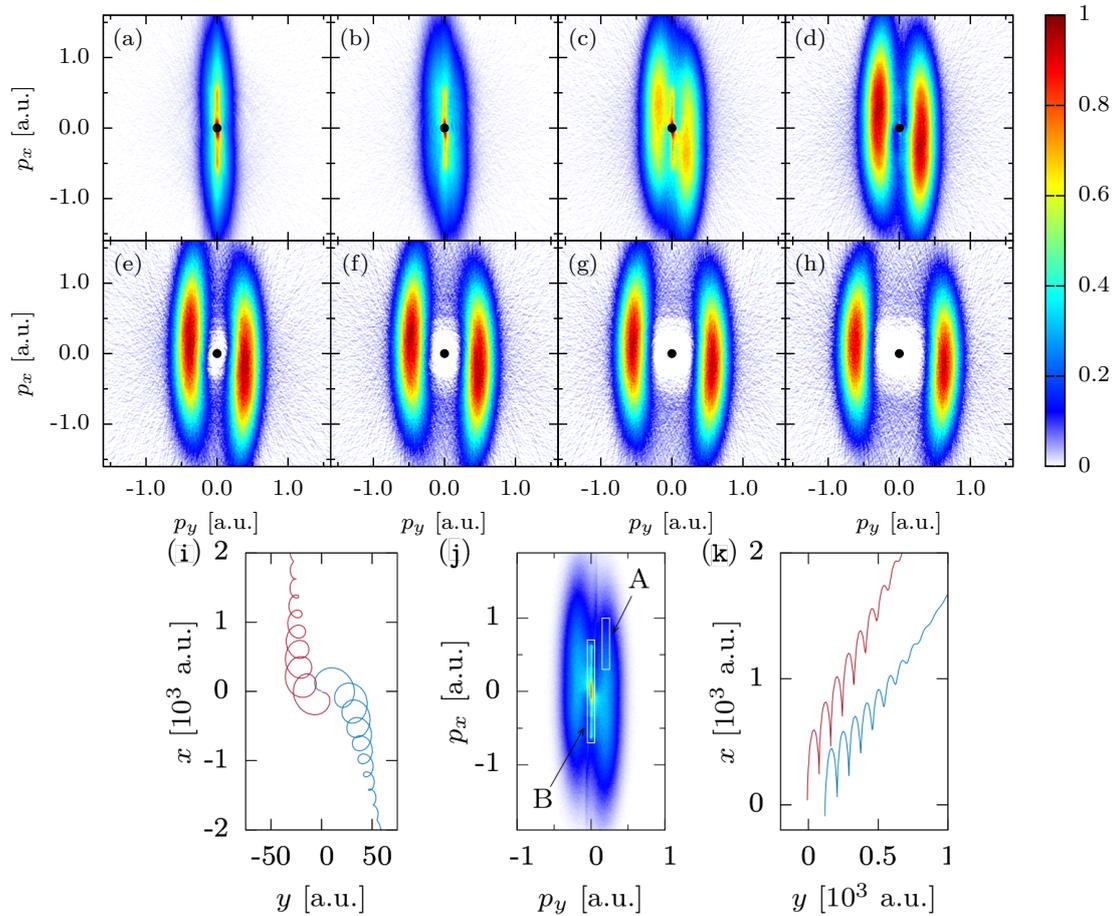
Figure 5.1: We show the PMDs in the polarization plane observed at laser field peak intensity of $6 \cdot 10^{13}$ W/cm^2 for the ellipticities 0.0, 0.03, 0.07, 0.11, 0.15, 0.19, 0.23, 0.26, in (a) to (h), respectively. The central spot was cut out for illustration purposes as it stems for Rydberg states. More accurately, the PMDs are projections of the cuts limited by the range $|p_z| < 0.06$ a.u. onto the laser polarization plane. A sharp line structure emerges in the PMDs at ellipticities of $\epsilon = 0.07$ and $\epsilon = 0.11$ and disappears at larger ellipticities $\epsilon \geq 0.15$. The central panel (j) in the bottom shows how we separate the PMD into the two lobes of type A electrons and into the central structure of type B electrons at $\epsilon = 0.07$. CTMC simulations have revealed that the typical trajectory of type B electrons manifest at least one rescattering (exemplary trajectories shown in panel (i)) whereas type A electron are direct and hence without any recollisions as expected (exemplary trajectories shown in panel (k)). (This figure shows experimental and simulation results obtained by our collaborators and was published in our paper [194].)

longer surprising. On the other hand, the experiment has shown that the peak offset is not constant and depends on the ellipticity. Even to such an extent that it exhibits a transition from negative to positive values with increasing ellipticity as shown in Fig. 5.2 (taken from [194]). We will address the nondipole effects in the Sec. 5.3, where we will also show how our deeper understanding of the two drifts can help us to get a better insight into the dynamics of the tunneled wave packet in the continuum and offer new
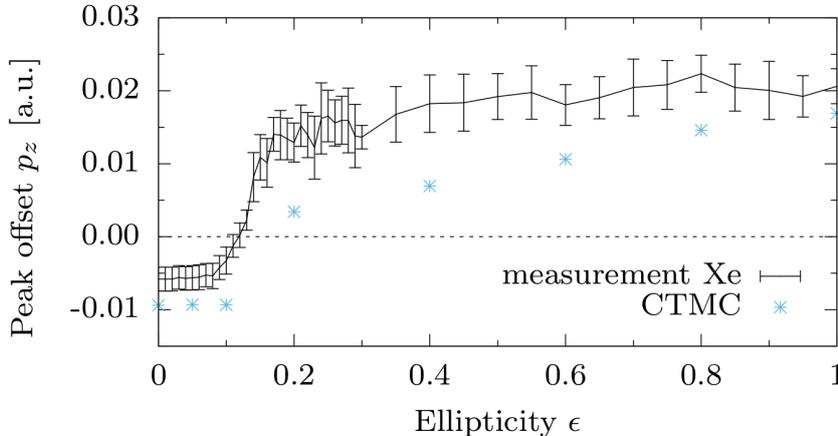
Figure 5.2: We carried out the p_z-position of the peak of the complete projection of the measured PMDs onto the beam propagation axis (p_z) as a function of ellipticity for constant intensity. A transition from negative to positive values of p_z with a zero crossing at $\epsilon \approx 0.12$ can be observed. The results obtained by CTMC simulations with varying CEP phase and ionization along whole laser pulse are carried out by blue points. The results reproduce the transition and are in overall agreement with the experimental data. We attribute the discrepancy to the focal averaging, which was omitted in the simulation. (This figure shows experimental and simulation results obtained by our collaborators and was published in our paper [194].)

possibilities for its experimental investigations.

5.1 Tunneled electrons in elliptically polarized laser fields

In this section, we are going to generalize our analytical model from Sec. 2 for elliptically polarized lasers. Then, the trajectory of a recolliding electron can be found as the solution of the classical equations of motion in an elliptically polarized laser field, while treating the Coulomb field effect as a perturbation which affects the electron trajectory near the tunnel exit and at recollisions. Nevertheless, we will assume thorough this chapter that the ellipticity does not disturb the recollisions severly our analytical formulas from Secs. 2.3 and 2.5 can still be applied. This may not be true for large values of ellipticity close to 1, but it is well justified for small values of ellipticity which will be of our main concern here.

The electric field of the laser field is

$$\begin{aligned} E_x &= E_0 \cos \eta \\ E_y &= \epsilon E_0 \sin \eta, \end{aligned} \tag{5.1}$$

with the phase of the laser field $\eta = \omega(t - z/c)$, the ellipticity $0 \leq \epsilon \leq 1$, the laser field amplitude E_0, the frequency ω, and the speed of light c. The envelope of the pulse is neglected. Atomic units are used throughout.

For the electron dynamics in the plane laser field the canonical momentum in the polarization plane is conserved

$$
\begin{aligned}
p_x - A_x(\eta) &= \text{const} \\
p_y - A_y(\eta) &= \text{const},
\end{aligned}
\tag{5.2}
$$

with the electron kinetic momentum components $p_{x,y}$ in the polarization plane, and the laser vector-potential $\mathbf{A}(\eta) = (A_x(\eta), A_y(\eta), 0)$:

$$
\begin{aligned}
A_x(\eta) &= -\frac{E_0}{\omega} \sin \eta \\
A_y(\eta) &= \epsilon \frac{E_0}{\omega} \cos \eta.
\end{aligned}
\tag{5.3}
$$

The electron momentum in the laser polarization plane after the ionization is

$$
p_x = -\frac{E_0}{\omega}(\sin \eta - \sin \eta_i) + p_{xi}
\tag{5.4}
$$

$$
p_y = \epsilon \frac{E_0}{\omega}(\cos \eta - \cos \eta_i) + p_{yi}.
\tag{5.5}
$$

where η_i is the ionization phase, $\mathbf{p}_i = (p_{xi}, p_{yi}, p_{zi})$ are the components of the initial electron momentum.

After leaving the tunnel exit a momentum transfer arises due to the Coulomb force $\delta \mathbf{p}_i^C = (\delta p_{xi}^C, \delta p_{yi}^C, \delta p_{zi}^C)$. For a simplified analysis we include this into the initial conditions of the laser driven electron trajectories:

$$
\mathbf{p}_i = \mathbf{p}_e + \delta \mathbf{p}_i^C,
\tag{5.6}
$$

where $\mathbf{p}_e = (p_{ex}, p_{ey}, p_{ez})$ is the electron momentum at the tunnel exit. At the tunnel exit the electron momentum is transverse to the laser field polarization direction: $\mathbf{p}_{\perp e} = \mathbf{p}_e - \mathbf{p}_{||e}$, with a vanishing component along the polarization $\mathbf{p}_{||e} = \hat{\mathbf{e}}(\mathbf{p}_e \cdot \hat{\mathbf{e}}) = 0$. Here, the laser polarization vector is

$$
\begin{aligned}
\hat{\mathbf{e}} &= (\cos \phi, \sin \phi, 0) \\
&= \left(\frac{\cos \eta_i}{\sqrt{\cos^2 \eta_i + \epsilon^2 \sin^2 \eta_i}}, \frac{\epsilon \sin \eta_i}{\sqrt{\cos^2 \eta_i + \epsilon^2 \sin^2 \eta_i}}, 0 \right),
\end{aligned}
\tag{5.7}
$$

with $\tan \phi = \epsilon \tan \eta_i$.

For the electron dynamics in a plane laser field there is a third integral of motion, besides the transverse canonical momentum of Eq. (5.2), due to the space-time translation symmetry:

$$
\Lambda \equiv \frac{\varepsilon - c p_z}{c^2} = \text{const},
\tag{5.8}
$$

with the electron energy $\varepsilon = c\sqrt{p_x^2 + p_y^2 + p_z^2 + c^2}$.

The electron momentum along the laser propagation direction can be found from Eq (5.8):

$$p_z = \frac{p_x^2 + p_y^2 + c^2(1 - \Lambda^2)}{2c\Lambda}. \tag{5.9}$$

As $c^2(1 - \Lambda^2)/(2c\Lambda) = p_{zi} - (p_{xi}^2 + p_{yi}^2)/(2c\Lambda)$, we have for the longitudinal momentum

$$p_z = p_{zi} + \frac{(p_x^2 + p_y^2) - (p_{xi}^2 + p_{yi}^2)}{2c\Lambda}. \tag{5.10}$$

As the ionized electron appears at the tunnel exit with a velocity much smaller than the speed of light, one has $\Lambda \approx 1 - p_{zi}/c \approx 1$, and in the order of $1/c$ the longitudinal momentum is

$$p_z \approx p_{zi} + \frac{1}{2c} \left[\mathbf{A}(\eta) - \mathbf{A}(\eta_i)\right]^2 + \frac{\mathbf{p}_i}{c} \cdot \left[\mathbf{A}(\eta) - \mathbf{A}(\eta_i)\right]. \tag{5.11}$$

From Eqs. (5.4),(5.5) and (5.11), the electron relativistic equations of motion in the laser field read:

$$\Lambda\omega\frac{dx}{d\eta} = -\frac{E_0}{\omega}\left(\sin\eta - \sin\eta_i\right) + p_{xi} \tag{5.12}$$

$$\Lambda\omega\frac{dy}{d\eta} = \epsilon\frac{E_0}{\omega}\left(\cos\eta - \cos\eta_i\right) + p_{yi}, \tag{5.13}$$

$$\Lambda\omega\frac{dz}{d\eta} = \frac{1}{2c}\left[\mathbf{A}(\eta) - \mathbf{A}(\eta_i)\right]^2 + \frac{\mathbf{p}_i}{c}\cdot\left[\mathbf{A}(\eta) - \mathbf{A}(\eta_i)\right] + p_{zi}. \tag{5.14}$$

which is derived using the relation $(\varepsilon/c^2)d\eta/dt = \omega\Lambda$. The solution of the latter is

$$x = \frac{E_0}{\omega^2}\left(\cos\eta - \cos\eta_i\right) + \left[p_{xi} + \frac{E_0}{\omega}\sin\eta_i\right]\frac{(\eta - \eta_i)}{\omega} + x_i, \tag{5.15}$$

$$y = \epsilon\frac{E_0}{\omega^2}\left(\sin\eta - \sin\eta_i\right) + \left[p_{yi} - \epsilon\frac{E_0}{\omega}\cos\eta_i\right]\frac{(\eta - \eta_i)}{\omega} + y_i, \tag{5.16}$$

$$z = \frac{1}{2c}\int_{\eta_i}^{\eta}\left[\mathbf{A}(\eta') - \mathbf{A}(\eta_i)\right]^2\frac{d\eta'}{\omega} + p_{zi}\frac{(\eta - \eta_i)}{\omega} + z_i$$
$$+ \frac{1}{c}\int_{\eta_i}^{\eta}\mathbf{p}_i\cdot\left[\mathbf{A}(\eta') - \mathbf{A}(\eta_i)\right]\frac{d\eta'}{\omega}, \tag{5.17}$$

where the initial coordinates at the ionization phase η_i correspond to the tunnel exit:

$$x_i \approx -\frac{I_p E_x(\eta_i)}{E^2(\eta_i)} = -\frac{I_p}{E_0}\frac{\cos\eta_i}{\cos^2\eta_i + \epsilon\sin^2\eta_i},$$
$$y_i \approx -\frac{I_p E_y(\eta_i)}{E^2(\eta_i)} = -\frac{I_p}{E_0}\frac{\epsilon\sin\eta_i}{\cos^2\eta_i + \epsilon\sin^2\eta_i}, \tag{5.18}$$
$$z_i \approx 0.$$

Recollisions in an elliptically polarized laser field

Recollisions can happen not only in a linearly polarized laser field but also in a laser field of elliptical polarization. At least for small ellipticities, we can still assume that the motion along the major axis of polarization is dominant and therefore determines the rescattering points in the same way as disscussed in the Chapter 2.

In this subsection we are going to derive the conditions under which the recollision dynamics (recollision parameters) for elliptical polarization are similar to those in the case of a linear polarization, which will play a crucial role in understanding the observed features.

Linear polarization within dipole approximation

Let us consider the electron contributing to the ridge structure in the case of linear polarization with the dipole approximation, when the final transverse momentum of the electron is vanishing

$$p_{yf}^{(0)} \approx p_{zf}^{(0)} \approx 0. \tag{5.19}$$

The electron contributing to the ridge structure with an initial momentum $\mathbf{p}_i = (p_{xi}^{(0)}, p_{yi}^{(0)}, p_{zi}^{(0)})$ has the following recollision coordinates

$$
\begin{aligned}
x_r^{(0)} &= 0 & (5.20) \\
y_r^{(0)} &= p_{yi}^{(0)} \frac{\eta_r - \eta_i}{\omega}, & (5.21) \\
z_r^{(0)} &= p_{zi}^{(0)} \frac{\eta_r - \eta_i}{\omega}, & (5.22)
\end{aligned}
$$

where η_r is the recollision phase, and Eq. (5.20) defines the recollision. The momentum transfer upon recollision due to the Coulomb field is $\delta\mathbf{p}_r^{C(0)}$, and the final transverse momentum of the electron is vanishing in the case of linear polarization when it ends up at the ridge:

$$
\begin{aligned}
p_{yf}^{(0)} &= p_{yi}^{(0)} + \delta p_{yr}^{C(0)} = 0, \\
p_{zf}^{(0)} &= p_{zi}^{(0)} + \delta p_{yr}^{C(0)} = 0. & (5.23)
\end{aligned}
$$

Consequently, the initial momentum components transverse to the laser polarization are determined by the Coulomb momentum transfer at recollision:

$$
\begin{aligned}
p_{yi}^{(0)} &= -\delta p_{yr}^{C(0)}, \\
p_{zi}^{(0)} &= -\delta p_{zr}^{C(0)}. & (5.24)
\end{aligned}
$$

Elliptical polarization with dipole treatment

When ellipticity is introduced, the motion of the tunneled electron changes mainly along the minor axis of polarization as given by Eq. (5.16). The recollision point in the (y, z)-

transversal plane lies at

$$y_r^{(\epsilon)} = \epsilon \frac{E_0}{\omega^2} (\sin \eta_r - \sin \eta_i) + \left(p_{yi}^{(\epsilon)} - \epsilon \frac{E_0}{\omega} \cos \eta_i \right) \frac{(\eta_r - \eta_i)}{\omega} + y_i, \qquad (5.25)$$

$$z_r^{(\epsilon)} = p_{zi}^{(\epsilon)} \frac{\eta_r - \eta_i}{\omega}, \qquad (5.26)$$

with initial transversal momenta $p_{yi}^{(\epsilon)}$ and $p_{zi}^{(\epsilon)}$ and the superscript (ϵ) indicating the case of elliptical polarization.

Let us investigate, when the Coulomb momentum transfer will be similar to the linear case (i.e., $\delta p_{yr}^{C(\epsilon)} = \delta p_{yr}^{C(0)}$ and $\delta p_{zr}^{C(\epsilon)} = \delta p_{zr}^{C(0)}$). This can be easy to find out, when we assume only one dominant rescattering. The Coulomb momentum will be the same as the linear case when the recollision coordinates will be the same in both cases:

$$y_r^{(\epsilon)} = y_r^{(0)}, \qquad (5.27)$$

$$z_r^{(\epsilon)} = z_r^{(0)}. \qquad (5.28)$$

The second equation is trivially fulfilled when $p_{zi}^{(\epsilon)} = p_{zi}^{(0)}$. However, the first equation is non-trivial and leads to expression:

$$\begin{aligned} p_{zi}^{(\epsilon)} &= p_{zi}^{(0)} + \epsilon \frac{E_0}{\omega} \cos \eta_i - \epsilon \frac{E_0}{\omega} \left(\frac{\sin \eta_r - \sin \eta_i}{\eta_r - \eta_i} \right) - \frac{y_i \omega}{\eta_r - \eta_i}, \\ &\approx p_{zi}^{(0)} + \epsilon \frac{E_0}{\omega} \cos \eta_i \end{aligned} \qquad (5.29)$$

where we assumed that the last term is small due to the long wavelength and small ellipticity. The next to the last term has decreasing contribution with increasing η_r and is suppressed for dominant rescatterings of higher-order. The result of Eq. (5.29) shows that the Coulomb momentum transfer will be similar to the linear case, when the electron starts with positive offset in the $p_{zi}^{(\epsilon)}$ momentum which is compensating for the elliptical drift.

Elliptical polarization with nondipole treatment

According to Eq. (5.16), the electron transverse coordinates (with respect to the major axis of the polarization ellipse) at the recollision in the case of elliptical polarization are

$$y_r^{(\epsilon)} = \epsilon \frac{E_0}{\omega^2} (\sin \eta_r - \sin \eta_i) + \left(p_{yi}^{(\epsilon)} - \epsilon \frac{E_0}{\omega} \cos \eta_i \right) \frac{(\eta_r - \eta_i)}{\omega} + y_i, \qquad (5.30)$$

$$\begin{aligned} z_r^{(\epsilon)} &= \frac{1}{2c} \int_{\eta_i}^{\eta_r} [\mathbf{A}(\eta') - \mathbf{A}(\eta_i)]^2 \frac{d\eta'}{\omega} + p_{zi}^{(\epsilon)} \frac{(\eta_r - \eta_i)}{\omega} \\ &+ \frac{1}{c} \int_{\eta_i}^{\eta_r} \mathbf{p}_i^{(\epsilon)} \cdot [\mathbf{A}(\eta') - \mathbf{A}(\eta_i)] \frac{d\eta'}{\omega}, \end{aligned} \qquad (5.31)$$

where superscript (ϵ) indicates the case of elliptical polarization and the initial momenta are compactly written as a vector $\mathbf{p}_i^{(\epsilon)} \equiv \left(p_{xi}^{(\epsilon)}, p_{yi}^{(\epsilon)}, p_{zi}^{(\epsilon)} \right)$.

The recollision dynamics, i.e. the momentum transfer during recollision, in the case of elliptical polarization will be the same as in the case of linear polarization, i.e.,

$$
\begin{aligned}
\delta p_{yr}^{C(\epsilon)} &= \delta p_{yr}^{C(0)}, \\
\delta p_{zr}^{C(\epsilon)} &= \delta p_{zr}^{C(0)},
\end{aligned}
\tag{5.32}
$$

if the impact parameter is the same

$$
\begin{aligned}
y_r^{(\epsilon)} &= y_r^{(0)} \\
z_r^{(\epsilon)} &= z_r^{(0)}.
\end{aligned}
\tag{5.33}
$$

The latter, using Eqs. (5.21)-(5.22) and (5.30)-(5.31), reads:

$$
\epsilon \frac{E_0}{\omega^2} \left(\sin \eta_r - \sin \eta_i \right) + \left[p_{yi}^{(\epsilon)} - \epsilon \frac{E_0}{\omega} \cos \eta_i \right] \frac{(\eta_r - \eta_i)}{\omega} + y_i
$$
$$
\approx p_{yi}^{(0)} \frac{(\eta_r - \eta_i)}{\omega},
\tag{5.34}
$$

$$
\frac{1}{2c} \int_{\eta_i}^{\eta_r} \left[\mathbf{A}(\eta') - \mathbf{A}(\eta_i) \right]^2 \frac{d\eta'}{\omega} + p_{zi}^{(\epsilon)} \frac{(\eta_r - \eta_i)}{\omega}
$$
$$
+ \quad \frac{1}{c} \int_{\eta_i}^{\eta_r} \mathbf{p}_i^{(\epsilon)} \cdot \left[\mathbf{A}(\eta') - \mathbf{A}(\eta_i) \right] \frac{d\eta'}{\omega} \approx p_{zi}^{(0)} \frac{(\eta_r - \eta_i)}{\omega}
\tag{5.35}
$$

We consider slow recollisions (e.g., points B2 and B4 introduced in the next section) when the longitudinal velocity is vanishing $p_{rx} = 0$. This according to Eq. (5.4) reads

$$
\frac{E_0}{\omega} \left(\sin \eta_r - \sin \eta_i \right) = p_{xi}^{(\epsilon)}.
\tag{5.36}
$$

Then, we can derive from Eqs. (5.34)-(5.36)

$$
p_{yi}^{(\epsilon)} = p_{yi}^{(0)} + \epsilon \frac{E_0}{\omega} \cos \eta_i - \frac{\epsilon p_{xi}^{(\epsilon)} + y_i \omega}{\eta_r - \eta_i} \approx p_{yi}^{(0)} + \epsilon \frac{E_0}{\omega} \cos \eta_i,
\tag{5.37}
$$

$$
p_{zi}^{(\epsilon)} = p_{zi}^{(0)} - \frac{1}{2c(\eta_r - \eta_i)} \int_{\eta_i}^{\eta_r} \left[\mathbf{A}(\eta') - \mathbf{A}(\eta_i) \right]^2 d\eta'
$$
$$
- \quad \frac{1}{c(\eta_r - \eta_i)} \int_{\eta_i}^{\eta_r} \mathbf{p}_i^{(\epsilon)} \cdot \left[\mathbf{A}(\eta') - \mathbf{A}(\eta_i) \right] d\eta'
\tag{5.38}
$$

We estimated the last term in the first equality of Eq. (5.37) to be rather small. In fact, $|p_{xi}^{(\epsilon)}| = |\delta p_{xi}^{C(\epsilon)}| \approx \pi E(\eta_i)/(2I_p)^{3/2}$, and $\eta_r - \eta_i \sim 3\pi$ at the first soft recollision, and $|\epsilon p_{xi}^{(\epsilon)}/(\eta_r - \eta_i)| \sim 10^{-3}$, at $\epsilon \sim 0.1$, $\omega = 0.013$ (the laser wavelength of 3400 nm), $E_0 = 0.04$ (the laser intensity of 5.8×10^{13} W/cm^2). The ratio $|y_i \omega / \epsilon p_{xi}^{(\epsilon)}| \sim \sin \eta_i$ is also small at the same values of parameters, justifying dropping the last term in the first equality of Eq. (5.37).

We can conclude that the recollision dynamics in an elliptically polarized laser field is similar to the case of linear polarization with the dipole approximation, if the initial momentum fulfills the conditions of Eqs. (5.37) and (5.38), i.e., the electrons with appropriately shifted initial momenta at the tunnel exit will create a ridge structure similar to the linear polarization scenario.

Asymptotic momenta of recolliding electrons

The final momentum of the slow recolliding electrons which create the ridge structure in an elliptically polarized laser field can be found using Eqs. (5.5), (5.11) and (5.37)(5.38).

The electron momentum before the recollision is

$$p_{ry}^{(\epsilon-)} = p_{yi}^{(\epsilon)} + \epsilon \frac{E_0}{\omega}(\cos\eta_r - \cos\eta_i),$$ (5.39)

$$p_{rz}^{(\epsilon-)} = p_{zi}^{(\epsilon)} + \frac{1}{2c}\left[\mathbf{A}(\eta_r) - \mathbf{A}(\eta_i)\right]^2 + \frac{\mathbf{p}_i^{(\epsilon)}}{c} \cdot \left[\mathbf{A}(\eta_r) - \mathbf{A}(\eta_i)\right].$$

The recollision induces the momentum transfer $\delta\mathbf{p}_r^{C(\epsilon)}$, and the electron momentum after the recollision is

$$p_{ry}^{(\epsilon+)} = p_{yi}^{(\epsilon)} + \delta p_{ry}^{C(\epsilon)} + \epsilon\frac{E_0}{\omega}(\cos\eta_r - \cos\eta_i),$$

$$p_{rz}^{(\epsilon+)} = p_{zi}^{(\epsilon)} + \delta p_{rz}^{C(\epsilon)} + \frac{1}{2c}\left[\mathbf{A}(\eta_r) - \mathbf{A}(\eta_i)\right]^2$$

$$+ \frac{\mathbf{p}_i^{(\epsilon)}}{c} \cdot \left[\mathbf{A}(\eta_r) - \mathbf{A}(\eta_i)\right].$$ (5.40)

Then, the final photoelectron momentum is

$$p_{yf}^{(\epsilon)} = p_{ry}^{(\epsilon+)} - \epsilon\frac{E_0}{\omega}\cos\eta_r,$$

$$p_{zf}^{(\epsilon)} = p_{rz}^{(\epsilon+)} + \frac{\mathbf{A}^2(\eta_r)}{2c} - \frac{\mathbf{p}_r^{(\epsilon)}}{c} \cdot \mathbf{A}(\eta_r),$$ (5.41)

which after inserting Eq. (5.40) yields

$$p_{yf}^{(\epsilon)} = p_{yi}^{(\epsilon)} + \delta p_{ry}^{C(\epsilon)} - \epsilon\frac{E_0}{\omega}\cos\eta_i,$$

$$p_{zf}^{(\epsilon)} = p_{zi}^{(\epsilon)} + \delta p_{rz}^{C(\epsilon)} + \frac{\mathbf{A}^2(\eta_i)}{2c} - \frac{\mathbf{p}_i^{(\epsilon)}}{c} \cdot \mathbf{A}(\eta_i),$$ (5.42)

where we have used that $p_{rx}^{(\epsilon)} = A_x(\eta_r) - A_x(\eta_i) - p_{xi}$, and $p_{ry}^{(\epsilon)} = A_y(\eta_r) - A_y(\eta_i) - p_{yi}$.

Now we apply the initial conditions of Eqs. (5.37)-(5.38), which results in

$$p_{yf}^{(\epsilon)} = p_{yi}^{(0)} + \delta p_{ry}^{C(\epsilon)},$$

$$p_{zf}^{(\epsilon)} = p_{zi}^{(0)} + \delta p_{rz}^{C(\epsilon)} + \frac{\mathbf{A}^2(\eta_i)}{2c} - \frac{\mathbf{p}_i^{(\epsilon)}}{c} \cdot \mathbf{A}(\eta_i)$$

$$- \frac{1}{2c(\eta_r - \eta_i)}\int_{\eta_i}^{\eta_r}\left[\mathbf{A}(\eta') - \mathbf{A}(\eta_i)\right]^2 d\eta'.$$ (5.43)

$$- \frac{1}{c(\eta_r - \eta_i)}\int_{\eta_i}^{\eta_r}\mathbf{p}_i^{(\epsilon)} \cdot \left[\mathbf{A}(\eta') - \mathbf{A}(\eta_i)\right] d\eta'$$

Taking into account the conditions of Eqs. (5.24) and (5.32), i.e., $\delta p_{ry,rz}^{C(\epsilon)} \approx \delta p_{ry,rz}^{C(0)} \approx p_{yi,zi}^{(0)}$, we obtain the final momentum:

$$p_{yf}^{(\epsilon)} \approx 0,$$

$$p_{zf}^{(\epsilon)} \approx -\frac{1}{\eta_r - \eta_i}\int_{\eta_i}^{\eta_r}T_z(\mathbf{p}_i^{(\epsilon)}, \eta')d\eta'$$ (5.44)

where

$$T_z(\mathbf{p}_i^{(\epsilon)}, \eta) \equiv \frac{\mathbf{A}^2(\eta)}{2c} + \left[\mathbf{p}_i^{(\epsilon)} - \mathbf{A}(\eta_i)\right] \cdot \frac{\mathbf{A}(\eta)}{c}, \tag{5.45}$$

is the drift momentum along the laser propagation direction.

Our conclusion from Eq. (5.45) is that the ridge position for the slow recolliding electrons in the ellipically polarized laser field is not shifted along the minor axis of polarization, but it is shifted opposite the laser propagation direction by the value corresponding to the average drift momentum during the recollision.

Estimation of the momentum shift

We may estimate the momentum shift against the laser propagation direction from Eq. (5.44) as

$$p_{zf}^{(\epsilon)} \sim -\left\{\frac{\mathbf{A}^2(\tilde{\eta})}{2c} + \left[\mathbf{p}_i^{(\epsilon)} - \mathbf{A}(\eta_i)\right] \cdot \frac{\mathbf{A}(\tilde{\eta})}{c}\right\}, \tag{5.46}$$

with the effective phase during the excursion $\tilde{\eta}$, $p_{xi}^{(\epsilon)} = \delta p_{xi}^C = \pi E_0 \cos \eta_i / (2I_p)^{3/2}$, and $p_{yi}^{(\epsilon)} - A_y(\eta_i) = \delta p_r^C$. Thus,

$$
\begin{aligned}
p_{zf}^{(\epsilon)} \quad \sim \quad & -\left\{\frac{E_0}{c\omega}\left[\left(\frac{\pi E_0 \cos \eta_i}{(2I_p)^{3/2}} + \frac{E_0}{\omega}\sin \eta_i\right)\sin \tilde{\eta} + \delta p_r^C \epsilon \cos \tilde{\eta}\right] \right. \\
& \left. + \frac{\mathbf{A}^2(\tilde{\eta})}{2c}\right\}.
\end{aligned}
\tag{5.47}
$$

The value of $\delta p_r^C \sim 0.1$ can be read off from the Fig. 5.4 while $E_0/\omega \sim 3$, and $\pi E_0/(2I_p)^{3/2} \sim 0.1$.

For the final low longitudinal momenta $p_{xf} \to 0$, $\eta_i \to 0$, the first term in the square-brackets is small and

$$p_{zf}^{(\epsilon)} \sim -\frac{\mathbf{A}^2(\tilde{\eta})}{2c}. \tag{5.48}$$

Whereas when the final momentum p_{xf} is large and rescattering is negligible, the peak of the momentum distribution shifts along the laser propagation direction:

$$p_{zf}^{(\epsilon)} \approx \frac{\mathbf{A}^2(\eta_i)}{2c}. \tag{5.49}$$

A rough estimate of

$$\frac{\mathbf{A}^2(\tilde{\eta})}{2c} \sim \frac{\mathbf{A}^2(\eta_i)}{2c} \sim \frac{E_0^2}{4c\omega^2} \approx 0.017, \tag{5.50}$$

fits by an order of magnitude the experimental observation shown in Fig. 5.2. Moreover, we can see from our analysis that the rescattering plays an essential role for the sign of the peak offset, which shifts from negative to positive values as the recollisons get suppressed by the ellipticity.

5.2 The role of the drift induced by the ellipticity

As we already mentioned early in this chapter, the creation of the central structure is connected to the momentum drift induced by the ellipticity and not to the nondipole effects. In order to get better insight, we ran several CTMC simulations with the laser pulse corresponding to the experiment in the dipole approximation (i.e., neglecting the magnetic component $\mathbf{B}(u)$) based on the two-step model of strong-field ionization. The electron trajectories are obtained as a solution of the Newton's classical equations of motion given by Eq. (2.8) in the combined electric field of the laser and the Coulomb potential of the parent ion. The initial conditions are taken from the adiabatic tunnel ionization theory in parabolic coordinate [195] and from the ADK theory. Moreover, we have fixed the CEP phase and restricted the ionization only to the central half-cycle of the laser field in order to remove any possible CEP effects. This also breaks the symmetry of the two side-lobe of the PMD, which now exhibits only one side-lobe of direct electrons that makes the created cusp at the center more visible. We show our results in Fig.5.3 for three different ellipticities: $\epsilon = 0$, 0.07 and 0.11, where clear manifestation of the central vertical cusp can be found.

Since the features of the PMD are well understood in the case of linear polarization in the terms of laser-driven classical trajectories recolliding with the parent ion, let us concentrate on this case for now. Due to the nature of the Coulomb interaction, a bunching of electrons appears and is imprinted on the PMD in the form of caustics, see Fig. 5.3 for $\epsilon = 0$. There are two kinds of caustics: horizontal and vertical. Each horizontal caustic line in PMD corresponds to a certain kind of rescattered trajectory when the longitudinal momentum (with respect to the major polarization axis of the laser field) of the electron at the recollision is vansihing (the soft recollision condition depending on the ionization phase), which leads to the longitudinal bunching of electrons. On the other hand, the central vertical cusp is caused by Coulomb focusing (CF) and is observable for all ionization phases.

In order to get a better insight into the creation of the vertical cusp, we analyzed the initial transverse momentum distribution at the tunnel exit with momentum bins of $0.01 \times 0.01 \times 0.01$ dimensions placed at characteristic points of the PMD. We compare the phase spaces of corresponding points in linearly and elliptically polarized cases in Fig. 5.4. The cusp originates as the contraction of the transverse phase space. In the linearly polarized laser field the electrons contributing to the cusp are ionized with a nonvanishing transverse momentum at the tunnel exit and finally appear with the vanishing transverse momentum. Their initial distribution is a ring in (p_y, p_z)-transverse phase space, see Fig. 5.4, left column. In the case of linearly polarized laser field, the electrons which are distributed inside the ring in the transversal phase space, undergo hard recollisions and contribute mostly to the high energy region of the PMD (i.e., with energy larger than $2U_p$, , where U_p is the ponderomotive potential). Let us note that this region is not shown in Fig.5.3. However, there are exceptional electrons with specific trajectories originating from the inner rings in Figs. 5.4(a)-(c). The electrons from the inner rings also end at the center of the ridge, but, unlike the electron from the outer ring, this happens due to well-balanced role of multiple rescatterings. We used the term well balanced since the Coulomb momentum transfer to the electron switches its sign in the
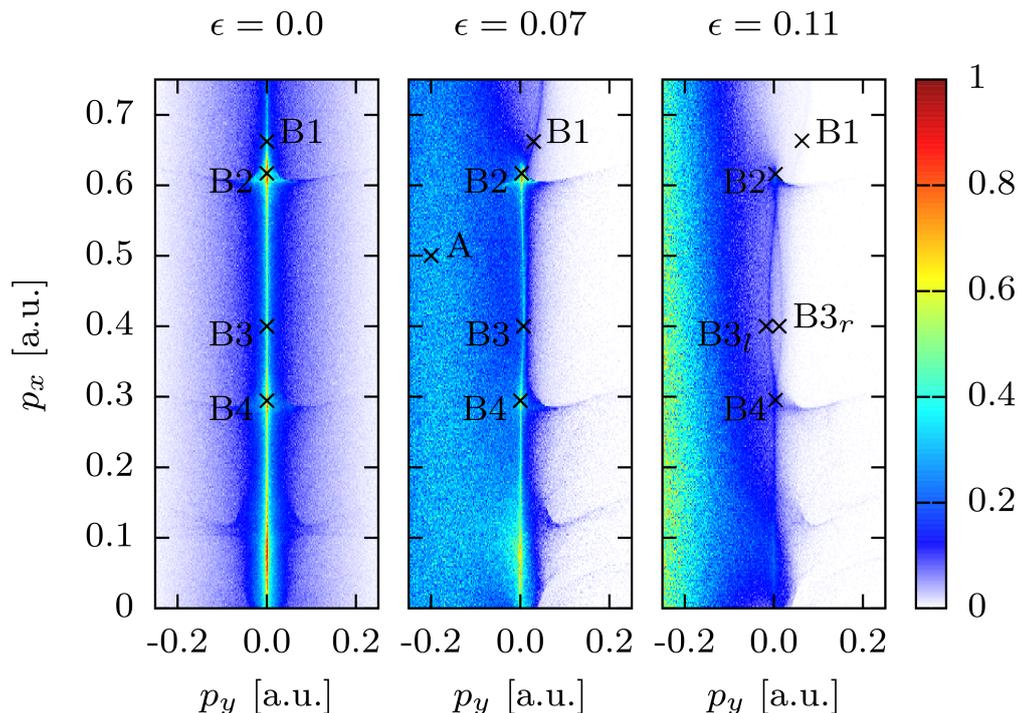
Figure 5.3: Comparison of PMD cuts with $|p_z| < 0.06$ obtained by CTMC simulations with fixed CEP phase and ionization restricted only to the central half-cycle for different ellipticities: $\epsilon = 0$, $\epsilon = 0.07$ and $\epsilon = 0.11$, respectively. We pointed out the characteristic points depending on the specific longitudinal momenta and marked them as Bn, where n stands for the number of recollisions in the case of linear polarization. Since the case of small ellipticities is similar to linear polarization, we can also find corresponding points in the central and right panel as marked. Point A stands for the center of the side-lobe and is originates from recollision-free trajectories. The points B2 and B4 correspond to the soft recollision condition ($p_{xr} = 0$), which manifests itself as visible horizontal caustics passing through B2 and B4. Moreover, the vertical caustic appears to be strongly dependent on the ellipticity as it deforms for $\epsilon = 0.07$ and even splits for $\epsilon = 0.11$ at intermediate longitudinal momenta as pointed out by point B3. The bend of the cusp above B2 is also ellipticity dependent as the changing transversal position of B1 in panels (a)-(c) shows. Moreover, we can see a suppression of its visibility with increasing ellipticity.

consecutive rescatterings and since the underlying trajectory strongly depends on the initial conditions of the electron. The balance is strongly distorted when the ellipticity is introduced. This can be concluded from the suppression and eventual vanishing of the inner rings in Figs. 5.4(d)-(j).

In the case of the laser field with small elliptical polarization, this picture holds and we can still identify analogous points for the ellipticities $\epsilon = 0.07$ and $\epsilon = 0.11$ as shown in Fig. 5.3, which manifest the deformation of the PMD via increasing ellipticity, leading to a split of the central cusp at the point B3 for $\epsilon = 0.11$. Nevertheless, we can identify two modifications to this picture. First of all, Coulomb focusing acts on such electrons which are originally distributed on a shifted ring in the initial phase
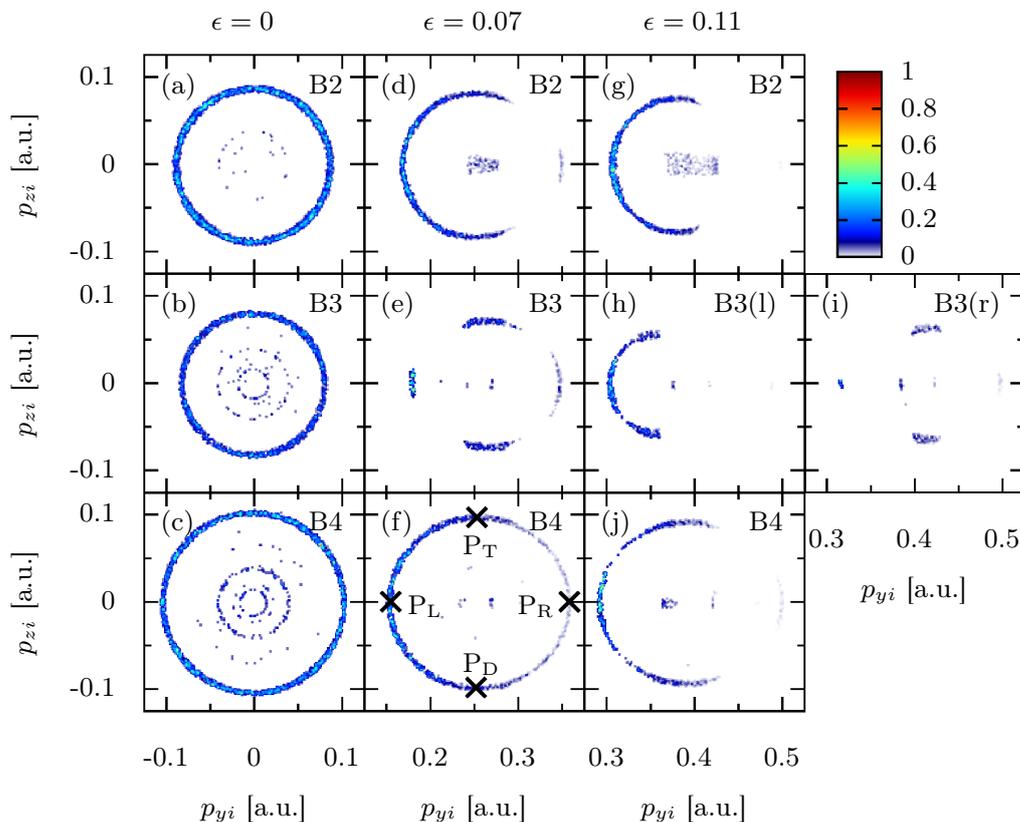
Figure 5.4: The initial momentum space distribution for trajectories ending in the momentum bins of $0.01 \times 0.01 \times 0.01$ dimensions at the asymptotic values of longitudinal momentum p_x: (a) 0.62, (b) 0.44 and (c) 0.3 $a.u.$, corresponding to the points B2, B3, B4 of Fig. 5.3, respectively. The laser field is linearly polarized in (first column), and elliptically polarized: with $\epsilon = 0.07$, in (second column), and $\epsilon = 0.11$, in (last two columns). Notice the positive offset in the p_{yi} of the structures in the right column due to the ellipticity. For $\epsilon = 0.11$ the ridge splits into two parts, represented by points $B3(l)$ and $B3(r)$ in panels (h) and (i), respectively. The pronounced left branch in (h) consists of electrons following linear-like trajectories, whereas the faint right branch comes from trajectories strongly influenced by the ellipticity. The points P_T, P_D, P_L, P_R are discussed in the text. In the CTMC simulations the dipole approximation is used along with fixed CEP phase and the ionization being restricted to the central half-cycle of the laser pulse.

space. This is similar to the case of nondipole effects in linear polarization and holds for small ellipticities, which we define in in Eq. (5.58) below. The shift is in the of the ring along the negative p_{yi} momentum and the prediction made by Eq. (5.29) agrees with the simulations in Fig. 5.4(d)-(j). The Coulomb focusing is indicated by the ring form of the initial distribution. The ring is not altered much in case of small elliptical polarization meaning that Coulomb focusing for is qualitatively the same. The electrons distributed on the shifted ring contribute to the line-shaped ridge observed in the PMD with elliptically polarized laser fields. The electrons with slow recollision contribute to the points B2 and B4 in Fig. 5.3. Interestingly, the position of these points in the PMDs does not change with the introduction of the ellipticity, which points out to similarity the similarity of the underlying trajectories.

Secondly, type A electrons with vanishing initial transverse momentum do not experience any recollisions for non-negligible ellipticities and the only momentum change happens through the initial Coulomb momentum transfer when the electron recedes from the tunnel exit. This type of electrons contributes to the two lobes in the final (p_x, p_y)-distribution. Unlike type B electrons, type A electrons originate on a point in the initial momentum space, see Fig. 5.5, indicating the absence of Coulomb focusing (the initial and the final phase space are the same).

A new type of recolliding trajectories ending at point B2 can be seen for $\epsilon = 0.07$ and $\epsilon = 0.11$. They manifest as small rectangle-like distributions placed inside the rings of the initial momentum distributions for B2. Nevertheless, the number of these trajectories is not high and we do not expect them to influence the PMD.

The shift of the initial momentum space of the ridge electrons.

We investigate the sharp ridge structure at the center of the PMD and is properties in this section. First of all, we have to find the electron initial momenta at the tunnel exit contributing to the ridge. The cusp electrons originate on a ring in the initial transverse momentum space (p_{yi}, p_{zi}), whose radius corresponds to the transverse momentum change due to Coulomb focusing [142]. The ridge is centered in the final PMD, in the case of linearly polarized laser field, at $p_y = 0$, $p_z = 0$ and the initial momentum ring is at the center of the transversal plane $p_{yi}^{(0)} = 0$, $p_{zi}^{(0)} = 0$. The ellipticity induces a momentum shift along the minor axis of the polarization ellipse (i.e., along the y-axis), and the nondipole effects induce momentum shift of the cusp structure along the negative z-axis. In order to find these shifts let us follow two electrons from opposite parts of the initial PMD-ring, which finally end up at the cusp with the same asymptotic momentum. For illustration, we mark such electrons in Fig. 5.4(f). At the beginning, we choose the left electron P_L with $p_{yi}^-, p_{zi} = 0$ and the right electron P_R with $p_{yi}^+, p_{zi} = 0$, both of which have the same vanishing final momentum at the cusp:

$$p_{yf}^- = p_{yf}^+. \tag{5.51}$$

We can use the solution to the electron's motion in the laser field given by Eq. (5.5), and account for the Coulomb momentum transfer at the tunnel exit $\delta p_{yi}^{C\pm}$ and at the

recollisions $\delta p_{yr}^{C\pm}$, yielding the final momentum

$$p_{yf}^{\pm} = -\epsilon \frac{E_0}{\omega} \cos \eta_i + p_{yi}^{\pm} + \delta p_{yi}^{C\pm} + \delta p_{yr}^{C\pm}, \tag{5.52}$$

with p_{yi}, η_i and ϵ being the electron momentum at the tunnel exit, the ellipticity of the laser and the ionization phase, respectively. It follows, from Eq. (5.51) that the radius $R_{p_{yi}}$ of the ring in the initial momentum distribution is given by the total Coulomb momentum transfer:

$$R_{p_{yi}} \equiv \frac{p_{yi}^{+} - p_{yi}^{-}}{2} \approx \frac{\delta p_{yr}^{C-} - \delta p_{yr}^{C+}}{2} \left(1 + \frac{2E(\eta_i)}{(2I_p)^2}\right) \approx \delta p_{yr}^{C-}. \tag{5.53}$$

where we used $\delta p_{yi}^{C\pm} \approx -2p_{yi}^{\pm} E(\eta_i)/(2I_p)^2$ from Eq. (2.87), $E(\eta_i) \ll E_a$, and $\delta p_{yr}^{C+} \approx -\delta p_{yr}^{C-}$. Under assumption that the center of the ridge is at $p_{yf} \approx 0$, we can find the initial momenta of the ridge electrons

$$p_{yi}^{\pm} = \epsilon \frac{E_0}{\omega} \cos \eta_i - \delta p_{yi}^{C\pm} - \delta p_{yr}^{C\pm}. \tag{5.54}$$

The center of the ring depends on the ellipticity as

$$p_{yi}^{(\epsilon)} \equiv \frac{p_{yi}^{+} + p_{yi}^{-}}{2} \approx \epsilon \frac{E_0}{\omega} \cos \eta_i \left(1 + \frac{2E(\eta_i)}{(2I_p)^2}\right) \approx \epsilon \frac{E_0}{\omega} \cos \eta_i. \tag{5.55}$$

Thus, in the case of elliptical polarization the ring of the initial momentum distribution for the sharp ridge electrons is shifted due to the elliptical drift momentum along the minor axis of polarization. Similar to the ring radius $R_{p_{yi}}$, the initial momenta of the ridge electrons can be expressed via the Coulomb momentum transfer at the recollisions:

$$p_{yi}^{\pm} = p_{yi}^{(\epsilon)} \pm R_{p_{yi}} \approx \left(\epsilon \frac{E_0}{\omega} \cos \eta_i \pm \delta p_{yr}^{C-}\right) \left(1 + \frac{2E(\eta_i)}{(2I_p)^2}\right) \tag{5.56}$$

The indicator of CF is the radius of the ring $R_{p_{yi}}$ in the initial transverse phase space distribution, which according to Eq. (5.53) is determined by the Coulomb momentum transfer at recollisions. Therefore, the radii of the rings (corresponding to the total momentum transfer and hence the CF) are also the same.

The comparison with the linear polarization case reveals, that the ellipticity induced shift of the initial momentum distribution corresponding to the ridge electrons dominates over the nondipole induced shift in the considered parameter regime, see Fig. 5.4.

The sharp ridge arises due to recollisions and exists as long as the required initial transverse momentum of type B electrons according to Eq. (5.54) is present within the tunneled electron wave packet. The width of the wave packet in the momentum space is given by $\Delta_{\perp}$, leading to condition:

$$\epsilon \frac{E_0}{\omega} \lesssim \Delta_{\perp}. \tag{5.57}$$
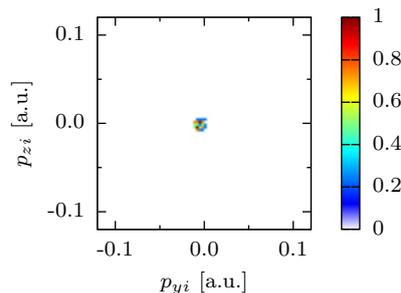
Figure 5.5: The initial momentum space distribution of direct electrons without Coulomb focusing which are ending in the center of the main lobe, point A in Fig. 5.3.

When we substitute for the width from Eq. 1.36, we conclude that the ridge in the PMD can exist up to ellipticities

$$\epsilon \lesssim \frac{\omega}{\sqrt{E_0}(2I_p)^{1/4}} \approx 0.07. \tag{5.58}$$

Nevertheless, the ellipticity introduces a complex modification of the rescattering trajectories, which cannot be easily compensated by adjustment of the initial transversal momentum. For this reason, ellipticity modifies also the rings as we can see in Fig. 5.4. The strongest modification is found at the point B3, which is split as $\epsilon = 0.11$. In the next section we are going to investigate the electron trajectories for the influence of the ellipticity. We note that there exist inner rings in the linear case in Fig. 5.4(a)-(c), which correspond to trajectories with multiple rescattering events yielding similar absolute values and various signs of the individual R-CMT. Nevertheless, such trajectories strongly depend on the initial conditions of the electrons and thus are strongly suppressed when ellipticity is introduced as we can see in Fig. 5.4(d)-(j).

The structure of the sharp ridge

Let us analyze the modifications of the central ridge as a function of ellipticity in terms of underlying trajectories. For the points B2 and B4 and for linear polarization the main Coulomb momentum transfer during recollision takes place at the slow recollision, $p_{xr} = 0$. This corresponds to the second recollision for B2, and the fourth near B4. Although there are two recollision points with $x_r = 0$ for B2 and even four for B4 (see Fig. 5.6), the Coulomb momentum transfer is the largest in both cases at the last revisit yielding slow recollision. We have calculated the Coulomb momentum transfer numerically for specific trajectories in Fig. 5.6. It is determined by the difference of the exact numerical solution for the momentum component $p_y^{num}(\eta)$ and the solution in the laser field, given by Eq. 5.5:

$$\delta p_y^C(\eta) \equiv p_y^{num}(\eta) - [A_y(\eta) - A_y(\eta_i) + p_{yi}], \tag{5.59}$$

with the ionization phase η_i, and the corresponding initial momentum p_{yi}.

As we can see the Coulomb momentum transfer at recollisions for all three points B2, B3, B4, is approximately the same as in the case of linear polarization demonstrating the similarity of both cases.

In the elliptical polarization case, the Coulomb focusing for the trajectory coming from the left part of the ring resembles the linear case, since the slow recollision has the same impact parameter and the same Coulomb momentum transfer during recollision.

The slow recollision is dominant over the other (fast) recollisions due to the magnitude of the R-CMT also in the case of elliptic polarization as we can see in Fig. 5.6. The dominance is even enhanced by the ellipticity because the impact parameters for the fast recollisions are larger than in the linear case due to the oscillating part of the y-coordinate, but the impact parameters for the slow recollision remain similar. Therefore, the total Coulomb momentum transfer represented by the radius of the left half-ring in Fig. 5.4 remains nearly the same for linear and elliptical polarizations, thereby creating the central ridge in the PMD in both cases.

In contrast, the trajectory from the right part of the ring at B2 in the elliptical polarization case differs from the linear one, see Fig. 5.6, upper right panel. The first rescattering for this trajectory, in addition to the slow recollision, takes place with smaller impact parameter than in the linear case due to the oscillating part of the y-component, resulting in an increase of the total Coulomb momentum transfer. This explains the larger radius of the right half-cycle of the ring structure at B2 in Fig. 5.4. The right-type trajectories are more sensitive to the initial conditions and, consequently, the width of the right part of the ring is significantly smaller. On the other hand, the rescatterings leading to the point B4 start to resemble the linear case again as the ring in Fig. 5.4(f) closes. We can notice that the right part of the ring is narrower and fainter than the left part. The latter is caused by the larger initial momenta of the ionized electrons needed to compensate the elliptic drift along with the Coulomb focusing. This also explains why the central ridge becomes less pronounced with increasing ellipticity as the rings shift to larger values of transversal momenta of decreasing abundance in the tunneled wave packet.

Therefore, let us divide the central cusp into three regions with respect to the longitudinal momenta: the longitudinal momenta above point B2 will be considered as large, the longitudinal momenta between B2 and B4 as intermediate, and we will consider the momenta below B4 as small. As in each of these regions the electrons have similar dynamics with the same number of recollisions, we can carry out our further investigation for each region individually.

At large longitudinal momenta: deflection

Above the point B2, when the photoelectrons rescatter only once, the ridge is bent (or rather deflected towards the positive nonvanishing p_y momenta), see Fig. 5.7(a), (b). One can deduce this by looking at the left trajectory for point B1 in Fig. 5.7(c). We can ignore the role of the second rescattering, since its importance diminishes with increase of the final longitudinal momentum, and assume the first rescattering only. For the single rescattering trajectories above the point B2, the rescattering coordinate is very similar to the linear polarization case. In the example presented in Fig. 5.7, the electrons from both sides of the initial momentum distribution ring ionized with the same phase η_i recollide at the same phase η_r and with the same impact parameter, i.e.,

$$y_r^{(\epsilon)-} = -y_r^{(\epsilon)+}.$$ (5.60)
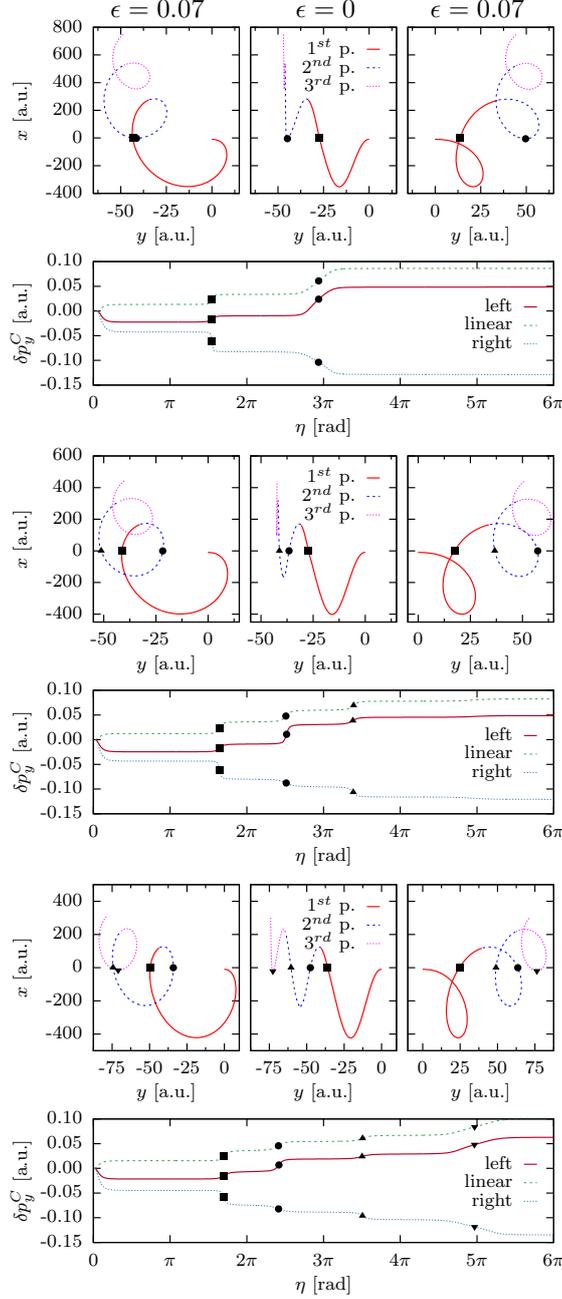
Figure 5.6: Typical photoelectron trajectories in a laser field with $\epsilon = 0.07$, as well as initial Coulomb momentum transfer and Coulomb momentum transfer during recollision. The trajectories originate on the left (left panels) and right part (right panels) of the initial transverse momentum distribution ring with $p_{zi} = 0$ and end up at the same point B2 (upper group), B3 (middle group), and B4 (bottom group). The middle panels show trajectories in the case of linear polarization. The slow recollisions are the second one in B2, and the fourth one in in B4. In the left panels the slow recollisions have the same impact parameters (y-coordinate) as in the linear polarization case (middle panel).
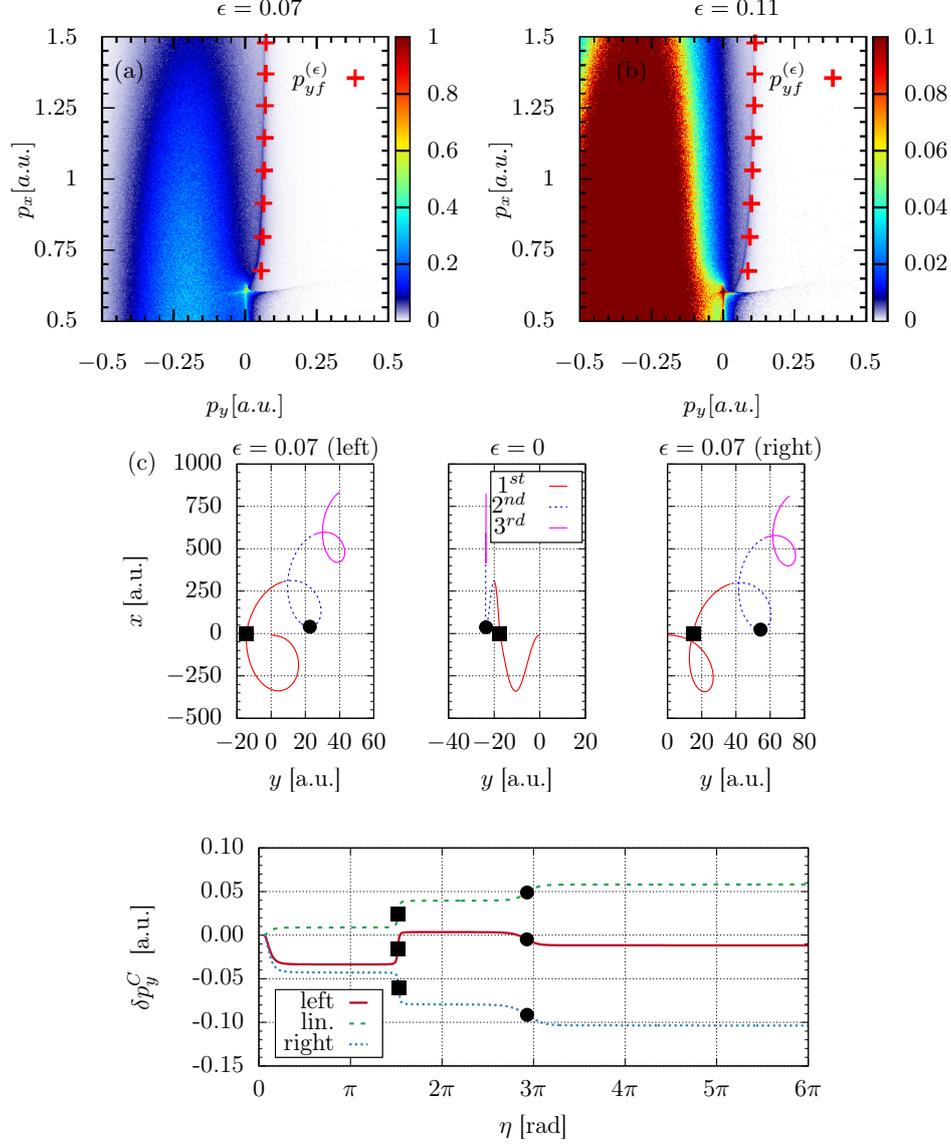
Figure 5.7: The bent central ridge above the point B2: the comparison of the CTMC simulations with the estimates of the deflected momentum $p_{yf}^{(\epsilon)}$ from Eq. (5.62) for (a) $\epsilon = 0.07$ and (b) $\epsilon = 0.11$, respectively; (c) Typical photoelectron trajectories in a laser field with $\epsilon = 0.07$, as well as the initial and recollision Coulomb momentum transfer. The trajectories originate on the left (left panels) and right part (right panels) of the initial transverse phase space distribution ring with $p_{zi} = 0$ and end up at the same point B1. The middle panel of trajectories shows the case of a linear polarization.
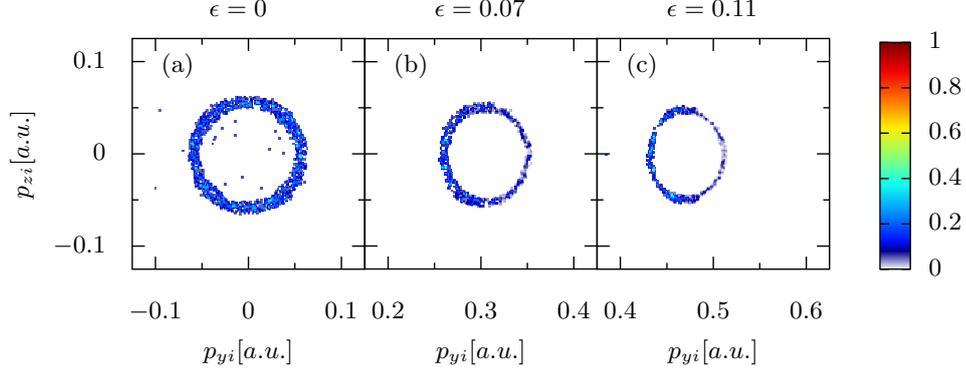
Figure 5.8: The initial transversal phase spaces for $\epsilon = 0$, $\epsilon = 0.07$, and $\epsilon = 0.11$ respectively, resulting in trajectories with a single rescattering event at B1. The ellipticity shifts the initial transverse momentum ring in the p_y-direction and causes a slight deformation.

The latter is ensured by proper values of $p_{yi}^{(\epsilon)-}$ and $p_{yi}^{(\epsilon)+}$ which can compensate for the transversal dynamic introduced by the ellipticity and hence lead to the same absolute value of Coulomb momentum transfer for the opposite trajectories with analogy to the linear case. From the condition of Eq. (5.60), and by using Eq. (5.30) with $y_i = 0$, we derive the momentum of the center of the initial momentum ring of the ridge electrons presented in Fig. 5.8:

$$p_{y0}^{(\epsilon)} \equiv \frac{p_{yi}^{(\epsilon)-} + p_{yi}^{(\epsilon)+}}{2} = \delta\bar{p}_{yi}^{C(\epsilon)} + \epsilon\frac{E_0}{\omega}\left(\cos\eta_i - \frac{\sin\eta_r - \sin\eta_i}{\eta_r - \eta_i}\right), \qquad (5.61)$$

where we have defined the averaged initial Coulomb momentum transfer for the ring's center as $\delta\bar{p}_{yi}^{C(\epsilon)} \equiv \frac{1}{2}\left(\delta p_{yi}^{C(\epsilon)-} + \delta p_{yi}^{C(\epsilon)+}\right)$. The final momentum of the ridge in this case is:

$$p_{yf}^{(\epsilon)} = p_{y0}^{(\epsilon)} - \epsilon\frac{E_0}{\omega}\cos\eta_i - \delta\bar{p}_{yi}^{C(\epsilon)} = -\epsilon\frac{E_0}{\omega}\left(\frac{\sin\eta_r - \sin\eta_i}{\eta_r - \eta_i}\right). \qquad (5.62)$$

The estimates of $p_{yf}^{(\epsilon)}$ is plotted in Fig. 5.7 and shows agreement with the simulations. A slight discrepancy appears near the point B2 which is caused by the omission of the second recollision which yields additional momentum transfer further diminishing $p_{yf}^{(\epsilon)}$. Moreover, $p_{yf}^{(\epsilon)}$ is positive for all single recollision trajectories and vanishes for linear polarization as expected.

At intermediate longitudinal momenta: bend and branching

The ring of the initial momenta of point B3 is deformed in a stronger way than that of B2. The deformation is due to the fact that both left and right trajectories are strongly perturbed with respect to the linear polarization case because of the quiver motion in the transversal y-direction. The perturbed trajectories are more sensitive to the initial conditions, which results in a variable width of the ring in the initial momentum

distribution. Moreover, the recollision coordinates for both left and right trajectories are different. Therefore, the Coulomb momentum transfer during recollision for the left and right trajectories are not symmetric which leads to a bend of the central ridge. Furthermore, at larger ellipticities, e.g. $\epsilon = 0.11$, the central ridge at B3 is split, when the left- and right-side trajectories yield different ridges B3(r) and B3(l), respectively, see Fig. 5.4(h)-(i). However, this splitting is not visible in the experimental data due to focal volume averaging, CEP averaging and the laser pulse envelope.

The trajectory analysis behind point B3 in Fig. 5.6 demonstrates the complexity of CF introduced by the ellipticity, inducing the fine splitting of the cusp, see Fig. 5.3 for $\epsilon = 0.11$. Let us firstly address the right branch of the split cusp. From Fig. 5.4 one can see that the main contribution to this branch comes from electrons which initially have large momentum p_{zi}, transverse to the polarization plane. In the linear polarization case this type of trajectories acquire CMT only in the z-direction, creating the cusp at final vanishing transverse momentum $p_{yf} = p_{zf} = 0$. We expect that the same type of trajectories (the total R-CMT is mostly in the z-direction, i.e., the y-component of the R-CMT is almost vanishing) create the cusp at low ellipticity values.

We analyzed the transversal trajectory with $p_{zi} \neq 0$ and $p_{yi} = p_{y0} = (p_{yi}^- + p_{yi}^+)/2$ (the center of the initial transverse momentum distribution) for the case of $\epsilon = 0.11$ in Fig. 5.9(c). These trajectories are 3D and their transversal part along the laser propagation axis resembles the linear case. Interestingly, these trajectories receive several Coulomb momentum transfers in the p_y direction, which compensate for each other yielding the same δp_y^C before the first and after the second rescattering, as shown by the red curve in the lowest plot in Fig. 5.9(c). Moreover, the R-CMT at the third recollision in the y-direction can be omitted due to its smallness leaving effectively only the I-CMT imprinted on the electron's momentum.

Let us make use of this new feature: cancellation of R-CMT at the first and second rescatering, yielding

$$\delta p_{yr,1}^C = \delta p_{yr,2}^C. \tag{5.63}$$

In order to estimate these R-CMT, we need to find the underlying trajectory. The motion along the major axis is still dominantly governed by Eq. (5.15) whose roots give us the recollision phases $\eta_{r,1}$ and $\eta_{r,2}$. The transversal motion can be described before the first rescattering as
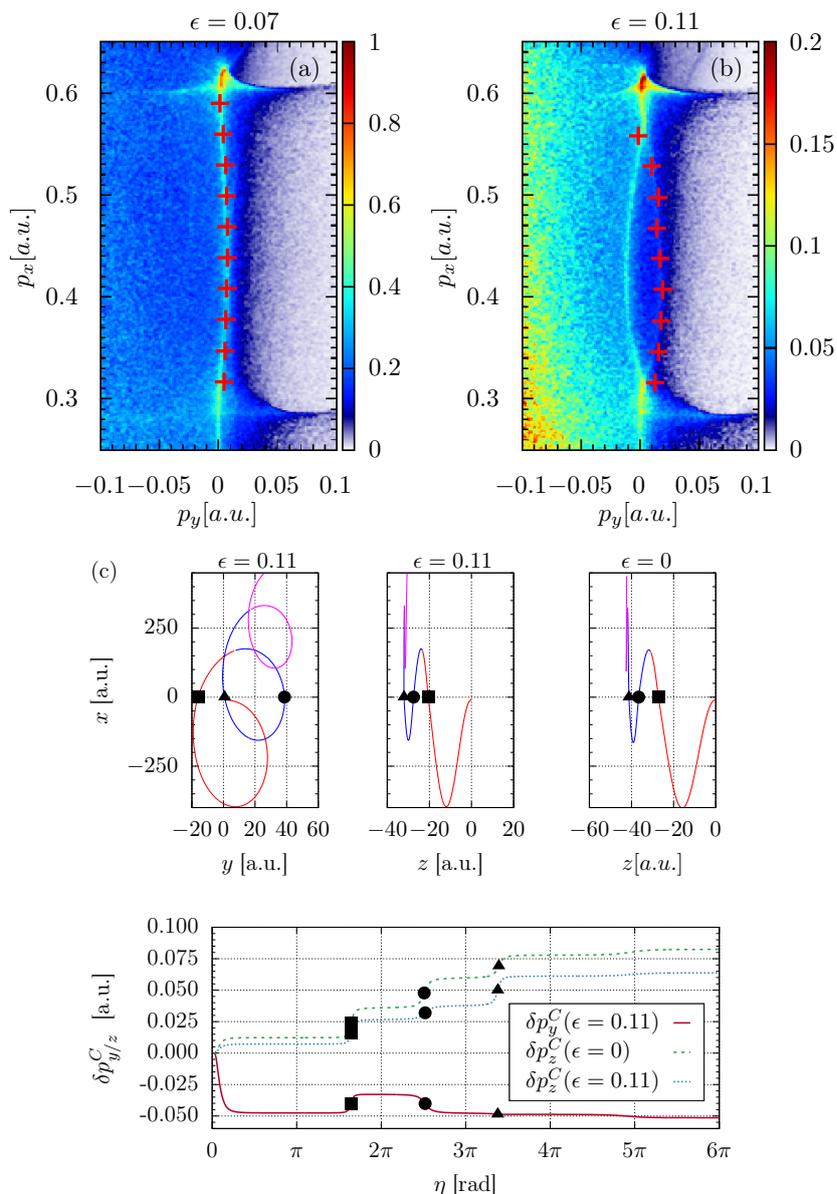
$$
\begin{aligned}
y_1(\eta) &= \epsilon \frac{E_0}{\omega^2} \left(\sin \eta - \sin \eta_i \right) \\
&\quad + \left[p_{yi} - \delta p_{yi}^C - \epsilon \frac{E_0}{\omega} \cos \eta_i \right] (t - t_i),
\end{aligned} \tag{5.64}
$$

$$z_1(\eta) = (p_{zi} - \delta p_{zi}^C)(t - t_i), \tag{5.65}$$

and after first rescattering $\eta_{r,1}$ as

$$
\begin{aligned}
y_2(\eta) &= y_1(\eta_{r,1}) + \epsilon \frac{E_0}{\omega^2} \left(\sin \eta - \sin \eta_{r,1} \right) \\
&\quad + \left[p_{yi} - \delta p_{yi}^C - \epsilon \frac{E_0}{\omega} \cos \eta_r + \delta p_{yr,1}^C \right] (t - t_{r,1}),
\end{aligned} \tag{5.66}
$$

$$z_2(\eta) = z_1(\eta_{r,1}) + (p_{zi} - \delta p_{zi}^C - \delta p_{zr,1}^C)(t - t_{r,1}), \tag{5.67}$$

Figure 5.9: Analysis of the bend between points B2 and B4 for $\epsilon = 0.07$ and $\epsilon = 0.11$ shown in the panels (a) and (b), respectively. In the right PMD we changed the range of the colorbar so all bins with larger intensity than 0.2 are plotted with red color in order to enhance the visibility of the split bend. The red crosses are obtained as numerical solutions of Eqs. (5.69) and (5.70). We compare the trajectories of electrons ending on the right part of the split with corresponding electrons in linear case. The similarity can be seen as a cancellation of the consecutive Coulomb momentum transfers δp_y^C in the p_y momentum (as the hump on the red line in the lowest figure at $\eta \approx 2\pi$).

where we introduced the R-CMT δp_{yr}^C and δp_{zr}^C. The I-CMT can be estimated as in

Eq. (4.9). The CMTR is

$$\delta p_{yr}^C \approx \frac{y}{(y^2 + z^2)^{3/2}} \delta t_r,$$

$$\delta p_{zr}^C \approx \frac{z}{(y^2 + z^2)^{3/2}} \delta t_r, \tag{5.68}$$

with the characteristic duration of the recollision proportional to the longitudinal velocity $\delta t_r = 2 \frac{\sqrt{y^2+z^2}}{p_x}$ (as shown in Sec. 2.3.3), which translates the condition of Eq. (5.63) to the following relation

$$\frac{|y_1(\eta_{r,1})|}{|y_2(\eta_{r,2})|} = \frac{\left[y_1^2(\eta_{r,1}) + z_1^2(\eta_{r,1})\right] |p_x(\eta_{r,1})|}{\left[y_2^2(\eta_{r,2}) + z_2^2(\eta_{r,2})\right] |p_x(\eta_{r,2})|}. \tag{5.69}$$

The x- and y-momentum components can be found from Eq. (5.4) and (5.5), respectively. The last unknown is the momentum p_{zi} which is determined by the fact that $p_{zf} = 0$. Since z-component of R-CMT for all three recollisions are approximately equal, we can roughly estimate $\delta p_{zr,1}^C = \frac{1}{f}(p_{zi} - \delta p_{zi}^C)$, which reads

$$\frac{2z_1(\eta_{r,1})}{\left[y_1^2(\eta_{r,1}) + z_1^2(\eta_{r,1})\right] |p_x(\eta_{r,1})|} = \frac{1}{f}(p_{zi} - \delta p_{zi}^C). \tag{5.70}$$

with a ratio factor f. Now, we are able to find for each ionization phase η_i the recollision phases $\eta_{r,1}$ and $\eta_{r,2}$ and hence the initial momenta p_{yi} and p_{zi} from Eqs. (5.69) and (5.70), such that the electrons with these initial conditions will end at the bent cusp. The final momentum at the cusp is calculated as $p_{yf} = p_{yi} - \delta p_{yi}^C - \epsilon \frac{E_0}{\omega} \cos \eta_i$.

While solving the Eqs. (5.69) and (5.70) numerically, we observed a strong dependency of the final cusp position on the ratio factor f, the value $f = 3$ in Eq. (5.70) being a very rough estimation. Instead, using f as a fitting parameter, we obtain agreement with the experiment, as shown in Fig. 5.9(a), (b) for both considered ellipticities. The value of the fitting parameter f in the case of $\epsilon = 0.11$, is $f = 3.5$ (for $p_{xf} = 0.33 \ldots 0.36$) and $f = 4.4$ (for $p_{xf} = 0.36 \ldots 0.48$) and $f = 6$ for (for $p_{xf} = 0.48 \ldots 0.56$), i.e., the ratio of CMTR $\delta_{zr,1}^C$ and $p_{zi} - \delta p_{zi}^C$ depends on p_{xf} and decreases with increasing p_{xf}.

The agreement with the CTMC simulations shows that even when the ellipticity is non-zero, similarities to the linear case can be found making several features of the PMD easier to understand. Nevertheless, any similarities are fast washed away with increasing ellipticity. This can be seen in the Fig. 5.9(b) where the right part of the fork is much weaker than the right part. This is due to the fact that the trajectories corresponding to the right part of the fork are distorted more strongly.

At small longitudinal momenta: straightening

The lower part of the central cusp seems to be quite resistant with respect to the introduced ellpiticity as shown in Fig. 5.3. This is because the underlying trajectories for B4, and trajectories ending up on the central ridge at $|p_x|$ smaller than for B4, start to resemble the linear case again. The resemblance can be understood via the small ionization phases that are characteristic for these trajectories, meaning also that the oscillating

part of the y-component does not perturb the recollision coordinates significantly. The condition for this is

$$|y_r^{(\epsilon)} - y_r^{(0)}| \ll y_r^{(0)}, \tag{5.71}$$

with the index $^{(0)}$ indicating the linear polarization, from which we can estimate the threshold ionization phase. Using Eq. (5.30) and (5.37), and the approximations $\eta_r^{(\epsilon)} = \eta_r^{(0)}$ and $\eta_i^{(\epsilon)} = \eta_i^{(0)}$, this condition reads

$$\left| \epsilon \frac{E_0}{\omega^2} (\sin \eta_r - \sin \eta_i) \right| \ll \left(p_{yi}^{(0)} + \delta p_{yi}^{C(0)} \right) \frac{(\eta_r - \eta_i)}{\omega}, \tag{5.72}$$

which can be expressed via the Coulomb momentum transfer at the recollision δp_{yr}^C:

$$|\sin \eta_r - \sin \eta_i| \ll \frac{\delta p_{yr}^C}{(\epsilon E_0/\omega)} (\eta_r - \eta_i). \tag{5.73}$$

The recollision phase is found from the condition $x(\eta_r) = 0$. Taking into account that for the first recollision $\eta_r \approx 2\pi - \eta_r'$, with $\eta_r' \ll 1$, we find

$$\eta_r' \approx \sqrt{4\pi \eta_i}, \tag{5.74}$$

and the condition of Eq. (5.73), at which the oscillating part of the y-coordinate does not perturb the recollision coordinates significantly, reads

$$\eta_i \ll \pi \left(\frac{\delta p_y^C}{(\epsilon E_0/\omega)} \right)^2 \approx 0.7, \tag{5.75}$$

for $\delta p_y^C = 0.1$, $\epsilon = 0.07$, and the laser parameters of the experiment $E_0 \approx 0.04$, $\omega \approx 0.013$. The latter means that at $\eta_i \lesssim 0.07$, which assumes $p_x \lesssim E_0 \eta_i/\omega \approx 0.2$, the recollisions and Coulomb focusing in the elliptical polarization case will be similar to the linear one. This estimate fits the CTMC calculation in Fig. 5.3.

5.3 The role of the drift induced by nondipole effects

In the previous section, we were able to link the newly measured central structure in the PMDs to rescattered trajectories and draw analogies to the central cusp of linear polarization. Moreover, we were able to explain the inner structure and dependency on the ellipticity thanks to the similarity of the underlying trajectories with the linearly polarized case. This similarity can be achieved when the tunneled electrons is able to compensate for the drift induced by the non-zero vector potential along the minor axis of polarization and derived the condition on visibility of the sharp ridge in Eq. (5.58).

The open question is, how does the situation change due to the nondipole effects as we introduce drift in the remaining transversal direction corresponding to the propagation direction of the laser?

In order to answer this question, we performed CTMC simulations including nondipole effects and plotted the resulting PMDs in Fig. 5.10. In the panels (a)-(c), we show the

the projections of the PMDs onto the (p_y-p_x)-plane. They mostly correspond to the dipole case allowing us to identify the very same significant points Bn as in Fig. 5.3. The means that the underlying trajectories and their classification with respect to the number of recollision did not change with the introduction of the nondipole effects keeping our analysis from Sec. 5.2 valid.

The novelty comes with the next set of panels: (d)-(f) placed in the second row of the figure showing the PMDs projected on the (p_z-p_x)-plane, where we can clearly recognize the counterintuitive bend of the central cusp. The panel (d) corresponds to linear polarization discussed thoroughly in Chap. 4 and poses no surprise. More importantly, the bend cusp appears also for $\epsilon = 0.07$ and $\epsilon = 0.11$ in the part with rescattered electrons below the point B2. It is no surprise that the bend cusp in the panels (e) and (f) does quantitatively correspond to the cusp in panel (d). By this we mean that the energy dependent shift is negative and has the same amplitude as in the linear case, which may not be obvious at first glance. Therefore, we plotted the initial distribution of the electrons ending at the points B2, B3 and B4 in Fig. 5.11. As we can see, the negative offset in p_{zi} direction of the rings is the same for every point Bn through all ellipticities. Moreover, the rings or half rings in the initial phase space are preserved from the dipole case presented in Fig. 5.4 meaning that the magnetic force introduces only a slight distortion of the underlying trajectories which can be compensated for by proper modification of the initial transversal momenta p_{zi}.

Disentanglement of ellipticity and nondipole effects

The magnetically induced drift shifts the initial momentum distribution for the sharp ridge electrons along the z-axis. To show this, let us first calculate the final momentum along the laser propagation direction. According to Eq. (5.11),

$$p_{zf} = p_{zi} + p_{zd}^{(i)} + \delta p_{zi}^C + \delta p_{zr}^C, \tag{5.76}$$

where $p_{zd}^{(i)} \equiv \frac{A^2(\eta_i)}{2c} - \mathbf{p}_i \cdot \frac{\mathbf{A}(\eta_i)}{c}$. The Coulomb momentum transfer at the recollision can be estimated (for more detain see Sec. 2.3.3) as

$$\delta p_{yr}^C \approx -\frac{y_r}{R_r^3} \delta t_r, \tag{5.77}$$

$$\delta p_{zr}^C \approx -\frac{z_r}{R_r^3} \delta t_r = \frac{z_r}{y_r} \delta p_{yr}^C \tag{5.78}$$

where y_r, z_r, and R_r are the recollision coordinates and the recollision distance, respectively, and δt_r is the recollision time. As we analyze the case $p_{zi} = 0$, the electron trajectory in the laser field via Eqs. (5.16)-(5.17) is

$$
\begin{aligned}
y_r &= \left(\epsilon \frac{E_0}{\omega} \frac{\sin \eta_r - \sin \eta_i}{\eta_r - \eta_i} + p_{yi} + \delta p_{yi}^C - \epsilon \frac{E_0}{\omega} \cos \eta_i \right)(t_r - t_i) \\
&\approx \left(p_{yi} + \delta p_{yi}^C - \epsilon \frac{E_0}{\omega} \cos \eta_i + \right)(t_r - t_i) = -\delta p_{yr}^C (t_r - t_i) \tag{5.79} \\
z_r &= (\bar{p}_{zd} + \delta p_{zi}^C)(t_r - t_i),
\end{aligned}
$$
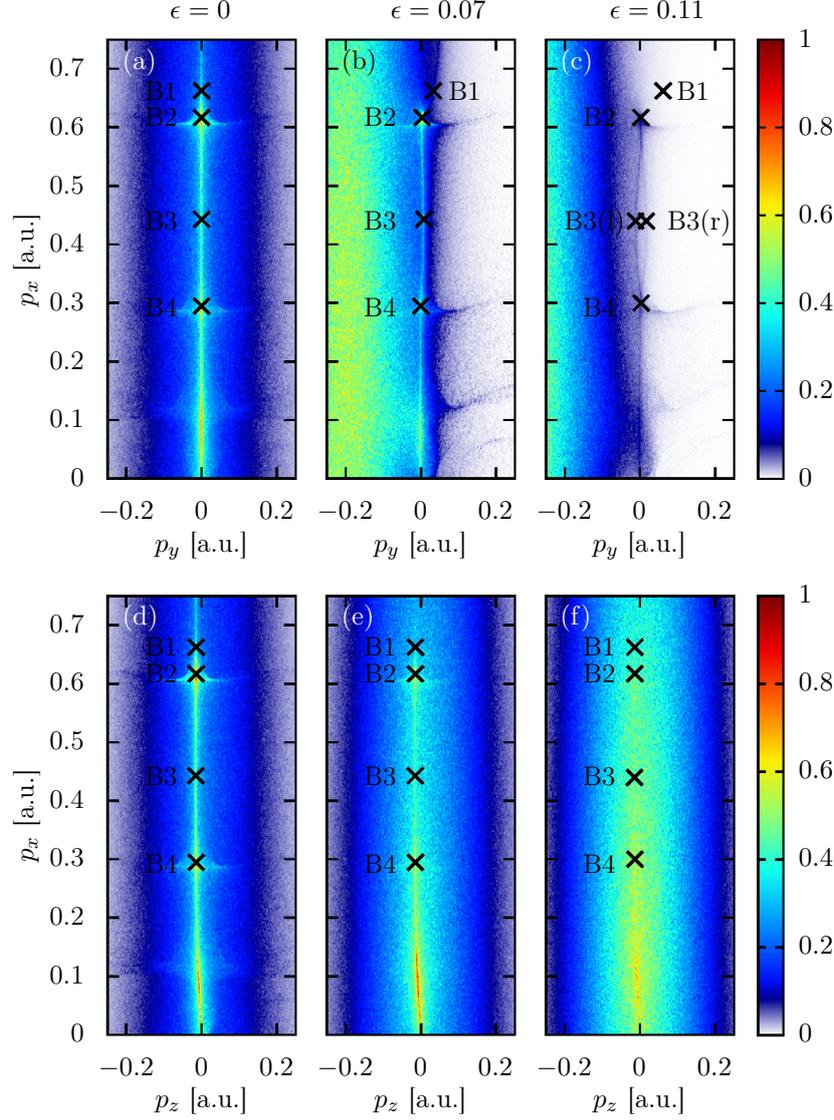
Figure 5.10: Comparison of PMD projections obtained by nondipole CTMC simulations with fixed CEP phase and ionization restricted only to the central half-cycle for different ellipticities: $\epsilon = 0$, $\epsilon = 0.07$ and $\epsilon = 0.11$ shown in the left, central and right column, respectively. The panels (a)-(c) show the projections along the p_z-axis and exhibit the same features as described in the dipole case of Fig. 5.3. The panels (d)-(f) show the the projections along p_y-axis and reveal the bend of the central cusp towards the negative p_z momentum. The panel (f) shows suppression of the vertical cusp due to ellipticity which can be identified up to the point B4, only anticipated between B4 and B2 and is not visible above B2.

where $\overline{p}_{zd} \equiv \frac{1}{2c} \int_{\eta_i}^{\eta_r} \left[\mathbf{A}(\eta') - \mathbf{A}(\eta_i) \right]^2 \frac{d\eta'}{\omega} + \frac{1}{c} \int_{\eta_i}^{\eta_r} \mathbf{p}_i \cdot \left[\mathbf{A}(\eta') - \mathbf{A}(\eta_i) \right] \frac{d\eta'}{\omega}$. In the second line we have taken into account the condition for the ridge electron from Eq. (5.54), as well as neglected the fist term in the brackets. This is well justified for slow recollisions, where
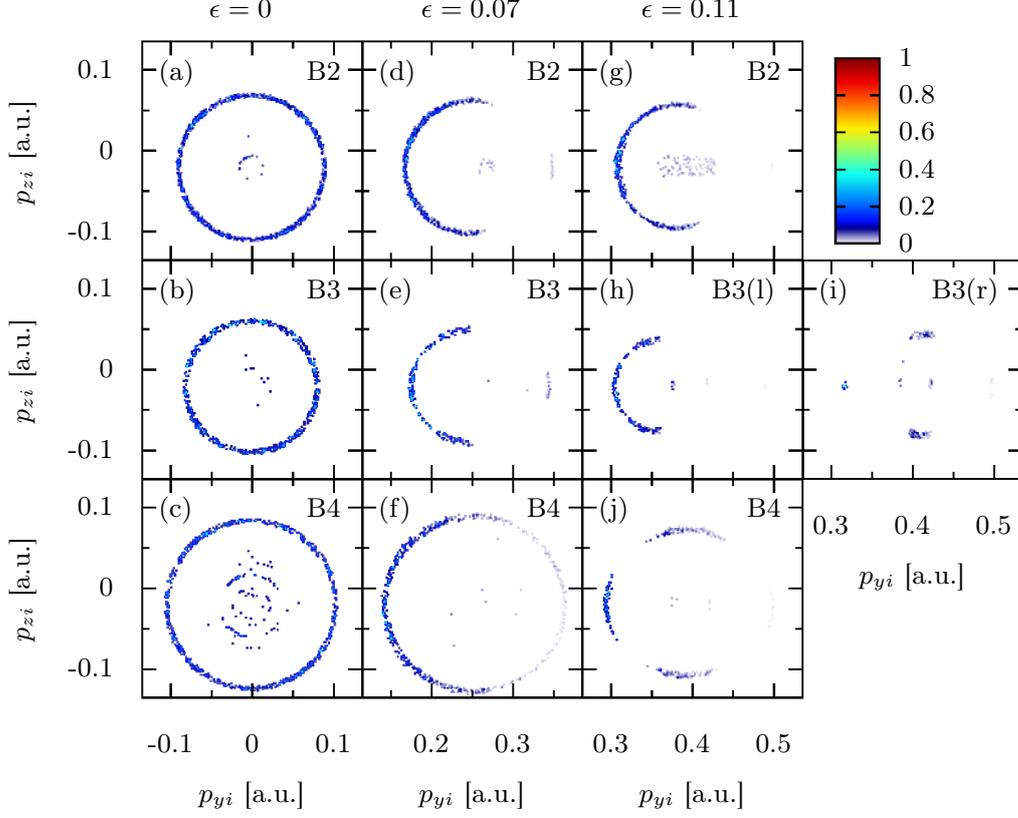
Figure 5.11: The initial momentum space distribution for trajectories ending in the momentum bins of $0.01 \times 0.01 \times 0.01$ dimensions at the asymptotic values of longitudinal momentum p_x: (a) 0.62, (b) 0.44 and (c) 0.3 $a.u.$, corresponding to the points B2, B3, B4 of Fig. 5.3, respectively. In contrast to the Fig. 5.4, we have taken into account also the nondipole effects causing the shift of the ionization regions to the negative p_{zi} momenta in correspondence with the prediction of the Eq. 5.82.

the term vanishes due to the slow recollision condition $p_{xr} \approx 0$ [i.e., at $\sin \eta_r \approx \sin \eta_i$, see Eq. (5.4)]. It is also reasonable for other recollisions, since the term will be small due to the relatively large $\eta_r - \eta_i$. As a consequence, we can conclude from the second expression of Eq. (5.78) that in the case of $p_{zi} = 0$,

$$\delta p_{zr}^C \approx -\overline{p}_{zd} - \delta p_{zi}^C, \tag{5.80}$$

and from Eq. (5.76) the z-component of the final momentum of the ridge electrons is

$$p_{zf} \approx -\overline{p}_{zd} + p_{zd}^{(i)}. \tag{5.81}$$

Furthermore, let us consider another electron in the initial momentum distribution ring, namely, with the initial vanishing momentum y-component ($p_{yi} = 0, p_{zi}$) marked as either P_T or P_B in Fig. 5.4(f). As it belongs to the sharp ridge with the same final momentum as in Eq. (5.81), we can use Eqs. (5.76) and (5.81) to find z-component of its initial

momentum:

$$p_{zi} = -\overline{p}_{zd} - \delta p_{rz}^C - \delta p_{iz}^C, \tag{5.82}$$

while in the dipole limit it is $p_{zi} = -\delta p_{rz}^C - \delta p_{iz}^C$, i.e., the nondipole effects shift the initial distribution ring for the sharp ridge electrons by $-\overline{p}_{zd}$ in the z-direction regardless of the ellipticity as long as we keep the peak intensity of the laser field constant. Let us stress that the latter is not completely true and holds only for small values of the ellipticity since it explicitly appears in the drift term $-\overline{p}_{zd}$ as terms is proportional to ϵ^2.

Ellipticity-dependent offset

Let us now concentrate on the ellipticity dependent peak offset of p_z momentum as presented at the beginning of this chapter in Fig. 5.2.

At larger ellipticities, when the sharp ridge disappears, the recollision effects are negligible leading to the conclusion that the final electron momentum component along the laser propagation direction is positive and determined by the nondipole drift momentum of free electrons given in Eq. 5.49 manifesting quantitative agreement with the estimation from Eq. 5.50.

At vanishing ellipticities, most of the electrons get rescattered and create the central bend cusp. Therefore, it is no surprise that the measured offset is negative and qualitatively corresponds to the estimate in Eq. 5.48. Nevertheless, the estimated absolute value of the offset is greater than the one obtained by the experiment. This is for several reasons: firstly, the estimated peak offset is for one particular value of the longitudinal momenta, but instead we have to average the whole bend cusp over all longitudinal momenta in order to reproduce the experiment; secondly, the our estimation does not take into account the effects of a long laser pulse and varying CEP phase. Because of the latter, we have performed CTMC simulations with ionization extended to the whole laser pulse and with randomly varying CEP phase for several values of the ellipticity and plotted the results in Fig. 5.2 using blue stars. The values were obtained from the projections of the PMDs onto the single p_z momentum by fitting with the Gaussian distribution.

Qualitatively the CTMC simulations reproduce the experimentally observed trend of the peak position as a function of the ellipticity and achieve better agreement at vanishing ellipticities than our simple estimate. The remaining discrepancy between the simulations and experiment can be explained by focal volume averaging, which is not included in our simulations.

So far, we have not discussed the most intriguing feature of Fig. 5.2: the transition from negative to positive peak offsets. As we have already shown, the positive offset can be attributed to the direct type A electrons without rescattering and the negative offset to the rescattered type B electrons. We have also shown in Sec. 5.2 that the ellipticity introduces a non-zero drift along the negative direction of the minor polarization axis. This drift has to be compensated by modification of initial transversal momentum p_{yi}, otherwise the electrons will not be Coulomb focused via multiple recollisions to the central line-shaped cusp. With increasing ellipticity, the correction to the initial momentum has to increase meaning that the weight of such trajectories in the tunneled

wave packet decreases exponentially with this correction and at some point such large initial transversal momenta are not available and the central structure of the rescattered electron disappears along with negative final momenta p_{zf}.

We estimated the condition for the existence of the sharp ridge in Eq. 5.58 as $\epsilon \approx 0.07$ being in the middle of the constant part of the peak offset. The latter shows that the width of the tunneled wave packet $\Delta_\perp$ was underestimated as the offset exhibits the transition at $\epsilon \approx 0.12$ in Fig. 5.2. This means that the structure of rescattered electrons disappears for $\epsilon \gtrsim 0.12$. This ellipticity can be used to determine the width of the initial wave packet from the this ellipticity-dependent momentum displacement $\Delta_\perp = \Delta p_y \approx \epsilon E_0/\omega \approx 0.37$ a.u. This value is slightly larger than one expected from tunnel ionization theory, $\Delta_\perp^{PPT} = 0.30$ a.u. However, we cannot expect an exact prediction of this threshold since the CTMC calculations based on tunnel ionization theory also predict a smaller final PMD due to a narrower initial momentum spread, which could be attributed to multielectron effects on the ionization of Xenon atoms [196]. As the spread of the wave packet $\Delta_\perp^{PPT} \propto I_p^{-1/4}$, there is only a weak dependence of the transition on the atomic species (see appendix B in [142]).

In order to illustrate the roles of the ellipticity and of the drift induced by the nondipole effects, we have plotted the modifications of the tunneled wave packed due to the Coulomb interaction in Fig. 5.12 for several ellipticities. For the sake of clarity, we plotted only slices of constant longitudinal momenta corresponding to the point B2. The panels (a), (c) and (e) show the initial transversal momentum distributions at the tunnel exit at a particular ionization phase u_i for various values of the ellipticity $\epsilon = 0$, 0.07 and 0.11, respectively. These initial momentum distributions will modified during the evolution of the tunneled wave packet in the combined laser and Coulomb field and end with asymptotic longitudinal momentum $p_x = -A_x(u_i)$ (in the case of our figure $p_x \approx 0.6$). In panels (b), (d), and (c), we plotted the asymptotic form of the initial distributions from panels (a), (c) and (e), respectively. The highlighted parts in (a), (c) and (e) undergo rescatterings and contribute to the highlighted cusps at the vanishing momenta in the panels (b), (d) and (f). This cusp corresponds to the line-shape central structure and is shifted along negative p_z-axis in correspondence to the results discussed in this section. With increasing ellipticity the highlighted area of rescattered electrons slips down from the peak of the distribution along the p_{yi}-axis leading to suppression of the central cusp in the right panels. This explains the fading of the central cusp with increasing ellipticity and hence the transition to positive peak offsets for p_z as the number of back-rescattered electrons decreases. In the panels (d) and (f) we can also identify the side lobes of direct electrons with positive p_z being the dominant part of the distributions. Let us also point out that the borders of the highlighted areas in panels (a), (c) and (e) correspond to the shifted circle-like structures from Fig. 5.11(a), (d) and (g). This also means that the radius of the highlighted area equals to the total Coulomb momentum transfer.

As we know already, the Coulomb focusing can compensate for a momentum drift introduced to the tunneled electrons ensuring that the total Coulomb momentum transfer remains unchanged as long as the introduced distortion does not change the underlying trajectories significantly.

From the experimental results in Fig. 5.1 we can see that the ellipticity transforms
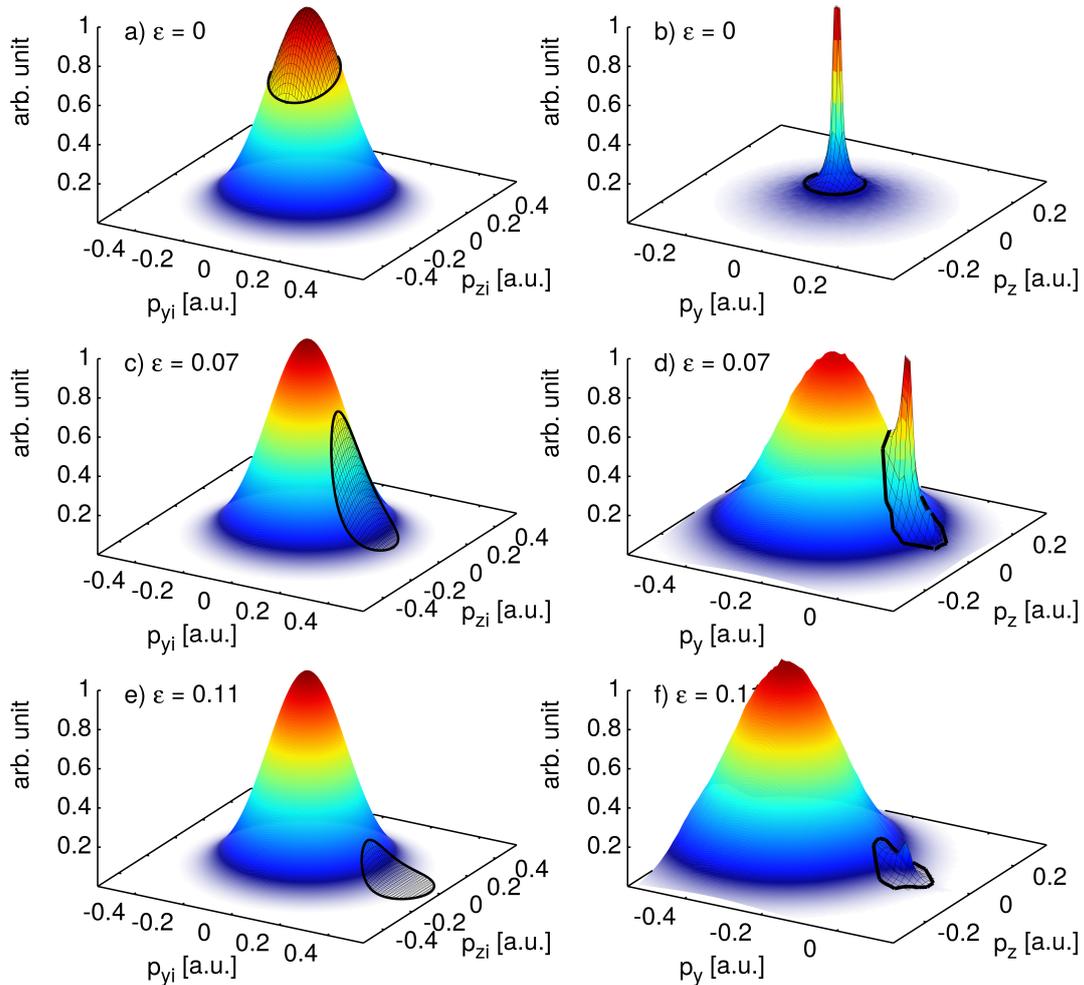
Figure 5.12: We show a slice at $p_{xi} \approx 0.63$ of the initial wave packet at the tunnel exit in the panels (a), (c) and (d) for ellipticities $\epsilon = 0$, $\epsilon = 0.07$ and $\epsilon = 0.11$, respectively. Then the wave packet evolves in the combined laser and Coulomb fields and the final distributions are shown in the right panels (b), (d), (e). Note the shift of the maxima towards the negative p_y momenta responsible for the side lobes and also the highlighted central cusp structure at vanishing p_y momentum. The electrons from the highlighted areas in the right panels are Coulomb focused and originate only in the highlighted areas in the left panels and nowhere else. As the ellipticity increases, the highlighted area slips from the distribution demonstrating the suppression mechanism due to the inability of the tunneled electrons to compensate for the drift induced by the ellipticity. Moreover, the disks in (a), (c) and (d) are shifted towards negative p_z momentum as well as the cusps in (b), (d) and (e) due to the nondipole effects. On the other hand, the direct electrons from the side lobes have positive p_z and the competition between these two electron types leads to the observed dependency from Fig. 5.2.

the single cigar-shaped PMD in panel (a) into the PMD with two lobes. There is a clear transition when the two lobes start to separate between the panels (b) and (c) corresponding to an ellipticity between 0.03 and 0.07. Therefore, let us assume that this

ellipticity introduces such a momentum drift $p_{yf} \approx \epsilon E_0/\omega$ that cannot be compensated any longer by the Coulomb focusing given by the Coulomb momentum transfer δp_y^C. The assumption that $\delta p_y^C \approx p_{yf}$ leads to the estimate of the averaged Coulomb momentum transfer $\delta p_y^C \approx 0.09 - 0.22$, which is in agreement with the radii of the circles in Fig. 5.11 and hence opens the possibility for measurement of the Coulomb momentum transfer in the experiment.

Let us note that this assumption actually describes the situation when the edge of the disk in the left panels in Fig. 5.12 touches the maximum of the distribution. The disk slips from the top of the distribution when the ellipticity (and therefore the induced drift) increases further. The drift cannot then be compensated for and the electrons at the maximum become effectively direct type A electrons and the separated lobes with final positive momentum p_z appear in the PMD.

Once the disk slips off the distribution completely, the cusp structure of type B electron disappears and the the standard PMD with two spatially separated lobes is restored in momentum space.

5.4 Summary

In this chapter we addressed the two newly observed features in the PMD of elliptically polarized laser fields: the central cusp structure and the transition of the negative peak offset of p_z momentum to positive values with increasing ellipticity. The first feature was linked to the rescattered type B electrons and identified as the exclusive feature of the introduced small ellipticity. We thoroughly investigated the underlying trajectories and exposed similarities to the case of linear polarization. We explored the latter in a thorough investigation of the form of the central structure in the center and in finding the limits on its existence. Moreover, we presented a method how to measure the averaged Coulomb momentum transfer which we linked to the ellipticity, when the two lobes in the PMD start to separate and achieved agreement with the results of the CTMC simulations. The second feature was link to nondipole effects and to the fraction of the rescattered versus direct electrons, as the Coulomb focused type B electrons end on the cusp with negative p_z momentum and the direct electrons on the lobes of direct type A electrons with positive p_z. We found that the ratio is driven by the ellipticity and the transition can be used to investigate the width of the tunneled wave packet. As an application, we reveled discrepancy between an ionization theory prediction for Xe and experimental results, which we attributed to the multielectron effects.

Chapter 6

Photoelectron holography

The strong-field photoelectron holography has gained a lot of attention in the last two decades which can be contributed to the rapid development of stable high-intensity sources of laser light. The standard holography [197] is based on interference of two light beams which can be created from a single beam of coherent light. The first beam is led to scatter of a target and hence carries information about the spatial structure of the target. On the other hand, the second beam stays untouched and serves as a reference. Then, the interference pattern created by these two beams also encodes the structural and temporal information about the target.

The strong-field holography does not rely on light beams but rather on an ionized electron wave packet which starts at the tunnel exit, evolves in the combined laser and Coulomb field afterwards and ends at the detector finally. The detected interference pattern exhibits a spider-like structure and encodes all the dynamics of the tunneled wave packet influenced by the long range Coulomb force of the parent ion on the tunneled electron driven by the oscillatory laser field [146, 147]. Although the dynamics is not trivial, we can illustrate the origin of the interference pattern as a two path interference in Fig. 6.1. One part of the tunneled wave packet with large initial transversal momentum is nearly uninfluenced by the Coulomb field (blue trajectory), but the part of the wave packet with small initial transversal momentum (red trajectory) rescatters at one recollision point (yellow star) and receives a large momentum transfer leading to the agreement of the final momenta for both trajectories. This makes the trajectories indistinguishable and leads to the creation of the interference pattern due to different accumulated phases. We point out that the interference pattern contains the information about both the target and the rescattered electron.

The main advantage of the strong-field holography is the fact that the recollision time $t_r(t_i)$ depends on the ionization time t_i, which also uniquely determines the final longitudinal momentum (as discussed in Chap. 2). This mechanism opens the possibility for time-resolved spectroscopy of atoms or molecules. With mid-IR laser pulses one can achieve femtosecond resolutions for the ions and attosecond resolutions for the electron dynamics [146, 147]. Moreover, the mid-IR wavelengths are rather long and can accelerate the photoelectrons to velocities such that their de Broglie wavelength becomes comparable to the interatomic distances in molecules and hence makes the investigation of molecular dynamics possible.

The crucial aspects in the holography are: the restriction of the Coulomb interaction to well defined rescattering points, which can be achieved by the amplitude of the quiver motion being larger than the size of an atom (i.e., $E_0/\omega^2 \gg 1\text{Å}$), and the averaged
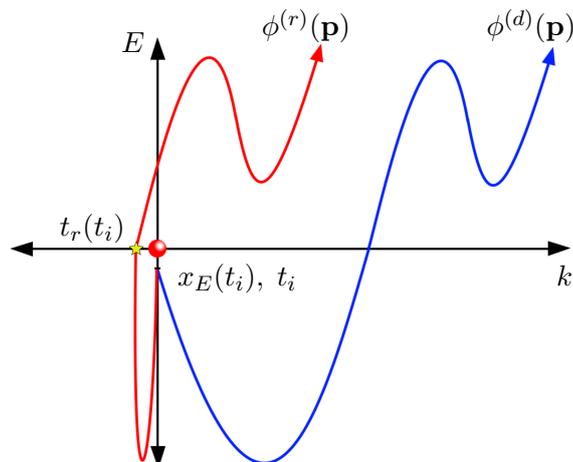
Figure 6.1: Illustration of the two path interference in the strong-field ionization hologra-
phy. The wave packet appears at the tunnel exit $x_e(t_i)$ in the time t_i and can be divided into
two parts: the direct part with large initial transversal momentum (blue trajectory) and the
rescattered part with small initial transversal momentum (red trajectory). The influence of
the atomic core (red point) on the blue path is negligible and therefore we can use it as the
reference signal. On the other hand, the Coulomb interaction leads to severe distortion of
the red path at the recollision point (yellow star) at the recollision time $t_r(t_i)$, which leads
to the same value of the final momenta $\mathbf{p}$. This leads to interference due t the difference of
the accumulated phases $\phi^{(d)}(\mathbf{p}) - \phi^{(r)}(\mathbf{p})$.

ponderomotive energy of the electron in the oscillating laser field being much larger
then the energy of the individual photons (i.e., $U_p = \frac{E_0^2 \lambda^2}{16\pi^2 c^2} \gg \hbar\omega$) so the photolectrons
behave classically. Both of these conditions are easier to satisfy with mid-IR laser pulses
than with shorter wavelengths which would require as a compensation high-intense lasers
leading to experimental and physical complications.

This chapter is based on [183] and addresses the strong-field photoelectron holography
theoretically in the nondipole regime induced by the mid-IR laser field. We are going
to apply three approaches for our investigation: the Strong-field approximation (SFA),
the Coulomb-corrected Strong-field approximation (CCSFA), and the Quantum trajec-
tory Monte Carlo (QTMC) simulation. Moreover, we will discuss the role of multi-path
interference within the frame of the CCSFA and the role of the ionization target (e.g.,
species, multi-electron effects or polarizability) on the interference pattern within the
frame of QTMC simulation. The results of the latter will be used to simulate the photo-
electron momentum distribution (PMD) for an atom of Xe and for an diatomic molecule
of O_2, which will be compared. Finally, we will discuss the scaling of the characteristic
interference features with parameters of the laser field.

6.1 The general setup

For simplicity, we consider ionization of a xenon atom in a strong linearly polarized laser
pulse. The xenon atom is in the ground state with the ionization potential $I_p = 12.13$
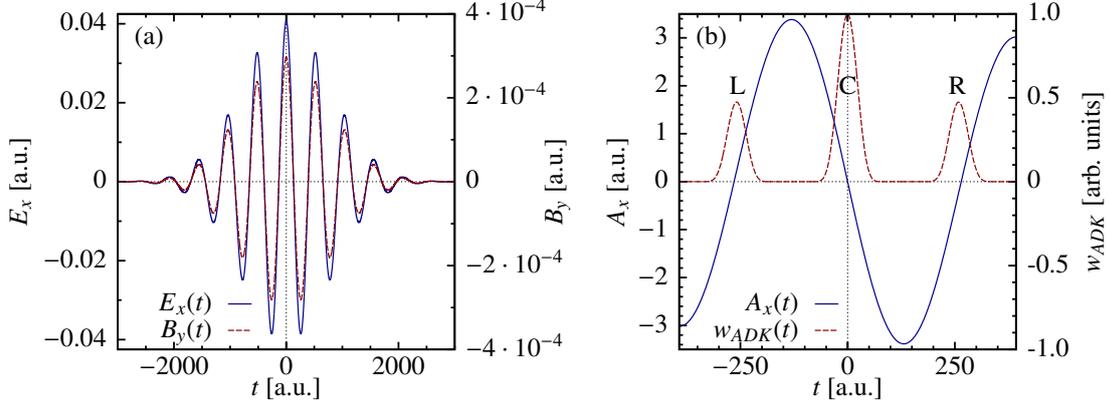
Figure 6.2: (a) The fields of the laser pulse; (b) The ionization rate in the laser pulse according to the Perelomov-Popov-Terent'ev (PPT) theory [25,30]. The ionization peaks in (b) correspond to the three half-cycles of the laser field in(a). We distinguish the ionization regions as right (R), central (C) and left (L).

eV ($I_p = \kappa^2/2$, with the bound state momentum $\kappa = 0.9435$ a.u.). The peak intensity of the laser pulse is $I = 5.8 \cdot 10^{13}$ W/cm^2 (the laser field amplitude is $E_0 = 0.0407$ a.u.), the wavelength $\lambda = 3.4$ μm (the angular frequency $\omega = 0.013$ a.u.). The short laser pulse is defined by its vector potential

$$\mathbf{A}(t) = \mathbf{e}_E \frac{E_0}{\omega} \sin(\omega t) \exp\left[-(t/\tau)^2/2\right], \tag{6.1}$$

with $\tau = 3\pi/\omega$, and the unit vector in the laser polarization direction $\mathbf{e}_E$, see Fig. 6.2 (the indices E and k at the vectors indicate the vector component along the laser field and the laser propagation direction, respectively). The ionization is in the tunneling regime as the Keldysh parameter [1] is small $\gamma \equiv \kappa\omega/E_0 \approx 0.28$. The tunneling dynamics is non-relativistic because $\kappa/c \approx 0.007$, with the speed of light c. The electron dynamics in the continuum after the tunneling is described by the relativistic field parameter $\xi \equiv E_0/c\omega \approx 0.025$, which is small but not negligible, indicating the weakly relativistic regime for the continuum motion. In this regime the magnetic field effect in the continuum dynamics is non-negligible, but next to the leading order relativistic corrections such as the mass shift can be neglected. As Fig. 6.2(b) shows, the ionization mostly takes place in the three half-cycles around the peak of the laser pulse.

The holographic picture of photoelectron momentum distribution, which is known to show spider-like structures [146, 147], is due to interference of two (or many) electron paths yielding the same final momentum. One of the paths is the direct trajectory without rescattering, other paths include rescatterings.

In the simple-man model the electron's final momentum is determined by the vector potential at the ionization time $p_E = -A(t_i)$. Therefore, one can deduce from Fig. 6.2(b) that for the photoelectron final momentum $p_E > 0$, the contributing trajectories are: the direct trajectory from the left (L-half-cycle) and right half-cycles (R-half-cycle) adjacent to the peak with the laser field $E < 0$, as well as the recolliding trajectories (the ionization
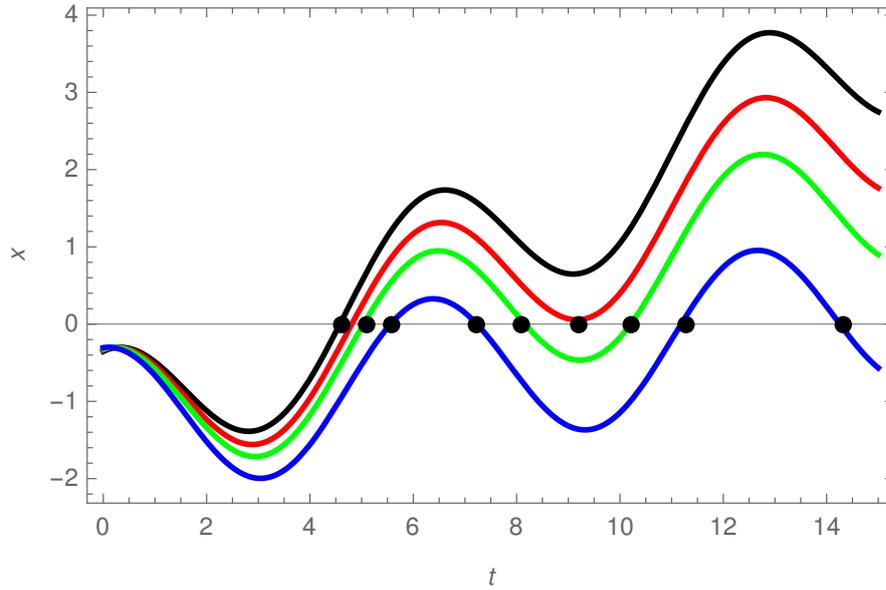
Figure 6.3: Examples of recolliding trajectories: the trajectory with a single return to the atomic core exists for $0.2E_0/\omega < |p_E| < E_0/\omega$ (black); the second and third returns exists for trajectories up to $0.1E_0/\omega < |p_E| < 0.2E_0/\omega \sim 0.7$ a.u. (green), the trajectories with four returns exists at $|p_E| < 0.1E_0/\omega$ (blue) and so on (the recollision points are indicated by dots). The role of the recollision is enhanced for the specific trajectory (red) when the longitudinal velocity vanishes at the recollision point.

time after the peak of the electric field) from the central half-cycle (C-half-cycle) $E > 0$. At $p_E < 0$, the contributing trajectories are: the direct trajectory from the C-half-cycle with $E > 0$, as well as the recolliding trajectories from the L-half-cycle and R-half-cycle with $E < 0$. Later we will see that the interference due to direct trajectories induces a horizontal interference structures, while the main holographic spider-like structure are due to the interference of recolliding trajectories. The number of recollisions depends on the ionization time or the final longitudinal momentum p_E of the electron, see Fig. 6.3. Along the trajectories that contribute to the holographic structure, the ionized electron may forward scatter by the atomic core at a recollision. At some recollisions the forward scattering could be negligible.

6.2 Quantum description via perturbative SFA

In this section, we calculate photoelectron momentum distribution using the perturbative Strong-field Approximation (SFA) [1–3], when the rescattering, i.e., the interaction of the electrons in the continuum with the atomic core, is treated as a perturbation. Rather than fully relativistic SFA [184], we use the nondipole SFA [131,198], when the relativistic Hamiltonian is expanded up to terms of the order of $1/c$. The Volkov wave function in

the nondipole case reads:

$$\Psi_V = \exp\left\{i\left[\mathbf{p} + \mathbf{A}(t) + \mathbf{T}(\mathbf{p}, t)\right] \cdot \mathbf{r} + iS_L(t)\right\}, \tag{6.2}$$

where

$$\mathbf{T}(\mathbf{p}, t) = \frac{\mathbf{e}_k}{c}\left[\mathbf{p} \cdot \mathbf{A}(t) + \mathbf{A}^2(t)/2\right] \tag{6.3}$$

is the magnetic dipole term describing the electron drift in the laser propagation direction, $\mathbf{e}_k$ is the unit vector in the laser propagation direction, and

$$S_L(t) = \int_t^\infty dt' \frac{[\mathbf{p} + \mathbf{T}(\mathbf{p}, t') + \mathbf{A}(t')]^2}{2}, \tag{6.4}$$

is the electron action in the laser field including first order laser magnetic field effects (atomic units are used throughout).

The unperturbed ionization amplitude with a given value of the electron's final momentum describes the direct electrons, i.e., electrons that do not scatter by the atomic core after ionization [187]:

$$M_{\mathbf{p}}^{(d)} = -\int dt \langle \mathbf{p} + \mathbf{A}(t)|Q_C \mathbf{r} \cdot \mathbf{E}(t)|\phi_0(t)\rangle \exp\left[-iS_L(t)\right], \tag{6.5}$$

where $Q_C = -4I_p/\mathbf{r} \cdot \mathbf{E}(t)$ is the Coulomb correction factor for tunneling as discussed in Sec. 1.2, $\langle \mathbf{r}|\phi_0(t)\rangle = \phi_0(\mathbf{r})\exp(I_p t)$ is the atomic bound state, $\mathbf{E} = -\partial_t \mathbf{A}$ is the laser field. The laser field $\mathbf{E}$ is described by the scalar and vector potentials in the Göppert-Mayer gauge [199]: $\mathbf{A} = -\mathbf{e}_k(\mathbf{r} \cdot \mathbf{E})/c$ and $\varphi = -\mathbf{r} \cdot \mathbf{E}$, respectively.

The second-order SFA amplitude describes the ionization path which includes a recollision [131]:

$$
\begin{aligned}
M_{\mathbf{p}}^{(r)} &= -\int dt \int dt' \int d^3\mathbf{q} \\
&\times \langle \mathbf{p} + \mathbf{A}(t) + \mathbf{T}(\mathbf{p}, t)|V_a|\mathbf{q} + \mathbf{A}(t) + \mathbf{T}(\mathbf{q}, t)\rangle \\
&\times \langle \mathbf{q} + \mathbf{A}(t')|Q_C \mathbf{r} \cdot \mathbf{E}(t')|\phi_0(t')\rangle \exp\left(-iS_L^{(r)}(t, t')\right),
\end{aligned}
\tag{6.6}
$$

where $V_a = -\exp(-\lambda r)/r$ is the potential of the atomic core with the screening parameter λ, $\mathbf{q}$ is the intermediate momentum, and

$$S_L^{(r)}(t, t') = \int_{t'}^t dt'' \frac{[\mathbf{p} + \mathbf{T}(\mathbf{p}, t'') + \mathbf{A}(t'')]^2}{2}, \tag{6.7}$$

is the action of the recolliding electron. The integrals in Eqs. (6.5),(6.6) are calculated via the saddle point method and the momentum distribution of photoelectrons is derived by

$$|M_{\mathbf{p}}|^2 = \left|M_{\mathbf{p}}^{(d)} + M_{\mathbf{p}}^{(r)}\right|^2. \tag{6.8}$$

The recolliding trajectories can be ordered by the time distance between ionization and recollision. For the spider-like structure the short trajectories (the time distance between
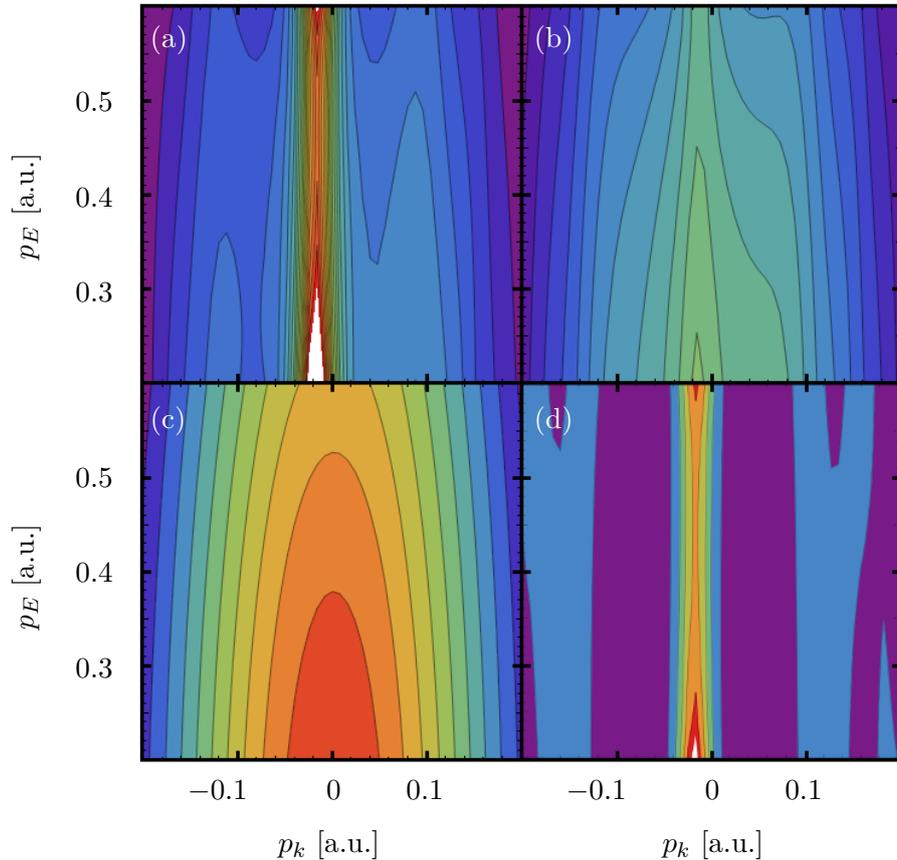
Figure 6.4: The photoelectron momentum distribution via second-order SFA ($\lambda = 0.0224$ a.u.): (a) calculation including four trajectories indicated in the text ; (b) calculation including two trajectories, without rescattering and with rescattering at the third return to the atomic core; (c) calculation including only the trajectory without rescattering; (d) the difference $|M_{\mathbf{p}}|^2 - |M_{\mathbf{p}}^{(d)}|^2$.

the ionization and recollision is less than half of a laser period) are responsible, while long ones lead to horizontal interference patterns. The photoelectron returns once to the atomic core if $0.2E_0/\omega < |p_E| < E_0/\omega \approx 3.1$, three times if $0.1E_0/\omega < |p_E| < 0.2E_0/\omega \approx 0.6$ and even more often for lower values of the longitudinal momentum, see Fig. 6.3.

In the second-order perturbative SFA, it is assumed that the ionized electron is either not scattered by the atomic core, or it scatters once at one of the recollision points. When there are many recollision points, the forward scattering can take place at any of them. The photoelectron spectrum calculated using the four trajectories is displayed in Fig. 6.4(a). Three of the four trajectories differ with location of the significant rescattering taking place at the first, the second or the third revisit of the ionized electron. Interference features (two wings) can be seen in the momentum distribution. This can
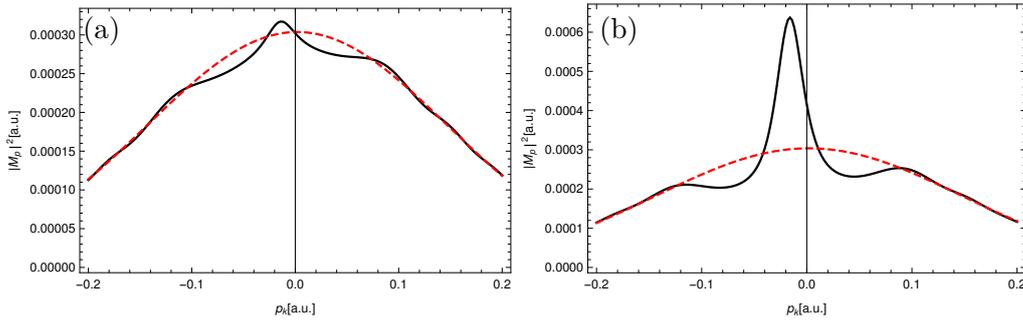
Figure 6.5: The photoelectron distribution over the transverse momentum via second-order SFA at $p_E = 0.5$ a.u. ($\lambda = 0.0224$ a.u.): (a) calculation using two trajectories (without rescattering and with rescattering at the third recollision) (solid) and only due to the trajectory without rescattering (dashed); (b) calculation using all four trajectories (solid) and only due to the trajectory without rescattering (dashed).

be displayed on the cut over the spectral distribution, e.g., at $p_E = 0.5$ a.u. which is shown in Fig. 6.5. It can be seen that the interference structure is shifted against the laser propagation direction and that the right wing is more dominant than the left wing. Moreover, the main features of the interference structure are already exhibited when one takes into account only two trajectories, one without rescattering and the second with a forward scattering at the third return, see Fig. 6.4(b). Fig. 6.4(c) shows the symmetric final momentum distribution of the unscattered electrons and is carried out by the red dashed lines in Figs. 6.5(a)-(b). In Fig. 6.5(d) we have plotted the difference between the distributions from Fig. 6.5(a) and Fig. 6.5(d). Note that the probability of the rescattering at the third return is enhanced due to the small recollision velocity [96, 105, 106], see the red trajectory in Fig. 6.3.

Thus, we can conclude that the interference structure arises already at the perturbative treatment of the recollisions. In the next section we will discuss how the features of the interference structure are modified when the Coulomb field of the atomic core is accurately accounted for during the continuum motion.

6.3 Description via the Coulomb-corrected SFA

In this section we analyze the role of the Coulomb field of the atomic core on the photo-electron momentum distribution. We apply the Coulomb-corrected strong-field approximation (CCSFA) similar to [32, 33] which will be explained in the following.

Rather than the Volkov wave function for the continuum electron, the CCSFA employs the electron wave function which takes into account the laser field and the Coulomb field of the atomic core in the eikonal approximation [28, 187] as discussed in the Sec. 1.2. Then, the ionization amplitude is expressed by a formula similar to Eq. (6.5), where one

has to replace the action by the Coulomb corrected one, $S_L \to S_L^{(C)}$:

$$S_L^{(C)}(t) = \int_t^\infty dt' \left\{ \frac{[\mathbf{p} + \mathbf{T}(\mathbf{p}, t') + \mathbf{A}(t')]^2}{2} + V_a(\mathbf{r}(t')) \right\},$$

(6.9)

where $\mathbf{r}(t)$ is the electron trajectory under the action of the laser and Coulomb field of the atomic core $V_a(r)$. The integration of the ionization amplitude from Eq. 6.6 is carried out by the saddle-point method, the photoelectron momentum distribution from Eq. 6.8 can be represented as follows

$$|M_\mathbf{p}|^2 \sim \left| \sum_s \frac{\Gamma(t_i^{(s)}, p_{k,i}^{(s)})}{[\partial_t^2 S_L^{(C)}(t_i^{(s)})]^{1/2}} \exp\left[i\mathcal{S}(t_i^{(s)}) \right] \right|^2,$$

(6.10)

where $\Gamma(t_i, p_{k,i}) = \exp\left[-(\kappa^2 + p_{k,i}^2)^{3/2}/3F_L(t_i) \right]$ is the Keldysh-tunneling exponent. The phase of the trajectory $\mathcal{S}(t)$ is determined by the classical action along the trajectory in the laser and the Coulomb fields. In the fully relativistic case it reads:

$$\mathcal{S}(t) = -\mathbf{p} \cdot \mathbf{r}(t_f) + \int_t^{t_f} dt' \left\{ \mathcal{L}(t') + (c^2 - I_p)t' - V_a(\mathbf{r}(t')) \right\},$$

(6.11)

where $\mathcal{L}$ is the Lagrangian of the electron in the laser field [173]:

$$\mathcal{L} = -c^2 \sqrt{1 - \frac{v^2}{c^2}} - \mathbf{A} \cdot \mathbf{v} + \varphi.$$

(6.12)

In the leading order relativistic corrections,

$$\mathbf{E}\left(t - \frac{\mathbf{e}_k \cdot \mathbf{r}}{c} \right) \approx \mathbf{E}(t) - \dot{\mathbf{E}}(t)\frac{\mathbf{e}_k \cdot \mathbf{r}}{c},$$

(6.13)

with dot denoting derivative with respect to time. Therefore, we can write in the order of $\mathcal{O}(1/c)$:

$$\begin{aligned}
\mathcal{S}(t) \approx & -\mathbf{p} \cdot \mathbf{r}(t_f) + I_p t + \int_t^{t_f} dt \left\{ \frac{\dot{\mathbf{r}}^2(t')}{2} - V_a(\mathbf{r}(t')) \right. \\
& \left. - \mathbf{r}(t') \cdot \left(\mathbf{E}(t') - \dot{\mathbf{E}}(t')\frac{\mathbf{e}_k \cdot \mathbf{r}(t')}{c} \right) \left(1 - \frac{\mathbf{e}_k \cdot \dot{\mathbf{r}}(t')}{c} \right) \right\}.
\end{aligned}$$

(6.14)

In Eq. (6.10) the summation is carried out over all possible trajectories of the electron in the laser and Coulomb fields that yield the given final momentum for the electron. The trajectories start at the ionization time $t_i = t_i(\mathbf{p})$ at the tunnel exit $\mathbf{r}_i = (I_p/F_L(t_i), 0)$ with the initial velocity $\dot{\mathbf{r}}(t_i) = (0, p_{k,i}(\mathbf{p}))$ and end up asymptotically at a given final momentum of the photoelectron $\mathbf{p} = (p_E, p_k)$. The trajectories are found solving classical Newton equations numerically. Taking into account that in the plane laser field the

magnetic field $\mathbf{B}$ is transverse to the electric field $\mathbf{E}$, $\mathbf{B} = (\mathbf{e}_k \times \mathbf{E})/c$, the Newton equations read

$$\frac{d\mathbf{p}}{dt} = -\mathbf{E}\left(1 - \frac{\mathbf{e}_k \cdot \mathbf{r}}{c}\right) - \frac{\mathbf{e}_k}{c}\left[\mathbf{v} \cdot \mathbf{E}\left(1 - \frac{\mathbf{e}_k \cdot \mathbf{r}}{c}\right)\right] + \mathbf{F}_a(\mathbf{r}). \tag{6.15}$$

where $\mathbf{F}_a(\mathbf{r}) = -\mathbf{r}/r^3$ is the Coulomb force of the atomic core. In the weakly relativistic regime using the expansion of Eq. (6.13), we have

$$\begin{aligned}\ddot{\mathbf{r}}(t) &= -\mathbf{E}(t)\left(1 - \frac{\mathbf{e}_k \cdot \dot{\mathbf{r}}(t)}{c}\right) - \mathbf{e}_k\left(\frac{\mathbf{E}(t) \cdot \dot{\mathbf{r}}(t)}{c}\right) \\ &+ \dot{\mathbf{E}}(t)\frac{\mathbf{e}_k \cdot \mathbf{r}(t)}{c} - \frac{\mathbf{r}(t)}{r^3(t)}.\end{aligned} \tag{6.16}$$

While the first two terms in the equation above are due to the electric and magnetic dipole interactions, the third term is due to the electric quadrupole interaction.

The trajectories are modified due to the Coulomb field. However, one can again apply the classification based on the number of recollisions. Whereas for $|p_E| > 0.5$ a.u. there are only two trajectories that fulfill the initial and final conditions: (i) the trajectory which has no significant rescattering; (ii) the trajectory with one significant rescattering at the single return to the atomic core, see Fig. 6.6(a). For smaller drift momenta there are four types of contributing trajectories ($|p_E| > 0.2$): one direct and three with one significant rescattering which takes place either at first return to the atomic core, or at the second, or at third, see Fig. 6.6(b). For momenta smaller than $|p_E| < 0.2$ the electron revisits the atomic core more than three times and multiple rescatterings are possible.

The photoelectron momentum distribution using CCSFA is shown in Fig. 6.7(a). In the calculation of these spectra we included the main two trajectories: the direct trajectory and the trajectory with a single rescattering, which takes place either at the single ($|p_E| > 0.5$ a.u.) or at the third return ($|p_E| < 0.5$ a.u.) to the atomic core. In the latter case the scattering probability is enhanced because of the low recollision velocity. We also separate the distribution into the regions with respect to the number of recollisions and hence also to the number of interfering electron paths. We separated the regions with respect to the number of recollisions, which also corresponds to the number of interfering paths. In the region of $1 + 1$, one direct and one rescattered trajectory exist as shown in the Fig. 6.6(a). The region $3 + 1$ corresponds to trajectories with three rescatterings which leads to four-path interference of one direct and three rescattered trajectories as illustrated in Fig. 6.6(b).

The role of other trajectories is clarified in Fig. 6.7(b) and (c), where the zoom in the photoelectron distribution is calculated using either the two main trajectories or all four available trajectories, respectively. The conclusion drawn from this comparison is that the momentum distribution becomes more smooth and the intensity of lobes gradually decreases with increasing p_E by tahing all trajectories into account. However, the main features of the interference structure are already given by the spectra based on two trajectories.

The photoelectron spectrum reveals interference structure with a middle lobe and with side wings, which have qualitatively already been expected from the non-relativistic
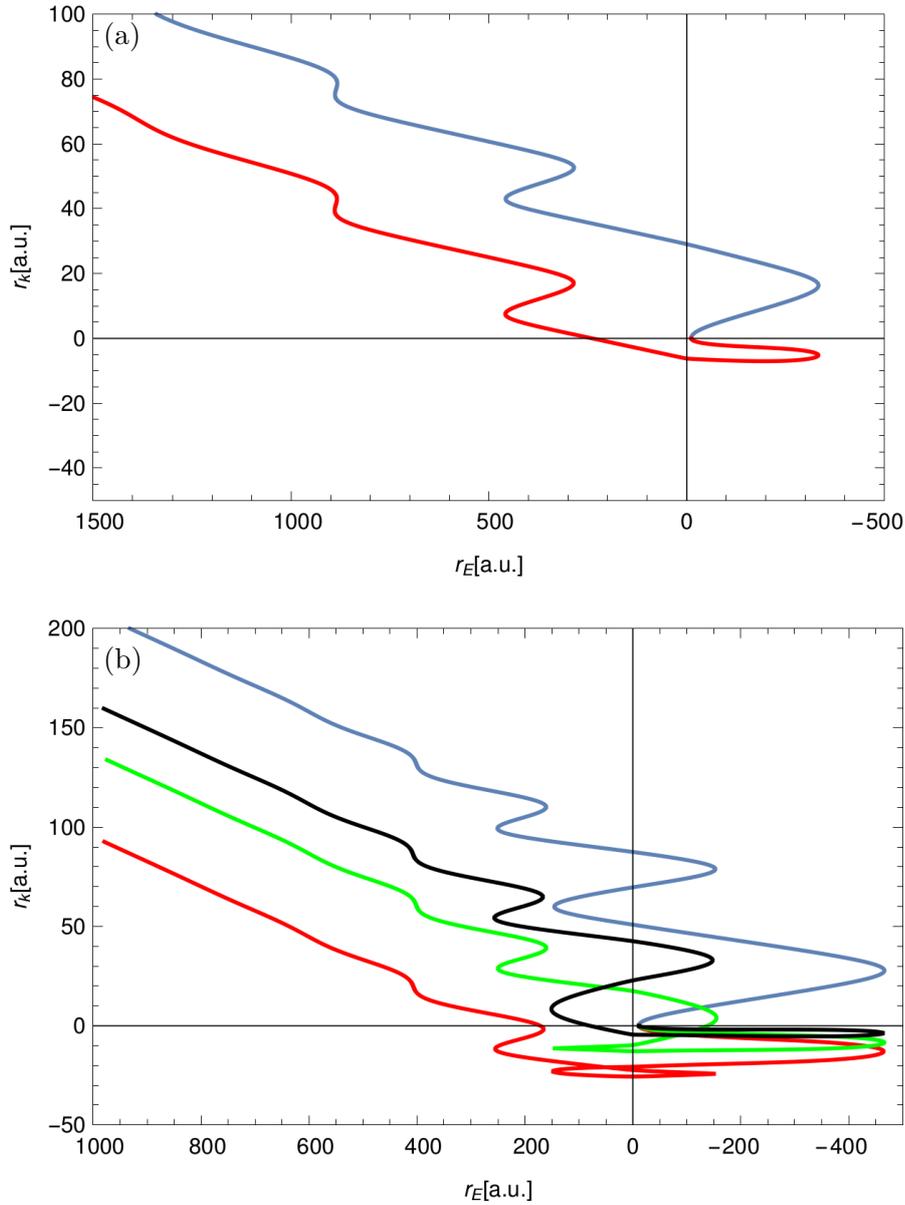
Figure 6.6: The trajectories used in CCSFA: (a) for $p_E = 1$ a.u. and $p_k = 0.05$ a.u. there are two trajectories, without significant rescattering (blue) and with one rescattering (red) at the single recollision; (b) for $p_E = 0.4$ a.u. and $p_k = 0.05$ a.u. there are four trajectories, without significant rescattering (blue), and with one rescattering at the first recollision (black), the second (green), and at the third (red). The last trajectory is the most significant rescattered trajectory.

regime [146]. A comparison with the perturbative result of Fig. 6.4 shows that the effect of the Coulomb field is to squeeze the interference structure in the transverse direction,
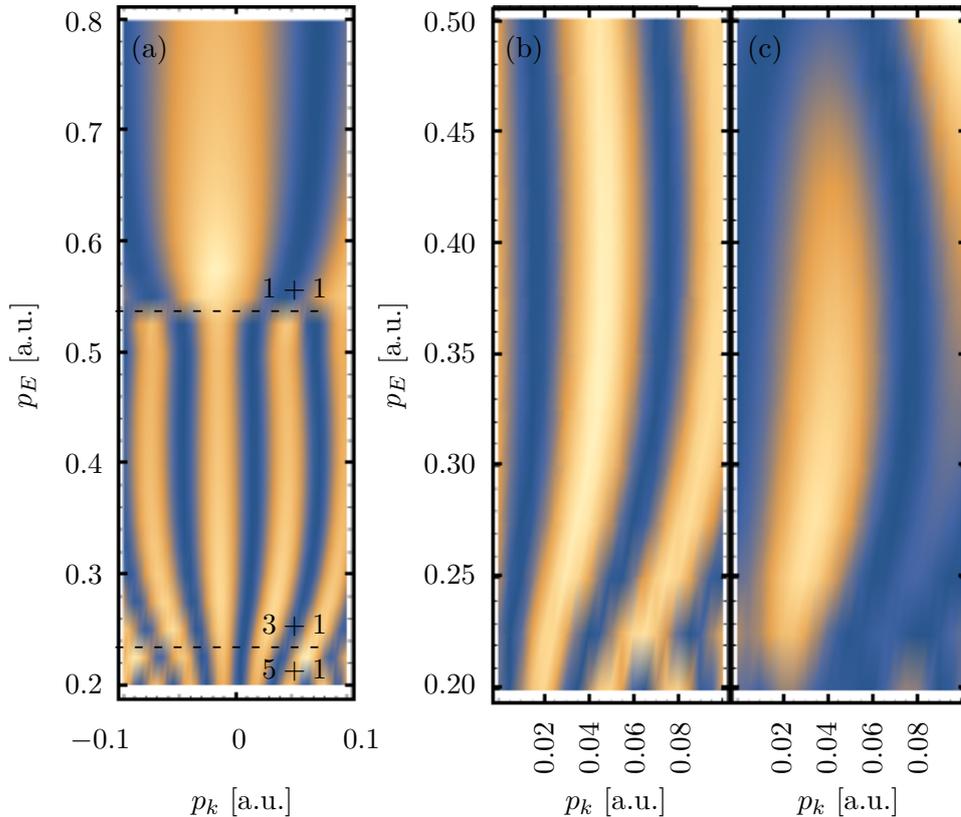
Figure 6.7: Photoelectron momentum distribution via CCSFA: (a) based on two trajectories: without significant rescattering and with the significant rescattering at the third return to the atomic core; (b) zoom of the panel (a); (c) based on four trajectories, one direct and three with one significant rescattering which takes place either at first return to the atomic core, or at the second, or at the third. We also denoted the regions in (a) with respect to possible number of interfering trajectories (as number of rescattered trajectories plus one direct), which corresponds to the number of recollisions via the longitudinal momentum p_E.

which is also known as Coulomb focusing [75, 93, 191]. Moreover, the visibility of the interference structure is significantly enhanced. The interference structure is shifted against the laser propagation direction. The right wing is slightly stronger than the left wing. The wings end at approximately $p_E \sim 0.56$ a.u..

The calculation in CCSFA including all trajectories is rather cumbersome for the full range of the momentum distribution. In the next section we provide Quantum-trajectory Monte-Carlo (QTMC) simulations which include all possible trajectories in the full range of the momentum distribution.

6.4 Quantum-trajectory Monte-Carlo simulation

In this section we describe the photoelectron momentum distribution using QTMC simulation [200], which includes all possible trajectories as well as takes into account the

Coulomb field of the atomic core for the continuum dynamics exactly. In our 3D QTMC simulation, the ionized electron wave packet is formed according to the PPT ionization rate [25, 30] and further propagates classically. In the tunneling regime $\gamma \ll 1$ at low frequencies ($\omega \ll I_p$), the semiclassical approach is justified because the photon energy is much less than the characteristic electron energies of the process I_p and U_p. The electrons are born with following conditions: along the laser polarization direction, the initial position $x_E = x_E(t_i)$ corresponds to the tunnel exit coordinate from the effective potential, the initial longitudinal velocity of the electron is vanishing, $v_{Ei} = 0$; the transverse coordinates are $y_i = 0$ and $z_i = 0$, and the transverse velocities $v_{ti} = v_{yi} = v_{\perp 0} \cos \phi$ and $v_{ki} = v_{zi} = v_{\perp 0} \sin \phi$, where ϕ is randomly distributed within the interval of $(0, 2\pi)$, and $v_{\perp 0}$ follows the PPT-distribution for the transverse momentum [25, 27]. The index t refers to the direction $\mathbf{e}_k \times \mathbf{e}_E$. The positions and momenta of electrons after the laser pulse are used to calculate the final asymptotic momenta [201] at the detector.

The QTMC simulation is based on the path-integral formulation of quantum mechanics and allows to include interference between different trajectories. A phase is attached to each trajectory according to Eq. (6.11). For QTMC we employed a fully relativistic representation of the phase:

$$
\begin{aligned}
\mathcal{S}(t) \;=\; & -\int_t^{t_f} \mathrm{d}t' \left\{ \varepsilon(t') - c^2 + I_p + \left[V_a(\mathbf{r}(t')) - \mathbf{r} \cdot \nabla V_a(\mathbf{r}(t')) \right] \right. \\
& \left. - \frac{\mathbf{e}_k \cdot \mathbf{r}(t')}{c} \mathbf{v}(t') \cdot \mathbf{E}\left(t' - \mathbf{e}_k \cdot \mathbf{r}(t')/c \right) \right\},
\end{aligned}
\tag{6.17}
$$

with the electron energy $\varepsilon(t)$. In Eq. (6.17) we have used the identity $\mathbf{p}(t_f) \cdot \mathbf{r}(t_f) - \mathbf{p}(t_i) \cdot \mathbf{r}(t_i) = \int_t^{t_f} \mathrm{d}t' \frac{\mathrm{d}}{\mathrm{d}t'} \mathbf{p}(t') \cdot \mathbf{r}(t')$, as well as the relativistic classical equations of motion from Eq. (6.15). Moreover, the term in the square brackets simplifies for the specific case of a Coulomb potential in the following manner:

$$
V_a(\mathbf{r}(t')) - \mathbf{r} \cdot \nabla V_a(\mathbf{r}(t')) = -\frac{2Z}{|\mathbf{r}|}.
\tag{6.18}
$$

The factor of two is important since it leads to a better agreement with the solutions of the time-dependent Schrödinger equation [162]. Once the laser pulse is gone, the position and momentum of the electron yield $\mathbf{r}(t_f)$ and $\mathbf{p}(t_f)$, respectively. It is possible to account for the Coulomb potential in the absence of the laser field and determine its asymptotic momentum at the detector via the Kepler analytic formula [202]:

$$
\mathbf{P} = |\mathbf{P}| \frac{|\mathbf{P}| (\mathbf{L} \times \mathbf{A}) - Z\mathbf{A}}{Z^2 + \mathbf{P}^2 \mathbf{L}^2},
\tag{6.19}
$$

where

$$
\begin{aligned}
\mathbf{P}^2 \;&=\; \mathbf{p}^2(t_f) - \frac{2Z}{|\mathbf{r}(t_f)|}, \\
\mathbf{A} \;&=\; \mathbf{p}(t_f) \times \mathbf{L} - \frac{Z}{|\mathbf{r}(t_f)|} \mathbf{r}(t_f), \\
\mathbf{L} \;&=\; \mathbf{r}(t_f) \times \mathbf{p}(t_f).
\end{aligned}
\tag{6.20}
$$

Here $\mathbf{P}^2/2$ corresponds to the conserved total energy of the electron at the the end of the laser pulse t_f, $\mathbf{A}$ is the Runge–Lenz vector and $\mathbf{L}$ is the angular momentum.

We also take into account the phase accumulated after the switch-off of the laser pulse at the time t_f and before detection [162] as

$$\Phi^C(t_f) = -\sqrt{b}\left[\ln g + \arcsin\left(\frac{\mathbf{r}(t_f)\cdot\mathbf{p}(t_f)}{g\sqrt{b}}\right)\right], \tag{6.21}$$

where $b \equiv 1/(\mathbf{P}^2)$ and $g \equiv \sqrt{1 + \mathbf{P}^2\mathbf{L}^2}$.

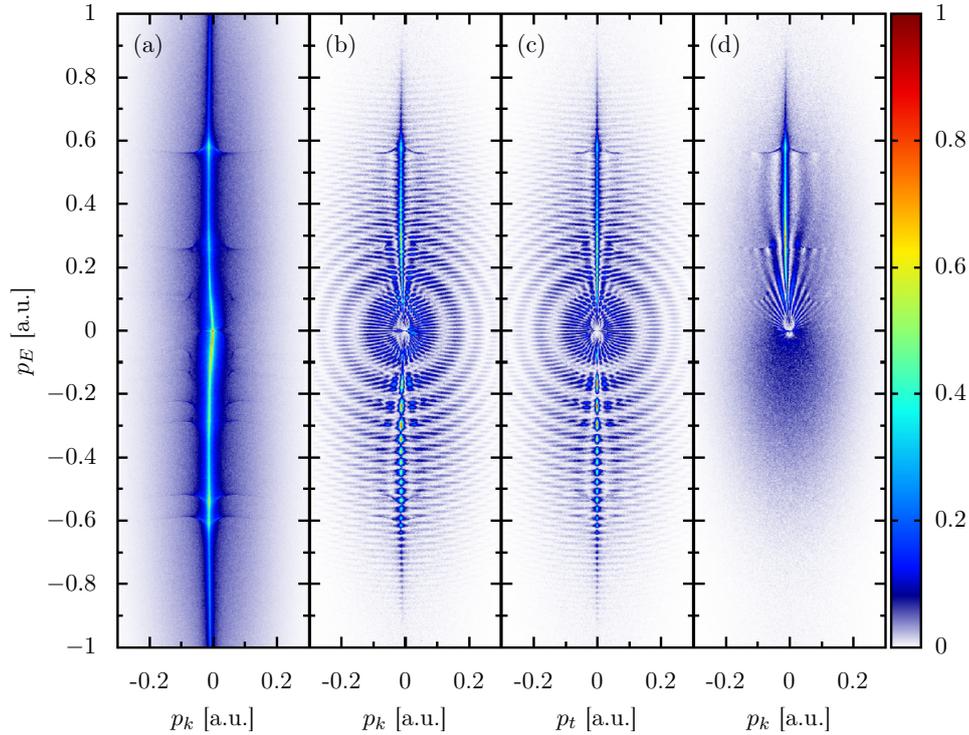The photoelectron momentum distribution is calculated as a sum over all N trajectories ending in the same bin

$$|M_{\mathbf{p}}|^2 \quad \sim \quad \lim_{t\to\infty}\frac{1}{N}\left|\sum_{i=1}^{N}\sqrt{W(p_{\perp i})}\exp[i\phi_i(t)]\right|^2, \tag{6.22}$$

$$\phi_i(t) \quad \equiv \quad \mathcal{S}_i(t) + \phi_{in,i} + \Phi_i^C(t_f), \tag{6.23}$$

where $W(p_{\perp i})$ is the ADK ionization probability (for the atom) or the MO-PFT tunneling rate from Eq. (1.91) (for the diatomic molecule) at the tunnel exit with the initial transverse momentum $p_{\perp i}$ of the electron at the tunnel exit for the given i^{th}-trajectory. For the molecule we also have to add the phase at the tunnel exit ϕ_{in} given by Eq. (1.93), while for the atom $\phi_{in} = 0$.

The photoelectron momentum distribution via QTMC simulation is shown in Fig. 6.8. For comparison we give also the result of the Classical Trajectory Monte-Carlo (CTMC) simulation. From Fig. 6.8 we can deduce that the main ridge of the momentum distribution is of classical nature. There are peaks on the main ridge with wings for large longitudinal momenta. They correspond to the so called soft recollision condition (to the peak of the momentum transfer at a recollision) [93, 97], when the electron momentum is vanishing at the recollision point (see the recollision for the red trajectory in Fig. 6.3). The main ridge in Fig. 6.8(a), (b) and (d) is curved due to the nondipole effects. It is shifted nonuniformly to the negative transverse (along the laser propagation) momentum region for relatively low longitudinal momenta (along the laser polarization, p_x) and to the positive transverse momentum region for relatively high longitudinal momenta. The main ridge is split at negative p_x momentum values. Each of the sub-ridges arises from the trajectories originating either in the L-half-cycle, or in the R-half-cycle ($E < 0$). The physical reasons of all features of the momentum distribution will be discussed in Sec. 6.6. Let us note that Fig. 6.8(c) resembles the nondipole case as the nondipole effects do not break symmetry along the y-axis.

The main effect of the quantum consideration is the appearance of interference structures. The zoom into the the central part of the interference structure is given in Fig. 6.9. There are three types of interference modulations in the momentum distribution. First of all, these are the horizontal interference peaks with a low separation (the energy difference is of the order of the laser photon energy). It arises due to interference of the direct trajectory and the recollided trajectories, the time of ionization of these trajectories being separated by an half-cycle. In fact, when we leave only trajectories born in

Figure 6.8: Photoelectron momentum distribution for the laser and atom parameters given in Sec. 6.1 represented by projections of all electrons with $|p_{y,z}| < 0.02$ a.u.: (a) classical calculation via CTMC simulation; (b) calculation via QTMC which includes quantum mechanical interference; (c) the same as in (b) but for the (p_E, p_t)-distribution which is unaffected by the magnetic field and manifest unbroken symmetry; (d) calculation via QTMC where the ionization is restricted to take place only in the main half-cycle, with $E > 0$, at the peak of the laser pulse.

the main half-cycle, with $E > 0$, at the peak of the laser pulse, then the horizontal interference structure disappears, see Fig. 6.8(d). The second type of interference structure is the modulation of the main ridge (at energies larger than the laser photon energy) in the negative direction of momenta. It is easily proved that this interference structure is due to interference of trajectories originating from the L- and from the R-half-cycles, see Fig. 6.2. The third type of interference structure which, in fact, constitutes the holography pattern, are the spider-like wings at low momentum values $|p_x| < 0.2$ a.u., see Figs. 6.9 and 6.8(d). They arise from the interference of the recolliding trajectories which originate in the main half-cycle for $p_x > 0$ (or in the L- and the R-half-cycle for $p_x < 0$). These insight is in agreement with the analysis presented in [152].

To figure out which trajectories are mostly responsible for the interference, we analyse the phases ϕ_i of the trajectories. The phases of the electron trajectories that end up with $p_x = 0.1$ a.u. are shown in Fig. 6.10. Following [147], we classify the trajectories with the
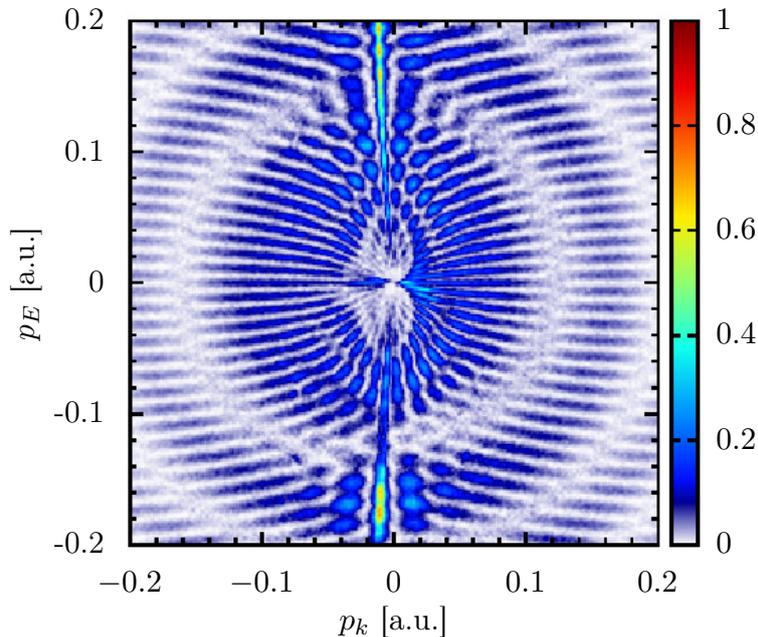
Figure 6.9: Zoom in the photoelectron momentum distribution in quantum mechanical calculation of Fig. 6.8(b).

relative sign of the electron initial momentum p_{zi} with respect to the final one p_{zf}, i.e., (A) in the case of $p_{zi}p_{zf} > 0$, the direction of the electron drift in the transverse direction does not change due to Coulomb focusing, or (B) $p_{zi}p_{zf} < 0$, the electron drift in the transverse direction is reversed due to Coulomb focusing. When one takes into account only the most probable points (green) in Fig. 6.10, then it appears that for the given value of p_z, one has two possible values of the phase, one in Fig. 6.10(a) and another in Fig. 6.10(b), i.e., belonging either to the A- or the B-type trajectories. We will call them below as direct and rescattered trajectories, although the "direct" trajectory is also affected by the Coulomb field.

6.5 The role of the target on the holographic pattern

One of the main motivations behind the photoelectron holography is the investigation of molecular structures which leave imprints in the holographic spider-like pattern. Nevertheless, even for atoms it is not clear how sensitive the pattern is to the strong-field effects as Stark shift, polarizability or the multielectron effects. Moreover, the molecules possesses more complication due to their ionization dependency on their orientation with respect to the ionizing field as discussed in Sec. 1.5.

The aim of this section is to analyze the role of the effects for the atomic target of Xe and the role of the orientation for diatomic molecules. In order to do so, we performed restricted QCTMC (RQTMC) simulations for layouts at $p_x = 0.6$ a.u., and including
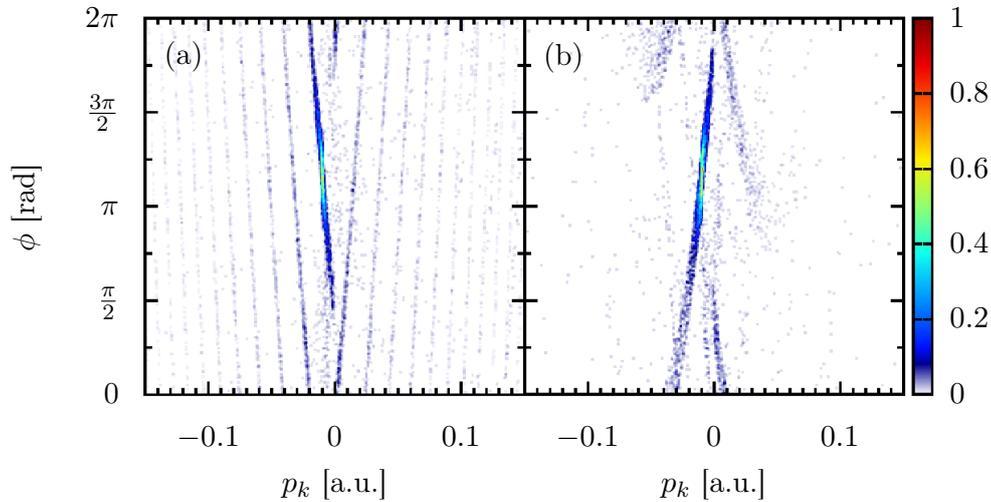
Figure 6.10: Photoelectron asymptotic phases in QTMC simulation for Xe, when the ionization is restricted to take place only in the main half-cycle, with $E > 0$, at the peak of the laser pulse, $p_E = 0.1$ a.u., $|p_y| \leq 0.002$: (a) For the tajectories of type A, $p_{zi}p_{zf} > 0$, see the text; (b) For the tajectories of type B, $p_{zi}p_{zf} < 0$. The different branches of the plot are continuation of the same curve.

only the type A and selected type B electrons. The used type B electrons correspond to the electrons with the significant recollision at the third rescattering point which already capture the main properties of the spider-like structure as discussed in Secs. 6.2 and 6.3.

6.5.1 The role of the potential

As we have shown in Eq. (6.18), the potential energy should be accounted for twice in the relativistic action $\mathcal{S}(t)$ in Eq. (6.17). We compare the results of the RQTMC in Fig. 6.11(a) for Xe atoms. As we can see, the position of the interference maxima depend severely on this term. When we take into account only one single term from Eq. (6.18), we obtain widely spread maxima. This case corresponds to the original QTCM [200] and reproduces the spread obtained via SFA in Sec. 6.2. On the other hand, we obtain a narrower structure and agreement with the results via CCSFA in Sec. 6.3 while taking both terms in Eq. (6.18) into account. We are going to use both terms from now on for the better agreement with the time-dependent Schrödinger equation as discussed in previous section.

Furthermore, the ionized Xe atom has nontrivial electronic structure and multielectron effects could also happen to influence the holographic pattern. Some effective potentials for Xe were obtained from ab initio calculations in [203, 204] or from rescattering experiments [205] and references therein. From the latter we have effective potential of

Xe^+:

$$V_s(\mathbf{r}) = -\frac{1 + a_1 e^{-a_2|\mathbf{r}|} + a_3 e^{-a_4|\mathbf{r}|} + a_5 e^{-a_6|\mathbf{r}|}}{|\mathbf{r}|}, \tag{6.24}$$

with $a_1 = 51.356$, $a_2 = 2.112$, $a_3 = -99.927$, $a_4 = 3.737$, $a_5 = 1.644$, and $a_6 = 0.431$ for xenon. The effective potential resembles the Coulomb potential at large distances. We plotted the resulting cut in Fig. 6.11(a) and we can see that the patterns are nearly indistinguishable from the case of a Coulomb potential. This is no big surprise as the restriction on the simulation excludes trajectories with rescatterings close to the atomic core where the difference between the Coulomb and the effective potential is the greatest. Therefore, we performed full scale QTMC simulations including all trajectories but without seeing any noticeable difference for the spider-like structure. This is probably due to the diminished role of the excluded trajectories.

Assuming the Coulomb potential of a charge q at the center of the coordinate system in the case of the ionic O_2 molecule leads to an unwanted oversimplification because the molecular structure is neglected. Therefore, we use the potential of the ionized molecule in the following form

$$V_m(\mathbf{r}) = -\frac{1}{2|\mathbf{r} - \mathbf{R}/2|} - \frac{1}{2|\mathbf{r} + \mathbf{R}/2|}, \tag{6.25}$$

describing the field at $\mathbf{r}$ from two charges $q/2$ located at $\pm\mathbf{R}/2$ as shown in Fig. 1.4.

We are going to include the potential $V_m(\mathbf{r})$ also in the equation for action $\mathcal{S}(t)$ in Eq. (6.17) instead of the atomic potential $V_a(\mathbf{r})$ whenever we are going to talk about O_2. Nevertheless, we assume that the electron is far away from the molecular ion at the end of the laser pulse, $|\mathbf{r}(t_f)| \gg |\mathbf{R}|/2$, which is well justified for most of the electrons except small part of the electron spectrum with vanishing energy. Under this assumption we can use the formulas for the asymptotic evolution in Eqs. (6.19) and (6.21) without modifying the potential $V_m(\mathbf{r}) \approx -1/|\mathbf{r}|$ in this region.

6.5.2 Role of polarizability

Atoms in strong electric fields experience several effects as induced dipole moment and Stark shift. These effects also influence the position of the tunnel exit x_E. In this short subsection we are going to address both these effects for Xe and O_2.

Polarizability

The external electric field $\mathbf{E}(t)$ induces a dipole moment $\mathbf{d}(t)$ in dielectric materials. The dipole moment of an atomic ion is given by

$$\mathbf{d}(t) = \alpha^I \mathbf{E}(t), \tag{6.26}$$

where α^I is the polarizability of the atomic ion.

The induced dipole moment for a molecule is generally nontrivial as the polarizability is a three-by-three matrix in such a case. Nevertheless, this problem simplifies as only polarizability along the molecular axis is known. When the orientation of the molecule

(a) Xe

(b) Xe

(c) O_2: $\theta_M = 42.4°$

(d) O_2: $\theta_M = 0^+$
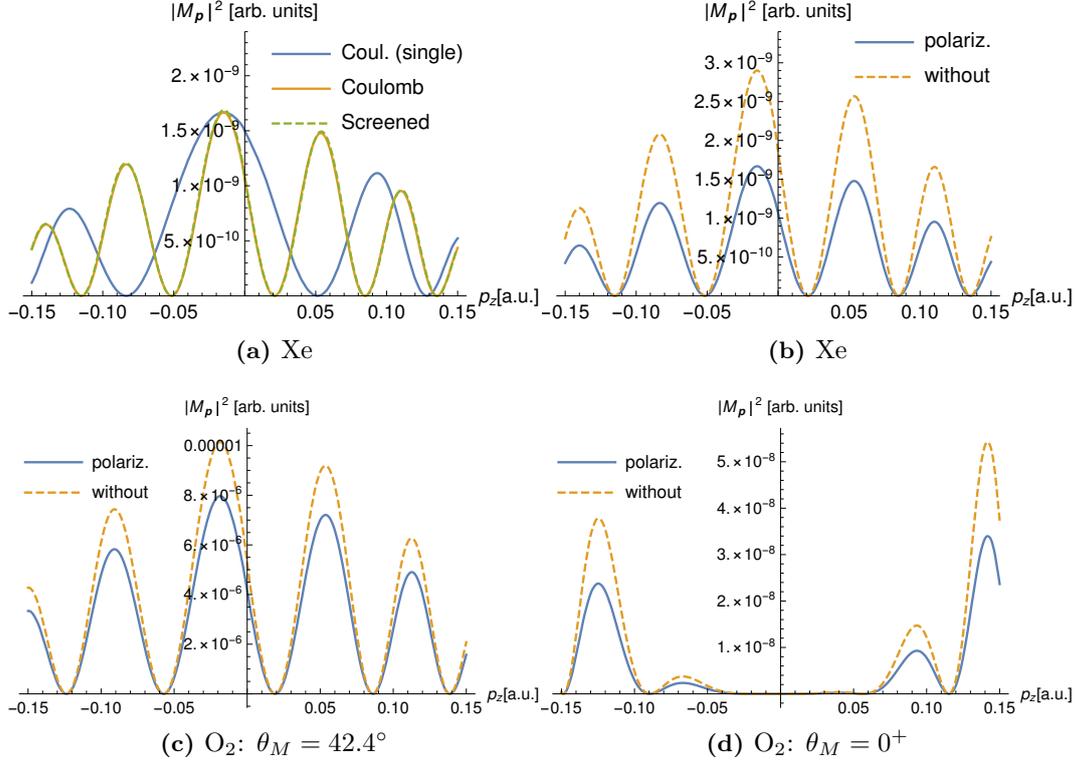
Figure 6.11: The layouts of the holographic structure at $p_x = 0.6$ *a.u.* for Xe in (a) and (b) and for O_2 in (c) and (d). We investigate the role of the atomic potential in panel (a), where we address the importance of the two terms in Eq. (6.18) (see text) and the difference between Coulomb potential (full, orange) and effective potential including multielectron effects (dashed, green). The role of the polarizability is addressed for Xe in (b) and for two different cases of alignment of O_2 in (c) and (d). The polarizability of the molecule changes its ionization potential I_p which modifies the ionization rate and influences the visibility of the holographic pattern. Polarizability of the ion O_2^+ influences the trajectory of the tunneled electron but as we can see, its effect on the position of the lobes is rather negligible.

is in the x-y plane defined by the unit vector $\mathbf{e}_M = (\cos\theta_M, \sin\theta_M, 0)$, we can express the laser induced polarization of the ion as

$$\mathbf{d}(t) = \alpha^I \left[\mathbf{E}(t) \cdot \mathbf{e}_M\right] \mathbf{e}_M, \tag{6.27}$$

with unit vector along the molecular axis

$$\mathbf{e}_M \equiv \left(\cos\theta_M, \sin\theta_M \cos\varphi_M, \sin\theta_M \sin\varphi_M\right). \tag{6.28}$$

The dipole moment $\mathbf{d}(t)$ influences the electron in the continuum, which feels the dipole electric field [173]

$$\mathbf{E}_d(t) = \frac{3\left[\mathbf{n}(t) \cdot \mathbf{d}(t)\right]\mathbf{n}(t) - \mathbf{d}(t)}{\left|\mathbf{r}(t)\right|^3}, \tag{6.29}$$

with the unit vector $\mathbf{n}(t) \equiv \mathbf{r}(t)/|\mathbf{r}(t)|$ pointing from the center of the atom or molecule to the tunneled electron. The electric field of the induced dipole can also be introduced into Eqs. (6.16) leading to the equation of motion

$$\begin{aligned} \ddot{\mathbf{r}}(t) &= -[\mathbf{E}(t) + \mathbf{E}_d(t)]\left(1 - \frac{\mathbf{e}_k \cdot \dot{\mathbf{r}}(t)}{c}\right) - \mathbf{e}_k \left(\frac{\mathbf{E}(t) \cdot \dot{\mathbf{r}}(t)}{c}\right) \\ &+ \left[\dot{\mathbf{E}}(t) + \dot{\mathbf{E}}_d(t)\right]\frac{\mathbf{e}_k \cdot \mathbf{r}(t)}{c} - \nabla V(\mathbf{r}(t)), \end{aligned} \tag{6.30}$$

which will be used in our QTMC and RQTMC simulations from now on with the corresponding potential $V(\mathbf{r}(t))$ from Eq. (6.24) or (6.25).

Stark shift

The quadratic Stark shift for an atom placed in the external electric field $\mathbf{E}(t)$ yields [205]

$$I_p\left(\mathbf{E}(t)\right) = I_p(0) + \frac{1}{2}(\alpha^N - \alpha^I)\mathbf{E}^2(t), \tag{6.31}$$

with ionization potential $I_p(0)$ and polarizabilities α^N and α^I of the neutral and singly ionized atom, respectively. For Xe we have $I_p(0) = 0.4456$, $\alpha^N = 27.292$ and $\alpha^I = 21.324$ [206].

The Stark shift for a general molecule is given as [207]

$$I_p\left(\mathbf{E}(t)\right) = I_p(0) + \mathbf{\Delta\mu} \cdot \mathbf{E}(t) + \frac{1}{2}\mathbf{E}^T(t)\mathbf{\Delta\alpha}\mathbf{E}(t), \tag{6.32}$$

with dipole moment vector $\mathbf{\Delta\mu} = \mathbf{\mu}^M - \mathbf{\mu}^I$ and polarizability matrix $\mathbf{\Delta\alpha} = \mathbf{\alpha}^M - \mathbf{\alpha}^I$. The superscript M stands for the neutral molecule and the superscript I for the positive ion.

The molecule O_2 has no inherited dipole moment due to its heteroatomic nature and only quadratic Stark shift influences the ionization potential. Since we know only the values of the polarizability for O_2 along the molecular axis, the Stark-shifted ionization potential reduces to

$$I_p\left(\mathbf{E}(t)\right) = I_p(0) + \frac{1}{2}(\alpha^M - \alpha^I)\cos^2\theta_M\mathbf{E}^2(t), \tag{6.33}$$

for the electric field $\mathbf{E}(t)$ and the unaffected ionization potential $I_p(0) = 0.4438$ a.u. The oxygen molecule O_2 has measured polarizability $\alpha_N = 1.562\text{Å}^3 = 10.54$ a.u. and its cation O_2^+ has computed polarizability $\alpha_I = 0.867\text{Å}^3 = 5.85$ a.u. [206].

Tunnel exit

As the electron orbitals try to adjust to the external electric field, also the tunneling dynamic is influenced. The main effect can be found for the position of the tunnel exit x_E which shifts closer to the atomic center. This behavior is described in the so called TIPIS model [195] via the 1D effective potential for the tunneling in Xe:

$$V(\eta, E(t)) = -\frac{1 - \sqrt{\frac{2I_p(E(t))}{2}}}{2\eta} - \frac{1}{8}\eta E(t) + \frac{m^2 - 1}{8\eta^2} + \frac{\alpha^I E(t)}{\eta^2}, \tag{6.34}$$

with parabolic coordinate η, the electric field $E(t) = |\mathbf{E}(t)|$, and the Stark-shifted potential $I_p(E(t))$ from Eq. (6.31). The tunnel exit x_E is a function of time and can be found as $x_E = -\eta_E/2$, where η_E solves the equation $V(\eta_E, E(t)) = -\frac{I_p(E(t))}{4}$. From now on, we also include the corrected tunnel exit in our QTMC and RQTMC simulations for Xe. Unfortunately, wince the extension for the O_2 molecule is not straightforward, we will stick with the tunnel-exit given by the zero-range potential as discussed in Sec. 1.5. Nevertheless, our analysis of Xe has shown that the position of the tunnel exit does not have significant impact on the holographic pattern and the results are quite robust with respect to the position of the tunnel exit.

Concluding the role of the polarizability

We examine the role of polarizability on holographic pattern in Fig. 6.11(b)-(d) for Xe and O_2 in two different orientations. The main influence of the polarizability of the molecule on the PMD is the change of the tunneling rate due to the change of ionization potential $I_p(E(t))$ via the Stark shift in Eqs. (6.31) and (6.33). The dipole moment $\mathbf{d}(t)$ introduced by the laser field and altering the electron dynamics via Eq. (6.30) does not noticeably influence the position of the lobes as we can see in Figs. 6.11(b)-(d).

6.5.3 Orientation of the diatomic molecule

Recently, several experiments with aligned molecules have shown the dependency of the holographic pattern on the alignment [49, 53]. Not only the recollision dynamics is influenced by the orientation of the molecule, but there also exists a nontrivial phase structure in the tunneled wave packet as we discussed in Sec. 1.5. Since these effects cannot be easily separated, we have to take them both into account hile investigating the role of the molecule's orientation.

In order to do so, we have performed several RQTMC simulations incorporating all the upper discussed effects of alignment, Stark shift, polarizability and asymptotic evolution in the simulations for different distinct orientations of the O_2 molecule. We show the resulting cuts at $p_x = 0.6$ a.u. in Fig. 6.12.

In the first two panels (a) and (b) of Fig. 6.12, we have concentrated on the orientation of the molecular axes yielding the largest ionization rates for $\theta_M^{(\max)} = 42.368°$ and $137.632°$ as shown in Subsec. 1.5.1. As we can see, the two remaining angles do not influence the position of the interference maxima significantly. The measured holographic spectrum would be a incoherent addition of all the curves represented by the black dotted line.

In the last two panels (c) and (d) of Fig. 6.12, we have concentrated on the more unfavorable orientations yielding small ionization rates (by two orders of magnitude) but large differences in the phase structure (see Subsec. 1.5.2). The holographic pattern differs severely as the initial phase difference at the tunnel exit differs for the direct and rescattered electrons by $\approx \pi$. Our simulations for O_2 qualitatively correspond to the experimental results for N_2 in [49]. Nevertheless, any closer correspondence is excluded because the role of the rescattering on the molecular potential from Eq. (6.25) cannot be properly addressed with our RQTMC simulations as we do dot consider electrons approaching closely the molecular ion. For this purpose it would be more suitable to
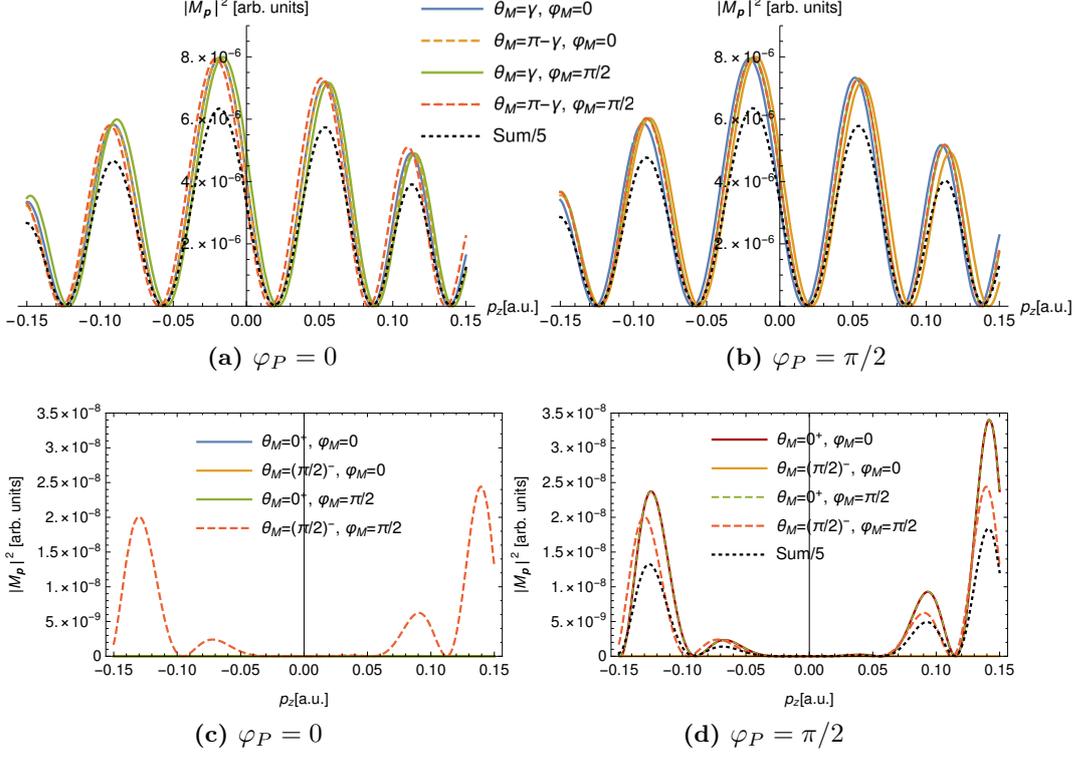
Figure 6.12: The layouts for $p_x = 0.6$ a.u. show the role of the molecule's and orbitals' alignment for the holographic pattern. The negative shift of the central peaks is caused by the nondipole effects caused by the laser propagating along the z-axis. The tunneling dominantly happens for alignment given by $\theta_M = \gamma$ and $\pi - \gamma$ with $\gamma = 42.4°$ as shown in panel (a) and (b). The other parameters of the alignment as φ_M and φ_P play rather negligible role on the position of the peaks. On the other hand, the extreme alignment of $\theta_M \to 0^+$ or $\theta_M \to 90^-$ alters the holographic pattern significantly as shown in panels (c) and (d). This effect is expected due to the nontrivial phase structure of the tunneled wave packet as indicated in Figs. 1.9(b)-1.9(d). For such alignments, vanishing transversal momenta p_{zi} are suppressed and only large values manifest leading to the disappearance of the central peak. Let us note for completeness that the non-visible lines in Figs. 6.12(c)-6.12(d) have similar structure as the layouts with $\theta_M = \gamma$ in Fig. 6.12(a) but are suppressed by five orders of magnitude (this applies for our case of $\theta_M = 0.5°$). We expect them to vanish completely in the limit of $\theta_M \to 0$.

145
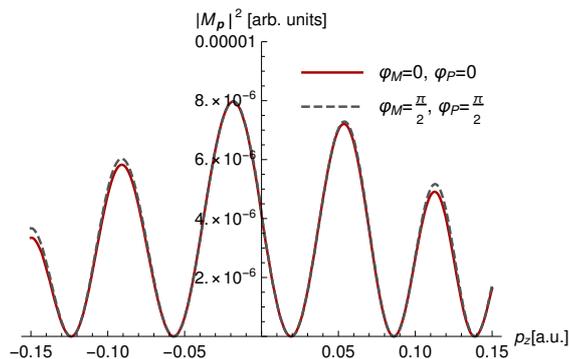
Figure 6.13: The final alignments for QTMC simulation (with $\theta_M = 42.4°$) do not severely differ and we can use any of those.

perform full QTMC simulations. Nevertheless, we have already shown in Sec. 6.3 that the other trajectories have only little influence on the position of the interference maxima and therefore we consider the RQTMC simulation in this section as sufficient for the longitudinal momentum of our interest. Let us also note that presented features for the positions of lobes correspond to the analysis given in [61].

There remain further questions: how would look like the holographic spider-like structure for an initially unaligned (or rather randomly aligned) molecule of O_2 and can it be distinguished form the structure created by Xe atom? The random alignment manifests mainly during high number of repetitions of the ionization of molecular gas in order to collect enough data for the photoelectrom momentum spectrum. We know from Subsec. 1.5.1 that the highest ionization rates are for alignments $\theta_M^{(\max)} = 42.4°$ and $137.6°$, which will contribute dominantly to the photoelectron momentum spectrum. Instead of averaging over the two remaining orientation angles φ_M and φ_P, we can choose particular values giving the same positions of the interference maxima as the incoherently added dotted black lines in Fig. 6.12(a) and (b). This leads to two candidates for the representative alignment:

1. $\theta_M = 42.4°$, $\varphi_M = 0$ and $\varphi_P = 0$,

2. $\theta_M = 42.4°$, $\varphi_M = \pi/2$ and $\varphi_P = \pi/2$,

which we compare in Fig. 6.13. The position of the first lobes does not differ and we can use any of those alignments to get the correct position of the lobes in our QTMC simulations.

We performed two QCMT simulations including all discussed effects for Xe and O_2 with the orientation $\theta_M = 42.4°$, $\varphi_M = 0$ and $\varphi_P = 0$ and ionization restricted to the central half-cycle. The results are plotted in Fig. 6.14(a) and (c), respectively. In the panels (b) and (d) we plotted the distributions of the transversal momenta p_z in the cut-outs of the PMD corresponding to strips of $|p_x - p_{\text{PMD}}| < 0.05$ a.u., where $p_{\text{PMD}} = 0.7, 0.6, 0.5, 0.4, 0.3, 0.2$, and 0.1. As we can see, the spider-like pattern does not severely differ with respect to the used target and we cannot use it for distinction. It is not surprising that the horizontal lines corresponding to slow recollision condition are

located at same position, since they are completely determined by the electrons dynamics in the continuum. It is worth mentioning that the cut-out manifests the negative shift and hence negative offset of the most dominant maxima which can be seen as the classical effect.

6.6 Scaling of characteristic features of the holography pattern

In this section we discuss the scaling laws for the characteristic features of the holographic interference structure in the photoelectron momentum distribution.

As already said, the features of the spider-like structure in the momentum distribution are due to the interference of the direct and the rescatterd electrons [146]. These electrons acquire different phases $\phi^{(d)}(\mathbf{p})$ and $\phi^{(r)}(\mathbf{p})$ during their travel from the tunnel exit to the detector. The phases depend on the final momentum and the coherent sum of ionization amplitudes oscillates with respect to the final momentum:

$$\left| \exp\left[i\phi^{(d)}\right](\mathbf{p}) + \exp\left[i\phi^{(r)}\right](\mathbf{p}) \right|^2 = 2\left\{ 1 + \cos[\phi^{(d)}(\mathbf{p}) - \phi^{(r)}(\mathbf{p})] \right\}. \tag{6.35}$$

The difference between these phases can be expressed via the accumulated action of the electron between the ionization and recollision times due to the transverse kinetic energy of the direct electron, see Eq. (3) in [147]. In the weakly-relativistic regime it is:

$$\begin{aligned} \Delta\phi &\equiv \phi^{(d)} - \phi^{(r)} = \int_{t_i}^{t_r} dt \frac{v_k^2}{2} \\ &= \int_{t_i}^{t_r} dt \frac{[p_k + T_k(p_E, t)]^2}{2}, \end{aligned} \tag{6.36}$$

with electron velocity component v_k in the laser propagation direction, and the recollision time t_r. The position of the interference maximum in the spectrum is defined by the phase difference via

$$\Delta\phi = 2\pi n, \tag{6.37}$$

with an integer n. As $\Delta\phi = 0$ is not possible, the main middle lobe of the spectrum ($n \approx 0$) is then defined by the minimum of the phase difference, i.e., by $\mathrm{d}\Delta\phi/\mathrm{d}p_k = 0$, which yields the condition for the final transversal momentum of the main interference lobe

$$p_k^{(0)} = -\frac{1}{t_r - t_i} \int_{t_i}^{t_r} \mathrm{d}t \, T_k(p_E, t). \tag{6.38}$$

The position of the lobe $p_k^{(0)}$ is shifted against the laser polarization direction compared to the symmetric non-relativistic description and it depends on p_E. It can be qualitatively estimated as follows

$$p_k^{(0)} \sim -T_k(p_E, \tilde{t}) = -\left(p_E A(\tilde{t}) + \frac{A^2(\tilde{t})}{2} \right), \tag{6.39}$$
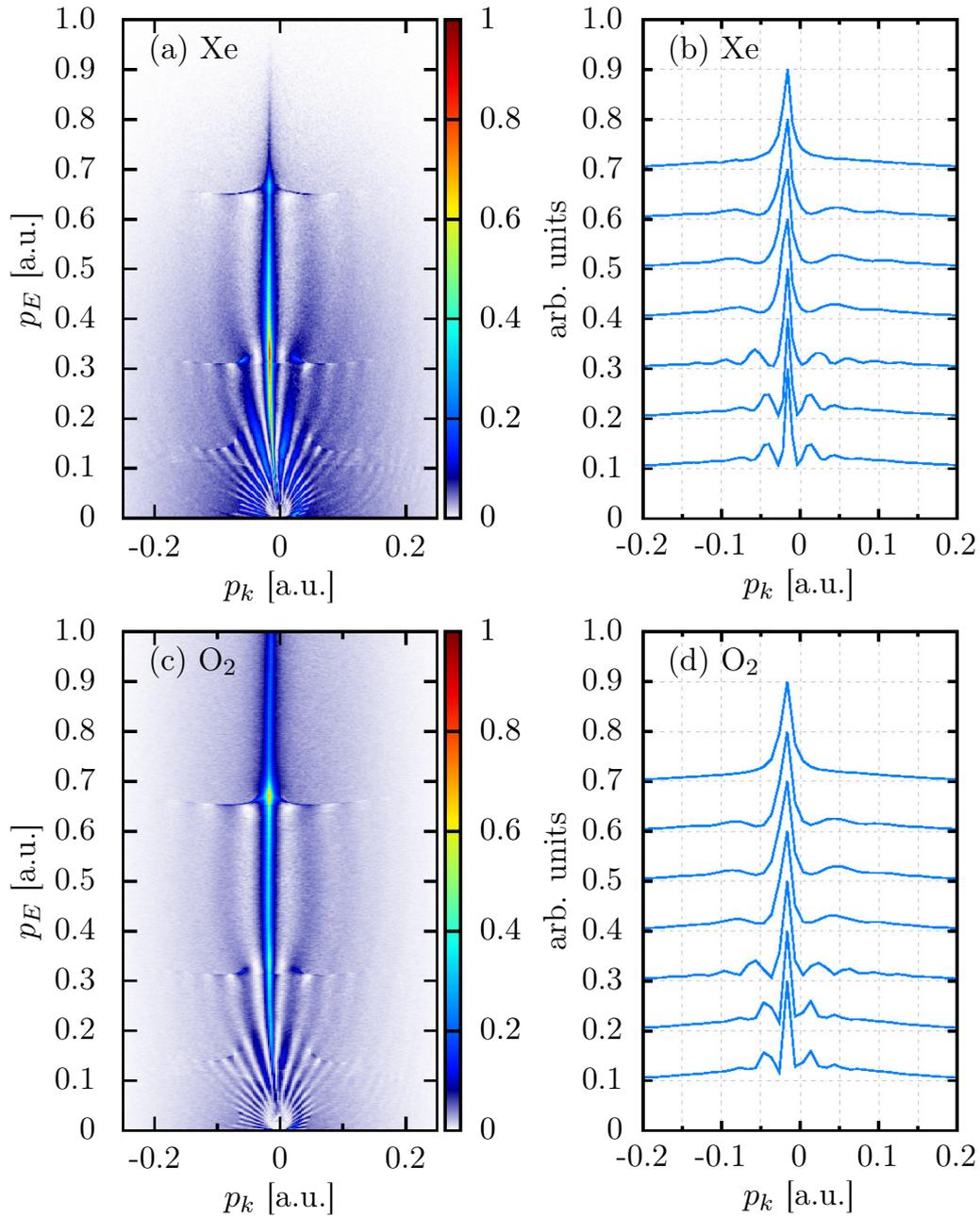
Figure 6.14: We plotted the results of the QTMC simulations for Xe [panel (a)] and for O_2 [panel (c)]. Both exhibit the interference fringes located at same positions for both elements and with the same pitch as we can read out from panels (b) and (c), where we have plotted distribution of the p_z momentum in stripes of width $\Delta p_x = 0.1$ and with their center located at $p_x = 0.7$, 0.6, 0.5, 0.4, 0.3, 0.2, 0.1 (plotted in the figures from the top to the bottom). Both PMDs also exhibit the same horizontal cusps of the Coulomb focusing, which are also separating the regions with different structure of interference fringes, e.g., at $p_x \approx 0.32$ a.u.

where $t_i < \tilde{t} < t_r$. For low values of p_E we can estimate $p_k^{(0)} \sim -A^2(\tilde{t})/2 \sim -U_p/c$, where $U_p = (E_0/\omega)^2/4$ is the ponderomotive potential, and we use $|p_E| = |A(t_i)| \ll A(\tilde{t})$. In the given case of $E_0 = 0.0407$ and $\omega = 0.013$ ($U_p = 2.45$) the momentum of the main ridge is $p_k^{(0)} \approx -0.018$, which is in accordance with the perturbative result of Fig. 6.5, the results of CCSFA of Fig. 6.7(a), as well as with the QTMC simulatios, Fig. 6.9.

The position of the side-lobes in the spectrum is determined by the phase difference condition $\Delta\phi = 2\pi n$. The latter can be estimated from Eq. (6.36) as follows:

$$\Delta\phi \sim \frac{\left[p_k + T_k(p_E, \tilde{t})\right]^2}{2}(t_r - t_i) = 2\pi n. \tag{6.40}$$

Roughly estimating the rescattering time $(t_r - t_i) \sim 2\pi\delta/\omega$, as a δ-fraction of the laser period. Then, the momentum corresponding to the nth-lobe is

$$p_k^{(n)} \sim -T_k(p_E, \tilde{t}) \pm \sqrt{2n\omega/\delta}, \tag{6.41}$$

which is also shifted against the laser propagation direction compared to the non-relativistic description. The distance between the main and the second lobes, for instance, can be estimated as

$$|p_k^{(1)} - p_k^{(0)}| \approx \sqrt{2\omega/\delta}, \tag{6.42}$$

which at the given frequency $\omega = 0.013$, is $|p_k^{(1)} - p_k^{(0)}| \approx 0.16$ a.u.. It is in accordance with the perturbative spectra shown in Fig. 6.5, which do not include Coulomb focusing. The interference wings are much closer in the case of CCSFA, Fig. 6.7(a), because of the Coulomb focusing effect.

Further, let us see why the left lobe is weaker than the right one. For this we estimate the initial transversal momentum corresponding to the side-lobes. For the direct electrons:

$$p_{k,i}^{(n)} = p_k^{(n)} + T_k(p_E^{(n)}, t_i). \tag{6.43}$$

Assuming for an estimation that $p_E = -A(t_i) \approx 0$, yields $T_k(p_E^{(n)}, t_i) \approx 0$ and $p_{k,i}^{(n)} = p_k^{(n)}$. It is clear that the left side-lobes have larger transverse momentum $p_k^{(n)} \approx -T_k(p_E, \tilde{t}) - \sqrt{2n\omega/\delta}$ than the right ones of the same n^{th}-order. Therefore, the probability of the left side-lobes $W_{n<0}$ is suppressed compared to the right-lobes $W_{n>0}$ due to a smaller tunneling probability:

$$\frac{W_{n<0}}{W_{n>0}} = \exp\left\{-\frac{p_k^{2\,(n<0)} - p_k^{2\,(n>0)}}{\Delta_k^2}\right\} \approx \exp\left\{-2\sqrt{\frac{nI_p}{\omega\delta}}\xi\right\}, \tag{6.44}$$

where $\Delta_k = \sqrt{E_0/\kappa}$ is the width of the transverse momentum distribution at the tunneling ionization [27], and the estimate $T_k \approx U_p/c$ is used. For instance $W_{-1}/W_1 \approx 0.75$ at given parameters.
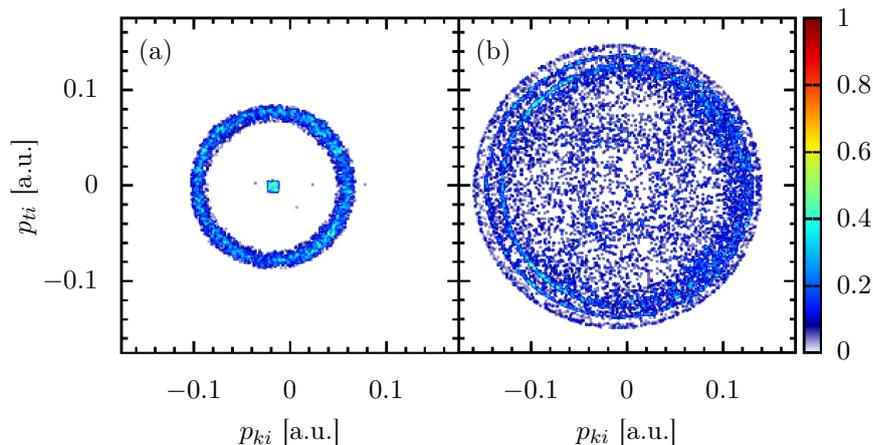
Figure 6.15: Phase space of the initial electron distribution at the tunnel exit: (a) the part which contributes to the final momentum bin at $p_E = 0.588$ a.u., and $p_k = -0.0157$ a.u., corresponding to the first soft recollision. The central spot is the contribution of the direct trajectories. Note that the central spot is the center of the ring and it is shifted to the negative p_k direction. (b) the part which contributes to the bin at the vanishing final momentum. The inner ring is symmetric, while the outer one is shifted in the negative p_k direction.

From Fig. 6.8 we have deduced that the position of the main ridge is of classical origin, see also [114, 191]. The cusp at vanishing transverse momentum in the main ridge arises due to Coulomb focusing. The latter causes transformation of the transverse phase space of the ionized electron wave packet during propagation from the tunneling exit to asymptotics. In the non-relativistic case when the drift due to the laser magnetic field is neglected, the electrons initially distributed in a ring in the transverse phase space (p_k, p_t) asymptotically move in a small cycle near the vanishing transverse momentum, $p_k = 0$ and $p_t = 0$, because of the momentum transfer to the atomic core during the recollision. The magnetically induced relativistic drift will change the electron recollision parameters and will modify the phase space transformation due to the Coulomb field. However, if the electron at the tunnel exit has an appropriate initial transverse momentum p_{ki}, such that the recollision coordinate x_k in the case of the drift is the same as in the case without drift, then the momentum transfer due to the Coulomb effect will be the same as in the non-relativistic case.

In the non-relativistic case the recollision x_k-coordinate of the electron, ionized with the momentum $p_{ki}^{(0)}$, is $x_{kr}^{(0)} = p_{ki}^{(0)}(t_r - t_i)$. Due to the recollision the momentum transfer to the Coulomb field is δp_k^C, and final momentum of the electron, initially in the mentioned ring, is vanishing $p_{kf} = p_{ki}^{(0)} - \delta p_k^C = 0$. Consequently, $p_{ki}^{(0)} = \delta p_k^C$, and $x_{kr}^{(0)} = \delta p_k^C(t_r - t_i)$.

For the relativistic electron motion in the laser field we have:

$$
\begin{aligned}
p_E(\eta) &= A(\eta) - A(\eta_i) + p_{Ei}, \\
p_k(\eta) &= p_{ki} + \frac{p_E^2(\eta) - p_{Ei}^2}{2\Lambda},
\end{aligned}
\tag{6.45}
$$

where η_i is the initial phase, and p_{Ei} and p_{ki} are the initial momentum components of the electron, $\Lambda = (\varepsilon_i - p_{ki})/c \approx c$ is the integral of motion in the plane laser field. The electron recollision coordinate in the weakly relativistic regime is

$$
x_{kr} = p_{ki}(t_r - t_i) + \int_{t_i}^{t_r} dt \frac{[A(t) - A(t_i)]^2}{2c},
\tag{6.46}
$$

where we set the ionized electron momentum $p_{Ei} = 0$. The condition $x_{kr} = x_{kr}^{(0)}$, when the recollision in the relativistic case takes place with the same impact parameter as in the non-relativistic case, reads

$$
p_{ki} = \delta p_k^C - \frac{1}{t_r - t_i} \int_{t_i}^{t_r} dt \frac{[A(t) - A(t_i)]^2}{2c}.
\tag{6.47}
$$

At the recollision point the electron momentum components according to Eq. (6.45) are

$$
\begin{aligned}
p_E(t_r^-) &= A(t_r) - A(t_i), \tag{6.48}\\
p_k(t_r^-) &= p_{ki} + \frac{[A(t_r) - A(t_i)]^2}{2c}, \tag{6.49}
\end{aligned}
$$

while after the recollision they become

$$
\begin{aligned}
p_E(t_r^+) &\approx A(t_r) - A(t_i), \tag{6.50}\\
p_k(t_r^+) &= p_{ki} - \delta p_k^C + \frac{[A(t_r) - A(t_i)]^2}{2c}, \tag{6.51}
\end{aligned}
$$

where we have taken into account that $\delta p_E^C \ll \delta p_k^C$. Then the asymptotic momentum at the detector according to Eq. (6.45) is

$$
\begin{aligned}
p_E &\approx -A(t_i), \\
p_k &= p_{ki} - \delta p_k^C + \frac{A(t_i)^2}{2c} = -\frac{1}{t_r - t_i} \int_{t_i}^{t_r} dt \frac{[A(t) - A(t_i)]^2 - A(t_i)^2}{2c} \\
&= -\frac{1}{t_r - t_i} \int_{t_i}^{t_r} dt \, T_k(p_E, t).
\end{aligned}
\tag{6.52}
$$

Concluding the discussion about the main ridge, the Coulomb focusing in the case of the relativistic drift will be similar to the non-relativistic case. The only change is the shift of the cusp in the transverse momentum distribution against the laser propagation direction by the value of the drift momentum

$$
p_k = -p_k^{(d)} \equiv -\frac{1}{t_r - t_i} \int_{t_i}^{t_r} dt \, T_k(p_E, t).
\tag{6.53}
$$

The initial phase space at the tunnel exit which is squeezed into the central cusp is a ring of the radius δp_k^C centered around the momentum value

$$p_{ki} = -p_k^{(d)} - \frac{A(t_i)^2}{2c}, \tag{6.54}$$

see Fig. 6.15. The part of the initial phase space at the tunnel exit which contributes to the final momentum bin at the vanishing momentum is shown in Fig. 6.15(b). The inner ring is symmetric, while the outer one is shifted in the negative p_k direction. The asymmetric ring is produced by electrons which are ionized in the L-half-cycle. The asymmetry is again described by Eq. (6.53). The inner ring in Fig. 6.15(b) is produced by electrons which are ionized either in the C-half-cycle, or in the R-half-cycle. The inner ring is not asymmetric, because the trajectory analysis shows that in this case the Coulomb focusing arises after switching off the laser field. Then, there is no relativistic drift and there is no asymmetry along the p_k direction.

Note that the main lobe of the quantum interference pattern, Eq. (6.38), coincides with the position of the cusp due to the classical Coulomb focusing given by Eq. (6.53).

Eq. (6.53) describes the shift of the main ridge in the region when the rescattering plays a significant role. The shift is negative. It depends on p_E, increasing with p_E by absolute value. For such large p_E, or large p_k, when rescattering is not important, the shift of the momentum distribution with respect to the non-relativistic case is in positive p_k direction: $p_{ki} \rightarrow p_{ki} + A(t_i)^2/2c$, according to Eq. (6.45).

A final observation is that the wings of the spider-like structure end at a longitudinal momentum of $p_E \sim 0.65$ a.u. which can be explained by a cutoff rule of the trajectories with soft recollisions [106]. For values of the longitudinal momentum larger than the cutoff only one return of the trajectory to the core is possible.

Concluding, with these simple estimates all qualitative features of the interference structure can be reproduced, showing how the magnetic dipole interaction alters the holography image of the momentum distribution.

6.7 Summary

In this section we have investigated the strong-field photoelectron holography with mid-IR laser beyond the dipole approximation for xenon and molecular oxygen. Firstly, we have introduced the concept of the photoelectron holography, its manifestation via the spider-like structure and explained the origin of the structure due to existence of multi-path interference introduced by forward scatterings of the ionized target. We investigated the holographic patterns by several methods: SFA, CCSFA, QTMC, RQTMC and by simple analytical estimates.

In the SFA, we have taken the Coulomb potential of the parent ion perturbatively into account. Already the perturbative treatment of the recollision yields qualitative interference patterns. The further inclusion of the Coulomb potential can be achieved in CCSFA, where we can take into account the Coulomb momentum transfer at one recollision point (although multiple recollisions can happen). Via the CCSFA we found out that the interference maxima are situated closer towards the center. Moreover, we

investigated the role of multiple paths and concluded that the main features of the spider-like structures are already given by two-path interference of the direct and recollided electrons with momentum transfer at the slow recollision. Inclusion of the other paths smoothens the distribution leads to a gradual decrease of the intensity in the spectra with increasing p_E. This is true for regions with large longitudinal momenta (i.e., $p_E > 0.25$ a.u. in our setup), where only up to three recollisions take place. Smaller values of final longitudinal momenta could not be estimated by this method.

The full inclusion of the Coulomb potential was made in the numerical QTMC simulations, where we have also taken into account the effects of the strong laser field on the target. Features as multi-electron effect, polarizability of the ionic target, quadratic Stark shift or shift of the tunnel exit due to polarizability were shown to play only a minor role on the position of the interference maxima via RQTMC simulation. Not like the orientation of a diatomic molecule of O_2, which can have a strong influence on the tunneling rates an the phase structure of the tunneled wave packet. The latter was contributed to the nontrivial phase structure of the tunneled wave packet. We have also found one particular orientation of the O_2, which yields the highest ionization rate and the right position of the interference maxima. This orientation can be used in the simulations for unaligned O_2 in order to avoid the need for averaging over all three alignment angles. We also employed these results and compared the spider-like structure created by Xe and by unaligned O_2 via QTMC simulations, while finding no observable difference in the spider-like structure.

Moreover, we analyzed the role of the pulse length on the interference pattern due to ionization taking place at multiple half-cycles. We identified the interference features with respect to the origin of the tunneled electron.

Finally, we used analytical estimates for explanation of the features in the holographic pattern as negative shift against the laser propagation direction, position of the central lobe, spread of the interference maxima and suppression of the intensities at the first left and right lobe. The overall negative offset, along with the position of the central lobe, and asymmetry in the intensities at the first left and right lobe were contributed to the nondipole effects. Eventually, the position of the main lobe was shown to correspond to the position of the vertical cusp arising classically due to the Coulomb focusing.

Conclusions

In this work we have addressed the role of the Coulomb potential in the strong-field ionization physics beyond the dipole approximation. As we tried to illustrate in the introduction, the Coulomb force acting on the ionized electron is essential and leads to many new phenomena. Therefore, the Coulomb interaction can not be neglected neither during electrons promotion to the continuum (inization) nor during the evolution in the continuum for proper understanding of the underlying physics.

In Chap. 1, we concentrated on the Strong-field approximation (SFA) and its Coulomb-corrected version (CCSFA). We introduced the basic idea behind the SFA in Sec. 1.1 and the way how the CCSFA accounts for the Coulomb potential via first-order correction obtained from the eikonal expansion of the electron wave function in the continuum in Sec. 1.2. We repeated the calculations from the literature and showed how the Coulomb singularity in the first-order correction term can be avoided by saddle-point integration . Moreover, we showed that the correction term leads to reproduction of the PPT tunneling rate. The novelty brought by this thesis is the analysis of the higher-order correction term from the eikonal expansion and their role in the ionization process. The higher-order terms are neglected in the standard CCSFA and were not addressed previously. We have analyzed the role of the second-order correction terms in 1D and identified classical and quantum contributions and discussed their influence on the nonadiabatic momentum shift in Sec. 1.3. Finally, we drew conclusions for more realistic 3D case yielding a negative nonadiabatic momentum shift. In Sec. 1.4, we briefly discussed other extensions of the CCSFA to the relativistic regime and the alternative Analytical R-Matrix theory.

Furthermore, we were motivated by the recent attention gained by the strong-field ionization of molecules, as it promises a new tool for investigation of molecular structures and dynamics. Therefore, we investigated the strong-field ionization process of the diatomic molecule O_2 by Partial-Fourier-transformation method in Sec. 1.4. We have generalized the known formulas for arbitrary alignment of the molecule with respect to a linearly polarized laser field and reproduced the orientation-dependent ionization rates. Moreover, we were able to retrieve the phase structure of the tunneled wave packet, which plays an important role in strong-field holography, addressed in the last chapter of this thesis.

In the next part of the thesis, we investigated the influence of the Coulomb interaction between tunneled electron and its parent ion on the electron's dynamics in the continuum. The Coulomb potential causes bunching in the photoelectron momentum diagram and is therefore called Coulomb focusing. In the first section of Chap. 2, we introduced the classical analytical theory for the description of Coulomb focusing in linearly polarized laser fields. We included the nondipole effects accounting for the magnetic field induced drift of the ionized electron along the propagation direction of the laser during the electron's excursion in the laser field. We treated the Coulomb interaction as a per-

turbation to the laser driven trajectory and restricted it to the so called recollision points. Furthermore, we have classified the recollision points as slow and fast and with respect to the electron's velocity at the recollision in Sec. 2.2. After we restricted the interaction to these well defined points, we derived in Sec. 2.3 analytic formulas for the Coulomb momentum transfer to the recolliding electron at these points. We also discussed the simple-man's approximation of the Coulomb momentum transfer at recollision (R-CMT) as a product of the acting Coulomb force and the recolision's duration. The scaling of R-CMT was derived with respect to the rescattering parameters (momentum and impact parameter) as well as with respect to the laser intensity and wavelength and further analyzed in Sec. 2.4, where the Coulomb interaction was assumed as global perturbation in the dipole case. In addition, we provided the higher-order corrections to the initial Coulomb momentum transfer at the tunnel exit in Sec. 2.5. The correction appeared to be necessary for preservation of the overall precision of the model.

When we captured the Coulomb interaction via the Coulomb momentum transfers, we estimated the total Coulomb momentum transfer in dipole regime in Chap. 3. For this purpose, we addressed the generalization of the recollision points for any electron trajectory and the suitability of the analytic formulas in Sec. 3.1. Furthermore, we developed two methods for the estimation of the total Coulomb momentum transfer in Sec. 3.2: a fully perturbative zero-order method and a step-by-step method. Whereas in the first method we consider the Coulomb effect as a global perturbation to the laser driven trajectory, in the second method the electron momentum is adjusted after each recollision leading to a change in the trajectory. The latter allows us to extend the treatment of the Coulomb focusing beyond the perturbative regime. In particular, we devoted special attention to the contribution of high-order rescattering events and to the derivation of the effective number of rescatterings. In Sec. 3.3, we used both methods to derivate the photoelectron momentum diagram using a modified Classical-trajectory Monte Carlo simulation. Both methods were shown to reproduce the main features of the Coulomb focusing. In addition, we proposed an alternative way of treating the Coulomb focusing as a transformation of the momentum phase space undisturbed by the Coulomb field in Sec. 3.4, where we have shown that the I-CMT contributes to the spatial focusing of the tunneled wave function. Finally, we employed the analytical framework in Chap. 4 to investigate the counterintuitive bend of the central cusp in the nondipole regime. We discussed the modification of the rescatterings and, hence, of the Coulomb focusing due to the magnetic force in Sec. 4.1. Moreover, we revealed fine interplay between the nondipole and Coulomb field effects resulting in the energy-dependent bend of the cusp. In Sec. 4.2, we investigated the role of high-order rescatterings and found a direct relation between the number of rescatterings and the fine structure of the cusp.

In Chap. 5, this analytical framework was used for investigation of the the newly observed features of the Coulomb focusing in elliptically polarized laser fields. We extended our framework for the elliptical polarization to the dipole and the nondipole regime in Sec. 5.1, while exposing similarity of the drift opposite the direction of the minor axis of polarization ellipse and the magnetically induced drift due to the nondipole effects. We modeled the experiment with CTMC simulations in Sec. 5.2 for the dipole case, reproduced the observed central cusp and revealed its inner structure. The cusp was divided into three parts with respect to the number of recollisions experienced by the underlying

electron trajectories and we addressed each part with our framework while expose analogies to the linear case. Nondipole effects were included and analyzed in Sec. 5.3, where we revealed the roles of Coulomb focusing and ellipticity for the measured transition of the negative peak offset to positive values. Due to this deeper understanding of the underlying processes, we were able to estimate the average size of Coulomb focusing and the width of the tunneled wave packet from experimental data and found it to be in agreement with the simulations.

In addition, we investigated the role of the nondipole effects on the strong-field photo-electron holography in Chap. 6. After we introduced our ionization setup in Sec. 6.1, we addressed the influence of nondipole effects on the spider-like structure arising in the mid-infrared strong-field tunneling regime using several quantum descriptions: second-order perturbative SFA, CCSFA and Quantum-trajectory Monte Carlo simulation (QTMC). First, we showed in Sec. 6.2 that the "spider legs" arise already in the second-order perturbative SFA along with the overall negative shift introduced by the nondipole effects. We addressed the role of multi-path interference for the pattern yielding enhancement of the central cusp but having no influence on the positions of the interference maxima (i.e., the "spider-legs"). Furthermore, we included the Coulomb potential fully via CCSFA and revealed that the Coulomb potential of the parent ion changes the positions of the interference maxima in Sec. 6.3. We also investigated the multi-path interference and concluded that the main features of the spider-like structure are already captured by two-path interference. In Sec. 6.4, we revised the QTMC simulation and used it to reproduce of the intracycle spider-like and the typical multi-cycle interferometric structures. We defined a restricted QTMC simulation in Sec. 6.5 and used it to investigate the interferometric spider-like structure with respect to the properties of the ionized atomic or molecular target. As targets we took atomic Xenon and diatomic molecule of Oxygen. We found that the multi-electron effects represented by effective atomic potential for Xenon do not change the position of the interference maxima. Moreover, we found that the polarizability of the atom or the molecule (manifest as a quadratic-Stark shift and induced electric dipole of the ion) does not change the position of the interference maxima. The quadratic-Stark shift merely changes the ionization rate but the effect of the induced dipole on the electron's dynamics in the continuum is negligible. Furthermore, we investigated the role of the molecule's alignment (with respect to the linearly polarized laser field) for the holographic spider-like structure. We found that the structure changes severely with different orientations of the molecule, which can be contributed to the non-trivial and also orientation-dependent phase structure of the tunneled wave packet. Nevertheless, the ionization rate is not independent of the orientation and influences the intensity of the spider-like structures. Thus, we found one particular orientation of the Oxygen molecule which can be used to represent the interferometric spectrum created by unaligned molecule. In the last part of the section, we compared results from two QTMC simulations: for Xenon and for the molecular Oxygen aligned by the representative angles. We have not found any observable difference in the reproduced holographic patterns. In the end, we investigated the scaling of the characteristic features of the strong-field mid-infrared holography in the nondipole regime in Sec. 6.6. We applied the three-step model and found that the negative shift of the central interference lobes corresponds to the previously investigated classical negative offset, which

we interpret as a correspondence between the classical and quantum Coulomb focusing. Finally, we explained the relative weakness of the left wing with respect to the right wing (as already shown in the second-order perturbative SFA approach) arising due to the nondipole effects.

Outlook

The results presented in this thesis addressed several phenomena in the strong-field ionization physics arising due to interplay between Coulomb interaction and nondipole effects. The proposed classical as well as quantum mechanical formalisms for treating these effects need further development. Thus, the analysis of the high-order terms of the CCSFA was made only for linearly polarized laser field in 1D case. An extension of the calculation to 3D case would be more suitable for more precise comparison with the nowadays attoclock experiments, where high ellipticity of the laser field is used to extract the nonadiabatic momentum shift.

Furthermore, our classical analytical model is suitable for description of the rescattering event only in the regime, where the nondipole terms are just a correction and can be neglected during the recollision. As we explained, this works well for the common shapes of the laser pulse because an increase of the nondipole effects increases the induced momentum drift which causes the tunneled wave packet to miss the parent ion and hence suppresses recollisions. However, in the case of specially tailored laser pulses, the recollions can be restored and the nondipole effects would most-likely influence the Coulomb momentum transfer during the rescattering in such setup. Therefore, the classical analytical model should be modified in the case of the tailored laser pulses. Moreover, our classical analytical model is developed for the case of linearly polarized laser fields, which should be extended to the general case of elliptical polarization. Especially, the possibility of the nonadiabatic change of the laser field orientation during the recollision should be addressed by a proper modification of our model.

We have defined a method to determine the recollision points for any arbitrary trajectory of the tunneled electron and the corresponding Coulomb momentum transfers. However, the method can be improved by imposing a larger set of selection rules addressing multiple recollisions more accurately that is important for a better treatment of the low energy electron dynamics and of the trapping in the Rydberg states.

The developed analytical tool for the analysis of Coulomb effects can be applied for explanation of nontrivial Coulomb focusing features in more complicated laser configurations, such as two-color orthogonal linearly polarized laser fields, or in bicircular field configurations.

There is a discrepancy between the experimental and theoretical results of the ellipticity dependent momentum shift along the laser propagation direction for moderate values of the ellipticity. This possibly comes from the significantly modified rescattering process at intermediate ellipticities and needs careful investigation.

Finally, we discussed in the last chapter the strong-field holography beyond the dipole regime and several analytical models. We found agreement between two models: the CCSFA and the QTMC simulation. In future, we should compare these models with the experimental results and validate them along with our conclusions. Preliminary

comparison with the experimental holography pattern shows a slight but systematic deviations of the interference fringes positions. This may arise due to the quantum scattering phase during recollisions, which should be systematically calculated.

Bibliography

[1] L. V. Keldysh, Zh. Eksp. Teor. Fiz. **47**, 1945 (1964).

[2] F. H. M. Faisal, "Multiple absorption of laser photons by atoms," J. Phys. B **6**, L89 (1973).

[3] H. R. Reiss, Phys. Rev. A **22**, 1786 (1980).

[4] Y. Gontier, M. Poirier, and M. Trahin, "Multiphoton absorptions above the ionisation threshold," Journal of Physics B: Atomic and Molecular Physics **13**, 1381 (1980).

[5] Y. Gontier and M. Trahin, "Energetic electron generation by multiphoton absorption," Journal of Physics B: Atomic and Molecular Physics **13**, 4383 (1980).

[6] M. Göppert-Mayer, "Über elementarakte mit zwei quantensprüngen," Annalen der Physik **401**, 273 (1931).

[7] A. McPherson, G. Gibson, H. Jara, U. Johann, T. S. Luk, I. A. McIntyre, K. Boyer, and C. K. Rhodes, "Studies of multiphoton production of vacuum-ultraviolet radiation in the rare gases," J. Opt. Soc. Am. B **4**, 595 (1987).

[8] M. Ferray, A. L'Huillier, X. Li, L. Lompre, G. Mainfray, and C. Manus, "Multiple-harmonic conversion of 1064 nm radiation in rare gases," J. Phys. B **21**, L31 (1988).

[9] M. Lewenstein, P. Balcou, M. Y. Ivanov, A. L'Huillier, and P. B. Corkum, "Theory of high-harmonic generation by low-frequency laser fields," Phys. Rev. A **49**, 2117 (1994).

[10] P. Agostini and L. F. DiMauro, Rep. Prog. Phys. **67**, 813 (2004).

[11] D. N. Fittinghoff, P. R. Bolton, B. Chang, and K. C. Kulander, "Observation of nonsequential double ionization of helium with optical tunneling," Phys. Rev. Lett. **69**, 2642 (1992).

[12] B. Walker, B. Sheehy, L. F. DiMauro, P. Agostini, K. J. Schafer, and K. C. Kulander, "Precision measurement of strong field double ionization of helium," Phys. Rev. Lett. **73**, 1227 (1994).

[13] B. Feuerstein, R. Moshammer, D. Fischer, A. Dorn, C. D. Schröter, J. Deipenwisch, J. R. Crespo Lopez-Urrutia, C. Höhr, P. Neumayer, J. Ullrich, H. Rottke, C. Trump, M. Wittmann, G. Korn, and W. Sandner, "Separation of recollision mechanisms in nonsequential strong field double ionization of Ar: The role of excitation tunneling," Phys. Rev. Lett. **87**, 043003 (2001).

[14] W. Becker, X. Liu, P. J. Ho, and J. H. Eberly, "Theories of photoelectron correlation in laser-driven multiple atomic ionization," Rev. Mod. Phys. **84**, 1011 (2012).

[15] This approach named as a Simpleman theory, has been proposed more than 25 years ago in different variations by several authors, see M. Yu. Kuchiev, Pis'ma Zh. Eksp. Teor. Fiz. 45, 319 (1987) [Sov. Phys. JETP Lett. 45, 404 (1987)]; H. B. van Linden van den Heuvell and H. G. Muller, in Multiphoton Processes, ed. S. J. Smith and P. L. Knight, Cambridge University Press (1988); K. J. Schafer, B. Yang, L. F. DiMauro, and K. C. Kulander, Phys. Rev. Lett. **70**, 1599 (1993); P. B. Corkum, Phys. Rev. Lett. **71**, 1994 (1993), and proved to have a high predicitve power in discussions of strong-field ionization phenomena.

[16] D. M. Wolkow, Z. Phys. **94**, 250 (1935).

[17] W. Becker, J. K. McIver, and M. Confer, "Total multiphoton-ionization rates for an extremely short-ranged potential," Phys. Rev. A **40**, 6904 (1989).

[18] W. Becker, S. Long, and J. K. McIver, "Modeling harmonic generation by a zero-range potential," Phys. Rev. A **50**, 1540 (1994).

[19] H. R. Reiss, Phys. Rev. A **19**, 1140 (1979).

[20] D. Bauer, D. B. Milošević, and W. Becker, "Strong-field approximation for intense-laser–atom processes: The choice of gauge," Phys. Rev. A **72**, 023415 (2005).

[21] M. Klaiber, K. Z. Hatsagortsyan, and C. H. Keitel, "Gauge-invariant relativistic strong-field approximation," Phys. Rev. A **73**, 053411 (2006).

[22] F. H. M. Faisal, J. Phys. B **40**, F145 (2007).

[23] F. H. M. Faisal, "Gauge-equivalent intense-field approximations in velocity and length gauges to all orders," Phys. Rev. A **75**, 063412 (2007).

[24] A. M. Perelomov, V. S. Popov, and V. M. Terent'ev, Zh. Exp. Theor. Fiz. **51**, 309 (1966).

[25] A. M. Perelomov and V. S. Popov, Zh. Exp. Theor. Fiz. **52**, 514 (1967).

[26] V. S. Popov, V. P. Kuznetsov, and A. M. Perelomov, Zh. Exp. Theor. Fiz. **53**, 331 (1967).

[27] V. S. Popov, Phys. Usp. **47**, 855 (2004).

[28] V. S. Popov, Phys. Atom. Nuclei **68**, 686 (2005).

[29] S. V. Popruzhenko, "Keldysh theory of strong field ionization: history, applications, difficulties and perspectives," J. Phys. B **47**, 204001 (2014).

[30] M. V. Ammosov, N. B. Delone, and V. P. Krainov, "Tunnel ionization of complex atoms and of atomic ions in an alternating electromagnetic field," Zh. Eksp. Teor. Fiz. **91**, 2008 (1986).

[31] N. B. Delone and V. P. Krainov, J. Opt. Soc. Am. B **8**, 1207 (1991).

[32] S. V. Popruzhenko, G. G. Paulus, and D. Bauer, "Coulomb-corrected quantum trajectories in strong-field ionization," Phys. Rev. A **77**, 053409 (2008).

[33] S. V. Popruzhenko and D. Bauer, J. Mod. Opt. **55**, 2573 (2008).

[34] M. Klaiber, E. Yakaboylu, and K. Z. Hatsagortsyan, "Above-threshold ionization with highly charged ions in superstrong laser fields. i. coulomb-corrected strong-field approximation," Phys. Rev. A **87**, 023417 (2013).

[35] M. Klaiber, E. Yakaboylu, C. Müller, H. Bauke, G. G. Paulus, and K. Z. Hatsagortsyan, "Spin dynamics in relativistic ionization with highly charged ions in super-strong laser fields," J. Phys. B **47**, 065603 (2014).

[36] E. Yakaboylu, M. Klaiber, and K. Z. Hatsagortsyan, "Above-threshold ionization with highly charged ions in superstrong laser fields. iii. spin effects and their dependence on laser polarization," Phys. Rev. A **91**, 063407 (2015).

[37] L. Torlina and O. Smirnova, "Time-dependent analytical r-matrix approach for strong-field dynamics. i. one-electron systems," Phys. Rev. A **86**, 043408 (2012).

[38] L. Torlina, M. Ivanov, Z. B. Walters, and O. Smirnova, "Time-dependent analytical r-matrix approach for strong-field dynamics. ii. many-electron systems," Phys. Rev. A **86**, 043409 (2012).

[39] J. Kaushal and O. Smirnova, "Nonadiabatic coulomb effects in strong-field ionization in circularly polarized laser fields," Phys. Rev. A **88**, 013421 (2013).

[40] C. Figueira de Morisson Faria, H. Schomerus, and W. Becker, "High-order above-threshold ionization: The uniform approximation and the effect of the binding potential," Phys. Rev. A **66**, 043413 (2002).

[41] R. Kopold, W. Becker, and M. Kleber, "Quantum path analysis of high-order above-threshold ionization1dedicated to marlan o. scully on the occasion of his 60th birthday.1," Optics Communications **179**, 39 (2000).

[42] M. Klaiber, E. Yakaboylu, and K. Z. Hatsagortsyan, "Above-threshold ionization with highly charged ions in superstrong laser fields. i. coulomb-corrected strong-field approximation," Phys. Rev. A **87**, 023417 (2013).

[43] P. Eckle, M. Smolarski, F. Schlup, J. Biegert, A. Staudte, M. Schöffler, H. G. Muller, R. Dörner, and U. Keller, Nature Phys. **4**, 565 (2008).

[44] P. Eckle, A. N. Pfeiffer, C. Cirelli, A. Staudte, R. Dörner, H. G. Muller, M. Büttiker, and U. Keller, "Attosecond ionization and tunneling delay time measurements in helium," Science **322**, 1525 (2008).

[45] A. S. Landsman, M. Weger, J. Maurer, R. Boge, A. Ludwig, S. Heuser, C. Cirelli, L. Gallmann, and U. Keller, "Ultrafast resolution of tunneling delay time," Optica **1**, 343 (2014).

[46] M. Busuladžić, A. Gazibegović-Busuladžić, D. B. Milošević, and W. Becker, "Angle-resolved high-order above-threshold ionization of a molecule: Sensitive tool for molecular characterization," Phys. Rev. Lett. **100**, 203003 (2008).

[47] X.-B. Bian and A. D. Bandrauk, "Orientation-dependent forward-backward photo-electron holography from asymmetric molecules," Phys. Rev. A **89**, 033423 (2014).

[48] M. Li, X. Sun, X. Xie, Y. Shao, Y. Deng, C. Wu, Q. Gong, and Y. Liu, "Revealing backward rescattering photoelectron interference of molecules in strong infrared laser fields," Scientific Reports **5**, 8519 EP (2015). Article.

[49] M. Meckel, A. Staudte, S. Patchkovskii, D. M. Villeneuve, P. B. Corkum, R. Dörner, and M. Spanner, "Signatures of the continuum electron phase in molecular strong-field photoelectron holography," Nature Phys. **10**, 594 (2014).

[50] D. Pavičić, K. F. Lee, D. M. Rayner, P. B. Corkum, and D. M. Villeneuve, "Direct measurement of the angular dependence of ionization for n_2, o_2, and co_2 in intense laser fields," Phys. Rev. Lett. **98**, 243001 (2007).

[51] S. Petretti, Y. V. Vanne, A. Saenz, A. Castro, and P. Decleva, "Alignment-dependent ionization of $\mathbf{n}_2$, $\mathbf{o}_2$, and co_2 in intense laser fields," Phys. Rev. Lett. **104**, 223001 (2010).

[52] J. Muth-Böhm, A. Becker, and F. H. M. Faisal, "Suppressed molecular ionization for a class of diatomics in intense femtosecond laser fields," Phys. Rev. Lett. **85**, 2280 (2000).

[53] M.-M. Liu, M. Li, C. Wu, Q. Gong, A. Staudte, and Y. Liu, "Phase structure of strong-field tunneling wave packets from molecules," Phys. Rev. Lett. **116**, 163004 (2016).

[54] X. M. Tong, Z. X. Zhao, and C. D. Lin, "Theory of molecular tunneling ionization," Phys. Rev. A **66**, 033402 (2002).

[55] T. K. Kjeldsen and L. B. Madsen, "Strong-field ionization of n 2 : length and velocity gauge strong-field approximation and tunnelling theory," Journal of Physics B: Atomic, Molecular and Optical Physics **37**, 2033 (2004).

[56] D. B. Milošević, "Strong-field approximation for ionization of a diatomic molecule by a strong laser field," Phys. Rev. A **74**, 063404 (2006).

[57] M. Busuladžić, A. Gazibegović-Busuladžić, D. B. Milošević, and W. Becker, "Strong-field approximation for ionization of a diatomic molecule by a strong laser field. ii. the role of electron rescattering off the molecular centers," Phys. Rev. A **78**, 033412 (2008).

[58] M. Busuladžić, A. Gazibegović-Busuladžić, and D. B. Milošević, "Strong-field approximation for ionization of a diatomic molecule by a strong laser field. iii. high-order above-threshold ionization by an elliptically polarized field," Phys. Rev. A **80**, 013420 (2009).

[59] R. Murray, W.-K. Liu, and M. Y. Ivanov, "Partial fourier-transform approach to tunnel ionization: Atomic systems," Phys. Rev. A **81**, 023413 (2010).

[60] M. Liu and Y. Liu, "Application of the partial-fourier-transform approach for tunnel ionization of molecules," Phys. Rev. A **93**, 043426 (2016).

[61] M.-M. Liu and Y. Liu, "Semiclassical models for strong-field tunneling ionization of molecules," Journal of Physics B: Atomic, Molecular and Optical Physics **50**, 105602 (2017).

[62] R. Murray, M. Spanner, S. Patchkovskii, and M. Y. Ivanov, "Tunnel ionization of molecules and orbital imaging," Phys. Rev. Lett. **106**, 173001 (2011).

[63] T. Brabec, M. Y. Ivanov, and P. B. Corkum, "Coulomb focusing in intense field atomic processes," Phys. Rev. A **54**, R2551 (1996).

[64] S. P. Goreslavski, G. G. Paulus, S. V. Popruzhenko, and N. I. Shvetsov-Shilovski, "Coulomb asymmetry in above-threshold ionization," Phys. Rev. Lett. **93**, 233002 (2004).

[65] P. B. Corkum, Phys. Rev. Lett. **71**, 1994 (1993).

[66] N. I. Shvetsov-Shilovski, S. P. Goreslavski, S. V. Popruzhenko, and W. Becker, "Ellipticity effects and the contributions of long orbits in nonsequential double ionization of atoms," Phys. Rev. A **77**, 063405 (2008).

[67] X. Wang and J. H. Eberly, "Effects of elliptical polarization on strong-field short-pulse double ionization," Phys. Rev. Lett. **103**, 103007 (2009).

[68] X. Wang and J. H. Eberly, "Elliptical polarization and probability of double ionization," Phys. Rev. Lett. **105**, 083001 (2010).

[69] F. Mauger, C. Chandre, and T. Uzer, "From recollisions to the knee: A road map for double ionization in intense laser fields," Phys. Rev. Lett. **104**, 043005 (2010).

[70] C. Liu and K. Z. Hatsagortsyan, "Coulomb focusing in above-threshold ionization in elliptically polarized midinfrared strong laser fields," Phys. Rev. A **85**, 023413 (2012).

[71] A. Kamor, F. Mauger, C. Chandre, and T. Uzer, "How key periodic orbits drive recollisions in a circularly polarized laser field," Phys. Rev. Lett. **110**, 253002 (2013).

[72] D. Dimitrovski, J. Maurer, H. Stapelfeldt, and L. B. Madsen, "Low-energy photoelectrons in strong-field ionization by laser pulses with large ellipticity," Phys. Rev. Lett. **113**, 103005 (2014).

[73] D. Dimitrovski and L. B. Madsen, "Theory of low-energy photoelectrons in strong-field ionization by laser pulses with large ellipticity," Phys. Rev. A **91**, 033409 (2015).

[74] G. L. Yudin and M. Y. Ivanov, "Physics of correlated double ionization of atoms in intense laser fields: Quasistatic tunneling limit," Phys. Rev. A **63**, 033404 (2001).

[75] D. Comtois, D. Zeidler, H. Pépin, J. C. Kieffer, D. M. Villeneuve, and P. B. Corkum, "Observation of coulomb focusing in tunnelling ionization of noble gases," J. Phys. B **38**, 1923 (2005).

[76] R. Moshammer, J. Ullrich, B. Feuerstein, D. Fischer, A. Dorn, C. D. Schröter, J. R. Crespo Lopez-Urrutia, C. Hoehr, H. Rottke, C. Trump, M. Wittmann, G. Korn, and W. Sandner, "Rescattering of ultralow-energy electrons for single ionization of ne in the tunneling regime," Phys. Rev. Lett. **91**, 113002 (2003).

[77] A. Rudenko, K. Zrost, C. D. Schröter, V. L. B. de Jesus, B. Feuerstein, R. Moshammer, and J. Ullrich, "Resonant structures in the low-energy electron continuum for single ionization of atoms in the tunnelling regime," J. Phys. B **37**, L407 (2004).

[78] K. I. Dimitriou, D. G. Arbó, S. Yoshida, E. Persson, and J. Burgdörfer, "Origin of the double-peak structure in the momentum distribution of ionization of hydrogen atoms driven by strong laser fields," Phys. Rev. A **70**, 061401 (2004).

[79] A. Rudenko, K. Zrost, T. Ergler, A. B. Voitkiv, B. Najjari, V. L. B. de Jesus, B. Feuerstein, C. D. Schröter, R. Moshammer, and J. Ullrich, "Coulomb singularity in the transverse momentum distribution for strong-field single ionization," J. Phys. B **38**, L191 (2005).

[80] B. Wolter, M. G. Pullen, M. Baudisch, M. Sclafani, M. Hemmer, A. Senftleben, C. D. Schröter, J. Ullrich, R. Moshammer, and J. Biegert, "Strong-field physics with mid-ir fields," Phys. Rev. X **5**, 021034 (2015).

[81] C. I. Blaga, F. Catoire, P. Colosimo, G. G. Paulus, H. G. Muller, A. P., and L. F. DiMauro, "Strong-field photoionization revisited," Nat. Phys. **5**, 1745 (2009).

[82] F. Catoire, C. Blaga, E. Sistrunk, H. Muller, P. Agostini, and L. DiMauro, "Mid-infrared strong field ionization angular distributions," Laser Physics **19**, 1574 (2009).

[83] W. Quan, Z. Lin, M. Wu, H. Kang, H. Liu, X. Liu, J. Chen, J. Liu, X. T. He, S. G. Chen, H. Xiong, L. Guo, H. Xu, Y. Fu, Y. Cheng, and Z. Z. Xu, "Classical aspects in above-threshold ionization with a midinfrared strong laser field," Phys. Rev. Lett. **103**, 093001 (2009).

[84] C. Y. Wu, Y. D. Yang, Y. Q. Liu, Q. H. Gong, M. Wu, X. Liu, X. L. Hao, W. D. Li, X. T. He, and J. Chen, "Characteristic spectrum of very low-energy photoelectron from above-threshold ionization in the tunneling regime," Phys. Rev. Lett. **109**, 043001 (2012).

[85] B. Wolter, C. Lemell, M. Baudisch, M. G. Pullen, X.-M. Tong, M. Hemmer, A. Senftleben, C. D. Schröter, J. Ullrich, R. Moshammer, J. Biegert, and J. Burgdörfer, "Formation of very-low-energy states crossing the ionization threshold of argon atoms in strong mid-infrared fields," Phys. Rev. A **90**, 063424 (2014).

[86] J. Dura, N. Camus, A. Thai, A. Britz, M. Hemmer, M. Baudisch, A. Senftleben, C. D. Schröter, J. Ullrich, R. Moshammer, and J. Biegert, "Ionization with low-frequency fields in the tunneling regime," Scientific Reports **3**, 2675 (2013).

[87] M. G. Pullen, J. Dura, B. Wolter, M. Baudisch, M. Hemmer, N. Camus, A. Senftleben, C. D. Schröter, R. Moshammer, J. Ullrich, and J. Biegert, "Kinematically complete measurements of strong field ionization with mid-IR pulses," J. Phys. B **47**, 204010 (2014).

[88] Q. Z. Xia, D. F. Ye, L. B. Fu, X. Y. Han, and J. Liu, "Momentum Distribution of Near-Zero-Energy Photoelectrons in the Strong-Field Tunneling Ionization in the Long Wavelength Limit." Scientific reports **5**, 11473 (2015).

[89] K. Zhang, Y. H. Lai, E. Diesen, B. E. Schmidt, C. I. Blaga, J. Xu, T. T. Gorman, F. Légaré, U. Saalmann, P. Agostini, J. M. Rost, and L. F. DiMauro, "Universal pulse dependence of the low-energy structure in strong-field ionization," Phys. Rev. A **93**, 021403 (2016).

[90] E. Diesen, U. Saalmann, M. Richter, M. Kunitski, R. Dörner, and J. M. Rost, "Dynamical Characteristics of Rydberg Electrons Released by a Weak Electric Field," Phys. Rev. Lett. **116**, 143006 (2016).

[91] J. B. Williams, U. Saalmann, F. Trinter, M. S. Schöffler, M. Weller, P. Burzynski, C. Goihl, K. Henrichs, C. Janke, B. Griffin, G. Kastirke, J. Neff, M. Pitzer, M. Waitz, Y. Yang, G. Schiwietz, S. Zeller, T. Jahnke, and R. Dörner, "Born in weak fields: below-threshold photoelectron dynamics," J. Phys. B **50**, 034002 (2017).

[92] F. H. M. Faisal, "Strong-field physics: Ionization surprise," Nat. Phys. **5**, 319 (2009).

[93] C. Liu and K. Z. Hatsagortsyan, "Origin of unexpected low energy structure in photoelectron spectra induced by midinfrared strong laser fields," Phys. Rev. Lett. **105**, 113003 (2010).

[94] T.-M. Yan, S. V. Popruzhenko, M. J. J. Vrakking, and D. Bauer, "Low-energy structures in strong field ionization revealed by quantum orbits," Phys. Rev. Lett. **105**, 253002 (2010).

[95] J. Guo, X.-S. Liu, and S.-I. Chu, "Exploration of strong-field multiphoton double ionization, rescattering, and electron angular distribution of he atoms in intense long-wavelength laser fields: The coupled coherent-state approach," Phys. Rev. A **82**, 023402 (2010).

[96] C. Liu and K. Z. Hatsagortsyan, "Wavelength and intensity dependence of multiple forward scattering of electrons at above-threshold ionization in mid-infrared strong laser fields," J. Phys. B **44**, 095402 (2011).

[97] A. Kästner, U. Saalmann, and J. M. Rost, "Electron-energy bunching in laser-driven soft recollisions," Phys. Rev. Lett. **108**, 033201 (2012).

[98] C. Lemell, K. I. Dimitriou, X.-M. Tong, S. Nagele, D. V. Kartashov, J. Burgdörfer, and S. Gräfe, "Low-energy peak structure in strong-field ionization by midinfrared laser pulses: Two-dimensional focusing by the atomic potential," Phys. Rev. A **85**, 011403 (2012).

[99] L. Guo, S. S. Han, X. Liu, Y. Cheng, Z. Z. Xu, J. Fan, J. Chen, S. G. Chen, W. Becker, C. I. Blaga, A. D. DiChiara, E. Sistrunk, P. Agostini, and L. F. Di-Mauro, "Scaling of the low-energy structure in above-threshold ionization in the tunneling regime: Theory and experiment," Phys. Rev. Lett. **110**, 013001 (2013).

[100] E. Pisanty and M. Ivanov, "Slalom in complex time: Emergence of low-energy structures in tunnel ionization via complex-time contours," Phys. Rev. A **93**, 043408 (2016).

[101] T. Keil, S. V. Popruzhenko, and D. Bauer, "Laser-Driven Recollisions under the Coulomb Barrier," Phys. Rev. Lett. **117**, 243003 (2016).

[102] D. B. Milošević, "Reexamination of the improved strong-field approximation: Low-energy structures in the above-threshold-ionization spectra for short-range potentials," Phys. Rev. A **88**, 023417 (2013).

[103] D. B. Milošević, "Low-frequency approximation for above-threshold ionization by a laser pulse: Low-energy forward rescattering," Phys. Rev. A **90**, 063423 (2014).

[104] W. Becker, S. P. Goreslavski, D. B. Milošević, and G. G. Paulus, "Low-energy electron rescattering in laser-induced ionization," J. Phys. B **47**, 204022 (2014).

[105] M. Möller, F. Meyer, A. M. Sayler, G. G. Paulus, M. F. Kling, B. E. Schmidt, W. Becker, and D. B. Milošević, "Off-axis low-energy structures in above-threshold ionization," Phys. Rev. A **90**, 023412 (2014).

[106] W. Becker and D. B. Milošević, "Above-threshold ionization for very low electron energy," J. Phys. B **48**, 151001 (2015).

[107] S. A. Kelvich, W. Becker, and S. P. Goreslavski, "Coulomb focusing and defocusing in above-threshold-ionization spectra produced by strong mid-IR laser pulses," Phys. Rev. A **93**, 033411 (2016).

[108] J. G. Leopold and I. C. Percival, "Ionisation of highly excited atoms by electric fields. III. Microwave ionisation and excitation," J. Phys. B **12**, 709 (1979).

[109] B. Hu, J. Liu, and S. Chen, "Plateau in above-threshold-ionization spectra and chaotic behavior in rescattering processes," Phys. Lett. A **236**, 533 (1997).

[110] J. S. Cohen, "Reexamination of over-the-barrier and tunneling ionization of the hydrogen atom in an intense field," Physical Review A **64**, 043412 (2001).

[111] D. D. Hickstein, P. Ranitovic, S. Witte, X.-M. Tong, Y. Huismans, P. Arpin, X. Zhou, K. E. Keister, C. W. Hogle, B. Zhang, C. Ding, P. Johnsson, N. Toshima, M. J. J. Vrakking, M. M. Murnane, and H. C. Kapteyn, "Direct visualization of laser-driven electron multiple scattering and tunneling distance in strong-field ionization." Phys. Rev. Lett. **109**, 073004 (2012).

[112] J. Liu, W. Chen, B. Zhang, J. Zhao, J. Wu, J. Yuan, and Z. Zhao, "Trajectory-based analysis of low-energy electrons and photocurrents generated in strong-field ionization," Phys. Rev. A **90**, 063420 (2014).

[113] K. Sasaki, X. M. Tong, and N. Toshima, J. Phys. B **42**, 165603 (2009).

[114] A. Ludwig, J. Maurer, B. W. Mayer, C. R. Phillips, L. Gallmann, and U. Keller, "Breakdown of the dipole approximation in strong-field ionization," Phys. Rev. Lett. **113**, 243001 (2014).

[115] S. Chelkowski, A. D. Bandrauk, and P. B. Corkum, "Photon-momentum transfer in multiphoton ionization and in time-resolved holography with photoelectrons," Phys. Rev. A **92**, 051401 (2015).

[116] J. F. Tao, Q. Z. Xia, J. Cai, L. B. Fu, and J. Liu, "Coulomb rescattering in nondipole interaction of atoms with intense laser fields," Phys. Rev. A **95**, 011402 (2017).

[117] P.-L. He, D. Lao, and F. He, "Strong Field Theories beyond Dipole Approximations in Nonrelativistic Regimes," Physical Review Letters **118**, 163203 (2017).

[118] T. Keil and D. Bauer, "Coulomb-corrected strong-field quantum trajectories beyond dipole approximation," J. Phys. B **50**, 194002 (2017).

[119] M. Førre, J. P. Hansen, L. Kocbach, S. Selstø, and L. B. Madsen, "Nondipole ionization dynamics of atoms in superintense high-frequency attosecond pulses," Phys. Rev. Lett. **97**, 043601 (2006).

[120] A. Di Piazza, C. Müller, K. Z. Hatsagortsyan, and C. H. Keitel, "Extremely high-intensity laser interactions with fundamental quantum systems," Rev. Mod. Phys. **84**, 1177 (2012).

[121] M. C. Kohler, T. Pfeifer, K. Z. Hatsagortsyan, and C. H. Keitel, "Chapter 4 - frontiers of atomic high-harmonic generation," in "Adv. At. Mol. Phys.", , vol. 61, E. A. Paul Berman and C. Lin, eds. (Academic Press, 2012), pp. 159 – 208.

[122] H. R. Reiss, "Limits on tunneling theories of strong-field ionization," Phys. Rev. Lett. **101**, 043002 (2008).

[123] C. H. Keitel and P. L. Knight, "Monte carlo classical simulations of ionization and harmonic generation in the relativistic domain," Phys. Rev. A **51**, 1420 (1995).

[124] M. W. Walser, C. H. Keitel, A. Scrinzi, and T. Brabec, "High harmonic generation beyond the electric dipole approximation," Phys. Rev. Lett. **85**, 5082 (2000).

[125] D. B. Milošević, S. Hu, and W. Becker, "Quantum-mechanical model for ultrahigh-order harmonic generation in the moderately relativistic regime," Phys. Rev. A **63**, 011403(R) (2000).

[126] N. J. Kylstra, R. M. Potvliege, and C. J. Joachain, "Photon emission by ions interacting with short intense laser pulses: beyond the dipole approximation," J. Phys. B **34**, L55 (2001).

[127] T. Popmintchev, M. C. Chen, D. Popmintchev, P. Arpin, S. Brown, S. Alisauskas, G. Andriukaitis, T. Balciunas, O. D. Mucke, A. Pugzlys, A. Baltuska, B. Shim, S. E. Schrauth, A. Gaeta, C. Hernández-García, L. Plaja, A. Becker, A. Jaron-Becker, M. M. Murnane, and H. C. Kapteyn, "Bright Coherent Ultrahigh Harmonics in the keV X-ray Regime from Mid-Infrared Femtosecond Lasers," Science **336**, 1287 (2012).

[128] S. Palaniyappan, I. Ghebregziabher, A. D. DiChiara, J. MacDonald, and B. C. Walker, Phys. Rev. A **74**, 033403 (2006).

[129] M. Klaiber, K. Z. Hatsagortsyan, J. Wu, S. S. Luo, P. Grugan, and B. C. Walker, "Limits of Strong Field Rescattering in the Relativistic Regime," Physical Review Letters **118**, 093001 (2017).

[130] M. Dammasch, M. Dörr, U. Eichmann, E. Lenz, and W. Sandner, Phys. Rev. A **64**, 061402 (2001).

[131] M. Klaiber, K. Z. Hatsagortsyan, and C. H. Keitel, "Above-threshold ionization beyond the dipole approximation," Phys. Rev. A **71**, 033408 (2005).

[132] A. D. DiChiara, I. Ghebregziabher, R. Sauer, J. Waesche, S. Palaniyappan, B. L. Wen, and B. C. Walker, Phys. Rev. Lett. **101**, 173002 (2008).

[133] N. Ekanayake, S. Luo, P. D. Grugan, W. B. Crosby, A. D. Camilo, C. V. McCowan, R. Scalzi, A. Tramontozzi, L. E. Howard, S. J. Wells, C. Mancuso, T. Stanev, M. F. Decamp, and B. C. Walker, "Electron shell ionization of atoms with classical, relativistic scattering," Phys. Rev. Lett. **110**, 203003 (2013).

[134] C. Smeenk, L. Arissian, A. Staudte, D. Villeneuve, and P. Corkum, "Momentum space tomographic imaging of photoelectrons," J. Phys. B **42**, 185402 (2009).

[135] M. Klaiber, E. Yakaboylu, H. Bauke, K. Z. Hatsagortsyan, and C. H. Keitel, "Under-the-barrier dynamics in laser-induced relativistic tunneling," Phys. Rev. Lett. **110**, 153004 (2013).

[136] S. Chelkowski, A. D. Bandrauk, and P. B. Corkum, "Photon momentum sharing between an electron and an ion in photoionization: From one-photon (photoelectric effect) to multiphoton absorption," Phys. Rev. Lett. **113**, 263005 (2014).

[137] D. Cricchio, E. Fiordilino, and K. Z. Hatsagortsyan, "Momentum partition between constituents of exotic atoms during laser-induced tunneling ionization," Phys. Rev. A **92**, 023408 (2015).

[138] S. Chelkowski, A. D. Bandrauk, and P. B. Corkum, "Photon-momentum transfer in multiphoton ionization and in time-resolved holography with photoelectrons," Phys. Rev. A **92**, 051401 (2015).

[139] C. Huang, Q. Liao, Y. Zhou, and P. Lu, "Role of coulomb focusing on the electron transverse momentum of above-threshold ionization," Opt. Express **18**, 14293 (2010).

[140] S. A. Berman, C. Chandre, and T. Uzer, "Persistence of coulomb focusing during ionization in the strong-field regime," Phys. Rev. A **92**, 023422 (2015).

[141] S. A. Kelvich, W. Becker, and S. P. Goreslavski, "Caustics and catastrophes in above-threshold ionization," Phys. Rev. A **96**, 023427 (2017).

[142] J. Maurer, B. Willenberg, J. Daněk, B. W. Mayer, C. R. Phillips, L. Gallmann, M. Klaiber, K. Z. Hatsagortsyan, C. H. Keitel, and U. Keller, "Probing the ionization wave packet and recollision dynamcis with an elliptically polarized strong laser field in the nondipole regime," Phys. Rev. A **97**, 013404 (2018).

[143] C. I. Blaga, J. Xu, A. D. DiChiara, E. Sistrunk, K. Zhang, P. Agostini, T. A. Miller, L. F. DiMauro, and C. D. Lin, "Imaging ultrafast molecular dynamics with laser-induced electron diffraction," Nature **483**, 194 EP (2012).

[144] M. Y. Ivanov, "Single molecules filmed dancing on a table top," Nature **483**, 161 EP (2012).

[145] M. G. Pullen, B. Wolter, A.-T. Le, M. Baudisch, M. Hemmer, A. Senftleben, C. D. Schröter, J. Ullrich, R. Moshammer, C.-D. Lin, and J. Biegert, "Imaging an aligned polyatomic molecule with laser-induced electron diffraction," Nat. Commun. **6**, 7262 (2015).

[146] Y. Huismans, A. Rouzée, A. Gijsbertsen, J. H. Jungmann, A. S. Smolkowska, P. S. W. M. Logman, F. Lépine, C. Cauchy, S. Zamith, T. Marchenko, J. M. Bakker, G. Berden, B. Redlich, A. F. G. van der Meer, H. G. Muller, W. Vermin, K. J. Schafer, M. Spanner, M. Y. Ivanov, O. Smirnova, D. Bauer, S. V. Popruzhenko, and M. J. J. Vrakking, "Time-resolved holography with photoelectrons," Science (New York, N.Y.) **331**, 61 (2011).

[147] Y. Huismans, A. Gijsbertsen, A. S. Smolkowska, J. H. Jungmann, A. Rouzée, P. S. W. M. Logman, F. Lépine, C. Cauchy, S. Zamith, T. Marchenko, J. M. Bakker, G. Berden, B. Redlich, A. F. G. van der Meer, M. Y. Ivanov, T.-M. Yan, D. Bauer, O. Smirnova, and M. J. J. Vrakking, "Scaling Laws for Photoelectron Holography in the Midinfrared Wavelength Regime," Phys. Rev. Lett. **109**, 013002 (2012).

[148] M. Spanner, O. Smirnova, P. B. Corkum, and M. Y. Ivanov, "Reading diffraction images in strong field ionization of diatomic molecules," Journal of Physics B: Atomic, Molecular and Optical Physics **37**, L243 (2004).

[149] X.-B. Bian, Y. Huismans, O. Smirnova, K.-J. Yuan, M. J. J. Vrakking, and A. D. Bandrauk, "Subcycle interference dynamics of time-resolved photoelectron holography with midinfrared laser pulses," Phys. Rev. A **84**, 043420 (2011).

[150] C. Liu, G. Golovin, S. Chen, J. Zhang, B. Zhao, D. Haden, S. Banerjee, J. Silano, H. Karwowski, and D. Umstadter, "Generation of 9 mev x -rays by all-laser-driven compton scattering with second-harmonic laser light," Opt. Lett. **39**, 4132 (2014).

[151] A. S. Maxwell, A. Al-Jawahiry, T. Das, and C. F. d. M. Faria, "Coulomb-corrected quantum interference in above-threshold ionization: Working towards multitrajectory electron holography," Phys. Rev. A **96**, 023420 (2017).

[152] N. I. Shvetsov-Shilovski and M. Lein, "Effects of the coulomb potential in interference patterns of strong-field holography with photoelectrons," Phys. Rev. A **97**, 013411 (2018).

[153] T. Marchenko, Y. Huismans, K. J. Schafer, and M. J. J. Vrakking, "Criteria for the observation of strong-field photoelectron holography," Phys. Rev. A **84**, 053427 (2011).

[154] X.-B. Bian and A. D. Bandrauk, "Attosecond time-resolved imaging of molecular structure by photoelectron holography," Phys. Rev. Lett. **108**, 263003 (2012).

[155] M. Li, J. Yuan, X. Sun, J. Yu, Q. Gong, and Y. Liu, "Recollision-induced subcycle interference of molecules in strong laser fields," Phys. Rev. A **89**, 033425 (2014).

[156] T. Zuo, A. Bandrauk, and P. Corkum, "Laser-induced electron diffraction: a new tool for probing ultrafast molecular dynamics," Chemical Physics Letters **259**, 313 (1996).

[157] H.-C. Shao and A. F. Starace, "Detecting electron motion in atoms and molecules," Phys. Rev. Lett. **105**, 263201 (2010).

[158] M. Haertelt, X.-B. Bian, M. Spanner, A. Staudte, and P. B. Corkum, "Probing molecular dynamics by laser-induced backscattering holography," Phys. Rev. Lett. **116**, 133001 (2016).

[159] S. G. Walt, N. Bhargava Ram, M. Atala, N. I. Shvetsov-Shilovski, A. von Conta, D. Baykusheva, M. Lein, and H. J. Wörner, "Dynamics of valence-shell electrons and nuclei probed by strong-field holography and rescattering," Nature Communications **8**, 15651 EP (2017). Article.

[160] M. Li, J.-W. Geng, H. Liu, Y. Deng, C. Wu, L.-Y. Peng, Q. Gong, and Y. Liu, "Classical-quantum correspondence for above-threshold ionization," Phys. Rev. Lett. **112**, 113002 (2014).

[161] M. Li, J.-W. Geng, M. Han, M.-M. Liu, L.-Y. Peng, Q. Gong, and Y. Liu, "Subcycle nonadiabatic strong-field tunneling ionization," Phys. Rev. A **93**, 013402 (2016).

[162] N. I. Shvetsov-Shilovski, M. Lein, L. B. Madsen, E. Räsänen, C. Lemell, J. Burgdör-fer, D. G. Arbó, and K. Tőkési, "Semiclassical two-step model for strong-field ion-ization," Phys. Rev. A **94**, 013415 (2016).

[163] X.-Y. Lai, C. Poli, H. Schomerus, and C. F. d. M. Faria, "Influence of the coulomb potential on above-threshold ionization: A quantum-orbit analysis beyond the strong-field approximation," Phys. Rev. A **92**, 043407 (2015).

[164] X. Lai, S. Yu, Y. Huang, L. Hua, C. Gong, W. Quan, C. F. d. M. Faria, and X. Liu, "Near-threshold photoelectron holography beyond the strong-field approximation," Phys. Rev. A **96**, 013414 (2017).

[165] A. J. F. Siegert, "On the derivation of the dispersion formula for nuclear reactions," Phys. Rev. **56**, 750 (1939).

[166] O. I. Tolstikhin and T. Morishita, "Adiabatic theory of ionization by intense laser pulses: Finite-range potentials," Phys. Rev. A **86**, 043417 (2012).

[167] Y. Zhou, O. I. Tolstikhin, and T. Morishita, "Near-forward rescattering photoelec-tron holography in strong-field ionization: Extraction of the phase of the scattering amplitude," Phys. Rev. Lett. **116**, 173001 (2016).

[168] M. Klaiber, J. Daněk, E. Yakaboylu, K. Z. Hatsagortsyan, and C. H. Keitel, "Strong-field ionization via a high-order coulomb-corrected strong-field approxi-mation," Phys. Rev. A **95**, 023403 (2017).

[169] J.-P. Connerade, *Highly Excited Atoms* (Cambridge, UK: Cambridge University Press, 2005).

[170] G. F. Gribakin and M. Y. Kuchiev, "Multiphoton detachment of electrons from negative ions," Phys. Rev. A **55**, 3760 (1997).

[171] B. M. Karnakov, V. D. Mur, V. S. Popov, and S. V. Popruzhenko, "Ionization of atoms and ions by intense laser radiation," JETP Letters **93**, 238 (2011).

[172] P. P. Pereyra, *Fundamentals of Quantum Physics. Undergraduate Lecture Notes in Physics.* (Springer, Berlin, Heidelberg, 2012).

[173] L. D. Landau and E. M. Lifshitz, *The Classical Theory of Fields* (Elsevier, Oxford, 1975).

[174] R. Loudon, "One-Dimensional Hydrogen Atom," Am. J. Phys. **27**, 649 (1959).

[175] R. Loudon, "One-dimensional hydrogen atom," Proc. Roy. Soc. (London) A **472**, 20150534 (2016).

[176] G. Abramovici and Y. Avishai, "The one-dimensional coulomb problem," Journal of Physics A: Mathematical and Theoretical **42**, 285302 (2009).

[177] H. Kleinert, *Path Integrals in Quantum Mechanics, Statistics, Polymer Physics, and Financial Markets* (World Scientific, Singapore, 2006).

[178] S. V. Popruzhenko, V. D. Mur, V. S. Popov, and D. Bauer, "Strong field ionization rate for arbitrary laser frequencies," Phys. Rev. Lett. **101**, 193003 (2008).

[179] T. Nubbemeyer, K. Gorling, A. Saenz, U. Eichmann, and W. Sandner, "Strong-field tunneling without ionization," Phys. Rev. Lett. **101**, 233001 (2008).

[180] U. Eichmann, T. Nubbemeyer, H. Rottke, and W. Sandner, "Acceleration of neutral atoms in strong short-pulse laser fields," Nature **461**, 1261 (2009).

[181] E. P. Wigner, Phys. Rev. **98**, 145 (1955).

[182] E. Yakaboylu, M. Klaiber, and K. Z. Hatsagortsyan, "Wigner time delay for tunneling ionization via the electron propagator," Phys. Rev. A **90**, 012116 (2014).

[183] J. Maurer, J. Daněk, B. Willenberg, B. W. Mayer, C. R. Phillips, L. Gallmann, M. Klaiber, K. Z. Hatsagortsyan, C. H. Keitel, and U. Keller, "Photoelectron holography," (2018). In preparation.

[184] H. R. Reiss, Phys. Rev. A **42**, 1476 (1990).

[185] H. R. Reiss, "Relativistic strong-field photoionization," J. Opt. Soc. Am. B **7**, 574 (1990).

[186] T. Keil and D. Bauer, "Coulomb-corrected strong-field quantum trajectories beyond dipole approximation," Journal of Physics B: Atomic, Molecular and Optical Physics **50**, 194002 (2017).

[187] M. Klaiber, E. Yakaboylu, and K. Z. Hatsagortsyan, "Above-threshold ionization with highly charged ions in superstrong laser fields. ii. relativistic coulomb-corrected strong-field approximation," Phys. Rev. A **87**, 023418 (2013).

[188] M. Klaiber, , K. Z. Hatsagortsyan, and C. H. Keitel, "Tunneling dynamics in multiphoton ionization and attoclock calibration," Phys. Rev. Lett. **114**, 083001 (2015).

[189] X.-Y. Lai, C. Poli, H. Schomerus, and C. F. d. M. Faria, "Influence of the coulomb potential on above-threshold ionization: A quantum-orbit analysis beyond the strong-field approximation," Phys. Rev. A **92**, 043407 (2015).

[190] M. Dantus, R. M. Bowman, and A. H. Zewail, "Femtosecond laser observations of molecular vibration and rotation," Nature **343**, 737 EP (1990).

[191] J. Daněk, K. Z. Hatsagortsyan, and C. H. Keitel, "Analytical approach to coulomb focusing in strong field ionization," Submitted, preprint on arXiv:1707.06921v2.

[192] I. S. Gradshteyn and I. M. Ryzhik, *Table of Integrals, Series, and Products* (Academic Press, New York and London, 1965).

[193] N. Shvetsov-Shilovski, S. Goreslavski, S. Popruzhenko, and W. Becker, "Capture into rydberg states and momentum distributions of ionized electrons," Laser Physics **19**, 1550 (2009).

[194] J. Daněk, M. Klaiber, K. Z. Hatsagortsyan, C. H. Keitel, B. Willenberg, J. Maurer, B. W. Mayer, C. R. Phillips, L. Gallmann, and U. Keller, "Interplay between coulomb-focusing and non-dipole effects in strong-field ionization with elliptical polarization," Submitted.

[195] A. N. Pfeiffer, C. Cirelli, M. Smolarski, D. Dimitrovski, M. Abu-samha, L. B. Madsen, and U. Keller, "Attoclock reveals natural coordinates of the laser-induced tunnelling current flow in atoms," Nature Phys. **8**, 76 (2012).

[196] P. A. Batishchev, O. I. Tolstikhin, and T. Morishita, "Atomic siegert states in an electric field: Transverse momentum distribution of the ionized electrons," Phys. Rev. A **82**, 023416 (2010).

[197] D. Gabor, "Nobel lecture: Holography," (1971).

[198] C. C. Chirilă, N. J. Kylstra, R. M. Potvliege, and C. J. Joachain, Phys. Rev. A **66**, 063411 (2002).

[199] H. Reiss, "Theoretical methods in quantum optics: S-matrix and Keldysh techniques for strong-field processes," Prog. Quant. El. **16**, 1 (1992).

[200] M. Li, J.-W. Geng, H. Liu, Y. Deng, C. Wu, L.-Y. Peng, Q. Gong, and Y. Liu, "Classical-quantum correspondence for above-threshold ionization," Phys. Rev. Lett. **112**, 113002 (2014).

[201] L. D. Landau and E. M. Lifshitz, *Mechanics* (Pergamon, Oxford, 1993).

[202] N. I. Shvetsov-Shilovski, D. Dimitrovski, and L. B. Madsen, "Ionization in elliptically polarized pulses: Multielectron polarization effects and asymmetry of photoelectron momentum distributions," Phys. Rev. A **85**, 023428 (2012).

[203] Y. S. Lee, W. C. Ermler, and K. S. Pitzer, "Ab initio effective core potentials including relativistic effects. i. formalism and applications to the xe and au atoms," The Journal of Chemical Physics **67**, 5861 (1977).

[204] F. J. Rogers, "Analytic electron-ion effective potentials for $z \leq 55$," Phys. Rev. A **23**, 1008 (1981).

[205] D. B. Milošević, W. Becker, M. Okunishi, G. Prümper, K. Shimada, and K. Ueda, "Strong-field electron spectra of rare-gas atoms in the rescattering regime: enhanced spectral regions and a simulation of the experiment," Journal of Physics B: Atomic, Molecular and Optical Physics **43**, 015401 (2010).

[206] NIST Computational Chemistry Comparison and Benchmark Database (http://cccbdb.nist.gov/).

[207] D. Dimitrovski, C. P. J. Martiny, and L. B. Madsen, "Strong-field ionization of polar molecules: Stark-shift-corrected strong-field approximation," Phys. Rev. A **82**, 053404 (2010).

Acknowledgements

At this point I would like to thank all the people who lent me a helping hand during the preparations of my thesis and of my graduation.

First, I thank my fist supervisor Prof. Christoph H. Keitel very much for accepting me as a member of his division at the Max Planck Institute for Nuclear Physics in Heidelberg and for always being ready to support me and my research. I greatly profited from the cooperative and inspiring working environment in the division that he has created. I am very thankful that he was always there for me with his rich scientific experience and expertise to discuss the physics or the problems connected to publication of my results.

I would like to express my gratitude towards my mentor Dr. habil. Karen Z. Hatsagortsyan who introduced me to the field of strong-field ionization physics. He always supported me and my scientific growth. Moreover, he was extremely patient and encouraging during my first clumsy steps in the field. He always found time for a short discussion or to answer my questions. My research extended over several still unsettled branches of the strong-field physics addressed in a great details thanks to his guidance. I will always remember our long, but interesting and sometimes also very challenging discussions about ionization physics and new results in particular.

I would also like to thank our collaborator Dr. Michael Klaiber with whom I was working on the Coulomb-corrected Strong-field approximation. I strongly benefited from his insight into the Strong-field approximation and its extended versions. He was reachable for any questions and ready to help at any time.

I thank also our collaborators Dr. Jochen Maurer and Benjamin Willenberg from ETH Zürich who conducted several interesting experiments and involved us in the analysis of the results which motivated a substantial part of my research as presented in this thesis. I would also like to thank them for being always supportive and allowing me to use their results for presentations.

I would also like to thank Prof. Dr. Björn Malte Schäfer who agreed on being my second referee and, therefore, also on writing a report on my thesis.

Many thanks go also to the proofreaders of my thesis: Niklas Michel, Kamil Dzikowski, Chunhai Lyu, Halil Cakir, Daniel Bakucz Canário, Dr. Jonas Gunst and Shikha Bhadoria whose remarks significantly improved the manuscript.

In addition, I would also like to thank our division secretary Sibel Babacan for helping me to fight any administrative paper work.

Special thanks go to all my present or former officemates with whom I enjoyed my working days at the Max Planck Institute for Nuclear Physics over the last years, in

particular, Shikha Bhadoria, Niklas Michel, Dr. Jonas Gunst, Nicolas Teeny and Kamil Dzikowski.

Velký dík patří také mým rodičům, mojí babičce a mému nedávno zesnulému dědečkovi, kteří mě po celou dobu mého studia v Heidelbergu podporovali a stáli při mně. V neposlední řadě chci také poděkovat svému bratrovi i za jeho podporu, ale hlavně za jeho letní návštěvy.